



# Mechanics of super-insulating silica aerogel composites : a coupled experimental and numerical approach

Guillaume Hamelin

## ► To cite this version:

Guillaume Hamelin. Mechanics of super-insulating silica aerogel composites : a coupled experimental and numerical approach. Materials Science [cond-mat.mtrl-sci]. Université Grenoble Alpes [2020-..], 2021. English. NNT : 2021GRALI101 . tel-03601126

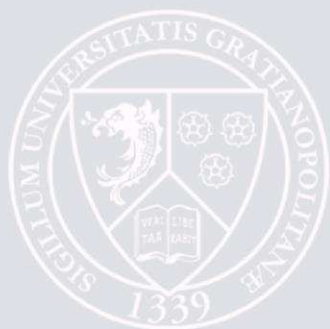
**HAL Id: tel-03601126**

**<https://theses.hal.science/tel-03601126>**

Submitted on 8 Mar 2022

**HAL** is a multi-disciplinary open access archive for the deposit and dissemination of scientific research documents, whether they are published or not. The documents may come from teaching and research institutions in France or abroad, or from public or private research centers.

L'archive ouverte pluridisciplinaire **HAL**, est destinée au dépôt et à la diffusion de documents scientifiques de niveau recherche, publiés ou non, émanant des établissements d'enseignement et de recherche français ou étrangers, des laboratoires publics ou privés.



## THÈSE

Pour obtenir le grade de

## DOCTEUR DE L'UNIVERSITÉ GRENOBLE ALPES

Spécialité : 2MGE : Matériaux, Mécanique, Génie civil,  
Electrochimie

Arrêté ministériel : 25 mai 2016

Présentée par

**Guillaume HAMELIN**

Thèse dirigée par **Christophe MARTIN**, Directeur de recherche,  
Université Grenoble Alpes  
et co-encadrée par **David JAUFFRES**, Grenoble INP  
et **Sylvain MEILLE**

préparée au sein du **Laboratoire Science et Ingénierie des  
Matériaux et Procédés**  
dans l'**École Doctorale I-MEP2 - Ingénierie - Matériaux,  
Mécanique, Environnement, Energétique, Procédés,  
Production**

**Comportement mécanique de composites  
super-isolants d'aérogel de silice : une approche  
couplée expérimentale et numérique**

**Mechanics of super-insulating silica aerogel  
composites: a coupled experimental and  
numerical approach**

Thèse soutenue publiquement le **7 décembre 2021**,  
devant le jury composé de :

**Monsieur Christophe MARTIN**

DIRECTEUR DE RECHERCHE, CNRS délégation Alpes, Directeur de  
thèse

**Monsieur Sylvain MEILLE**

PROFESSEUR DES UNIVERSITES, INSA Lyon, Co-directeur de thèse

**Monsieur Wim MALFAIT**

DOCTEUR EN SCIENCES, EMPA (Swiss Federal Laboratories for  
Materials Science and Technology), Rapporteur

**Madame Sylvie CALAS-ETIENNE**

MAITRE DE CONFERENCES HDR, Université de Montpellier,  
Rapporteuse

**Monsieur Etienne BARTHEL**

DIRECTEUR DE RECHERCHE, CNRS délégation Paris Centre,  
Président du jury

**Monsieur Damien ANDRE**

MAITRE DE CONFERENCE, Université de Limoges, Examineur

**Monsieur Sylvain DEVILLE**

DIRECTEUR DE RECHERCHE, CNRS délégation Rhône Auvergne,  
Examineur



# Abstract

As new regulations for energy efficiency tighten in the building sector, the thickness required for thermal insulation of buildings with conventional materials (glass wool, polymeric foams...) can become prohibitive. This is a strong driving force for the development of a new class of products, the Super-Insulation at Atmospheric Pressure (SIAP) materials, based on the use of Silica Aerogel Particles (SAP). Silica aerogels are characterized by a very high nanoporosity (95 %) responsible for their unprecedented low thermal conductivities but also for their very low mechanical properties, limiting the handling ability and the use of SIAP products in building applications. The objective of this work is to gain a better understanding of the mechanical behaviour of SIAP in order to improve their mechanical properties, mainly fracture toughness, while preserving their exceptional thermal properties (target thermal conductivity of approximately  $15 \text{ mWm}^{-1}\text{K}^{-1}$ ). The materials studied here are composite panels produced using a bimodal distribution of SAP and a latex binder. Different particulate composites are processed and their microstructural, mechanical and thermal properties are characterized. An original numerical model based on the Discrete Element Method (DEM) is then developed. First, mechanical characterization (crushing) of individual silica aerogel particles is used to calibrate the material parameters of the numerical particles. The simulated failure of these digital particles is accurate enough to reproduce crack patterns similar to those observed by X-ray tomography in real silica aerogel particles. Second, large numerical particulate composites are generated using the calibrated numerical silica aerogel particles in order to simulate the fracture of composite samples and extract macroscopic mechanical properties. The influence of the SAP size distribution and fiber incorporation on the composite fracture behaviour is assessed both experimentally and numerically. Lastly, the thermal performance of composite panels without and with fibers is characterized leading to the conclusion that properly managed fiber reinforcement can result in a significant increase in toughness (x1.5 to x2) while increasing the thermal conductivity by only 1-2  $\text{mWm}^{-1}\text{K}^{-1}$ .

**Keywords:** silica aerogel particles, particulate composites, thermal super-insulator, discrete element simulation, experimental characterization, fracture toughness





## Résumé

Avec le renforcement des réglementations concernant l'efficacité énergétique dans le secteur du bâtiment, l'épaisseur requise pour l'isolation thermique des bâtiments avec des matériaux conventionnels (laine de verre, mousses polymériques...) peut devenir prohibitive. C'est un puissant moteur pour le développement d'une nouvelle classe de produits, les matériaux Super-Isolants à Pression Atmosphérique (SIPA), basés sur l'utilisation de particules d'aérogel de silice (SAP). Les aérogels de silice sont caractérisés par une nanoporosité très élevée (95 %) à l'origine de leur faible conductivité thermique mais aussi de leurs très faibles propriétés mécaniques, limitant la capacité à manipuler et utiliser des produits SIPA pour des applications dans le secteur du bâtiment. L'objectif de ce travail est de mieux comprendre le comportement mécanique des SIPA afin d'améliorer leurs propriétés mécaniques, principalement la ténacité, tout en préservant leurs propriétés thermiques exceptionnelles (conductivité thermique cible d'environ  $15 \text{ mWm}^{-1}\text{K}^{-1}$ ). Les matériaux étudiés ici sont des panneaux composites produits à partir d'une distribution bimodale de SAP et d'un liant polymère. Différents composites sont fabriqués et leurs propriétés microstructurales, mécaniques et thermiques sont caractérisées. Un modèle numérique original basé sur la méthode des éléments discrets (DEM) est développé. La caractérisation mécanique (compression) des particules individuelles d'aérogel de silice est utilisée pour calibrer les paramètres matériau des particules numériques. La simulation de la rupture de ces particules numériques est suffisamment précise pour reproduire des réseaux de fissures similaires à ceux observés par tomographie à rayons X dans des particules réelles d'aérogel de silice. Des composites numériques de grande taille sont générés à l'aide des particules numériques calibrées d'aérogel de silice afin de simuler la rupture des échantillons composites et d'en extraire les propriétés mécaniques macroscopiques. L'influence de la distribution de taille des SAP et de l'incorporation des fibres sur le comportement à la rupture du composite est évaluée à la fois expérimentalement et numériquement. Enfin, la performance thermique des panneaux composites sans et avec fibres est caractérisée, ce qui amène à la conclusion qu'un renforcement fibreux optimisé du point de vue de l'homogénéité de la dispersion et de l'orientation des fibres peut permettre une augmentation significative de la ténacité (x1,5 à x2) tout en augmentant la conductivité thermique de seulement  $1\text{-}2 \text{ mWm}^{-1}\text{K}^{-1}$ .

**Keywords:** particules d'aérogel de silice, composites particulaires, super-isolant thermique, simulation par éléments discrets, caractérisation expérimentale, ténacité



# Acknowledgements

This thesis is part of the COMPASS project funded by the French region Auvergne Rhône-Alpes and managed by the CNRS. It brings together in a partnership the following French structures: the SIMaP (Grenoble) and Matéis (Lyon) laboratories, the companies EDF (Moret-Loing-et-Orvanne), Enersens (Bourgouin-Jaillieu) and CSTB (Grenoble). Completing a thesis is certainly not an easy task. That is why I would like to thank a number of people for their support and expertise over the three years of this work. First of all, I would like to thank my thesis director Christophe Martin (SIMaP) and my co-supervisors David Jauffrès (SIMaP) and Sylvain Meille (Matéis) who gave me great freedom of action while guiding and training me when I needed it. Similar thanks go to Geneviève Foray (Matéis) and Bernard Yrieix (EDF) who gave me a lot of their time and expertise as I made and characterized aerogel composites. Christophe Gourgues (EDF) is also thanked for his help during the manufacturing stages of the composites. I would also like to thank Pierre Lhuissier (SIMaP), Xavier Bataillon (SIMaP), Cyril Rajon (SIMaP), Stéphane Coindeau (SIMaP) and Karine Masenelli-Varlot (Matéis) who helped me to carry out X-ray tomography observations and to design the setup for in-situ tests. I would like to thank Julie Villanova and Pauline Gravier from the European Synchrotron Radiation Facility who performed X-ray tomography scans allowing a thorough observation of the microstructure of my materials. I would like to thank Claude Pompéo (CSTB) and Daniel Quenard (CSTB) as well as David Lesueur (Enersens) who provided the necessary equipment for thermal measurements and helped me process the associated data. In general, I would like to thank all the staff of the scientific and administrative teams of the SIMaP and Matéis laboratories who helped and supported me during these three years. Finally, I would like to thank the members of my thesis defense jury who came to hear me present my research, which was followed by a scientific discussion that I particularly appreciated. These people are Wim Malfait (EMPA, Swiss Federal Laboratories for Materials Science and Technology) and Sylvie Calas-Etienne (University of Montpellier) who reviewed my thesis manuscript, Etienne Barthel (CNRS) who led the jury, Damien André (University of Limoges) and Sylvain Deville (CNRS) who were examiners.



# Contents

<b>Abstracts</b>	<b>I</b>
I . . . . .	I
I . . . . .	III
<b>Acknowledgements</b>	<b>V</b>
<b>Table of Contents</b>	<b>X</b>
<b>Introduction générale</b>	<b>1</b>
0.1 Contexte et objectifs . . . . .	1
0.2 Un modèle par éléments discrets appliqué aux composites particulaires	
aérogel de silice . . . . .	2
0.3 Organisation du manuscrit du doctorat . . . . .	3
<b>1 General introduction</b>	<b>5</b>
1.1 Context and objectives . . . . .	5
1.2 A discrete element model applied to particulate silica aerogel composites	6
1.3 PhD manuscript organization . . . . .	6
<b>2 Literature review</b>	<b>9</b>
2.1 Thermal insulators applied to the building industry . . . . .	9
2.1.1 Environmental background . . . . .	9
2.1.2 Thermal insulation . . . . .	10
2.2 A competitive super-insulating material: silica aerogel . . . . .	12
2.2.1 Structure of silica aerogels . . . . .	12
2.2.2 Silica aerogels production process . . . . .	13
2.2.2.1 Gel preparation . . . . .	13
2.2.2.2 Hydrophobic silica aerogels . . . . .	13
2.2.2.3 Drying . . . . .	14
2.2.3 Thermal and mechanical properties . . . . .	14
2.2.3.1 Thermal properties . . . . .	15
2.2.3.2 Mechanical properties . . . . .	19
2.2.3.3 Conclusion on the mechanics of silica aerogel . . . . .	25
2.3 Super-insulating composites and products based on silica aerogels for	
the building industry . . . . .	25
2.3.1 Vacuum insulation panels (VIP) . . . . .	25
2.3.2 Aerogel glazing units (AGU) . . . . .	26
2.3.3 Blankets . . . . .	27
2.3.4 Cements, mortars and plasters . . . . .	28
2.3.5 Particulate aerogel composite insulating panels . . . . .	28

2.3.5.1	Basic composition and structure	29
2.3.5.2	Thermal and mechanical properties	30
2.4	Conclusion	31
<b>3</b>	<b>Experimental methods</b>	<b>33</b>
3.1	Visualization methods	33
3.1.1	X-ray tomography	33
3.1.1.1	X-ray micro-tomography: tungsten source	33
3.1.1.2	X-ray nano-tomography: synchrotron source	34
3.1.2	Scanning electron microscopy (SEM)	35
3.2	Structural and mechanical characterization of aerogel particles	36
3.2.1	Mercury porosimetry	36
3.2.2	Particle compression: statistical procedure	36
3.2.3	Particle compression with X-ray tomography observation	37
3.3	Particulate aerogel composite fabrication	39
3.3.1	Base components	39
3.3.2	Mixing	41
3.3.3	Molding	42
3.3.4	Drying	42
3.4	Mechanical characterization of particulate aerogel composites	43
3.4.1	Indentation	43
3.4.1.1	Instrumented macro-indentation	43
3.4.1.2	Instrumented micro-indentation	45
3.4.2	Uniaxial compression	46
3.4.3	Flexural tests	47
3.4.4	Double cleavage drilled compression tests (DCDC)	48
3.5	Thermal characterization of particulate aerogel composites	51
3.5.1	Fluxmeter measurements	51
3.5.2	CT-meter measurements	52
<b>4</b>	<b>Numerical methods</b>	<b>55</b>
4.1	Discrete element model (DEM) basics	55
4.1.1	What is DEM ?	55
4.1.2	DEM algorithm	56
4.1.2.1	Neighbors and contact detection	56
4.1.2.2	Interaction forces and moments calculation	58
4.1.2.3	Second law of Newton, Verlet integration	58
4.1.2.4	Physical parameters calculation and storage	58
4.2	Model description	59
4.2.1	Typical simulations and objectives	59
4.2.1.1	Silica aerogel particles	59
4.2.1.2	Silica aerogel particulate composites	60
4.2.2	Contact laws	61
4.2.2.1	Bonded contacts	61

4.2.2.2	Hertzian contacts	62
4.2.2.3	Fracture criterion	63
4.2.2.4	Contacts between particles and objects	64
4.2.3	Boundary conditions	64
4.2.4	Simulations stability	65
4.2.4.1	Numerical damping	65
4.2.4.2	Kinetic energy management	65
4.2.5	Macroscopic stresses calculation	66
4.3	Generation and testing of silica aerogel particles	66
4.3.1	Sample preparation	66
4.3.1.1	Initial discrete element packing	66
4.3.1.2	Shaping of aerogel particles	67
4.3.2	Uniaxial compression tests	68
4.3.3	Model calibration	69
4.4	Generation and testing of silica aerogel particulate composites	71
4.4.1	Sample preparation	71
4.4.1.1	Components	72
4.4.1.2	Packing of composite samples	72
4.4.1.3	Pre-processing of the packing	75
4.4.2	Tensile tests and fracture toughness calculation	75
4.4.3	Model calibration	77
4.5	Conclusion	80
<b>5</b>	<b>Mechanical properties of millimetric silica aerogel particles</b>	<b>83</b>
5.1	Introduction	83
5.2	Morphology of large 10-12 silica aerogel particles	83
5.3	Experimental results	84
5.3.1	Particle compression: statistical procedure	84
5.3.2	Particle compression with X-ray tomography observation	86
5.4	DEM simulations results	89
5.4.1	Calibration of DEM particles	89
5.4.2	Crack propagation in DEM and influence of initial cracks	89
5.5	Discussion	92
5.5.1	Macroscopic behaviour of aerogel particles in compression	92
5.5.2	Weibull distribution	93
5.5.3	DEM determination of Young's modulus and tensile strength	94
5.5.4	Influence of process induced cracks on the DEM mechanical be-	
	havior of aerogel particles	95
5.6	Conclusions	96
<b>6</b>	<b>Properties of particulate silica aerogel composites</b>	<b>99</b>
6.1	Introduction	99
6.2	Description of the studied composites	99
6.2.1	Experimental composites	99



6.2.2	DEM composites	101
6.3	Silica aerogel particulate composite structure	104
6.3.1	Porosity	104
6.3.2	Binder	106
6.3.3	Fibers	107
6.3.4	Polypropylene fibers	109
6.4	Composites elastic behaviour	111
6.4.1	Experimental results	111
6.4.1.1	Indentation	111
6.4.1.2	Uniaxial compression	114
6.4.2	DEM results	114
6.4.3	Discussion	116
6.5	Composite fracture behaviour	117
6.5.1	Experimental results	117
6.5.1.1	DCDC tests	117
6.5.1.2	SENB flexural testing	120
6.5.1.3	Uniaxial compression	120
6.5.2	DEM results	121
6.5.3	Discussion	124
6.6	Composite thermal properties	128
6.6.1	Flux-meter testing	128
6.6.2	Current Transformer (CT)-meter testing	128
6.7	Conclusion	130
<b>7</b>	<b>General conclusion and prospects</b>	<b>133</b>
7.1	Conclusion	133
7.2	Prospects	134
7.2.1	Composite preparation process	135
7.2.2	Complementary characterization of SAP	135
7.2.3	Precise measurement of fiber shear interfacial stress	136
7.2.4	Extended thermal characterization and simulation	136
7.2.5	DEM model structural parameters exploration	136
	<b>Appendices</b>	<b>137</b>
<b>A</b>	<b>DEM composite sample compaction with fibers: additional data</b>	<b>139</b>
<b>B</b>	<b>Fracture of DEM aerogel particles P2 to P5</b>	<b>141</b>
	References	145

# Introduction générale

## 0.1 Contexte et objectifs

Dans nos sociétés modernes où la majeure partie de l'énergie produite est encore obtenue par la combustion de combustibles non renouvelables comme le charbon, le pétrole ou le gaz naturel, la réduction des émissions de gaz à effet de serre est devenue l'un des principaux défis à l'échelle mondiale. En effet, il est désormais connu que les émissions de gaz à effet de serre provenant de l'activité humaine accélèrent fortement le réchauffement de la planète, mettent en danger la biodiversité et modifient le climat à l'échelle mondiale. Ces changements menacent déjà la vie et le foyer de millions de personnes dans le monde aujourd'hui et pourraient affecter encore plus de personnes à l'avenir.

La réduction de la consommation d'énergie à l'échelle mondiale est l'un des moyens les plus efficaces de réduire les émissions de gaz à effet de serre. Cette thèse se concentre sur l'énergie consommée pour la régulation de la température dans les bâtiments. Actuellement, la plupart de cette énergie est consommée en raison d'un manque d'isolation thermique dans les bâtiments, qui se détériore au fil du temps ou qui n'est pas suffisante dès le départ. Dans ce contexte, de nouvelles réglementations apparaissent et tendent à imposer une meilleure isolation thermique pour les structures en construction et à encourager les rénovations pour les bâtiments plus anciens. Ces exigences peuvent être difficiles à suivre car l'utilisation de matériaux d'isolation thermique standard (comme la laine de roche ou le polystyrène) devient prohibitive dans certains cas en raison de l'épaisseur de matériau requise pour se conformer aux nouvelles réglementations. En particulier, la rénovation d'anciens lieux de vie dont la surface habitable est déjà limitée est problématique, car dans la plupart des cas, les matériaux d'isolation doivent être placés à l'intérieur des murs, ce qui réduit la surface habitable. Cette situation encourage le développement de nouveaux matériaux isolants plus efficaces qui nécessitent la pose de couches plus fines de produits isolants.

Les aérogels de silice sont des matériaux prometteurs qui présentent une très faible conductivité thermique par rapport aux matériaux isolants standard. Ils sont même classés dans les matériaux super-isolants car leur conductivité thermique (environ  $13 \text{ mWm}^{-1}\text{K}^{-1}$ ) est inférieure à celle de l'air immobile sec ( $26 \text{ mWm}^{-1}\text{K}^{-1}$ ). Cette performance thermique provient de la structure nanoporeuse de ces matériaux qui a également pour conséquence leurs mauvaises performances mécaniques. En effet, les aérogels de silice dont la densité avoisine les  $100 \text{ kgm}^{-3}$ , nécessaire pour que la conductivité thermique soit suffisamment faible, sont particulièrement difficiles à manipuler sans casse. C'est pourquoi ils ne sont presque jamais utilisés directement sous forme de grands blocs (monolithes) à des fins d'isolation. Alors que plusieurs solutions existent déjà ou sont actuellement étudiées pour utiliser les aérogels de silice dans des produits d'isolation thermique qui compensent leur fragilité, cette thèse se concentre sur le développement de composites particuliers utilisant des particules d'aérogels de silice et un liant

polymère pour la création d'un produit conservant la faible conductivité thermique des aérogels de silice et présentant une résistance mécanique et une ténacité suffisamment élevées pour sa manipulation. Afin d'atteindre cet objectif principal, les axes suivants sont développés :

- Une étude de la morphologie des particules d'aérogel de silice et des mécanismes de fracture par le biais d'une caractérisation expérimentale et d'une simulation par éléments discrets. Les particules d'aérogel de silice étant le principal composant de nos composites particulaires, leurs propriétés mécaniques et leur comportement doivent être étudiés.
- Une étude des propriétés structurales, mécaniques et thermiques des composites à base de particules d'aérogel de silice par une caractérisation expérimentale et des simulations par éléments discrets.
- Une amélioration des composites particulaires d'aérogel de silice en incorporant des fibres dans les échantillons composites expérimentaux et numériques.

Le couplage entre la caractérisation expérimentale et la simulation par éléments discrets permet une meilleure compréhension du matériau qui ne peut être atteinte en étudiant uniquement les composites expérimentaux ou numériques séparément.

## **0.2 Un modèle par éléments discrets appliqué aux composites particulaires aérogel de silice**

Le modèle d'éléments discrets créé pour ce travail de thèse maille les particules d'aérogel de silice et les composites particulaires avec des sphères. Les contacts entre ces sphères sont définis par des lois de contact et permettent de simuler la déformation et la fracture de nos matériaux. Grâce à ce maillage discret, la méthode des éléments discrets (DEM) est particulièrement bien adaptée pour simuler la fracture et la propagation des fissures.

Les propriétés structurales et mécaniques mesurées expérimentalement sont utilisées pour générer des particules d'aérogel de silice réalistes. La forme et le comportement mécanique de ces particules DEM sont calibrés pour imiter les particules comprimées expérimentalement et ainsi fournir des propriétés mécaniques macroscopiques des aérogels de silice comme le module de Young qui est difficile à mesurer expérimentalement autrement en raison de la petite taille des particules d'aérogel de silice.

L'utilisation de ces particules d'aérogel de silice calibrées par DEM dans des composites DEM parmi d'autres composants, également calibrés selon différentes procédures, permet de simuler la fracture d'échantillons composites complets. La simulation de ces composites à l'aide de DEM permet d'étudier leur comportement mécanique en modifiant des paramètres qui seraient autrement difficiles à explorer expérimentalement. Par exemple, il est possible d'explorer une distribution de fibres différente de celle obtenue expérimentalement, ou encore de considérer numériquement un liant polymère aux propriétés différentes alors qu'aucun autre n'est disponible expérimentalement.

## 0.3 Organisation du manuscrit du doctorat

Afin de présenter correctement comment le couplage de la caractérisation expérimentale et des simulations par éléments discrets conduit à une meilleure compréhension des particules d'aérogel de silice et de la mécanique des composites particulaires, le travail effectué au cours de cette thèse sera présenté en cinq chapitres principaux.

Dans le chapitre 2, une revue de la littérature permet de mieux comprendre le contexte écologique et industriel des isolants thermiques. Le processus de production des aérogels de silice est présenté tandis que leurs propriétés structurales, mécaniques et thermiques typiques sont détaillées. Différents produits isolants basés sur l'utilisation d'aérogels de silice sont listés avec un développement sur les composites d'aérogels de silice particulaires précédemment étudiés dans d'autres travaux.

Les méthodes expérimentales mises en œuvre pour la préparation de nos composites particulaires et pour la caractérisation structurale, mécanique et thermique des particules d'aérogel de silice et des composites particulaires sont développées dans le chapitre 3. De même, les méthodes numériques, y compris le fonctionnement du modèle DEM, la génération et la calibration des particules d'aérogel de silice et des composites DEM, ainsi que les procédures d'essais numériques sont détaillées dans le chapitre 4.

Le comportement mécanique des particules d'aérogel de silice est étudié dans le chapitre 5 en couplant les résultats expérimentaux et numériques. Les particules DEM générées et calibrées dans ce chapitre sont utilisées à deux fins différentes. La première est d'extraire les propriétés macroscopiques de l'aérogel de silice qui n'ont pas pu être mesurées expérimentalement en raison de la petite taille et des formes complexes des particules. La seconde est d'incorporer ces particules dans les composites particulaires DEM du chapitre 6. Ce dernier chapitre consiste à utiliser les données expérimentales sur les composites particulaires d'aérogel de silice pour alimenter et calibrer le modèle à éléments discrets, de la même manière que ce qui est fait pour les particules d'aérogel de silice au chapitre 5. Dans le chapitre 6, la fracture d'échantillons composites en DEM permet d'étudier les influences de différents paramètres et composants sur la mécanique des composites qui n'ont pas pu être facilement étudiés expérimentalement. Cette étude mécanique de nos composites est complétée par une analyse thermique expérimentale qui permet de voir l'influence du renforcement mécanique (dans ce cas l'enrobage de fibres) sur la conductivité thermique des composites particulaires d'aérogel de silice.

---

# Chapter 1

## General introduction

### 1.1 Context and objectives

In our modern societies where most of the energy produced is still obtained by burning non-renewable fuels like coal, petrol or natural gas, the reduction of green-house gas emissions has become one of the main challenges at the present time. Indeed, it is now common knowledge that the greenhouse gas emissions originating from human activity are strongly accelerating global warming, endangering biodiversity and changing the climate at a global scale. These changes are already threatening the life and the home of millions of people in the world today and may affect even more people in the future.

Reducing the global energy consumption is one of the most effective ways to reduce the greenhouse gases release. Currently a large amount of energy is consumed due to poor thermal insulation of buildings, initially insufficient or deteriorating with time. In this context, new regulations are appearing and tend to impose better thermal insulation for new buildings and encourage thermal renovation for older buildings. Yet, the use of insulation materials currently considered standard (like rock wool or expanded polystyrene) becomes prohibitive in some cases due to the significant material thickness required to comply with these new regulations. Particularly, the renovation of old building with limited living space is problematic, as in most cases, insulation materials must be placed inside the walls, which reduces the living area. This situation is encouraging the development of new and more efficient insulating materials to allow thinner layers of insulating products.

Silica aerogels are promising materials displaying a very low thermal conductivity compared to standard insulating materials. They are classified as super-insulating materials as their thermal conductivity (approximately  $13 \text{ mWm}^{-1}\text{K}^{-1}$ ) is lower than the one of still dry air ( $26 \text{ mWm}^{-1}\text{K}^{-1}$ ). This thermal performance originates from the nanoporous structure of these materials, which also results in their poor mechanical performances. Indeed, silica aerogels with a density around  $100 \text{ kgm}^{-3}$  are especially difficult to handle without breaking them. This is why they are almost never used directly as large blocks (monoliths) for insulation purposes. Several solutions already exist on the market or are currently studied to compensate the brittleness of silica aerogels for their use in thermal insulating products. This PhD focuses on one potential solution to do so: the development of particulate composites using silica aerogel particles and a polymer binder. This solution aims to develop a product that retains both the low thermal conductivity of silica aerogels and has sufficiently high mechanical strength and fracture toughness for handling. In order to reach this main objective, the following axes are developed:

- An investigation of the silica aerogel particles morphology and of the fracture mechanisms through experimental characterization and discrete element simula-

tions. The silica aerogel particles being the main component of our particulate composites, their intrinsic mechanical properties and behaviour need to be studied.

- An investigation of the silica aerogel particulate composite structural, mechanical and thermal properties through experimental characterization and discrete element simulations. In particular, the influence of the aerogel particle size distribution and of the amount of inter-aerogel particle porosity are studied.
- An experimental and numerical study of the effect of short fibers additions in the composite for mechanical reinforcement purpose.

The dialogue between experimental characterization and discrete element simulations enables a better understanding of the material properties which cannot be reached by only studying experimental or numerical composites separately.

## 1.2 A discrete element model applied to particulate silica aerogel composites

The discrete element model created for this PhD work meshes silica aerogel particles and particulate composites with spheres. The contacts between these spheres are defined by contact laws and permit to simulate the deformation and fracture of the materials of interest. Due to its discontinuous framework, the discrete element method (DEM) is particularly well adapted to simulate fracture and crack propagation.

Structural and mechanical properties measured experimentally on individual particles are used to generate realistic silica aerogel particles. The shape and mechanical behaviour of these DEM particles are calibrated to mimic particles compressed experimentally and thus to provide macroscopic mechanical properties of the silica aerogel particles. The use of these calibrated DEM silica aerogel particles in DEM composites allows the simulation of full composite samples fracture.

## 1.3 PhD manuscript organization

The work carried out during this PhD work will be presented in five main chapters.

In chapter 3 a literature review presents the ecological and thermal insulators industry context. Silica aerogels production process is detailed while their typical structural, mechanical and thermal properties are detailed. Different insulating products based on the use of silica aerogels are discussed with further development on particulate silica aerogel composites previously studied in other works.

Experimental methods used for the preparation of particulate composites and for the structural, mechanical and thermal characterization of silica aerogel particles and particulate composites are presented in chapter 4.

Numerical methods, including the DEM model, the generation and calibration of DEM silica aerogel particles and composites and the numerical testing procedures are detailed in chapter 5.

The mechanical behaviour of silica aerogel particles is studied in chapter 6 by coupling experimental and numerical results. The DEM particles generated and calibrated in this chapter are used for two different purposes. First, we extract silica aerogel macroscopic properties. Second, we incorporate these calibrated particles in DEM particulate composites in chapter 6.

Chapter 6 is dedicated to the study of aerogel particulate composites based on their structural, mechanical and thermal characterization. Particular emphasis is placed on the mechanical behaviour of the composite studied experimentally and using DEM simulations. In particular, the influence of incorporating short fibers is assessed on both the mechanical and thermal performances.





# Chapter 2

## Literature review

### 2.1 Thermal insulators applied to the building industry

#### 2.1.1 Environmental background

For some decades now, a general awareness is growing in public views and political circles concerning the necessity to plan and execute an ecological transition on a global scale. This transition should aim to preserve biodiversity and promote sustainable development by changing our way to consume natural resources and energy. One of the main points of that transition is to reduce drastically greenhouse gas emissions generated by human activity, which are mainly responsible for the global warming observed since the early 20th century. Carbon dioxide is one of the greenhouse gases most responsible for global warming and Fig. 2.1 shows that its emissions have drastically increased in the last century.

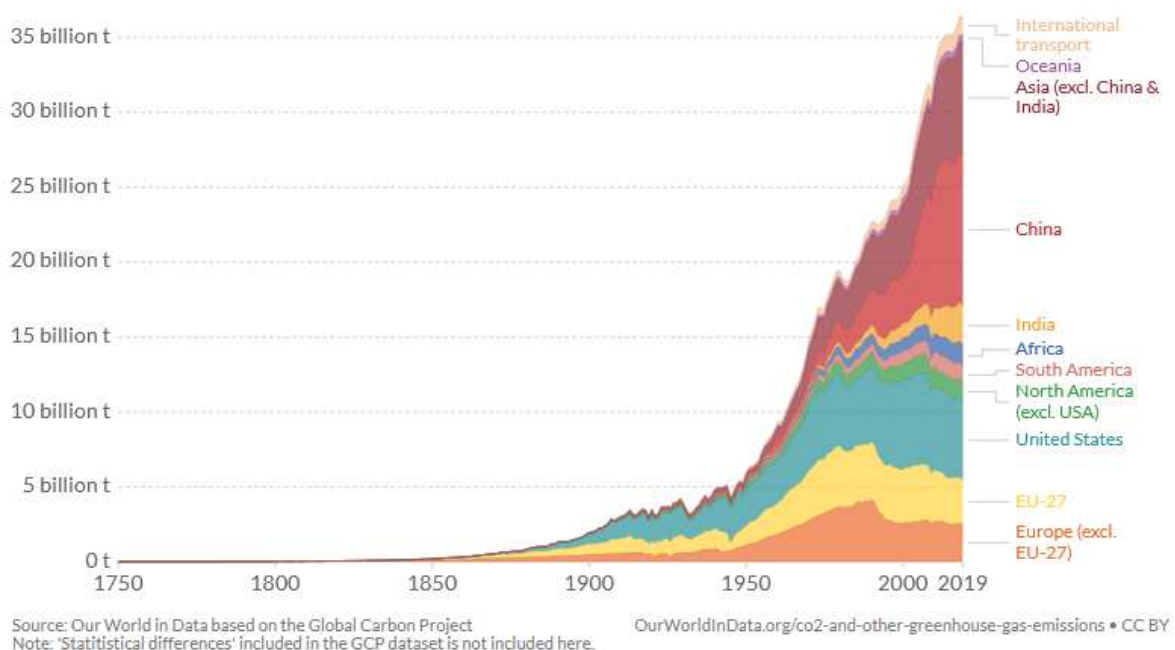


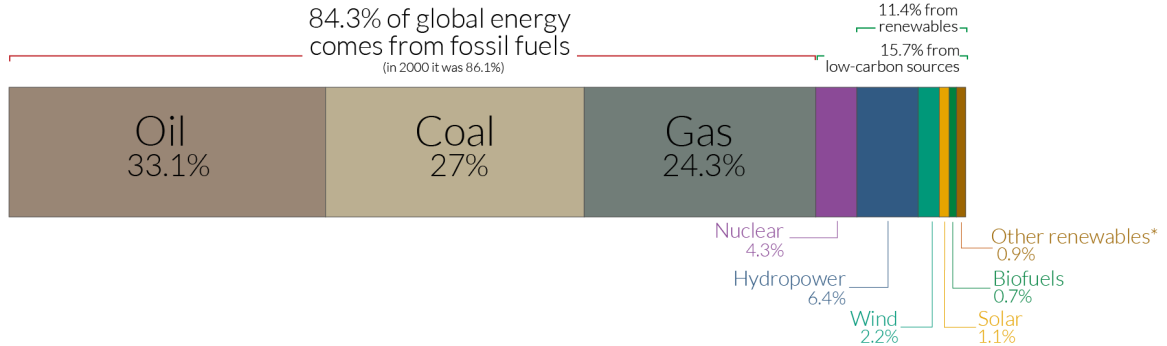
Figure 2.1: Estimated total carbon dioxide emitted by human activity since 1750 [1]

Reducing the global energy consumption is one of the most effective way to reduce greenhouse gases release as most of the energy production uses fossil fuels all around the world. In spite of the development of renewable energies and the use of nuclear energy by some countries like France, fossil energies are still the vast majority of global energy consumption as illustrated in Fig. 2.2 [1]. Some recent statistics published

by the International Energy Agency (IEA) [2] show the three main fields of energy consumption at a global scale: transport, industry and building (residential). Energy consumed for residential needs is roughly equal to the energy consumed in transports and at least 50% of this energy is generated using fossil fuels. Energy consumption in this field needs to be decreased for the global success of the ecological transition. In France, 45% of the total energy is consumed by residential and service sectors. It is interesting to note that 39% of this energy is used for heating resulting in 20% of the total energy consumed in France for this use [3]. Such a high consumption is mainly due to a poor insulation quality, most of the building in France necessitating retrofits in order to comply with new regulations.

## Global primary energy consumption by source

The breakdown of primary energy is shown based on the ‘substitution’ method which takes account of inefficiencies in energy production from fossil fuels. This is based on global energy for 2019.



\*‘Other renewables’ includes geothermal, biomass, wave and tidal. It does not include traditional biomass which can be a key energy source in lower income settings.  
 OurWorldinData.org – Research and data to make progress against the world’s largest problems.  
 Source: Our World in Data based on BP Statistical Review of World Energy (2020).  
 Licensed under CC-BY by the author Hannah Ritchie.

Figure 2.2: Global primary energy consumption by source [1]

### 2.1.2 Thermal insulation

In the building industry, thermal insulation aims at reducing the heat loss through the different surfaces separating a building from the exterior environment (walls, windows, roof, ...). When studying thermal insulators, the thermal resistance  $R$  is a key property to consider. It is a measurement of how a material subjected to a temperature difference  $\Delta T$  ( $K$ ) limits the heat flow  $\Phi$  ( $W$ ):

$$R = \frac{\Delta T}{\Phi} \quad (2.1)$$

Another property commonly used to characterize thermal insulators is the thermal conductivity  $\lambda$  ( $W.m^2.K^{-1}$ ). By applying the Fourier law in a steady-state regime, the thermal conductivity can be written for an insulator with a thickness  $e$ :

$$\lambda = \frac{\Phi e}{\Delta T} \quad (2.2)$$

From the combination of eqs. (2.1) and (2.2)  $R$  may be directly related to  $e$  and  $\lambda$ :

$$R = \frac{e}{\lambda} \quad (2.3)$$

Eq. (2.3) indicates that new regulations imposing more efficiency in the thermal insulation sector (larger thermal resistance) can be fulfilled either by using materials with smaller thermal conductivity or by increasing the thickness of insulators. Yet, increasing thickness is problematic when insulation from the inside is the only practical option, resulting in a decrease of the living area. It is therefore clear that developing new insulating solutions with a lower thermal conductivity is a promising way to comply with the new regulations in the building sector, while having a chance of being widely accepted by the population. The new regulations RT-2020 [3] in France requires for example a thermal resistance of  $4 \text{ m}^2 \cdot \text{K} \cdot \text{W}^{-1}$  for the walls of a building. This can be achieved either by installing thicker surfaces of the most widespread insulating materials on the market like rock wool or polystyrene or by using more advanced solutions like super-insulating materials, which are characterized by a thermal conductivity lower than the one of still dry air ( $26 \text{ mW} \cdot \text{m}^{-1} \cdot \text{K}^{-1}$ ). Fig. 2.3 summarize the thickness required for different insulators to comply with RT-2020 regulations. Super-insulators are generally much more expensive than conventional insulators but the investment can be offset in some cases by a smaller loss in living space, which retains most of the financial value of the renovated housing. In some situations, insulator thickness is by default limited by its application, privileging the use of super-insulating solutions. For example, the insulation of cooling systems or windows (shutters, glazing units, ...) requires efficient insulators.

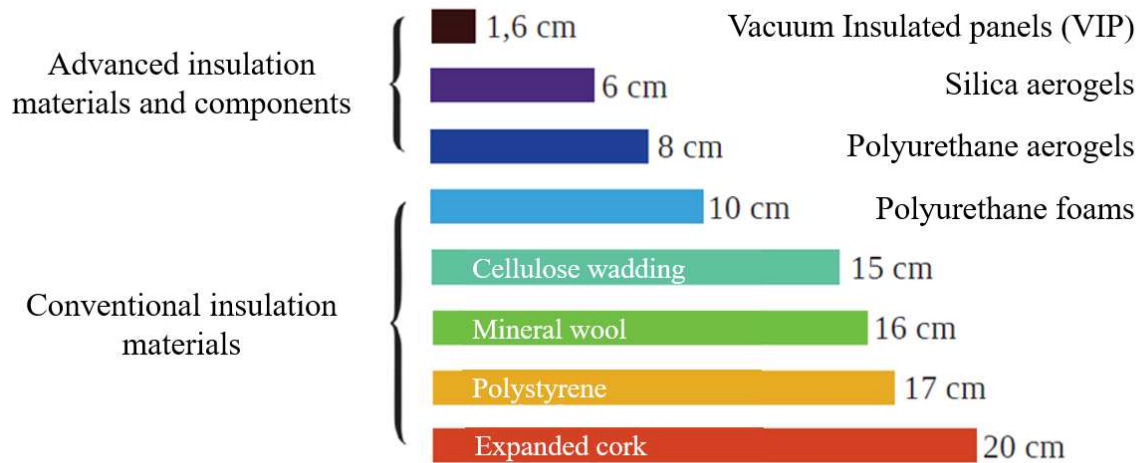


Figure 2.3: Required thickness of thermal insulators in the building sector necessary to comply with 2020 regulations in France. [4]

## 2.2 A competitive super-insulating material: silica aerogel

Silica aerogels are one of the most common super-insulators found on the current market. They have found these last years their place in the insulating materials market thanks to their super-insulator assets coupled with relatively easy production and low cost for their effectiveness [5].

### 2.2.1 Structure of silica aerogels

The low thermal conductivity of silica aerogels is ensured by a nano-structure consisting of a pearl-necklace of dense silica primary particles. The size of the silica particles forming the chains is generally between 3 et 7 nm [6]. At this scale, the structure displays a very high porosity, superior to 90%, and the typical pore characteristic size is in most cases around 10 nm [7-9]. The chains of primary silica particles group together to form larger particles called secondary particles of several hundred nanometers. The global porosity of silica aerogels is then bimodal with a large portion of the pores around 10 nm related to the pores around the silica chains inside secondary particles. The second part regroups pores larger than 10 nm and generally smaller than 100 nm formed by the agglomeration of secondary particles [10]. The primary and secondary silica particles are illustrated in Fig. 2.4.

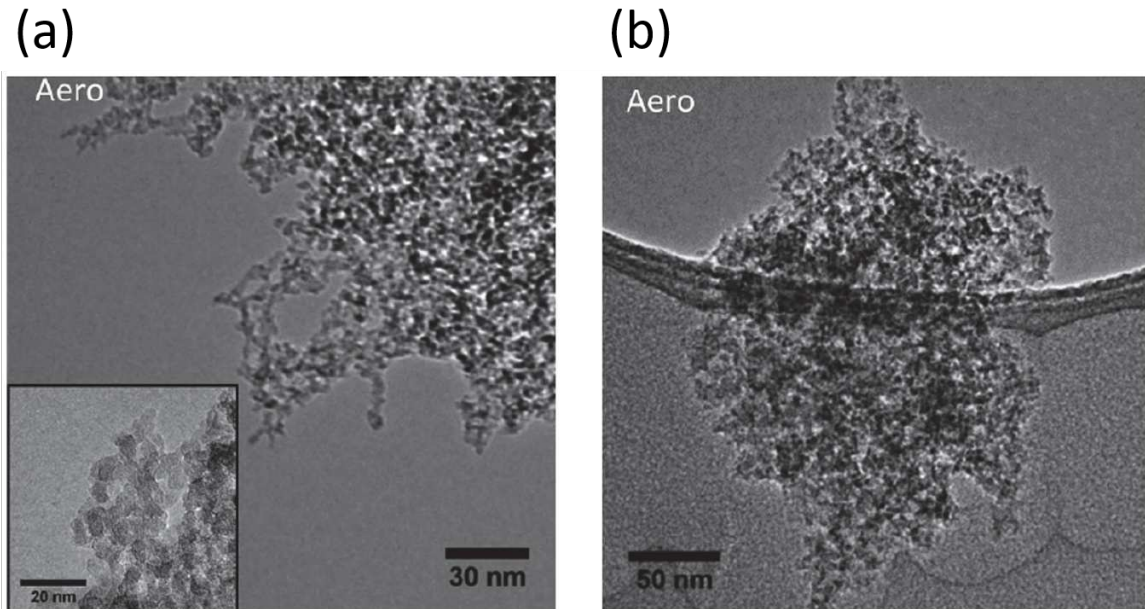


Figure 2.4: Transmission electron microscopy (TEM) carried out on secondary particles of silica aerogels by Roiban et al. [11]. a) Each black dot is a dense primary silica particle part of the pearl-necklace structure. b) An entire secondary particle of approximately 100 nm diameter has been captured.

This nano-scale structure and more precisely its large volume fraction of porosity is at the origin of the exceptional thermal properties of silica aerogels but generates

also mechanical weaknesses. It is problematic not only for the use of the material in different products but also during the synthesis process.

## 2.2.2 Silica aerogels production process

The silica aerogels synthesis is a complex issue with a large number of variables to consider. The main difficulty is to generate a highly nanoporous material and to maintain this structure through all the necessary production steps.

### 2.2.2.1 Gel preparation

The sol-gel process at ambient temperature is one of the most common ways to produce silica aerogels. It consists of creating siloxane bridges formed through hydrolysis condensation reactions. A precursor is necessary for these reactions. The first silica aerogel synthesized by Kistler in the 1930s [12] used sodium metasilicate as a precursor in a hydrochloric acid solution. This method produces NaCl, which is difficult to eliminate, so most silica aerogels are produced today starting from siliconalkoxydes like tetramethoxysilane (TMOS) or tetraethoxysilane (TEOS) [7]. During the hydrolysis the alkoxyde groups  $\text{Si}(\text{OCH}_3)_4$  are converted into silanol  $\text{Si-OH}$  groups which are then condensed into siloxane bridges  $\text{Si-O-Si}$  by reacting with another alkoxyde group [13]. The pH of the reactive solution has a strong influence on the nanostructure of the final aerogel. The generally observed influence is that acid solutions favour low branching in the silica network while base solutions lead to more condensed networks [14, 15].

The end of the hydrolysis and condensation reactions when the gel is already well formed is called the ageing step. During this step, the reactions are much slower and lead to the stiffening of the silica network due to the migration of dissolved silica to the neck of primary silica particles, resulting in neck growth [7, 16].

Once ageing is achieved, a washing step is necessary to remove the remaining precursors, water produced by the condensation reaction and additives. It is generally carried out by immersing the gel in the same alcohol used as a solvent during the gel preparation. By immersing the gel in successive steps, the liquids are exchanged in the pores and the unwanted elements are eliminated.

### 2.2.2.2 Hydrophobic silica aerogels

After the gelation and ageing steps, most of the silicon atoms are linked to two different oxygen atoms forming a siloxane bridge. Yet, some of the alkoxyde groups did not react ( $\text{Si}(\text{OCH}_3)_4$ ) or only partially reacted ( $\text{Si-OH}$ ).  $\text{Si-OH}$  groups can form hydrogen bonds with water and since the gel has a very large specific surface, water molecules have many potential adsorption sites. This is problematic because the presence of water in the nano-pores of the final silica aerogels induces large capillary forces, which possibly damage the material (fracture, densification). It is then necessary to include a step in the production process to create a hydrophobic aerogel. The objective is to replace the silanol groups  $\text{Si-OH}$  with a (apolar) hydrophobic group. This can be achieved before

or after the drying step but in the case of ambient pressure drying (see next section), it is always carried out prior to drying.

Several methods exist in order to change the surface chemistry of the gel and create hydrophobic silica aerogels. In the case of the aerogels studied in this work, silylation has been applied. This method consists of successive solvent exchanges containing reactants, substituting the polar silanol groups  $\text{Si-OH}$  with apolar silyl groups  $\text{SiR}_3$ . Formation of H bonds with water molecules is then impossible with most of the gel surface and the constant repulsion between apolar silyl groups prevents the densification of the porous nano-structure. [17, 18].

### 2.2.2.3 Drying

Once the final gel is obtained, the most critical step is performed: the drying of the gel. Depending on the procedure, this step can be more or less severe and may damage the nano-structure as capillary forces appear in the pores. Three main procedures exist for gel drying: super-critical drying (SCD), ambient pressure drying (APD) and freeze drying (FD).

SCD is currently the preferred drying method as it completely avoids surface tensions and shrinkage of the gel. It can be carried out either by converting the synthesis solvent in a supercritical fluid by increasing pressure and temperature or by exchanging the solvent with liquid  $\text{CO}_2$  which is converted in a supercritical fluid. The supercritical fluid is then vented and eliminated from the gel without the apparition of surface tensions [17, 19]. This is the preferred method for the production of large aerogel objects of several centimetres (silica aerogel monoliths). Fig. 2.5 illustrates the global synthesis process of a silica super-critically dried aerogel.

APD does not require the use of a supercritical fluid and by so, is generally more affordable. It simply consists of increasing temperature to evaporate the synthesis solvent. It requires a special treatment of the surface chemistry prior to the drying step though, as the capillary forces would be too high in the nano-porous structure. The silylation treatment presented in the precedent section is a good way to maintain pore integrity as repulsive forces due to apolar silyl groups prevent the pores to collapse while the solvent is eliminated [7, 20]. In most cases, surface tensions are not completely eliminated using this method and densification and fracture can occur. The creation of large and homogeneous aerogel objects is thus rare and difficult when the APD is applied.

The last method, FD, consists in freezing the synthesis solvent or an exchange solvent, which is then sublimated under vacuum. Although the creation of aerogel monoliths is not impossible using this method [21], it generally generates cracks due to crystals forming in the pores, leading in most cases in powder-like silica aerogels [7].

### 2.2.3 Thermal and mechanical properties

As previously discussed, the main interest of silica aerogels lies in their exceptionally low thermal conductivity. This performance originates from the nanoporous structure of



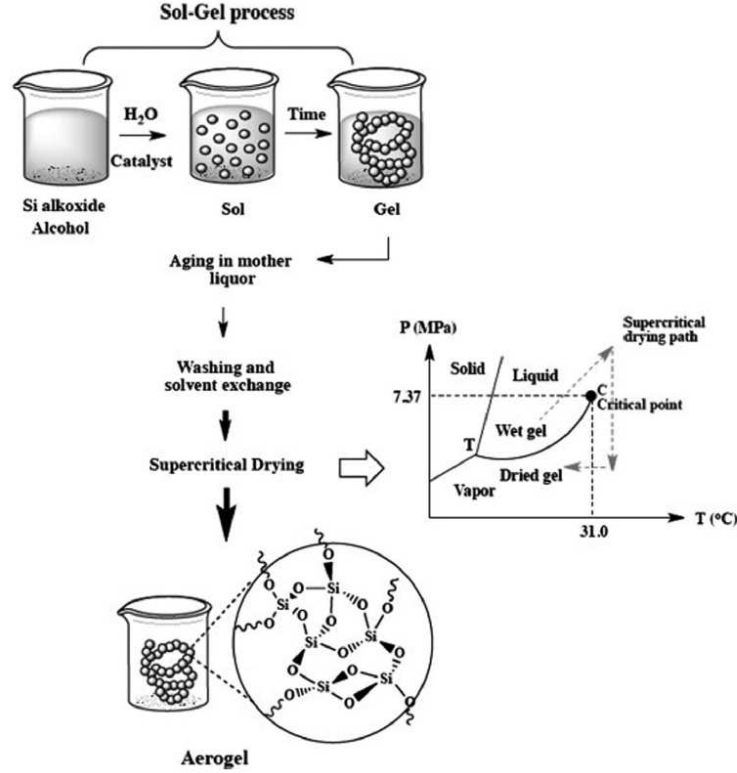


Figure 2.5: Typical sol-gel preparation procedure for silica aerogels. In this case supercritical drying (SCD) is used. Figure form Lamy Mendes et al. [7].

these materials but this structure does not only bring advantages as it is also responsible for poor mechanical properties with low fracture strength and low fracture toughness.

### 2.2.3.1 Thermal properties

Heat transfer occurs following three different paths in silica aerogels: solid conduction  $\lambda_s$ , gaseous conduction  $\lambda_g$  and radiative transmission  $\lambda_r$  (thermal conductivities in  $\text{W.m}^{-1}.\text{K}^{-1}$ ) and are illustrated in Fig. [2.6].

#### Solid conduction

Thermal energy transmission through the solid network of silica aerogels is described by the phonons theory. Silica network thermal conductivity can be expressed by [22]:

$$\lambda_0(T) = \frac{1}{3} \rho_0 c_v(T) l_{ph}(T) \nu_0(T) \quad (2.4)$$

where  $\rho_0$  is the bulk density of silica,  $c_v$  the heat capacity of silica at constant volume,  $l_{ph}$  the phonons mean free path,  $\nu_0$  the mean sound velocity in silica and  $T$  the temperature.  $l_{ph}$  can be divided into three different paths as described by:

$$l_{ph} = \frac{1}{l_v} + \frac{1}{l_s} + \frac{1}{l_t} \quad (2.5)$$

where  $l_v$ ,  $l_s$  and  $l_t$  are the mean free path attributed to phonon-phonon interactions



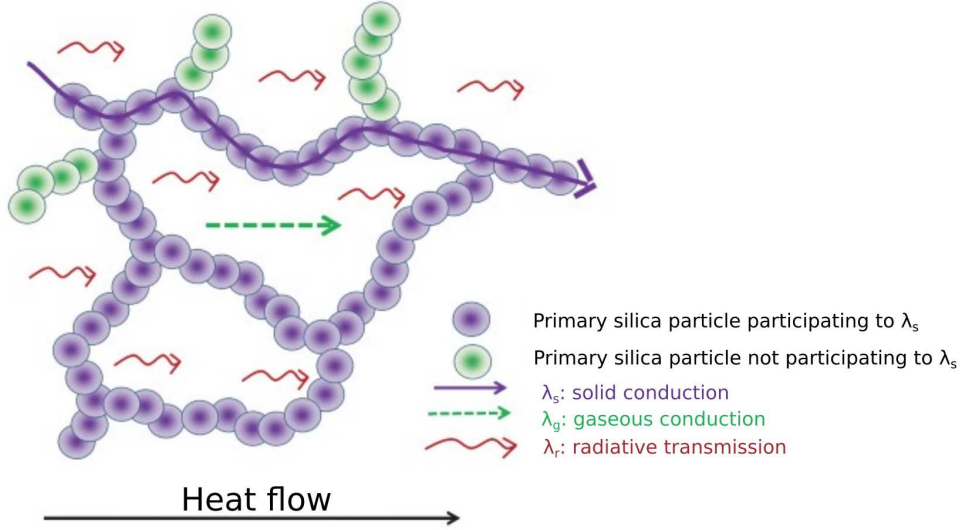


Figure 2.6: Schematics of the silica aerogel nanostructure and how thermal energy is transmitted [4]

(volume), phonon-surface interactions (interface between silica particles and air) and phonon-interface interactions (interface between silica particles), respectively.  $l_v$  is not influenced by the nanostructure of the aerogel and can be expressed using dense silica thermal conductivity  $\lambda_{silica}$  (value of 400 nm roughly):

$$l_{ph} = \frac{3\lambda_{silica}}{\rho_0 c_v \nu_0} \quad (2.6)$$

On the contrary,  $l_s$  and  $l_t$  depend on the geometry and the dimensions of the volume where phonons propagate:

$$l_s \approx \frac{3}{8} L \frac{b^2}{a^2} \quad (2.7)$$

$$l_t \approx a + b \quad (2.8)$$

where  $L$ ,  $a$  and  $b$  describe the dimensions and geometry of primary silica particles and are defined in Fig. 2.7.

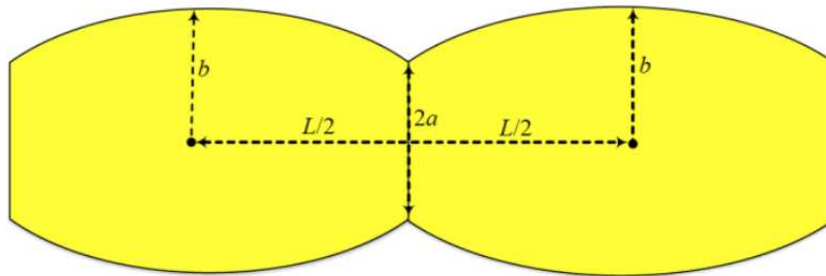


Figure 2.7: Schematics of the dimensions and contact between two primary silica particles [22]

In order to compute the solid conduction  $\lambda_s$  it is necessary to apply a multiplier  $G$

which depends on the aerogel density  $\rho$  :

$$\lambda_s(T, \rho) = G(\rho)\lambda_0(T) \quad (2.9)$$

$G$  is geometric multiplier which describes the complexity of the considered aerogel structure. It takes into account the curvature and the tortuosity of primary silica branches as well as the proportion of dead-end branches. Finally the solid conduction can be expressed by combining the previous equations:

$$\lambda_s = G \frac{\lambda_{silica}}{1 + \frac{l_n}{l_s} + \frac{l_n}{l_t}} \quad (2.10)$$

This equation highlights the influence of  $l_s$  and  $l_t$  on the solid conduction. Indeed, in primary silica particles these two means free path are limited by the small dimensions of the structure. The very low values of these mean free paths ensure then a low conduction in the solid network.

### Gaseous conduction

In a gas, without considering convection or obstacles, thermal energy propagation is possible thanks to the collisions between gas molecules. Applied to the case of silica aerogels, the situation is more complex as the silica solid network limits the gas molecules trajectories and the collisions between gas molecules and primary silica particles are added to the problem. The heat transfer in these situations is described by the Knudsen number:

$$K_n = \frac{l}{D} \quad (2.11)$$

where  $l$  is the mean free path of the gas molecules and  $D$  is the mean diameter of the aerogel pores. Depending on its value, the Knudsen number describes three different regimes [23]:

- $K_n \ll 1$ : The gas molecules collide predominantly with each other. This is the classical case of diffusive heat transfer where the gaseous thermal conduction is equal to the thermal conduction of the free gas.
- $K_n \gg 1$ : The gas molecules collides predominantly with the solid nanostructure of the aerogel.
- $K_n \approx 1$ : Mixed regime. Both types of collisions occur in approximately equal proportions.

The model of Kaganer et al. [24] derives the gaseous thermal conductivity of aerogels  $\lambda_g$  and takes into account the possibility of each regime by introducing the Knudsen number in the following equation:

$$\lambda_g = \frac{\lambda_{g0}}{1 + 2\beta K_n} \quad (2.12)$$

where  $\lambda_{g0}$  is the thermal conductivity of the gas in a free volume and  $\beta$  is a constant related to the gas. It is interesting to note that decreasing the pores size induces a decrease of the gaseous thermal conductivity. That dependence is called the Knudsen effect. In the case of silica aerogels, the Knudsen number is larger than one. This model does not consider the coupling between heat transfer in the solid nanostructure and the gaseous heat transfer. The consideration of these interactions would necessitate the use of more complex models [22, 25, 26]. We note that the Kaganer's model assumptions lead nonetheless to a satisfactory estimation of the gaseous conduction. The thermal conductivity of the gaseous phase calculated with Kaganer's model for three different pore diameters is showed in Fig. 2.8 [23].

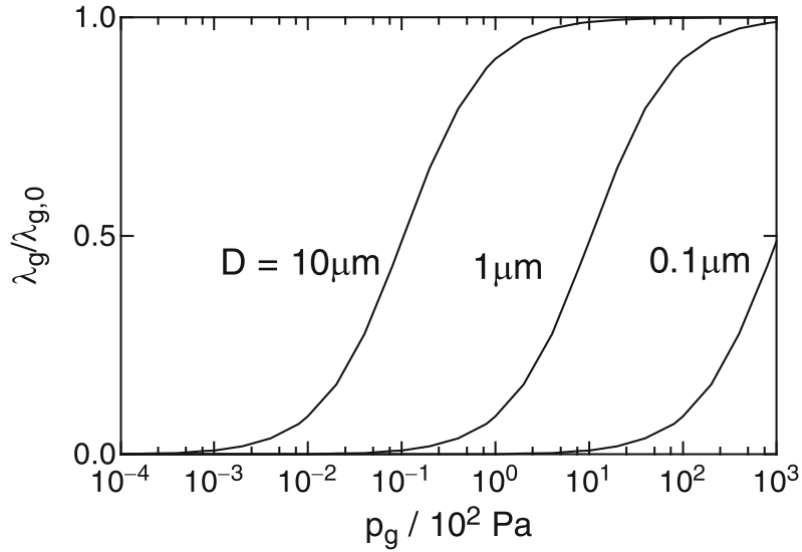


Figure 2.8: Evolution of the normalized gaseous thermal conductivity  $\lambda_g/\lambda_{g0}$  with pore diameter  $D$  and pressure  $p_g$  in a silica aerogel [23].

### Dependence of thermal conductivity to silica aerogels density

The thermal conductivity of silica aerogels is lower than the thermal conductivity of still dry air ( $\lambda_{air} = 26 \text{ mW.m}^{-1}.\text{K}^{-1}$ ) because of the nanometric dimensions of the silica network which influence both solid ( $\lambda_s$ ) and gaseous ( $\lambda_g$ ) conductions. Radiative transmission ( $\lambda_r$ ) has also an influence on the global thermal conductivity but does not contribute as much as the other two components and is not much influenced by the nanostructure dimensions. By combining these three components, the global thermal conductivity  $\lambda$  can be expressed as:

$$\lambda = \Phi \lambda_g + (1 - \Phi) \lambda_s + \lambda_r \quad (2.13)$$

where  $\Phi$  is the silica aerogel's pores volumic fraction. It is interesting to note the competition between gaseous and solid conductivity as a high porosity  $\Phi$  favours gaseous conduction while a low one favours solid conduction. Therefore, the thermal conductivity of silica aerogels shows a minimum for a given value of density. This minimum generally corresponds to  $12\text{-}16 \text{ mW.m}^{-1}.\text{K}^{-1}$  for a density between  $80\text{-}150 \text{ kg.m}^{-3}$  [26].

[30]. The evolution of  $\lambda$  with the density of an example aerogel is illustrated in Fig. 2.9 [27].

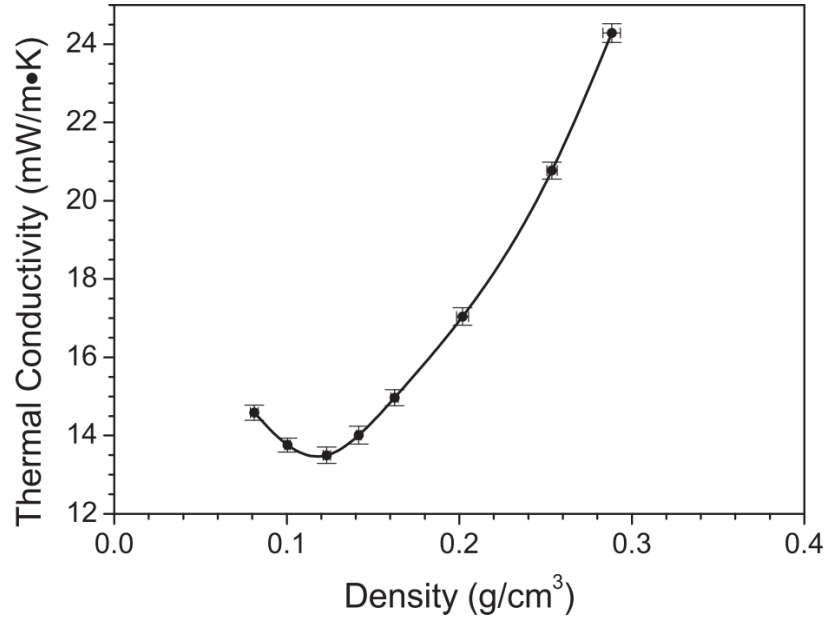


Figure 2.9: Thermal conductivity of a silica aerogel (PEDS precursor, SCD method) versus density. [27]

In the case of particles of silica aerogels intended to be introduced in composites or other insulating products, Neugebauer et al. [31] measured the density and conductivity of particles from different producers (Cabot and MIT granules). The method used for thermal conductivity measurement was hot-wire testing at ambient pressure and the values were found between 12 and 14 mW.m<sup>-1</sup>.K<sup>-1</sup>. Some measurements more related to our case were carried out by A. Perret with the use of a guarded hot plate [29] for silica aerogel particles from the producer Enersens (Bourgoin-Jallieu, France). By measuring the thermal conductivity of a bed of silica aerogel particles for various degrees of compactness, the thermal conductivity of the particles was estimated between 14 and 15 mW.m<sup>-1</sup>.K<sup>-1</sup>.

### 2.2.3.2 Mechanical properties

The nano-structure of silica aerogels responsible for their thermal performances has also a negative influence on the mechanical properties. The mechanical properties of these materials show logically a large dependence on density.

Wong et al. [27] identified three main mechanical behaviours in uniaxial compression for silica aerogels depending on the density range as illustrated in Fig. 2.10:

- $\rho > 0.2 \text{ g.cm}^3$ : silica aerogels show a brittle behaviour.
- $0.1 \text{ g.cm}^3 < \rho < 0.2 \text{ g.cm}^3$ : the aerogels exhibit large elastic strains and compressed samples can regain their initial dimensions for strains up to 40%.

- $\rho < 0.1 \text{ g.cm}^3$ : silica aerogels show a plastic behaviour. No clear fracture is identified during compression and most of the strain applied is not retrieved after relaxation.

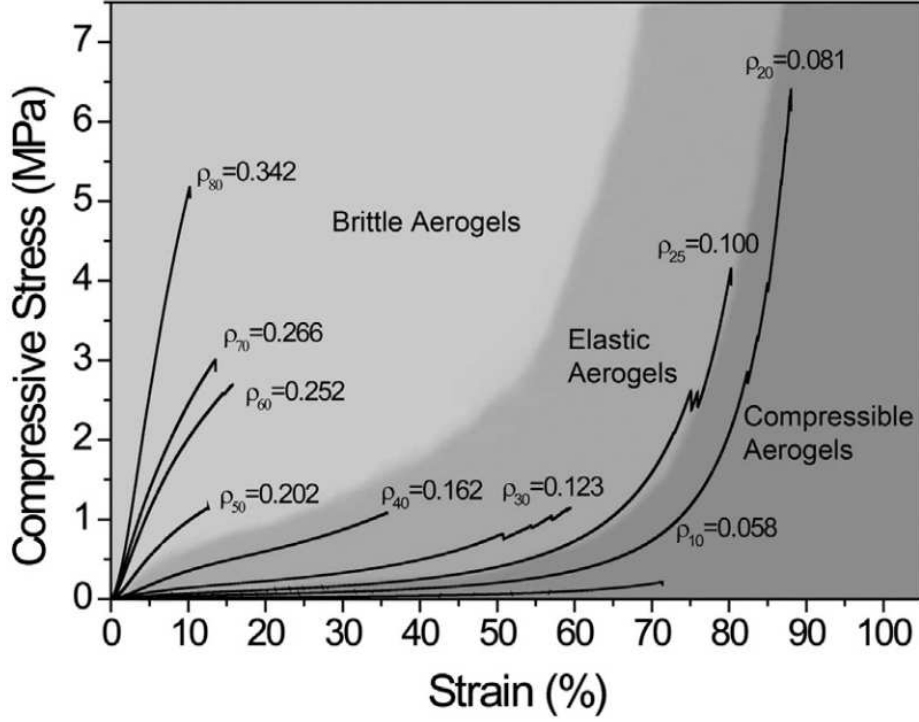


Figure 2.10: Mechanical behaviour in compression of silica aerogels for various densities [27].

These differences illustrate how complex and diverse the mechanical behaviour of silica aerogels can be. Aerogels mechanical aspects are generally less studied than their structural or thermal properties but some studies have been published on this topic. Because of the large influence of aerogels density on their mechanical behaviour, literature data has been searched for densities around  $0.1 \text{ g.cm}^{-3}$ .

### Elasticity

In the case of silica aerogels, the most usual way to describe the dependence of the Young's modulus on density is by considering the following power law:

$$E = c\rho^n \quad (2.14)$$

where  $c$  is a constant. One of the most complete experimental work regarding silica aerogel mechanical properties was published by Wong et al. in 2014 [27]. In this work, uniaxial compression tests led to a value of 3.6 for  $n$ . The corresponding data is illustrated in Fig. 2.11.

Other attempts to fit the Young's modulus evolution using Equation (2.14) can be found in the literature with various testing methods like uniaxial compression, bending or instrumented indentation. Molecular dynamics simulations, at the scale of  $100 \text{ nm}^3$

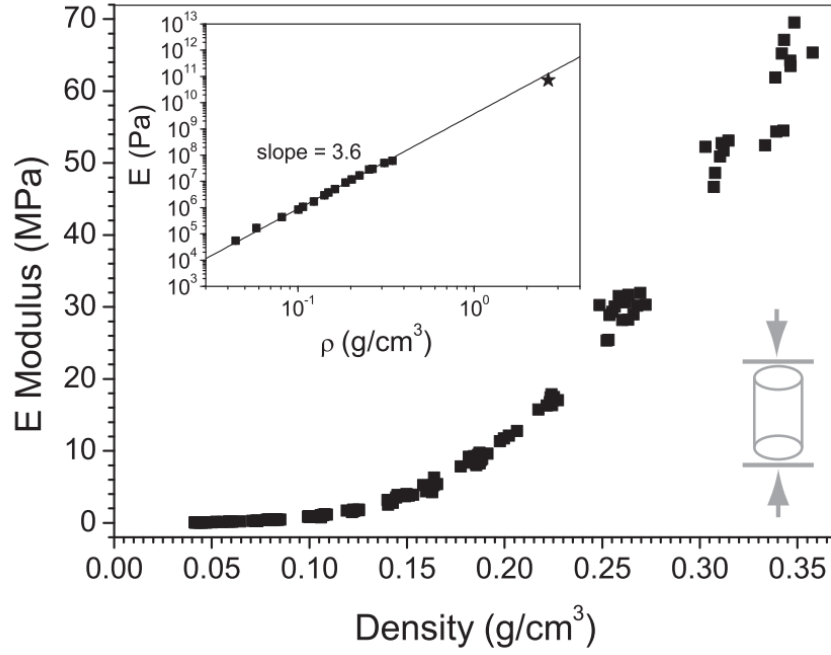


Figure 2.11: Power law fit of silica aerogels Young's modulus versus density [27].

volumes have also attempted to provide values for  $n$ . They are generally limited to intermediate densities ( $\rho > 0.250 \text{ g.cm}^{-3}$ ) and are cited here for completeness. Table 2.1 is a summary of the data which has been found in various works concerning the Young's modulus.

Table 2.1

	Method	$n$	Young's modulus (MPa) ( $\rho=0.1 \text{ g.cm}^{-3}$ )
Wong [27]	uniaxial compression	3.6	0.9 - 1.1
Woignier [32]	uniaxial compression	n.a.	0.5 - 3.0
Pekala [33]	uniaxial compression	2.9 - 3.8	n.a.
Arvidson [34]	uniaxial compression	n.a.	2.25
Kocon [28]	flexural tests	3.6 - 3.7	1.0 - 2.0
Faivre [35]	indentation	2.67 - 2.78	0.6 - 2.0
Gronauer [36]	ultrasonic velocities	3.7	n.a.
Perret [29]	mercury porosimetry	5.5	n.a.
Gonçalves [37]	molecular dynamics	3.8	n.a.

A. Perret et al. carried out hydrostatic compression tests in the chamber of the mercury porometer on millimetric and micrometric silica aerogel particles produced by Enersens company. This company is also the one providing the aerogel particles used during this PhD work. A Young's modulus was estimated roughly at 1 MPa for a bulk density measured at  $0.140 \text{ g.cm}^{-3}$  which is compatible with Wong et al. results [27].

Propagation of ultrasounds can be used for the measurement of elastic properties of various materials by considering the density of the material and longitudinal and transverse wave velocities. Haranath et al. [38] measured the Poisson's ratio of silica

aerogels using ultrasounds. They measured a Poisson's ratio between 0.205 and 0.228 for densities between 0.01 and 0.12 g.cm<sup>-3</sup>, highlighting the low dependency of the Poisson's ratio to density for silica aerogels.

### Strength

As for elasticity, the fracture behaviour of silica aerogel monoliths strongly depends on density. In the same publication cited before, Wong et al. [27] carried out their uniaxial compression tests until the sample failure, which allowed the determination of compressive strength. Brazilian tests were also carried out, thus providing tensile strengths. The results of both tests are showed in Fig. 2.12. The evolution of the compressive strength with density presents an anomaly with a local maximum around 0.1 g.cm<sup>-3</sup> but the error bars for these densities are very large. Wong et al. state that it could be explained by the significant densification of the samples before a clear fracture can be detected. On the contrary, tensile strength can be fitted with a power law similarly to the Young's modulus. For an aerogel with a density of 0.1 g.cm<sup>-3</sup>, the corresponding compressive and tensile strength are 2 MPa and 0.02 MPa, respectively. Such a high difference between these two values, compared to other more common brittle materials like ceramics or concretes with a compressive strength to tensile strength ratio around 10, highlights how the silica chains in the nano-structured network bend when the samples are compressed but badly support any tensile strain.

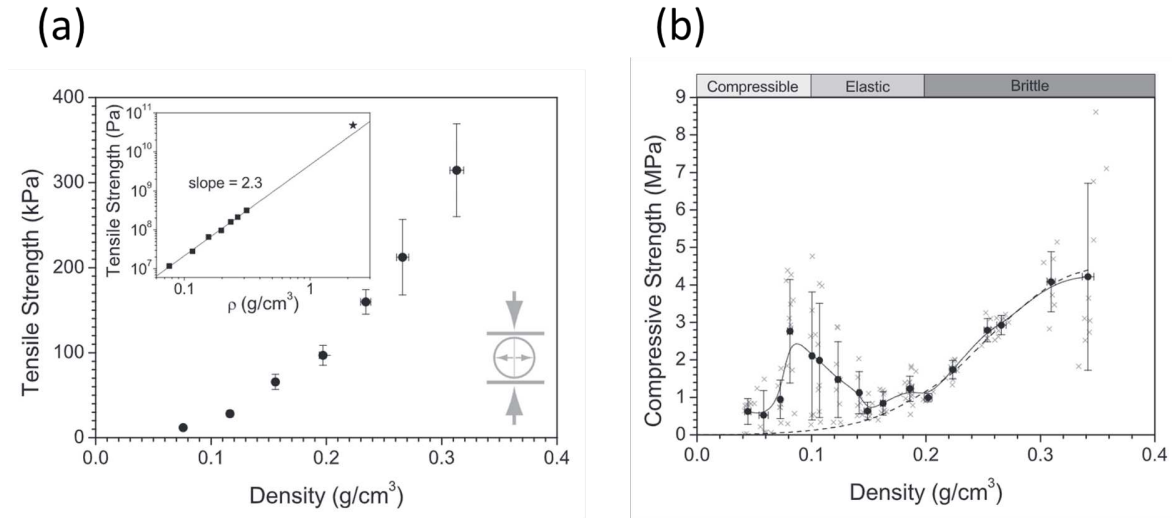


Figure 2.12: (a) Tensile, (b) compressive, strength dependency to density of silica aerogels [27].

The order of magnitude for the tensile strength is confirmed by flexural tests carried out by Kocon et al. [28] where a value of roughly 0.01 MPa was found for an aerogel with a density of 0.1 g.cm<sup>-3</sup>. This value is extracted from the graph showed in Fig. 2.13.

### Toughness

An important property to consider while studying the fracture behaviour of silica

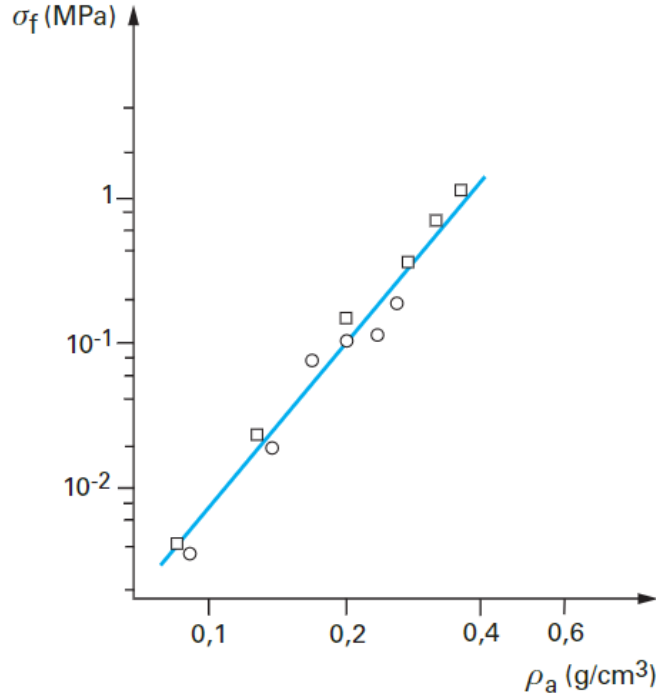


Figure 2.13: Tensile strength dependency to density measured with flexural tests [28].

aerogels is the fracture toughness  $K_{Ic}$  that gives information on the crack propagation resistance of the material. One of the most common method used to extract fracture toughness is the single edge notched beam (SENB) technique in three-point bending. Phalippou et al. used this technique [39] to measure fracture toughness for silica aerogel monoliths with a density close to 0.2 g.cm<sup>3</sup>. The results illustrated in Fig. 2.14 for two different silica aerogels (same precursor but different pH during sol-gel process) show once again a clear dependence of the fracture toughness on the aerogels density. For densities between 0.1 and 0.3 g.cm<sup>3</sup>,  $K_{Ic}$  lies in between 0.4 and 6 kPa.m<sup>1/2</sup>, which is very low compared to the fracture toughness of dense silica (800 kPa.m<sup>1/2</sup>).

Kucheyev et al. [40] used indentation tests to estimate a fracture toughness. Using a cube corner tip, an indent was made on a clean and smooth aerogel surface. The measurement of the radial cracks illustrated in Fig. 2.15 allows the calculation of a fracture toughness. The value found for  $K_{Ic}$  is 8 kPa.m<sup>1/2</sup> for an aerogel bulk density of 0.34 g.cm<sup>3</sup>. The validity of these results can be discussed as Kucheyev based his calculations on the expansion cavity model which assume the tested materials do not densify during the indentation. In the case of porous materials like silica aerogels, this assumption may not be correct [41].

Kocon et al. carried out Double Cleavage Drilled Compression tests (DCDC), which principle is explained further in chapter 3. These tests were carried out to measure crack propagation celerity with the variations of the stress intensity factor  $K_I$ . They proved that hydrophobic aerogels perform better against crack propagation with slower crack propagation, showing the influence of water during fracture situations.

In general the fracture toughness of silica aerogels, although depending a lot on



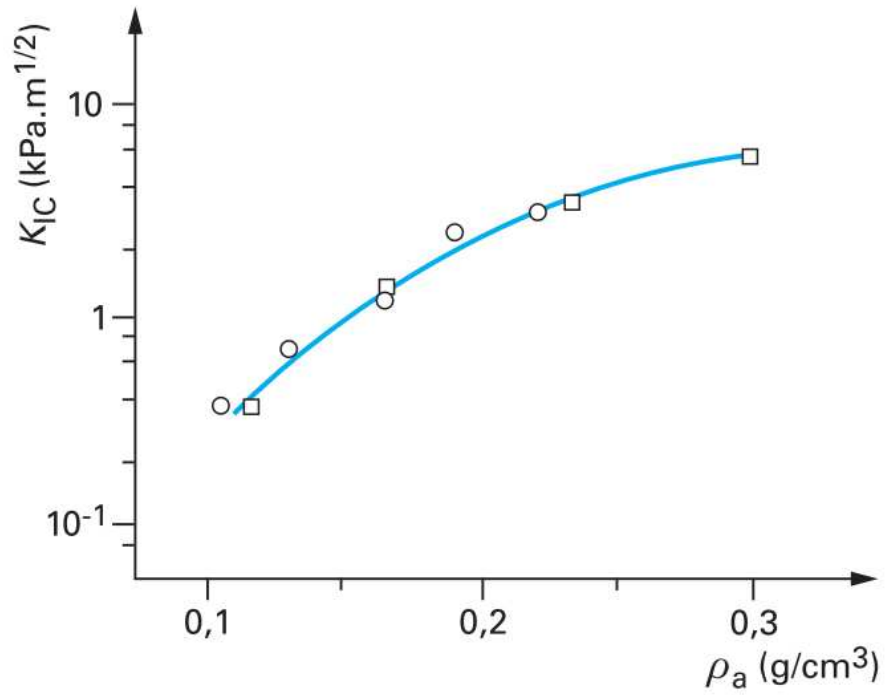


Figure 2.14: Silica aerogels fracture toughness dependency to density [39]

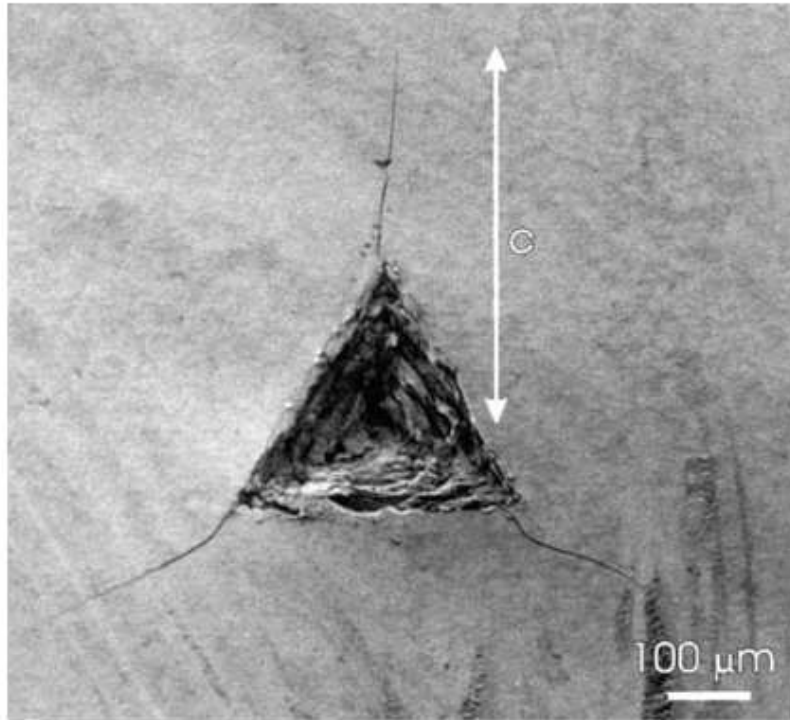


Figure 2.15: SEM image of a residual impression made on a silica aerogel by loading a cube corner tip to a maximum load of 1 Newton. The length of radial cracks  $c$  used in calculations of fracture toughness  $K_{1c}$  is illustrated. From [40].

their density, is exceptionally low compared to dense silica (around 100 times lower). Moreover, large aerogel samples (monoliths) are required for the measurements and making them can be especially difficult (correct geometry and no internal defects).

### 2.2.3.3 Conclusion on the mechanics of silica aerogel

Silica aerogel materials display poor mechanical strength for the densities that are the most interesting for optimal thermal performances. Several ways are currently investigated in order to compensate this weakness and some of them are even commercialized today like aerogel blankets or aerogel glazing units which will be described in the next section. In our case, the objective is to improve composites containing millimetric and micrometric aerogel particles. Although commercially available and used in numerous products, aerogel particles have rarely been characterized mechanically due to how the conventional mechanical testing methods are ill-adapted to these objects.

## 2.3 Super-insulating composites and products based on silica aerogels for the building industry

The question of the incorporation of silica aerogels in thermal insulating products is increasingly present today. A large part of the composites containing silica aerogels is still under development and is not available on the market but other products are already commercialized. We have shown in the previous section that the main weakness of silica aerogels is their poor mechanical performance with a compressive strength and a fracture toughness critically low compared to more conventional thermal insulation products. Thus, silica aerogels cannot be used directly as insulating products in the building industry as their strength and toughness need to be boosted. In this regard, a first method is to modify some parameters of the sol-gel process of silica aerogels or to copolymerize aerogel precursors with other components leading to a more flexible and/or resistant product [7, 42]. Another way, the one that is the most promising in regards to this work, is to compensate the mechanical weaknesses by incorporating silica aerogels in flexible composites easier to handle, which reinforce the mechanical resistances and preserve as much as possible the thermal properties of aerogels.

This section aims to provide a quick overview of the existing insulating products containing silica aerogels today with a particular focus on particulate aerogel composites containing a binding agent. Reinforcement of silica aerogels through the modification of the sol-gel process will not be discussed in this work.

### 2.3.1 Vacuum insulation panels (VIP)

Vacuum insulation panels are in most cases not silica aerogel composites but are a reference when talking about high performance super-insulating panels. VIP are made up of a highly porous core material, for example pyrogenic or precipitated silica [3, 43], wrapped in an airtight enclosure preserving the vacuum that has been imposed inside. This product is almost free of any gaseous conduction and convection and the

membrane is designed to reflect most of the radiations responsible for radiative heat transfer. The use of silica aerogels or silica aerogel composites as a core material is an option with promising results [44, 45].

VIP can reach thermal conductivities as low as  $3.5 \text{ mW.m}^{-1}.\text{K}^{-1}$  [46–48] which position this product as the most thermally efficient product on the market today. Yet, it comes with several restrictions and drawbacks. Firstly, the panels cannot be cut during their installation as the vacuum inside the product must be preserved. It also means that they must be meticulously handled to prevent the deterioration of the enclosure. Secondly, the core material, which structure is generally composed of nanometric pores and bridges, is prone to ageing at ambient temperature and humidity [49].

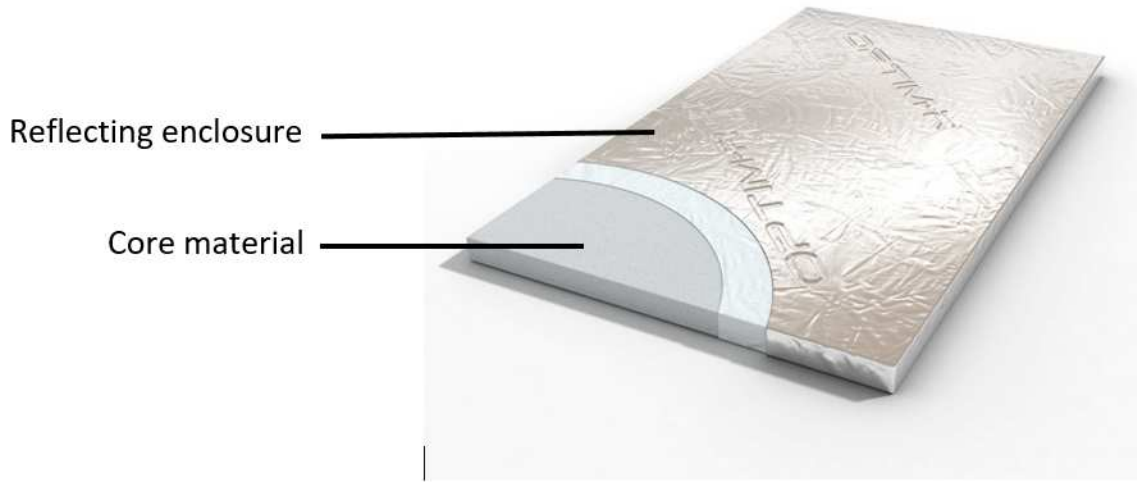


Figure 2.16: Example of a vacuum insulation panel (VIP) [50].

### 2.3.2 Aerogel glazing units (AGU)

Silica aerogel particles can be used to fill a space between two parallel surfaces (generally polymer panels). By filling this space, heat transfer via gaseous conduction and convection is minimized. The resulting AGU panels are translucent to daylight, which is an interesting property for architecture purposes. These panels can display thermal conductivities between  $19\text{--}23 \text{ mWm}^{-1}\text{K}^{-1}$  [51]. Thermal conductivity is highly dependent on the degree of compactness of aerogel particles [31]. Compactness needs to be sufficient to limit the presence of intergranular macro-pores, which do not benefit from the Knudsen effect and transfer the heat more easily than aerogel particles (see section 2.2.3.1). Particle size dispersion has thus a great influence on the global thermal performance of the product. It has been shown that smaller aerogel particles tend to improve the performances of AGU [51, 52].

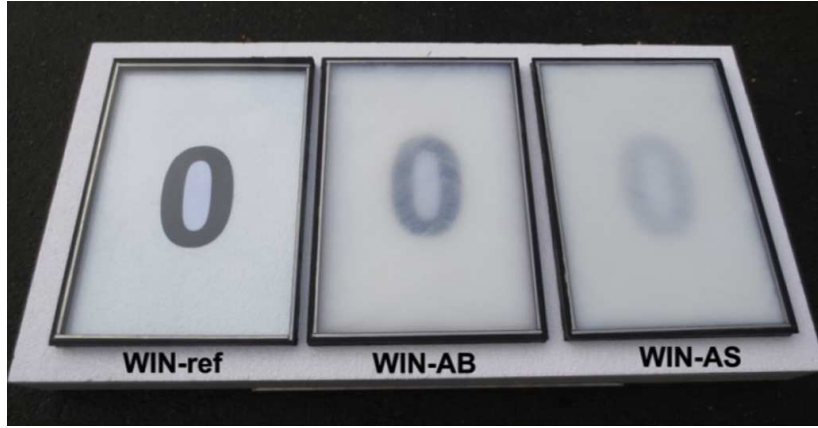


Figure 2.17: Aerogel glazing units from the work of Gao et al [52]. WIN-ref: no silica aerogel particles. WIN-AB: silica aerogel particles with sizes between 3 and 5 mm. WIN-AS: silica aerogel particles with sizes below 0.5 mm.

### 2.3.3 Blankets

An aerogel blanket is a layer of unwoven fibres impregnated with silica aerogel during the sol-gel process. Although the thickness of the fibre layer is limited because of the necessity for the sol to impregnate the whole volume before the end of the gelation (thickness rarely superior to 5 mm), these thin products present various advantages. Firstly, it takes advantage of the thermal performance of silica aerogels, which displays thermal conductivities generally around  $14 \text{ mWm}^{-1}\text{K}^{-1}$  [13]. Secondly, these blankets are characterized by a great flexibility, which provides an adaptability of these products to the surface to insulate. The flexibility and low thickness of aerogel blankets is also a great advantage for situations with space and weight restrictions [53–55]. A current disadvantage of this product is the deterioration of the aerogel where the product has been cut, which creates thermal insulation weaknesses at the borders of the blanket [49].



Figure 2.18: Spaceloft aerogel blanket product [56]

### 2.3.4 Cements, mortars and plasters

Silica aerogel particles can be incorporated in cements, mortars or plasters to improve the global thermal insulation of a building. Yet, mainly in the case of cements which require strong mechanical strength as they have a structural function, the fraction of introduced aerogels must remain limited. Several studies have shown the decrease of the compressive and flexural strengths with the increase of the silica aerogel weight fraction [57–59]. Mortars presented in a work by Hanif et al. [57] display one of the highest strength for these materials containing silica aerogel particles. In this work, a mortar containing around 50 vol% of silica aerogel particles displays a thermal conductivity of  $320 \text{ mW}\cdot\text{m}^{-1}\cdot\text{K}^{-1}$  ( $405 \text{ mW}\cdot\text{m}^{-1}\cdot\text{K}^{-1}$  without aerogel) and a compressive strength of 18.6 MPa (23.5 MPa without aerogel). In another work by Ng et al. a mortar containing up to 80 vol% of silica aerogel particles was tested. The thermal conductivities and compressive strengths obtained with these materials are shown in Fig. 2.19 [60, 61]. Fig. 2.19 illustrates how a compromise must be found between mechanical and thermal performances of the mortars depending on their applications.

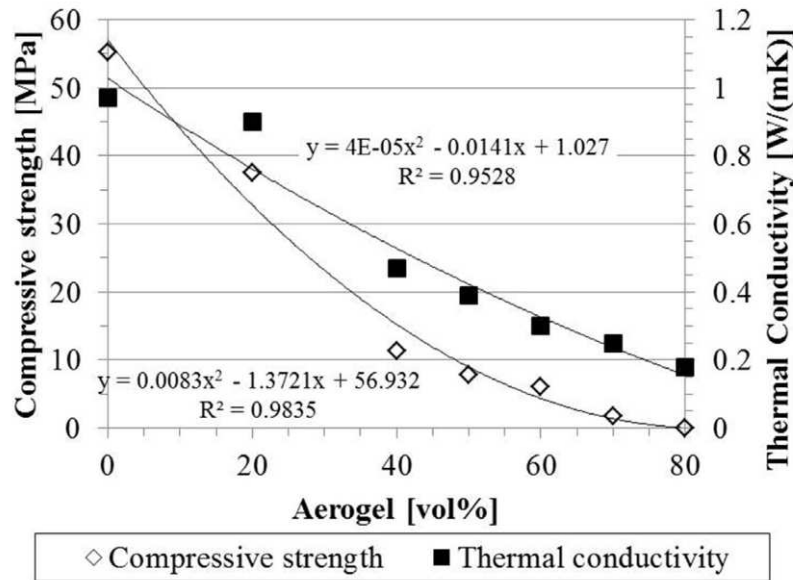


Figure 2.19: Compressive strengths and the corresponding thermal conductivity values of mortar samples containing only cement, silica fume, water and NRG-700 [61].

### 2.3.5 Particulate aerogel composite insulating panels

A particulate aerogel composite insulating panel is similar to the cements previously discussed in its preparation and structure but with a different objective. Mechanical performances can be lower than mortars as they don't have a mechanical structural function a building. The mechanical properties of the corresponding insulating panels only need to be sufficient for the self-preservation of the panels themselves and for their handling during installation. The main goal of this composite being its thermal performances, the volume fraction of silica aerogel particles is superior to 90 vol%.



These products are currently not common in the construction market because while the thermal properties of silica aerogels are well exploited, the mechanical strengths are low. Reinforcement of these panels is possible but the competition in the building sector with other technologies like blankets or AGUs does not encourage these developments. An example of a product based on the binding of particles of aerogel is the Aeverso panel [62]. Its thermal conductivity is  $16 \text{ mW.m}^{-1}.\text{K}^{-1}$  and its compressive strength is 100 kPa (Wong et al. [27] aerogel monoliths had a compressive strength around 1 MPa for a density around  $0.1 \text{ g.cm}^{-3}$ ). The compressive strength is very low, highlighting the necessity to develop new solutions to reinforce the strengths of these products.

The particulate aerogel composites elaborated and studied during the present PhD work are based on a patent filed by the French company EDF in 2011 [63]. The aerogel particles in the composite are mixed with a polymer binding agent that allows the moulding of insulating panels retaining most of the thermal performances of silica aerogel particles but with relatively poor mechanical strengths. Although mechanical performances are not the main objectives for this type of products, a too brittle material is problematic for the handling and installation of insulating panels.

The majority of the data and results showed in this section are from a PhD work by A. Perret [29] who studied composites with a composition and a structure very close to those studied in this work. However, her work was mainly focused on the morphological characterization of the composite and only preliminary mechanical characterizations were performed.

### 2.3.5.1 Basic composition and structure

Following the EDF patent [63], the composite panels and beams are produced by mixing together a solid phase composed with silica aerogel particles of different size and a liquid phase containing the binding agent and a surfactant. The resulting structure of the composite is thus composed of large silica aerogel particles surrounded by smaller particles and macro-pores. The X-ray tomography cross-section showed in Fig. 2.20 illustrates a typical structure of this particulate aerogel composite. This figure originates from A. Perret's PhD work and illustrates a composite with a composition almost identical to the composite studied in this PhD. The composition of the composite will be presented in this section and thoroughly discussed later in chapter 3.

The aerogel particles used in A. Perret PhD work have been provided by Enersens company [64]. These particles have been produced starting from TEOS (tetraethoxysilane) precursor and the gel has been dried at ambient pressure after a silylation treatment, which results in a hydrophobic aerogel. Particles have been divided in two different size bins for the composite production: particles between 1000 and 1250  $\mu\text{m}$  and particles below 100  $\mu\text{m}$  diameter introduced around a 3/2 mass ratio in the composite. The mass fraction of binding agent and surfactant in the dry composites is generally around 10 %.

A. Perret measured using different methods the porosity and density of this composite. This resulted in a density value of  $0.11 \pm 0.01 \text{ g.cm}^{-3}$  and an inter-particle macro-porosity of  $0.12 \pm 0.03$  (porosity between silica aerogel particles, nanoporosity

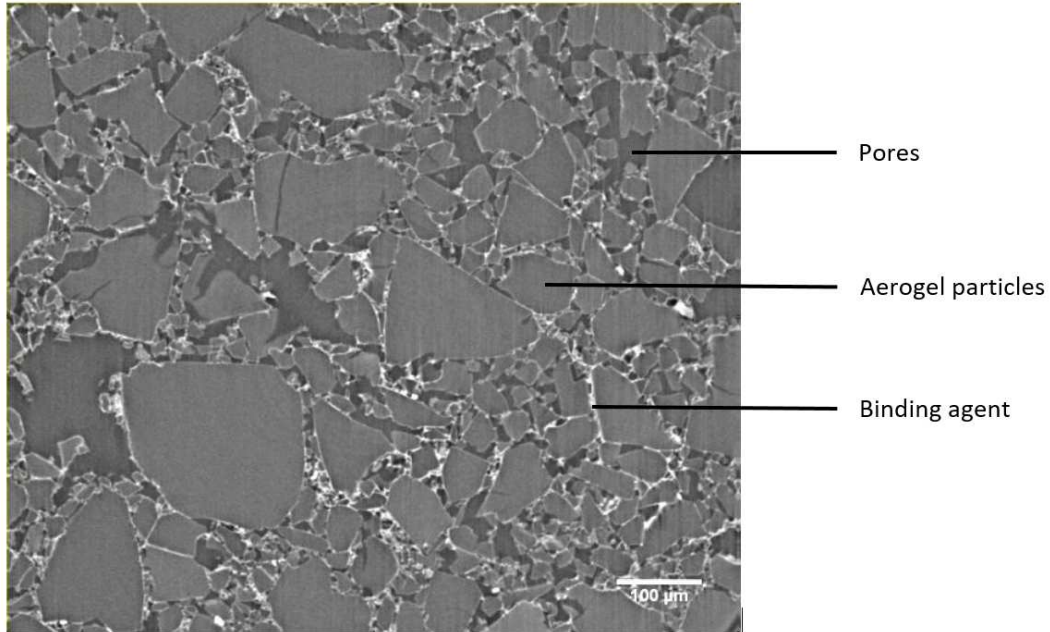


Figure 2.20: X-ray tomography cross-section of a particulate aerogel composite by A. Perret et al. [29]

of silica aerogels not included). The porosity of the composite is a key property for the efficiency of the product as a too large porosity results in a decrease of thermal performances (the Knudsen effect does not apply inside macropores) and a decrease of mechanical properties (the macropores create structural weaknesses).

The polymer binder incorporated in the composite can also degrade its thermal conductivity. A. Perret et al. estimated, by isolating the binder on X-ray tomography volume images, that with the base composite composition used in this PhD work, the binder network percolates up to 270  $\mu\text{m}$  from the surface inside the sample as illustrated in Fig. 2.21 [29]. This sample is similar to the reference one studied in this work (see chapter 6). The percolation not exceeding 5 % of the total sample thickness (200 mm) is an encouraging result for the good thermal performances of the composite as the effect of the binder on the deterioration of the thermal conductivity should be limited in this situation.

### 2.3.5.2 Thermal and mechanical properties

Thermal and mechanical characterization of the composite were not the main objectives of A. Perret's PhD work but some of the experimental work gave a good starting point for the development of other characterization methods carried out in this work and adapted to this type of materials (see chapter 3).

Thermal characterization was carried out using a fluxmetre. The global setup of the method is presented in chapter 3 as the protocol and equipment used by A. Perret were used for new measurements in this work. The thermal conductivity of the composite was measured at  $15.9 \text{ mW}\cdot\text{m}^{-1}\cdot\text{K}^{-1}$  while the aerogel particles have an intrinsic thermal conductivity of  $12 \text{ mW}\cdot\text{m}^{-1}\cdot\text{K}^{-1}$  according to the producer [64].

The macroscopic mechanical characterization of the composite by A. Perret consists

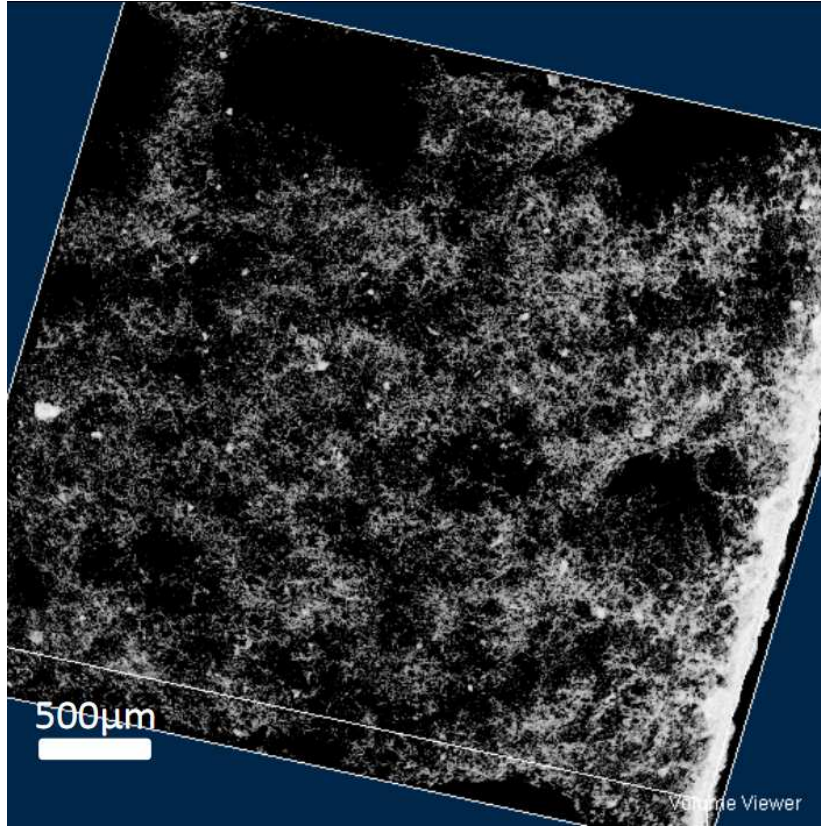


Figure 2.21: Segmentation of the binder in a X-ray tomography image volume of a composite sample. The binder is the most concentrated on the sample surface and a single percolating binder object has been identified up to 270  $\mu\text{m}$  under the surface. Figure and analysis from A. Perret PhD work [29].

of four-point flexural tests on composite beams (dimensions:  $20 \times 20 \times 80 \text{ mm}^3$ ). The complete protocol as well as the corresponding equations for the extraction of a Young's modulus and a tensile fracture strength are available in A Perret's PhD manuscript [29]. The composite Young's modulus  $E$  was measured at  $1.9 \pm 0.1 \text{ MPa}$  and the tensile fracture strength  $\sigma_r$  at  $59 \pm 7 \text{ kPa}$ . These values are close to the mechanical performances of silica aerogel monoliths of similar density ( $0.09 - 0.1 \text{ g.cm}^{-3}$ ) [27]. These values will be compared in the next chapters to the results obtained through other methods in this PhD work.

## 2.4 Conclusion

The actual ecological context and more precisely the necessity to reduce global greenhouse gas emissions is leading to more and more regulations in the building sector. Indeed, the building sector is one of the most energy consuming behind transport and industry at the global scale. A large fraction of this energy is dedicated to temperature regulation in buildings, highlighting the interest for the development of new thermal insulation solutions. In this regard, silica aerogels are promising materials and are already introduced in various products. These super-insulators display exceptionally low thermal conductivities and several products take also advantage of their translu-



cence. However, because of their porous nano-structure, at the origin of their thermal performances, the mechanical strength of these materials is very low compared to more conventional insulating materials. For this reason, silica aerogels are almost never used directly as thermal insulators. Other solutions appeared by combining different materials at different scales, producing hybrid materials at a molecular scale or creating composites at a larger scale with the addition of fibres or enclosures. A potential interesting solution is a particulate silica aerogel composite containing more than 90 vol% of aerogel particles and a polymer binding agent. This composite is still mechanically weak and needs to be reinforced for a potential commercialization, the biggest challenge being the conservation of the thermal performance of the product.

In this context, the aim of this PhD is to reinforce a silica aerogel particulate composite by the incorporation of fibers. A correct understanding of the mechanical behaviour of this composite and of the silica aerogel particles composing it is thus required. In this regard, a coupled experimental and discrete element approach is carried out. Silica aerogel particulate composites and silica aerogel particles are characterized experimentally, allowing the measurement of structural, mechanical and thermal properties. These characterization methods are described in chapter [3](#). Some of the experimental results are used as inputs for the calibration of a discrete element model aiming to simulate the fracture of silica aerogel particles and of particulate composites. The creation of this model as well as the generation and calibration procedures of the simulated objects are described in chapter [4](#). The analysis of experimental and numerical results concerning isolated silica aerogel particles is done in chapter [5](#) while the results on silica aerogel composites are analyzed in chapter [6](#).

## Chapter 3

# Experimental methods

In this chapter the methods and equipment used for the study of silica aerogels particles and their composites are listed and described. The observation and characterization methods used in this work give information on thermal, mechanical and structural properties of the materials.

### 3.1 Visualization methods

#### 3.1.1 X-ray tomography

X-ray tomography is a very useful observation method as it leads to a non-destructive characterization of a volume. By taking successive X-ray radiographies of a volume from different angles, a 3D image is reconstructed, giving information on the internal structure of the analyzed objects as the resulting contrast on the greyscale image is created by the different X-ray absorption or refraction of the material local composition. The reconstruction of a volume from 2D radiographs is a complex subject involving various methods that depend on the X-ray source used. The two methods used in this work are briefly presented in this section.

X-ray tomography is generally well-adapted to the study of composites. However, the low density of silica aerogels, associated to a low X-ray absorption, leads most of the time to challenging image post-processing and sensitivity to the artefacts introduced by the chosen reconstruction method and equipment. Due to these limitations, most of the analysis of X-ray tomography images carried out during the thesis and presented in this work focus on the qualitative information provided by these methods, with some exceptions where quantitative properties extraction was successful (porosity fraction and individual particles volume estimation).

##### 3.1.1.1 X-ray micro-tomography: tungsten source

The machine used is an X-ray tomograph (RX-Solution, Annecy, France) producing X-ray photons using a tube source with a tungsten anode [65]. This equipment can provide 3D-images with a minimum resolution of 1.7  $\mu\text{m}$ . This resolution being much larger than the nano-pores of the silica aerogels (around 10 nm), the tomograph cannot be used to characterize the nanostructure of the materials. Scans were performed under 40 kV and 250  $\mu\text{A}$  on the X-ray photon source. The voxel size, which is adjusted by tuning the distances source-object and object-sensor, varies between 1 and 15  $\mu\text{m}$  depending on the object scanned. The laboratory system is illustrated in Figure 3.1.

This method and equipment were applied for the following purposes during the PhD work:

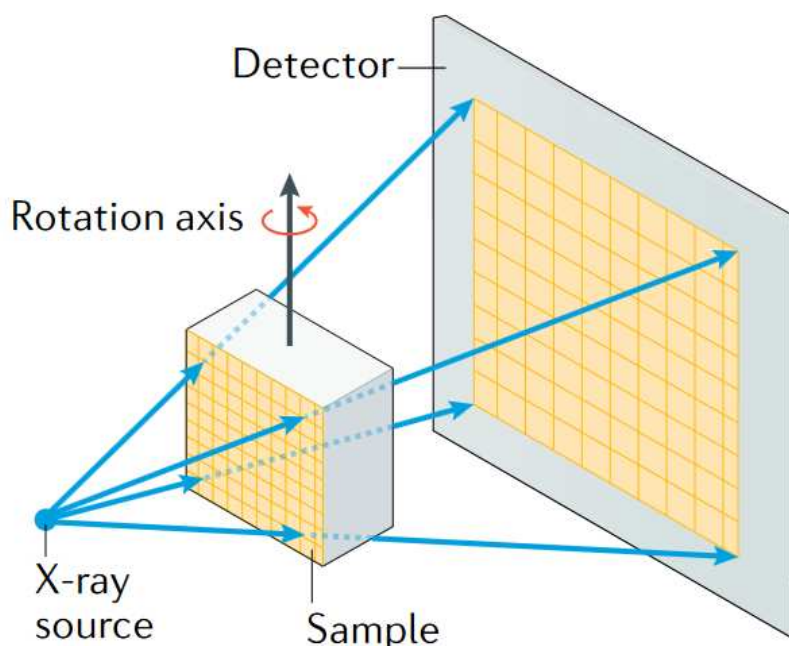


Figure 3.1: Cone beam lab X-ray tomography system. The resolution is determined by the distances between X-ray source, sample and detector. Figure from [65].

- Morphological observation of particulate silica aerogel composites
- Volume measurement of individual aerogel particles (see section 3.2.3)
- Uniaxial compression of individual particles (see section 3.2.3)
- Observation of the stable progression of a crack in aerogel composites during double cleavage drilled compression tests (see section 3.4.4)

### 3.1.1.2 X-ray nano-tomography: synchrotron source

The use of a synchrotron source brings several advantages in this work, the main one being the resolution that can be achieved with this source, which can go down to 20 nm, about 100 times less than what can be obtained with a conventional laboratory X-ray tomograph. This presents many interests for silica aerogel composites where small objects like thin polymer films or fibres are hardly perceptible with regular X-ray tomography and even harder to segment in post-processing. With a greater spatial resolution, the interfaces between these small objects and other macroscopic objects (aerogel particles, pores, ...) are easier to characterize. The volumes are reconstructed differently using a synchrotron source when compared to a laboratory tomograph. The holotomography approach, based on a coherent and monochromatic nano-focused X-ray source, consists in retrieving for each orientation of the sample the phase map from four radiographs taken at four different sample-detector distances. These phase maps are then used as an input to a conventional tomographic reconstruction algorithm. The contrast obtained in the reconstructed volumes corresponds to the deviation from unity of the local refractive index of the material, directly related to the local density

[66]. The observations realized during the PhD using a synchrotron X-ray source were carried out at the European Synchrotron Radiation Facility (Grenoble, France) on beamline ID16B with the help of J. Villanova and P. Gravier. The resolutions varied between 25 and 280 nm depending on the purpose of the scans which are:

- Structure illustration of aerogel composites with a binding agent
- Observation of the interface between a binding agent and polypropylene fibres

### 3.1.2 Scanning electron microscopy (SEM)

Scanning electron microscopy is a non-destructive visualization method using a focused beam of electron to scan surfaces. It provides information on the topography and the composition of the analysed surface depending on which electron detector is considered. A detector counting back-scattered electrons, electrons originating from the electron beam which are reflected by interacting with surface atoms, provides an image where the contrast gives information on the local chemistry of the surface. A detector counting secondary electrons, electrons ejected from the surface atoms because of interactions with primary beam electrons, provides an image where edges and steep surfaces are brighter than the rest of the surface due to a higher amount of emitted secondary electrons, resulting in a topographic contrast. A secondary electron detector is used in this work.

The use of SEM on silica aerogel samples and its composites requires some precautions. A high voltage electron beam or a long exposure of the samples may damage the nanostructure on the surface of silica aerogels. There is also the problem observed for most electrical insulators where samples do not discharge properly, resulting in local distortions and other artifacts on the final images as the samples were not metallized. The SEM images have been obtained using low electron beam energy between 1 and 5 keV. Before obtaining pictures, the focus and global tuning of the system were realised on a sacrificial part of the samples which is permanently damaged by the electron beam. Two different SEM microscopes have been used depending on the purpose of the scans:

- Tabletop scanning electron microscope (Phenom Pro model). The electron energy is 5 keV. This microscope has been used to observe individual silica aerogel particles and the fracture surface of silica aerogel composites. The maximum magnification achieved without the image being too much distorted is between 720 and 1100 X depending on the sample.
- Conventional scanning electron microscope (Zeiss SUPRA 55-VP model). The electron energy is 1 keV. This microscope has been used to observe fracture surface of silica aerogel composites and the interactions between fibres and the binding agent. The maximum magnification achieved without the image being too much distorted is 7500 X. These images have been recorded with the help of K. Masenelli-Varlot and G. Foray from MATEIS laboratory (Lyon, France).

The composite samples being very light, they must be properly held or bonded in order to limit any motion under the electron beam and during pressurisation and depressurisation of the microscope chamber.

## 3.2 Structural and mechanical characterization of aerogel particles

The shape and size of aerogel particles studied in this work prevent or make difficult the use of conventional mechanical characterization procedures used for the characterization of aerogel monoliths (flexural tests, uniaxial compression on cylinders, brazilian tests, ...). For this reason, the characterization methods are inspired by those used in soil mechanics, where the rather than the mechanical tests carried out on aerogel monoliths. Mechanical characterization of small or medium size particles is indeed common in soil mechanics [67, 68].

### 3.2.1 Mercury porosimetry

Mercury porosimetry is commonly applied to materials with open porosity. Due to its high surface tension, mercury does not infiltrate open pores spontaneously but by increasing progressively the pressure, large pores are filled first followed by smaller ones. Mercury porosimetry is generally used to determine the pore size distribution of non-deformable materials [29, 69] but was only used here to extract the particles density.

The density of the studied aerogel particles was measured on large particle batches (several hundreds of particles). Five particle batches were weighed (around 50 mg) and analyzed using a Micromeritics Autopore 4 9500 with an increasing pressure from 0.001 to 0.206 MPa. The sample volume is measured at 0.036 MPa. The two cells containing the particles and illustrated in Fig. 3.2 had volumes of 3 mL and 5 mL, respectively. The capillaries are extended inside the cell and prevent aerogel particles to contaminate the mercury in the capillary.

### 3.2.2 Particle compression: statistical procedure

Two types of uniaxial compression tests have been carried out on aerogel particles. The first procedure is a statistical study of fracture. More than 50 individual randomly selected particles were pressed between two plates up to failure. An example force-displacement curve is showed in Fig. 3.4. This procedure provides information on the scatter of the fracture force. The setup for these compression tests is shown in Fig. 3.3a and was used at two different loading velocities (0.3 and 1.5 mm min<sup>-1</sup>) [27]. The load cell used has a nominal force of 22 N and a sensitivity of 0.02 N. Tests were carried out using a Bose ElectroForce 3200 traction / compression machine (Prairie Valley, USA).

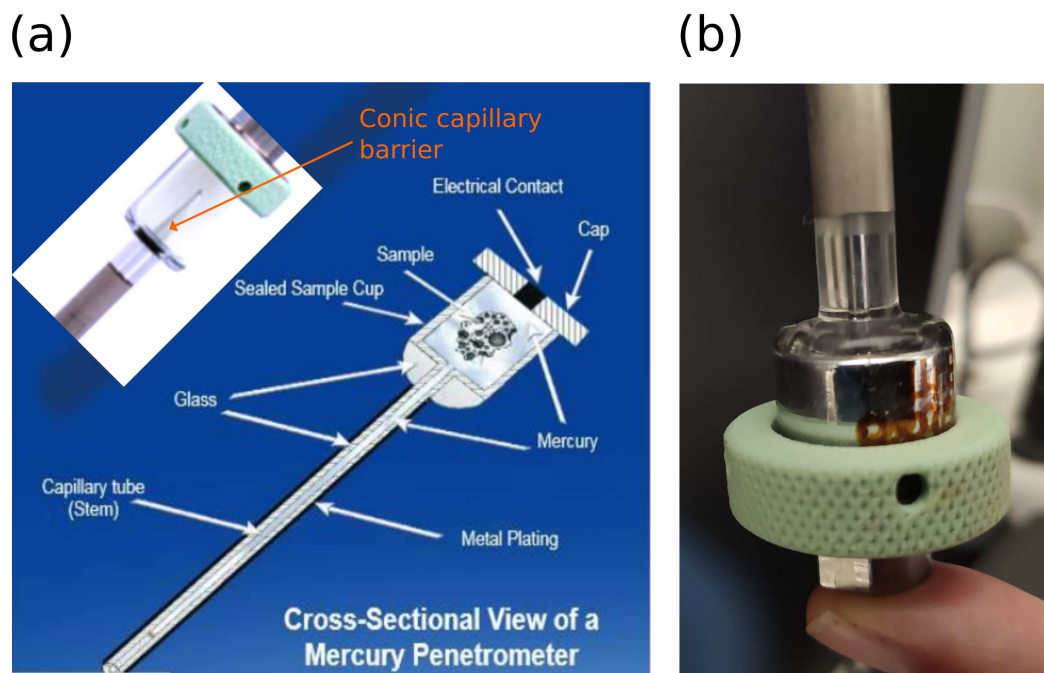


Figure 3.2: (a) Schematics of a mercury porosimetry penetrometer. The models used have a conic barrier inside the cell to protect the capillary from contamination. Figure adapted from [29]. (b) Penetrometer once filled with mercury and measures completed.

### 3.2.3 Particle compression with X-ray tomography observation

In-situ compression testing of individual aerogel particles was carried out within a X-ray tomograph. The compression device illustrated in Fig. 3.3c was designed to be placed inside a X-ray tomograph (RX-Solution, Annecy, France). Particle compression was performed right after a first tomography scan at 40 kV, 250  $\mu$ A. The density of each particle has been calculated before their compression using the volume determined from X-ray tomography and the mass measured with a XP26 Mettler Toledo microscale. Once a particle has been weighted, it only endures one transfer to the X-ray tomograph for initial scanning and is ready for mechanical testing with no additional manipulation. X-ray tomography is a convenient technique for monitoring aerogel fracture but some cautions are needed as these materials show a low absorption due to their extremely high porosity. Any material too dense compared to silica aerogels placed between the particle and the X-ray source or the CCD camera would absorb too many photons, possibly inducing a decrease of the contrast of the scans or artefacts. For this reason the window and the compression tools of the setup are made of polycarbonate. Low X-ray absorption and optimized thickness of polycarbonate prevent artifacts. Particle compression was carried out at 1.2 mm.mn<sup>-1</sup> and stopped at the first sign of fracture (detected by visual monitoring of 2D radiography). Due to some constraints of the setup, the force could not be recorded while the particle was compressed. The testing was paused several times (for a maximum of 20 seconds) once the particle had been compressed more than 20% of its initial height to record the force, as most of the silica



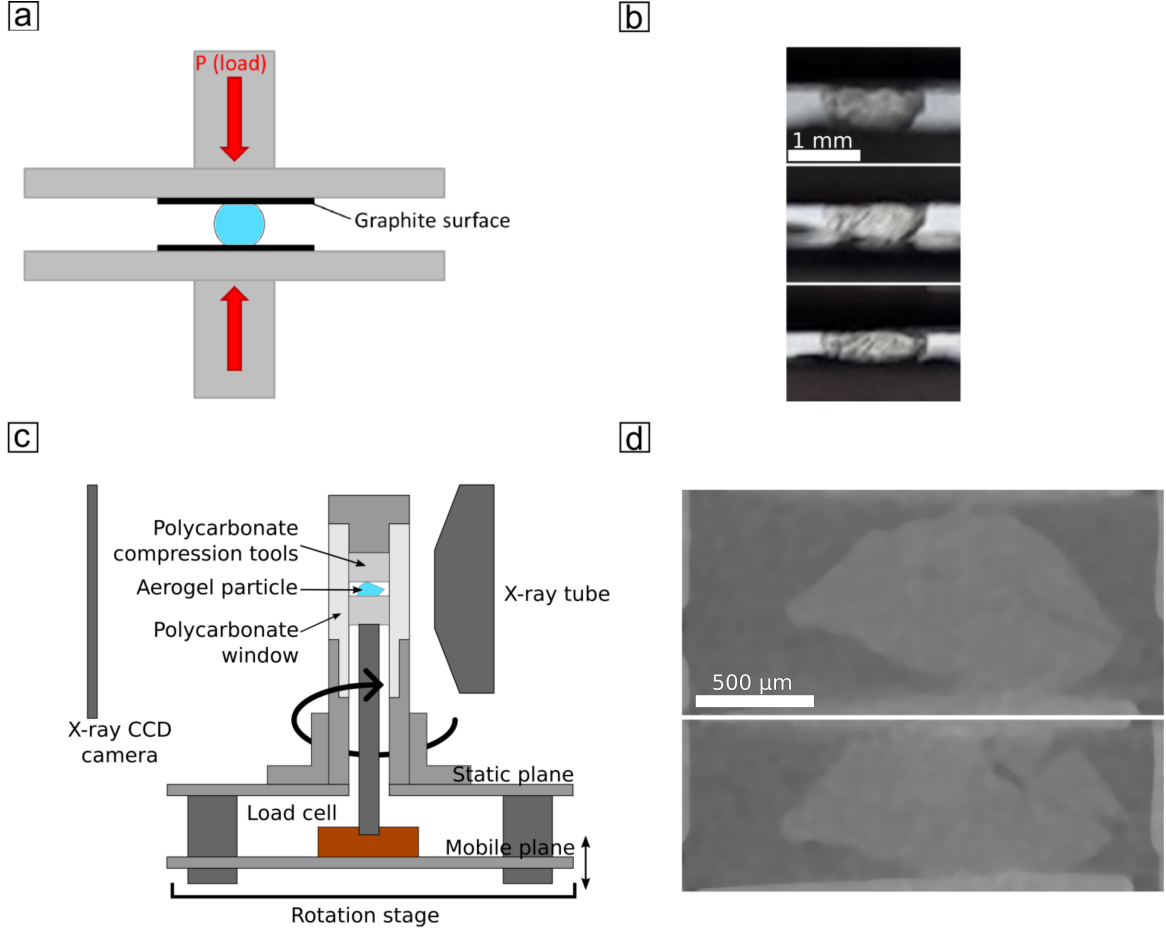


Figure 3.3: Compression setup for individual particle compression. a) Standard compression setup. b) Images of particles deformation while compressive load increases. c) Compression setup for X-ray tomograph compression. d) Tomographic cross section of a particle during fracture.

aerogel particles break after this value (experimented during statistical procedure). This procedure eased the determination of the particle fracture force  $F_f$  by detecting with more accuracy the fracture of the particle. In that case, fracture force  $F_f$  and fracture height  $h_f$  were estimated as the mean value of the two last recorded points with accordingly adjusted error bars (half interval between the two last points). Fracture force and fracture height were determined for each particle. At least two scans were acquired with a voxel size of  $2\ \mu\text{m}$ , one just before the beginning of the compression and one once crack propagation has been detected in the aerogel particle. Particles were not unloaded for the final scan in order to maintain their integrity. Image processing of the tomography scans allowed the extraction of particle's shape by applying a 3D median filter before segmentation of the aerogel phase by simple thresholding on gray-levels (Fiji software [70]). Process induced cracks within particles were manually segmented as no automated method has given acceptable results for these features.

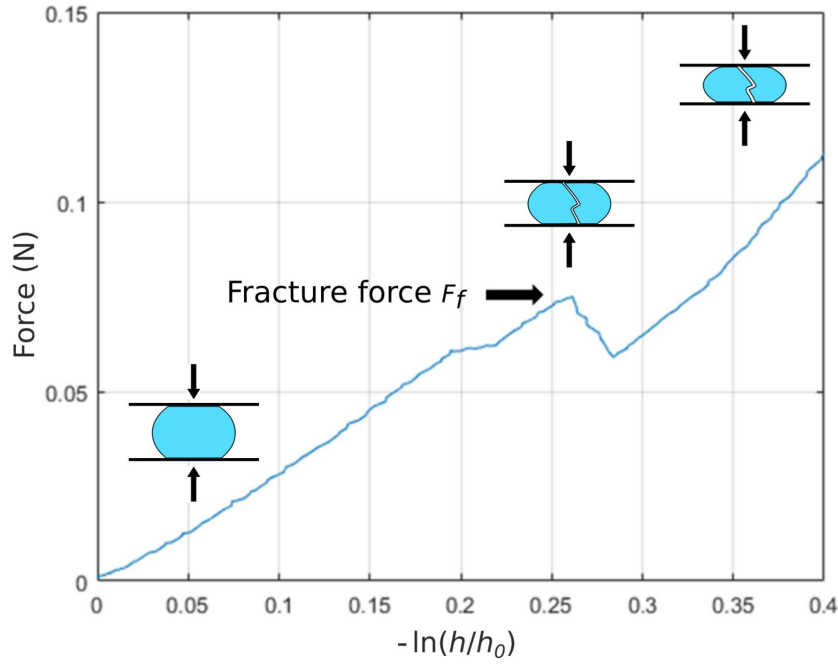


Figure 3.4: Experimental compression of an individual aerogel particle.  $h$  and  $h_0$  are the current and initial sample heights, respectively.

### 3.3 Particulate aerogel composite fabrication

The particulate composites fabricated and studied in this PhD are based on a patent by EDF company and MATEIS lab [63]. The structural, mechanical and thermal properties of these composites have been studied previously in the PhD thesis of A. Perret [29]. The fabrication procedure of the composites presented hereafter is mainly inspired by these two references.

#### 3.3.1 Base components

The main components of the composites studied in this work are silica aerogel particles provided by Enersens company (Bourgoin-Jallieu, France). These particles were sieved using a vibrating table with adapted screens, resulting in the collection of two size distributions. Metallic balls were added on the screens to break up the larger particles to the target size. The largest particles were sieved between 1000 and 1250  $\mu\text{m}$  (hereafter referred as 10-12 or large particles) and the smallest below 100  $\mu\text{m}$  (hereafter referred as inf100 or small particles).

The binding agent is a latex in the form of micrometric spheres of styrene butadiene acrylonitrile (SBA) coated with a thin layer of poly(methyl methacrylate) (PMMA). It has been provided in a 50w% concentrated aqueous solution by BASF company.

The aerogel particles and the binding agent are both hydrophobic. A surfactant presenting both hydrophobic and hydrophilic sites is necessary for the latex to form a film while in an aqueous solution during the mixing step, covering aerogel particles and binding them together. In our case, the surfactant is a molecule provided by



PCAS company (Bourgoin-Jallieu, France) hereafter referred as XPCAS (the molecule formulation is confidential). It is a large molecule with a ratio of two hydrophobic sites per hydrophilic site. This agent has also been provided in a 30w% concentrated aqueous solution.

In order to strengthen the composite and to ease its handling, fibres have been incorporated in the composites. This option was poorly explored in previous works [29, 63] and different types of fibers were tested here. The length of these fibers was capped at 5 mm to limit the potential increase in thermal conductivity of the composites. Detrimental thermal bridges are mitigated by this precaution because the processed composite objects have a thickness of 20 mm as described below. The components of the composites and their main characteristics are summarized in Fig. 3.5.

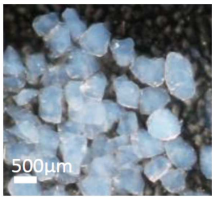
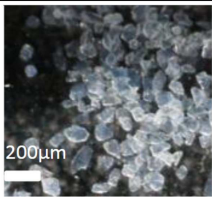
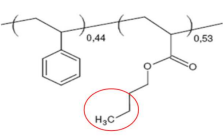
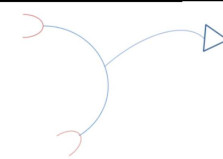
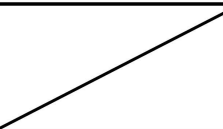
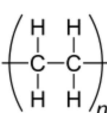
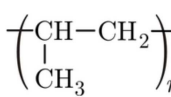
Component	Illustration	Details	Object size
Aerogel particles 10-12 (ENERSENS)		Polyhedral hydrophobic aerogel particles	1000-1250 µm
Aerogel particles inf100 (ENERSENS)		Polyhedral hydrophobic aerogel particles	< 100 µm
SBA-PMMA (BASF)		Binding agent Styrene Butyl Acrylate (SBA) coated with 3 w% Poly(Methyl MethAcrylate) (PMMA), Hydrophobic	210 nm
XPCAS (PCAS)		Surfactant Molecule presenting 2 hydrophobic sites for 1 hydrophilic site	20-70 nm
Glass fibers		High performance glass fibers. Bundles bound together with starch.	length: 3-7 mm radius: ~5 µm
Polyethylene (PET) fibers		2 types: bundles bound together with starch and PET roving	length: 3-7 mm radius: ~5 µm
Polypropylene (PP) fibers		fibers bundles roughly shredded in non cylindrical objects of various sizes	length: 3-7 mm radius: 2-100 µm

Figure 3.5: Components of the composites fabricated in this PhD work. Adapted from [29].

### 3.3.2 Mixing

During the mixing step of the composite preparation, the aerogel particles are blended together with an aqueous solution containing the binding and surfactant agents. The compositions are indicated below for the reference composite studied in this work inspired by the EDF patent [63]:

- Solid phase: 3/2 mass ratio between 10-12 aerogel particles and inf100 particles
- Aqueous phase: for each 10 g of silica aerogel particles, prepare a solution with 19 g of water, 2.4 g of the latex solution and 2.2 g of the XPCAS solution. It shall result in a solution with approximate concentrations of  $51.5 \text{ g L}^{-1}$  for latex and  $28.4 \text{ g L}^{-1}$  for XPACS.

The two phases are then blended together by hand in a spherical bowl until the mix takes the form of a single ball of paste without residual isolated aerogel particles (see Fig. 3.6a). The mix starts to take the texture of a paste very lately in the process, as the aqueous phase and the hydrophobic aerogel particles hardly interact in the beginning. Conventional mechanical mixing tools are not adapted to this process as their movement or geometry are not optimal to ensure an efficient coating of the particles by the agents in the aqueous solution. Some of them can even deteriorate the aerogel particles, which should be limited as much as possible to ensure good thermal performances. Hand mixing has been chosen to obtain an efficient coating of the particles limiting both particle deterioration and matter loss as the inf100 particles can be easily expelled of the container by sudden moves. The movement of the hand is a grasping and squeezing move, slightly compressing the aerogel particles together without breaking them. An audible crackling sound might indicate the deterioration of some particles, giving a clue on the pressure to apply in the movement. For the same reason, fingers from the index to the little finger stay joined together and the thumb never touches the rest of the hand during all the movement. Finally, the movement must reach the bottom of the container to include some of the aqueous solution and increase the interaction between aerogel particles and the components in solution.

In the case of fibre introduction in the mix, the proportions in the solid and aqueous phases stay the same but only half of the aqueous solution is introduced in the bowl initially. The other half is blended with the fibers in a separate container and added to the mix when the first clues of the binding agent coating the particles appear (see Fig. 3.6b). The most perceptible clue for this is the formation of small white beads in the particles phase formed by the agglomeration of small inf100 particles coated with the binding agent. This step generally appear after 10-20 minutes of mixing and the completion of the paste happens most of the time less than 10 minutes after. It can be noted that this duration corresponds to an approximate aerogel particle mass of 50 g. If the volume is more important, the aerogel surface to coat will be larger and the global mixing time will increase. The same remark applies when we modify the size ratio in the solid phase in favour of small aerogel particles as this also increases the total surface to coat.

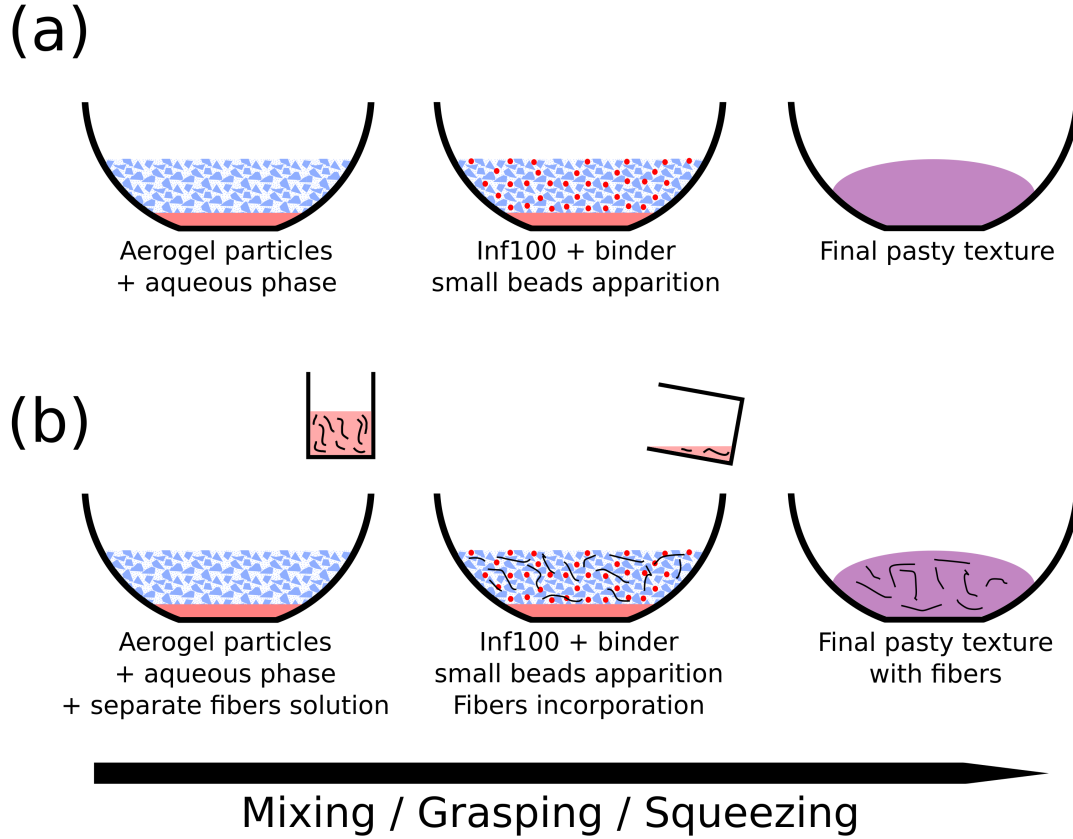


Figure 3.6: Mixing of the aerogel particles with the aqueous solution containing both binding and surfacing agents. (a) Fabrication of a standard particulate composite: aerogel particles + binder. (b) Fabrication of a fibrous particulate composite: aerogel particles + binder + fibers.

### 3.3.3 Molding

Once the paste has been fabricated, it is kept in the form of a ball in order to limit its desiccation during the next 30 minutes when samples are molded. Molds are rectangular and are made of movable Teflon partitions. These partitions limit the damages on the surfaces during the extraction of the wet samples. Two sizes are available for the molds:  $20 \times 20 \times 80 \text{ mm}^3$  and  $10 \times 10 \times 80 \text{ mm}^3$ , as illustrated in Fig. 3.7a. The composite paste is stretched in successive layers in the mold until a surplus is obtained at the top of the mold. The surplus is then removed by scratching the surface with a flat Teflon tool (see Fig. 3.7b). Wet samples are then released by removing the partitions in the right order by sliding the Teflon surfaces in parallel to the sample sides (see Fig. 3.7c). Once the wet samples are released, they are weighed and measured before the drying step.

### 3.3.4 Drying

The wet composite samples are put individually on expanded polystyrene holders and placed in a climatic chamber. The samples are dried at  $40^\circ\text{C}$  and 40% relative humidity

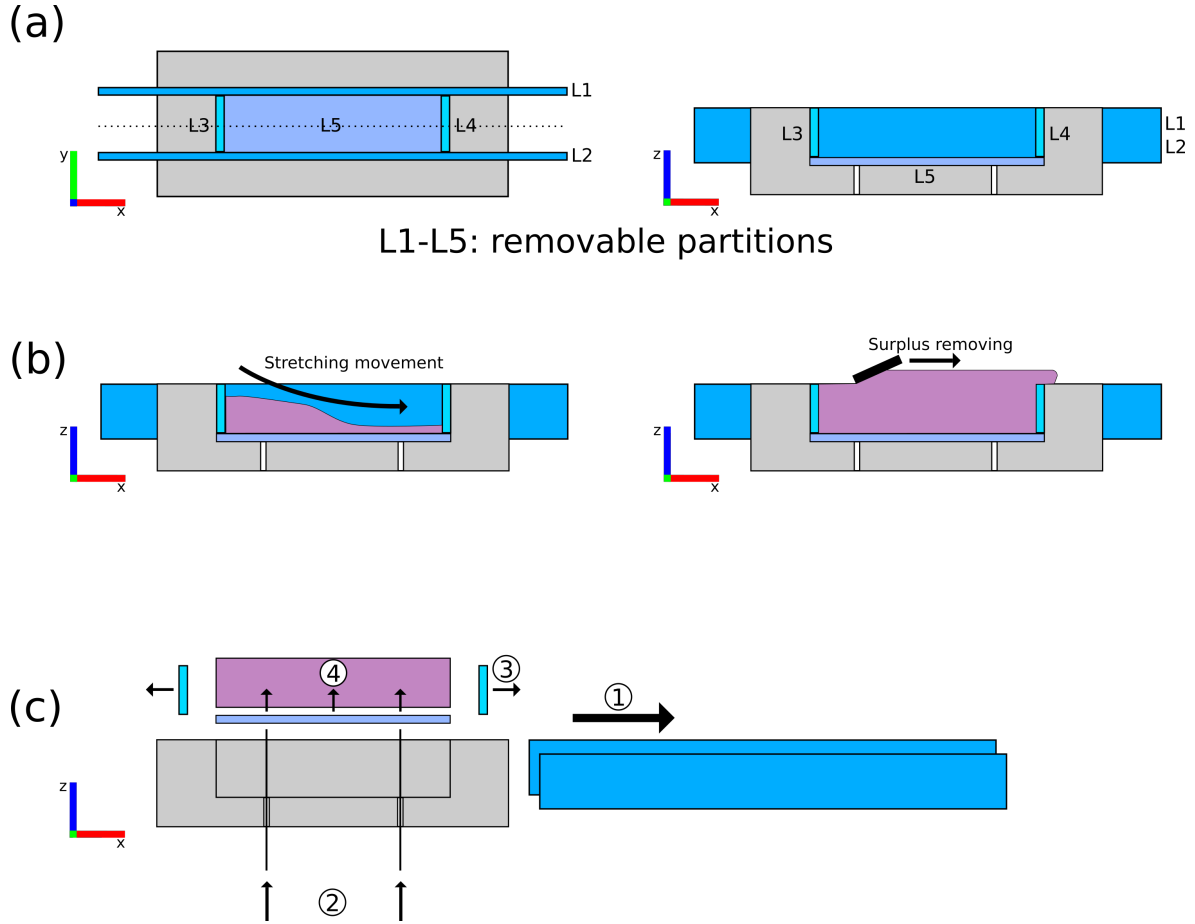


Figure 3.7: (a) Molds structure with removable partitions L1-L5. (b) Molding of the wet composite samples. (c) Release of the wet composite samples following an appropriate order when removing the partitions (1 to 5).

during at least 24 hours. The samples are weighed and measured again in order to compute the bulk density of the composites. Typical samples obtained after the drying step are shown in Fig. 3.8.

## 3.4 Mechanical characterization of particulate aerogel composites

### 3.4.1 Indentation

#### 3.4.1.1 Instrumented macro-indentation

Indentation has been performed on particulate composite surfaces previously polished with sand paper (silicon carbide with 16  $\mu\text{m}$  particles). The polishing step reduces the surface roughness which has a high impact on the indentation tests.

Tests were carried out using a Bose ElectroForce 3200 traction / compression machine (Prairie Valley, USA) with a spherical steel indenter of 5 mm diameter. The load cell has a maximal nominal load of 22 N with an accuracy of  $\pm 0.02$  N. Displacement

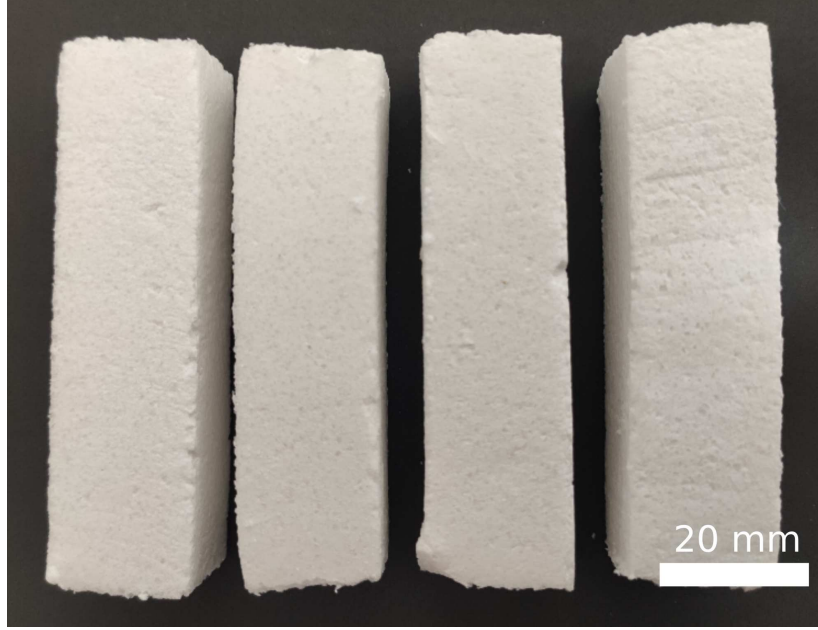


Figure 3.8: Typical composite samples obtained after the final drying step.

is measured by using a capacitive sensor with an accuracy of 50 nm but limiting the total indenter course to 1 mm. Once the surface is detected with a force of 0.02 N, the loading of the sample is carried out at  $1 \text{ mm min}^{-1}$  until a force of 0.5 N is reached. The indenter movement is then paused during 40 second before the unloading of the sample carried out at  $1 \text{ mm min}^{-1}$ .

Oliver & Pharr proposed a method to determine the hardness  $H$  (Meyer hardness: average contact pressure) and the Young's modulus  $E_{unload}$  as functions of the indenter penetration below the plane of contact  $h_c$  when analyzing the unloading data of the indentation tests [40, 71]. Their equations will be used in this work:

$$h_c = h - \epsilon \frac{P}{S} \quad (3.1)$$

$$\frac{1}{Er} = \frac{1 - (\nu^{sample})^2}{E^{sample}} + \frac{1 - (\nu^{indenter})^2}{E^{indenter}} \quad (3.2)$$

$$E_{unload}^r = \frac{S\sqrt{\pi}}{2\beta\sqrt{A(h_c)}} \quad (3.3)$$

$$H = \frac{P}{A(h_c)} \quad (3.4)$$

where  $h$  is the displacement of the indenter,  $P$  is the indenter load,  $S$  is the unloading stiffness ( $\frac{dP}{dh}$ ) calculated by linear fitting of the first steps of the unloading curve,  $E^{sample}$  and  $E^{indenter}$  are Young's modulus,  $\nu^{sample}$  and  $\nu^{indenter}$  are Poisson's ratios of the sample and of the indenter respectively,  $A(h_c)$  is the contact area projected on the contact plane and  $\epsilon$  and  $\beta$  are geometrical constants that depends on the type of indenter. In the case of a spherical indenter, these constants are derived from the analytical elastic solution for load-displacement curves in the linear-elastic region described by

Hertz [40, 72]. The corresponding values are  $\epsilon = 0.75$  and  $\beta = 1$ . Moreover, the surface contact for spherical tips can be calculated as  $A = 2\pi Rh_c - \pi h_c^2$ . In our case, applying a force of 0.5 N on particulate silica aerogel composites results in an indentation  $h_c$  between 0.4 and 0.5 mm. The corresponding surface contact  $A$  is thus 6 mm<sup>2</sup> roughly so, as the largest aerogel particles in the composites have a diameter around 1 mm, the tested area include the different phases of the composite samples (silica aerogel particles, binder and pores). A software developed by P. Clément from MATEIS laboratory (Lyon, France) [73] was used in this PhD work to estimate the Young's modulus and the hardness of silica aerogel composites. It allows a partially automated detection and calculation of the initial contact point and unloading stiffness of the load-displacement curves. An illustration of the process is given in Fig. 3.9.

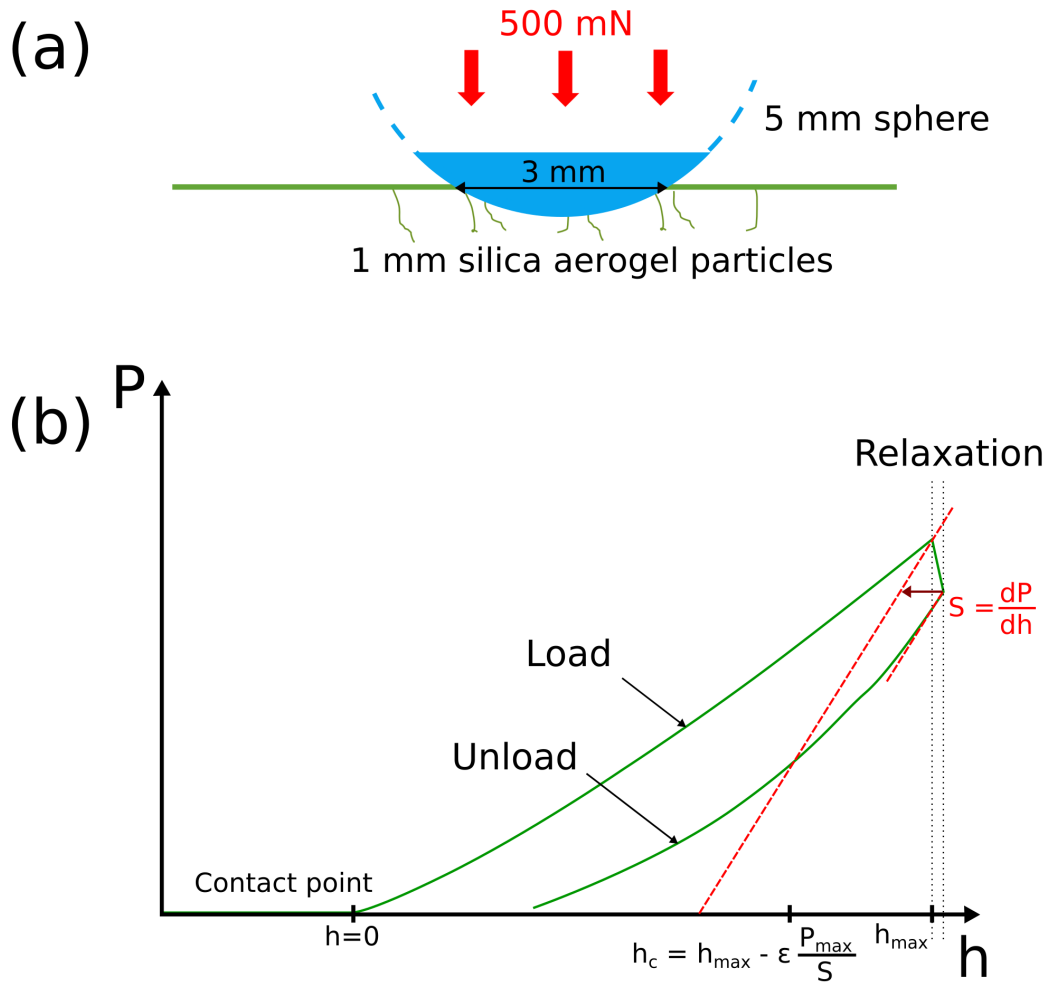


Figure 3.9: (a) Indentation process on particulate composites with a 5 mm sphere. (b) Corresponding data processing following Oliver & Pharr method.

### 3.4.1.2 Instrumented micro-indentation

Micro-indentation tests were carried out on the composite samples in order to obtain mechanical properties of the different phases present in the composite materials, namely the large aerogel particles (10-12 particles) and the cement between these (mix of inf100

particles and binding agent). For this purpose, a Agilent G200 nano-indenter were equipped with a 2 mm spherical indenter. The calculation of the Young's modulus is different from the method used for the macro-indentation tests presented previously because the continuous stiffness measurement (CSM) method is used. This involves applying a dynamic sollicitation (2 nm of amplitude at 45 Hz) on top of the quasi-static loading (see Fig.3.10) [74]. By analyzing the dynamic part of the displacement and the load, the Young's modulus and the hardness of the material can be calculated as a function of indentation depth.

This method requires the detection of the sample surface, which is delicate for our semi-translucent and low stiffness composite samples. In consequence, while the composite surfaces have been polished before the tests, a limited amount of zones have been successfully indented with this method. For the tests where the surface have been successfully found, a maximum indentation of 10  $\mu\text{m}$  has been applied with a strain-rate of  $0.05 \text{ s}^{-1}$ .

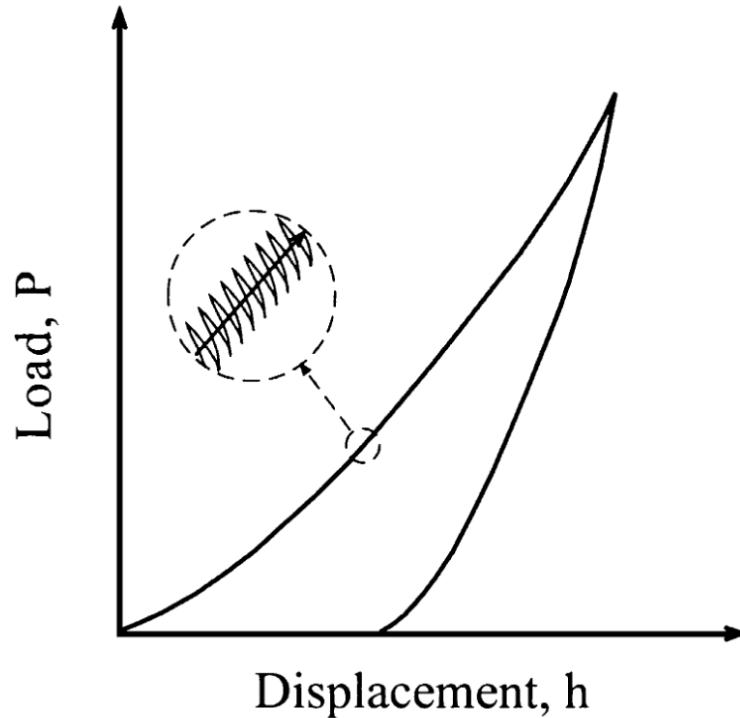


Figure 3.10: Schematic of the CSM loading cycle. Figure from [74].

### 3.4.2 Uniaxial compression

Uniaxial compression has been carried out on particulate aerogel composites cylinders. The preparation of samples requires special care as the composites break easily when using non-abrasive tools like scalpels or other blades. In order to shape samples, mechanical tools like saws or drills are more appropriate as the composites are very sensible to abrasion. The cylindrical samples have been cut using a hole saw attached to a column drilling machine. Their resulting dimensions are a diameter of 17 mm



and a height of 19 mm. The samples top and bottom surfaces are then polished to minimize the rugosity of surfaces in contact with the compression tools (sand paper, silicon carbide with grain size 16  $\mu\text{m}$ ).

Compression tests have been carried out using a MTS4M traction / compression machine equipped with a 500 N load cell with an accuracy of  $\pm 1$  N. The compression platens are aluminium cylinders. After having determined their precise dimensions and manually applied an initial load of 0.2 N, samples have been compressed at constant strain rate ( $0.001 \text{ s}^{-1}$ , corresponding to a cross-head velocity of  $1 \text{ mm min}^{-1}$  approximately) until fracture. The fracture point is not easily identifiable because most samples deteriorate gradually starting from the cylinder surface. The sample core stays intact whereas the samples volume decreases substantially by progressive spalling of the lateral surface. For this reason, the compressive strength is extracted as the maximum stress recorded during these tests. The Young's modulus is calculated for strains between 2 and 3 % in the linear elastic region of the stress-strain curves. Stress-strain curves were extracted without the use of an extensometer as the machine stiffness was far greater than that of the samples. A typical example of uniaxial compression is illustrated in Fig. 3.11.

### 3.4.3 Flexural tests

Flexural tests have been performed on Single Edge Notched Beams (SENB) in order to extract a fracture toughness. Samples are  $20 \times 20 \times 80 \text{ mm}^3$  beams with polished surfaces and with a 4 to 5 mm notch (cut by using a razor blade) centered on one side. Tests were carried out on a three point bending equipment mounted on a Bose ElectroForce 3200 traction / compression machine. The spacing  $l$  (Fig. 3.12) between the two bottom points is 50 mm. The load cell has a maximal nominal load of 22 N with an accuracy of  $\pm 0.02$  N. Displacement was measured using the internal sensor of the machine providing an accuracy of  $0.5 \mu\text{m}$  approximately.

Beam dimensions were measured before testing (width  $b$ , height  $H$  and notch length  $a$ ). Samples were then placed on the two bottom contact points, the notch oriented to the bottom side and aligned with the upper contact point as illustrated in Fig. 3.12. The initial contact was made for 0.01 N and beams were loaded with a crosshead velocity of  $1.5 \text{ mm min}^{-1}$  until the fracture point is reached. Fracture toughness were calculated with the following equation:

$$K_{1c} = \frac{3PL}{2bH^2} \sqrt{\pi a} * Y \quad (3.5)$$

where  $Y$  is a shape function that depends on notch size  $a$  and sample height  $H$ . Several models exist for this function. The model chosen in this work is the one suggested by standard ASTM D5045-14 [75] :

$$Y = \frac{1.99 - a/H(1 - a/H)(2.15 - 3.93a/H + 2.7(a/H)^2)}{(1 + 2a/H)(1 - a/W)^{2/3}} \quad (3.6)$$



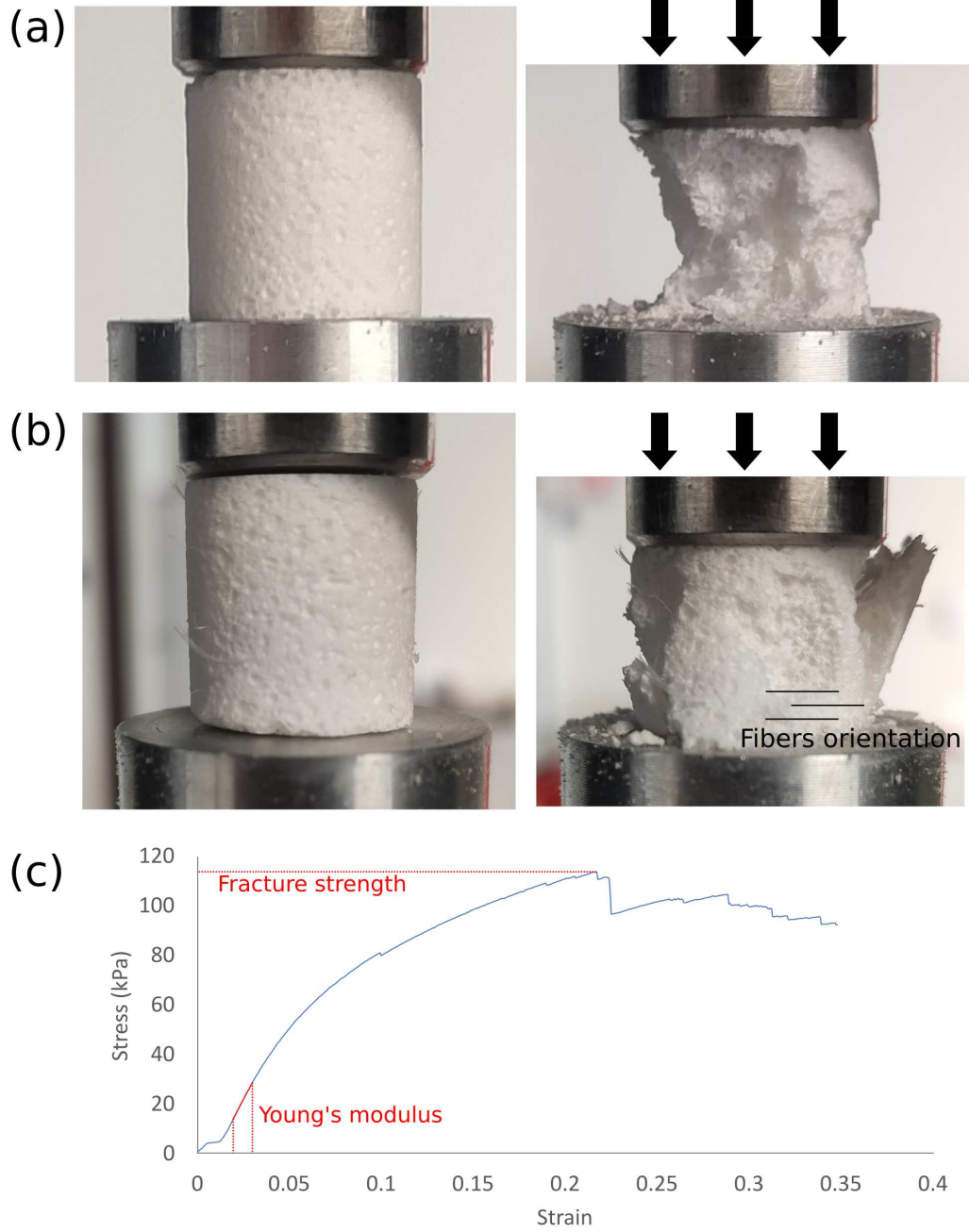


Figure 3.11: Uniaxial compression of a cylindrical particulate composite samples. (a) Sample with no fibers. (b) Sample with polypropylene fibers. (c) Stress-strain curve corresponding to sample (a).

#### 3.4.4 Double cleavage drilled compression tests (DCDC)

DCDC samples are rectangular beams with a hole drilled at mid-length. Two notches are introduced on each side of the hole, parallel to the length of the beams, as illustrated in Fig. 3.13a. Generally, the half-sample-width-to-hole radius ratio is around 4-6 ( $(2w)/D$ ), the height-to-width ratio is around 4 ( $l/(2W)$ ) and the sample thickness  $t$  is equal or inferior to its width  $w$  [76]. The compression of these samples along their length opens the notches and generates the stable propagation of two cracks. DCDC

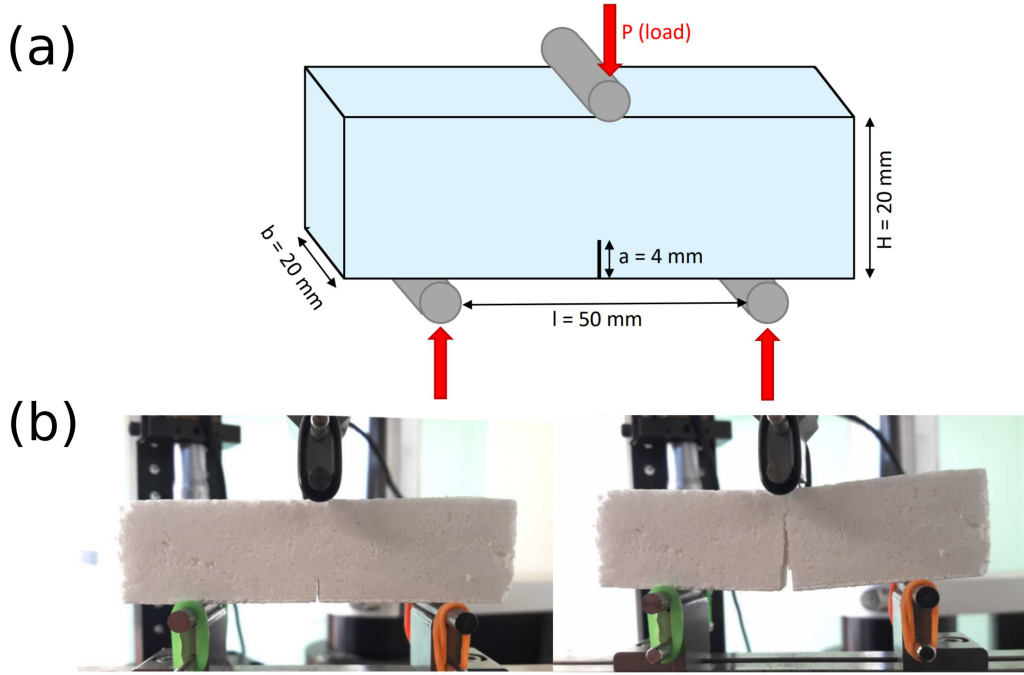


Figure 3.12: (a) Dimensions and position of the SENB samples. (b) Flexural test on a SENB particulate composite sample.

tests are usually carried out for brittle materials where the stable development of cracks provides valuable data of stress intensity factor versus crack velocity during subcritical crack growth [76–78]. In the case of particulate aerogel composites, these tests are meant to determine how the cracks propagate in the material and to identify the crack path through the microstructure of the samples. They also provide an alternative way to SENB flexural tests for the estimation of fracture toughness. Although most of the known applications of this method are in the field of glass and ceramics, it has already been applied to silica aerogel monoliths [32].

DCDC composite samples have been sawed to prepare  $8 \times 8 \times 25$  mm<sup>3</sup> beams. The central hole has been obtained with a 3 mm drill and the notches have been cut with a scalpel blade, resulting in an approximate notch length of 1 mm. The reason why the samples are so small, compared to what is possible to produce by machining our primary  $20 \times 20 \times 80$  mm<sup>3</sup> beams, is that the final objective is to compress these samples inside a X-ray tomograph in order to observe the gradual progression of cracks in the volumes. The compression system compatible with the laboratory X-ray tomograph (Simap, Grenoble, see section 3.1.1.1) imposes size limitations to the samples. This system (see Fig. 3.13b) is almost identical to the one illustrated in Fig. 3.1c, the only difference being the internal diameter of the compression column which is equal to 10 mm in this case. Tomography scans have been carried out approximately every 300 mN with a voxel size of 10  $\mu$ m. It was necessary to pause the compression during scans which lasted approximately 10 minutes. The initial state of a DCDC sample is illustrated in Fig. 3.13c.

DCDC samples with the same dimensions have also been compressed outside the X-ray tomograph. Nielsen et al. created an empirical model for estimating fracture

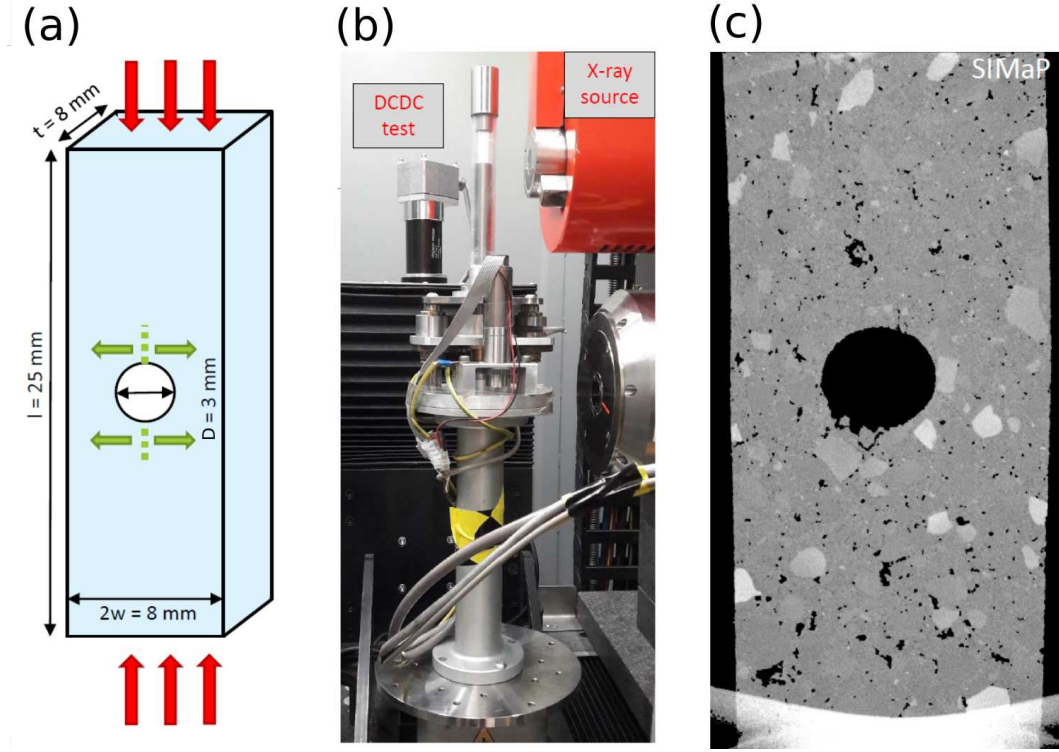


Figure 3.13: (a) Geometry of the samples and principle of DCDC tests. (b) Compression system compatible with X-ray tomography. (c) Initial state of a DCDC composite sample as seen through a tomography cross-section.

toughness using DCDC tests [79]. They found out that, if a linear section is observed in the axial stress vs. crack length curves as illustrated in Fig. 3.14a, the fracture toughness  $K_{Ic}$  can be calculated using the following equation:

$$K_{Ic} = \frac{3}{4}(D/w)^2\sigma_0\sqrt{w} \quad (3.7)$$

where  $D$  is the hole diameter,  $w$  is the half-width of the sample (Fig. 3.13b) and  $\sigma_0$  is the intercept of the regression line illustrated in Fig. 3.14a on the axial stress vs. crack length curve.

A precise monitoring of the crack length during these tests is necessary. A digital image correlation (DIC) system GOM Aramis 6M following this progression has been used. The DCDC samples have been speckled with black ink, resulting in a random array of black spots with an approximate density of  $400 \text{ mm}^{-2}$ . The DIC system allows the crack length to be accurately monitored by detecting the strain evolution perpendicular to the crack propagation as illustrated in Fig. 3.14c. The resulting axial stress vs. crack length curves does not present the necessary linear part for the determination of the parameter  $\sigma_0$ . The two limit cases illustrated in Fig. 3.14b are then considered and the difference between  $\sigma_0^{max}$  and  $\sigma_0^{min}$  generates the error bar for the corresponding fracture toughness.

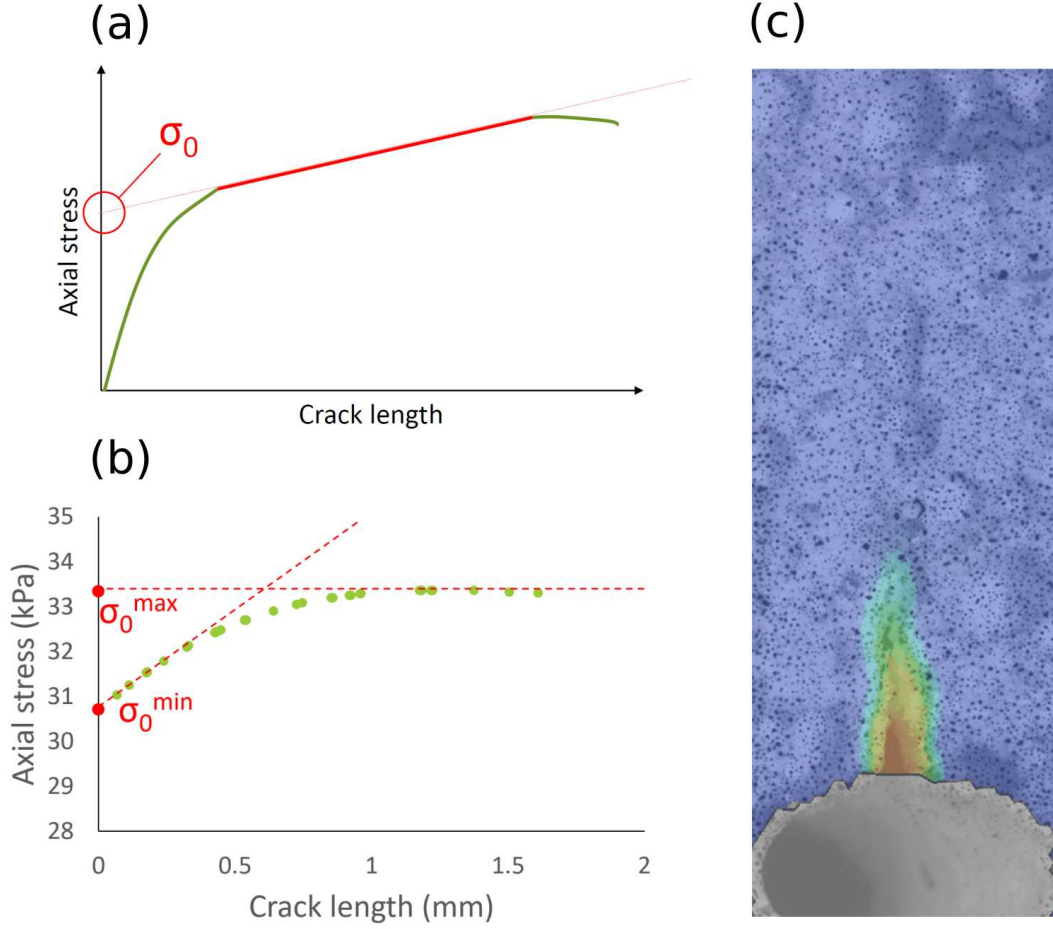


Figure 3.14: (a) Extraction of parameter  $\sigma_0$  during a DCDC test [79]. (b) Extraction of parameter  $\sigma_0$  for our composite samples. No linear section is identifiable on the curves so the two limit cases  $\sigma_0^{max}$  and  $\sigma_0^{min}$  are considered. (c) Following of the crack length of a DCDC sample by imaging the strain perpendicular to the crack propagation direction with using DIC data. Horizontal strain is increasing from cold to hot colors (see colored version of this figure).

## 3.5 Thermal characterization of particulate aerogel composites

### 3.5.1 Fluxmeter measurements

Fluxmeter tests consist of the measurement of a heat flux crossing a sample located between a hot plate at temperature  $T_h$  and a cold plate at temperature  $T_c$ . Flux sensors are present on each plate and allow the calculation of the thermal conductivity  $\lambda$  of the sample once the steady-state regime is reached:

$$\lambda = \frac{\Phi e}{A(T_h - T_c)} \quad (3.8)$$

where  $\Phi$  is the heat flux crossing the heat sensors,  $e$  is the sample thickness and  $A$  is the sensors surface area. In the case of our composite samples, it is necessary to use a system adapted for small samples ( $20 \times 20 \times 80 \text{ mm}^3$  samples). A system developed in a partnership between the companies EDF (Moret-Loing-et-Orvanne, France) and CSTB (Saint-Martin-d'Heres, France) consists of two rectangular aluminum plates ( $150 \times 150 \text{ mm}^2$ ) each with a circular heat flux sensor incorporated (10 mm diameter) [29]. Samples must be larger than  $20 \times 20 \times 2 \text{ mm}^3$  to prevent the unidirectional heat flow from being influenced by heat exchange across the sides of the samples. Moreover, a system producing stable temperatures  $T_h$  and  $T_c$  and providing an isolated environment without air convection is necessary. For this purpose, a fluxmeter usually adapted for larger samples ( $300 \times 300 \text{ mm}^2$  chamber) from Enersens company (Bourgouin-Jaillieu, France) is used.

Fluxmeter tests on our composite samples have been carried out by joining four polished  $20 \times 20 \times 80 \text{ mm}^3$  beams together to prepare a  $80 \times 80 \text{ mm}^2$  square. These samples are joined and compressed together in a polystyrene foam matrix. It allows most of the spacing between the samples to be eliminated and limits heat exchanges on the sides. In order to reach the dimensions of the Enersens fluxmeter chamber, the samples and the polystyrene matrix are surrounded by rock wool. This precaution allows air convection to be eliminated around the polystyrene matrix and the aluminum plates. The aluminum plates themselves are placed on each side of the samples, perfectly adapted to the polystyrene matrix. Special heat conducting rubber spacers (1 mm thick) are inserted between the samples and the aluminum plates in order to improve the contact quality with the sensors. The whole system is illustrated in Fig. 3.15. For each group of four samples, a temperature difference  $\Delta T$  of  $20 \text{ }^\circ\text{C}$  has been applied during 45 minutes. This duration corresponds to the time necessary to attain the steady-state regime.

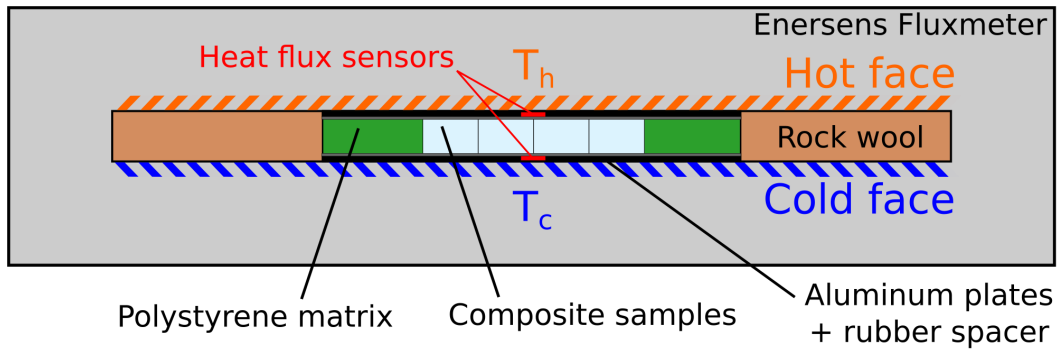


Figure 3.15: Heat flux measurement on four joined composite samples using Enersens fluxmeter for temperature stability and 10 mm heat flux sensors on aluminum plates.

### 3.5.2 CT-meter measurements

CT-meter measurements (also called hot-wire method) use a hot wire introduced between two sample layers to measure temperature increase during the transient regime of a pulse heating. Assuming a cylindrical heat propagation and a homogeneous and



isotropic sample, the following equation can be used to determine the thermal conductivity  $\lambda$  once a sufficient heating time  $t$  is achieved [80–82]:

$$\Delta T = \frac{q}{4\pi\lambda}(\ln(t) + C) \quad (3.9)$$

where  $\Delta T$  is the temperature difference  $T(t) - T_{init}$ ,  $T_{init}$  is the temperature of the sample before heating,  $q$  is the heat flow per meter and  $C$  is a constant. A linear regression on the  $\Delta T$  vs.  $\ln(t)$  allows the thermal conductivity of the sample to be calculated.

The CT-meter measurements have been carried out inside a vacuum chamber varying the pressure, allowing the influence of the gaseous heat conduction to be quantified in the composite samples. The minimum pressure reached is 0.075 mbar. Two different hot wires have been used in order to conduct two different measurements simultaneously in the chamber:

- 80 mm long hot wire, 8.41  $\Omega$ , intensity applied  $I = 0.07$  mA
- 50 mm long hot wire, 7.56  $\Omega$ , intensity applied  $I = 0.08$  mA

These hot wires have been located between two layers of  $20 \times 20 \times 80$  mm<sup>3</sup> samples joined together to make a  $80 \times 20 \times 80$  mm<sup>3</sup> sample encased in a polystyrene matrix similar to the one described in section 3.5.1. The pressure has been decreased to 0.075 mbar before the first measurements. Thermal conductivities have been measured regularly until the ambient pressure is reached (10 points in total). Heating time of the hot wires has been tuned to 120 seconds for these tests. The system is illustrated in Fig 3.16.

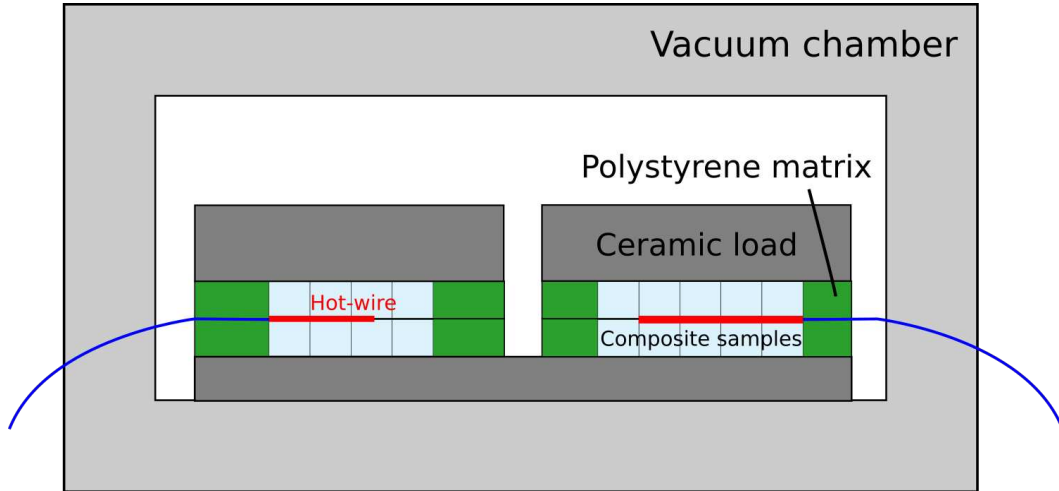


Figure 3.16: Hot-wire method applied to composite samples in a vacuum chamber. The first wire is 50 mm long and the second is 80 mm long, requiring different sample sizes.



# Chapter 4

## Numerical methods

### 4.1 Discrete element model (DEM) basics

#### 4.1.1 What is DEM ?

In order to simulate the fracture of different silica aerogel objects and composites, the discrete element method (DEM) has been chosen. DEM is particularly well suited to study fracture and crack propagation of a large spectrum of materials. This is because it uses an explicit discontinuous framework that is well adapted for the topological modifications that come with fracture phenomena. By defining interaction laws between elements of a discrete network, this method calculates at each time step the position and velocity of each element, making it a Lagrangian method. Here we use smooth DEM where discrete elements are allowed to overlap (in contrast with non-smooth DEM like in contact dynamics [83]). In this context, overlap allows contact forces and moments to be calculated and then the second law of Newton is applied on each element. The interactions (forces and moments) between discrete elements depend on the interaction laws implemented in the model.

Historically, DEM was pioneered by Cundall and Strack in 1979 [84] for the study of geomaterials but is also adapted for continuous materials [85–90]. Using DEM to study low-stiffness and brittle materials like silica aerogels was successfully carried out before with discrete elements representing primary silica particles, i.e. the silica particles forming the nanoscale pearl-necklace network of aerogels [91, 92]. Previous work simulating silica aerogel objects using Molecular Dynamics can also be found [Goncalves2018] but this method do not allow to study volumes larger than a few  $\mu\text{m}^3$ . Another simulation method, the hybrid finite-discrete element method (FDEM), is also well adapted to the study of continuous materials fracture as it combines the advantages of the finite element method for the study of continuum mechanical problems and the advantages of the discrete element method for the study of fracture phenomena [93–95]. FDEM has yet to be tested for aerogel particles fracture and this work will only focus on the use of DEM.

The DEM code used in this PhD, called dp3D<sup>1</sup> (standing for "discrete powder 3D"), uses spherical discrete elements, much easier to handle than arbitrary objects when searching for neighbors and processing contacts. It has been initially developed in 2000 by Prof. Martin (Univ. Grenoble Alpes) and Prof. Shima (Univ. Kyoto) and has evolved thanks to the input of Prof. Jauffrès, PhD students and post-docs working at SIMaP laboratory (Univ. Grenoble Alpes).

---

<sup>1</sup><https://simap.grenoble-inp.fr/fr/equipes/dp3d-dem-for-materials-science>



### 4.1.2 DEM algorithm

During a DEM simulation, the following procedure is repeated at each time step (see Fig. 4.1):

- For each particle, a list of all contacts with neighbors is created.
- Taking into account the properties of the particles and the defined interaction laws, contact forces and moments are calculated.
- The second law of Newton is applied to each particle using the sum of all the contact forces and moments. New positions and velocities are calculated.
- If needed at this time step macroscopic and microscopic physical quantities are calculated and saved for future analysis.

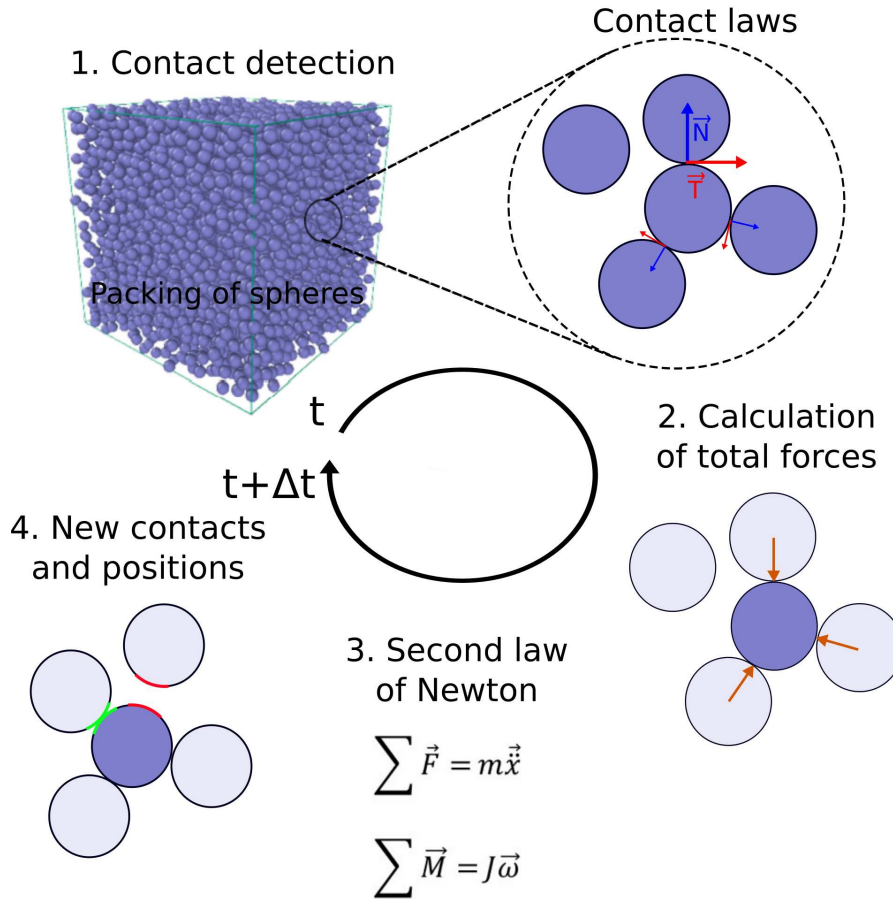


Figure 4.1: Algorithm of the discrete element method

#### 4.1.2.1 Neighbors and contact detection

The contacts between discrete elements are determined by calculating the distance between all spheres. A contact is fulfilled if the distance is less than the sum of the radius of both concerned discrete elements. This algorithm is very simple but it uses a

double loop to look for all possible contacts and its time complexity is in  $O(N^2)$  where  $N$  is the total number of discrete elements in the simulation. It is thus very costly in terms of calculation time to use for a too large number of objects.

An improved algorithm uses a grid where each sphere is assigned to a cell. Then, the contact detection algorithm, when searching the contacts with a given particle, only considers the closest cells as illustrated in Fig. 4.2 (half of the surrounding cells and the cell containing the particle). This algorithm is called "linked cell method" [96] and has a  $O(NN_n)$  time complexity where  $N_n$  is the number of particles contained in the cells (13 in 3D). In order to reduce even more the heaviness of these computations, it can be decided to search for potential contacts every  $P$  time step with a slightly increased distance (larger than the radius of the discrete elements) [97]. The contacts between particles are then searched at each time step considering only the list of potential contacts (Verlet list).  $P$  must be sufficiently small in order to ensure that no contact is missed due to a too large rearrangement of the particles between two potential contacts searches.

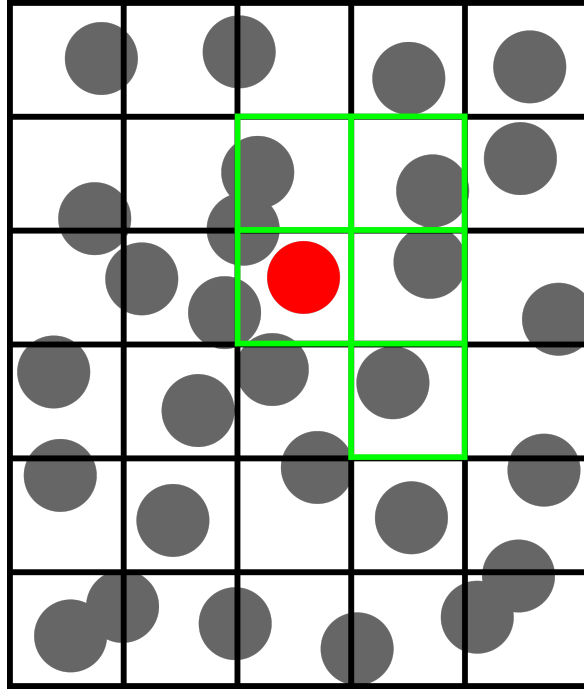


Figure 4.2: Neighbors detection of the red discrete element. The cell containing the discrete element and 4 of the adjacent cells are considered. Other cells are ignored.

The grid size is directly linked to the particle diameter. It must be slightly larger than the largest diameter of the particles to ensure that no potential contact is missed. For simulations where particle radii are sufficiently narrowly distributed, a single grid (combined with the Verlet list) is sufficient to have reasonable contact detection CPU time. If particle size distribution is too large, multiple grids must be defined. Although a single grid will be enough to simulate aerogel particles and most of the particulate aerogel composites studied in this work, the presence of fibers made of small spheres in some composites necessitates the consideration of additional grids (see chapter 6). In that case, a fast multilevel algorithm as proposed by Ogarko and Luding [98] was

implemented in dp3D to resolve effectively this issue.

#### 4.1.2.2 Interaction forces and moments calculation

Once contacts between particles have been identified, the forces and moments can be calculated for each particle. These interaction forces and moments depend on the interaction laws chosen for the simulation. The whole behaviour of the simulated materials will be influenced by these laws which must be thus carefully chosen and implemented. These laws can describe bonded or non-bonded particles and can take into account friction and adhesion forces amongst other possibilities. The contact laws used in this work are described in section 4.2.2 of this chapter.

#### 4.1.2.3 Second law of Newton, Verlet integration

The second law of Newton is applied for each discrete element using the interaction forces  $\sum \vec{F} = m\vec{\ddot{x}}$  and moments  $\sum \vec{M} = J\vec{\ddot{\theta}}$  calculated where  $m$  is the particle mass,  $\vec{\ddot{x}}$  is the particle acceleration,  $J$  is the moment of inertia and  $\vec{\ddot{\theta}}$  is the angular acceleration.

Positions, angles and velocities are determined at each time step  $dt$  by using the Verlet integration procedure described by the following equations for particle position and velocity:

$$\vec{x}(t + dt) = \vec{x}(t) + \vec{\dot{x}}(t)dt + \frac{1}{2}\vec{\ddot{x}}(t)dt^2 \quad (4.1)$$

$$\vec{\dot{x}}(t + dt) = \vec{\dot{x}}(t) + \frac{\vec{\ddot{x}}(t) + \vec{\ddot{x}}(t + dt)}{2}dt \quad (4.2)$$

This is an explicit method, meaning the DEM algorithm will be unstable if the time step is too high. The time step is thus calculated to be several times smaller than the smallest period of the oscillators in the system (induced by the stiffness of the simulated contacts) leading to a time step  $\Delta t$ :

$$\Delta t \propto \sqrt{\frac{m}{k}} \quad (4.3)$$

where  $m$  is the particle mass and  $k$  the particle stiffness in the system [99]. In the case of particles with different mass and stiffness, the lowest time step is chosen. According to equation 4.3, the time step  $\Delta t$  can be increased, thus decreasing the total computation time, by artificially increasing the discrete element mass or by decreasing their stiffness. The decrease of the stiffnesses is preferred when DEM is used to study the displacements of the discrete elements. However, we need to calculate realistic values for the microscopic and macroscopic stresses in this work. It is, thus, preferred to increase the discrete element mass to reduce the simulations computation time and ensure that the simulations are quasi-static i.e. the inertial effects are negligible.

#### 4.1.2.4 Physical parameters calculation and storage

At each timestep, the forces applied on particles as well as their position and velocity are known. It is possible to associate other properties to these particles or to couples

of particles (forces during previous timestep, Young's modulus, friction coefficient, ...). All the properties subsequently calculated (macroscopic stresses, density, number of broken bonds, ...) are derived from this data known at each timestep of the simulations but it is not possible to calculate and/or save them at the same frequency as the data size would be prohibitive. In consequence we consider a limited number of timestep where these properties are calculated and saved and an even more limited number of timestep where the coordinates and bonds between particles are saved.

## 4.2 Model description

DEM simulations have been carried out in order to simulate the elastic behaviour, densification and fracture of silica aerogel objects and of more complex composite samples. As previously presented, the DEM code used in this regard is the in-house code dp3D (SIMaP, Université Grenoble-Alpes) continuously improved and completed since 2000 by C. Martin et al. [100–103]. This code has been parallelized with openMP but the parallelization becomes inefficient when running on a too large number of CPUs. For this reason the number of CPUs working in parallel almost never exceeds eight. This also means that, while large calculation clusters were available for this PhD work, computation times can be excessively long (up to two weeks), particularly for silica aerogel particulate composites simulations that use more than one million of particles.

### 4.2.1 Typical simulations and objectives

#### 4.2.1.1 Silica aerogel particles

Numeric DEM silica aerogel particles (aggregates of discrete elements) have been generated based on the shape of real particles (large 10-12 particles) scanned using X-ray tomography (see section 3.2.3). As shown in Fig. 4.3, an aggregate is discretized with discrete elements (spheres) that represent material points bonded together. These spheres do not represent real entities but are used as meshing elements for the aggregate.

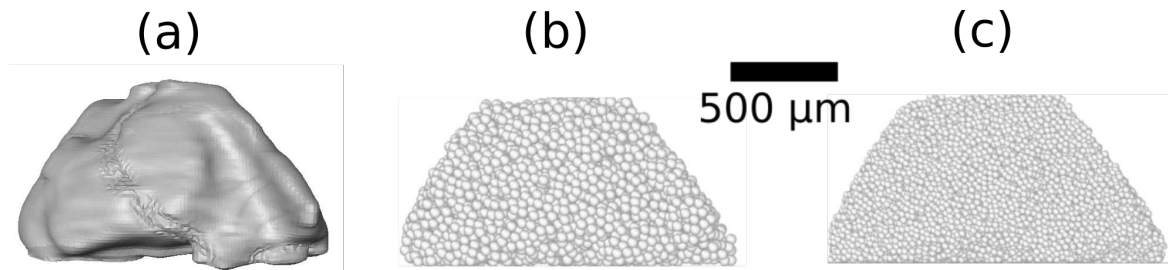


Figure 4.3: a) Silica aerogel particle imprint created from X-ray tomography scans. b) DEM particle generated using the imprint a); discrete elements radius of 25  $\mu\text{m}$ . c) DEM particle generated using the imprint a); discrete elements radius of 10  $\mu\text{m}$ .

The DEM silica aerogel particles are generated using X-ray tomography scans of real particles and have been compressed individually until fracture, meaning the fracture

strains and forces are known for each tested particle. The main goal of using DEM is to reproduce the particles fracture observed experimentally (see example in Fig. 4.4). This serves two purposes :

- Study the influence of particles shape, density and internal defects (cracks) on the fracture behaviour.
- Prepare realistic DEM silica aerogel particles which can be introduced in composites for more complex simulations.

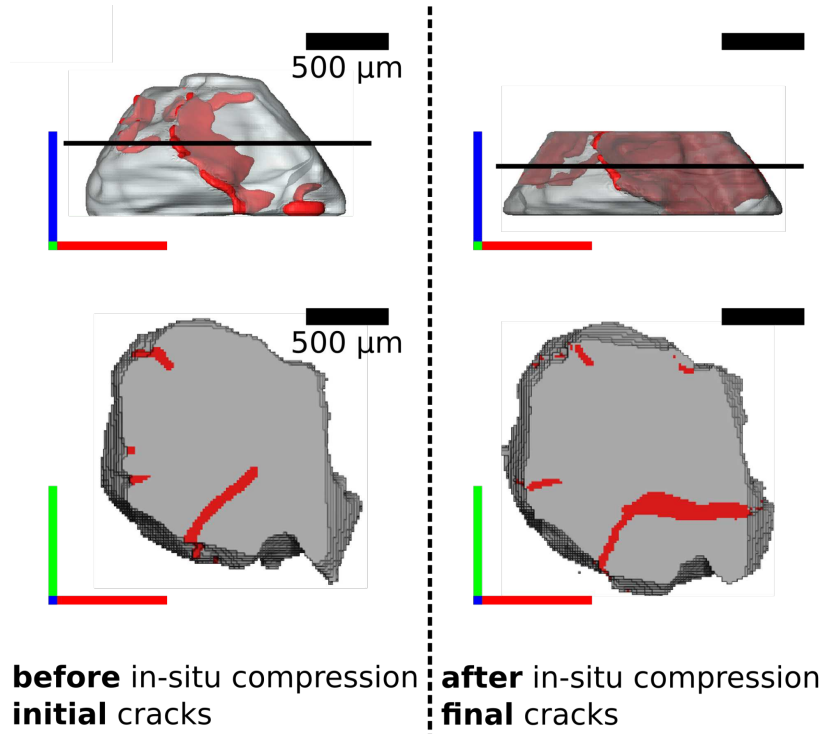


Figure 4.4: Large 10-12 silica aerogel particle compressed during X-ray tomography scans and used as a model to generate a realistic DEM particle. Cracks are indicated in red. Top line: 3D view, bottom line: cross section along the black line seen in top line images.

#### 4.2.1.2 Silica aerogel particulate composites

DEM particulate composites are complex samples due to the variety of objects and particles composing them. A X-ray tomography cross-section of a typical particulate silica aerogel composite is shown in Fig. 4.5 and illustrates the different components to be introduced in the DEM composites:

- Large silica aerogel particles (10-12) with realistic shapes and sizes
- Pores with different sizes
- A phase (named "cement") containing the small aerogel particles (inf100) bounded together

- Fibers (not visible in Fig. 4.5)

Once DEM composites have been generated and calibrated, the main objective is to carry out tensile tests on notched samples in order to calculate a fracture toughness and compare it to what has been measured experimentally. The generation, calibration of the model and tensile processes will be thoroughly presented in section 4.4.

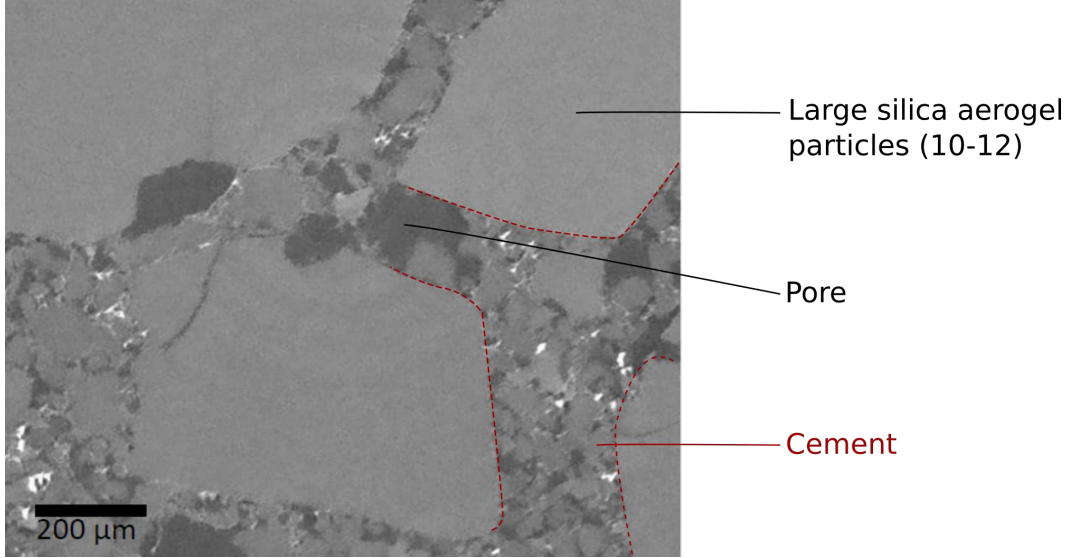


Figure 4.5: X-ray tomography cross-section of a silica aerogel particulate composite, highlighting the different components considered when generating DEM composites. Fibers are not visible using conventional laboratory X-ray tomography equipment.

## 4.2.2 Contact laws

In our models, discrete elements have no physical or structural meaning when compared to the real silica aerogel particles or composites. Indeed we use discrete elements for the modeling and meshing of continuous materials. A calibration of contact law parameters is thus required to reproduce the macroscopic properties and behaviour of the material. The contact laws and fracture criterion used in our models are presented below.

### 4.2.2.1 Bonded contacts

Bonded contacts are needed between discrete elements in our model in order to simulate continuous materials and their fracture. The microscopic beam model is used for this purpose. In order to describe this model, the effective radius  $R^*$  and effective normal and tangential stiffnesses  $K_N^*$  and  $K_T^*$  must be defined for a couple of bonded discrete elements:

$$R^* = \left( \frac{1}{R_p} + \frac{1}{R_q} \right)^{-1} \quad (4.4)$$

$$K_N^* = \left( \frac{1}{K_{N,p}} + \frac{1}{K_{N,q}} \right)^{-1}, \quad K_T^* = \left( \frac{1}{K_{T,p}} + \frac{1}{K_{T,q}} \right)^{-1} \quad (4.5)$$

where the subscripts  $p$  and  $q$  refer to particles  $p$  and  $q$  (see Fig. 5). The effective normal and tangential stiffnesses introduce size-dependency in the model, meaning the macroscopic properties are dependent of the particle size for a given set of microscopic properties  $K_N^*$  and  $K_T^*$ . For this reason, we prefer using the material parameters  $\sigma_N^* = \frac{K_N^*}{2R^*}$  and  $\sigma_T^* = \frac{K_T^*}{2R^*}$  which have the unit of stress. The normal and tangential forces at a bonded contact between two particles are thus given by:

$$\mathbf{N} = -4\sigma_N^* R^* \delta_N \mathbf{n} \quad (4.6)$$

$$\mathbf{T} = -4\sigma_T^* R^* \delta_T \mathbf{t} \quad (4.7)$$

where  $\delta_N$  and  $\delta_T$  are the normal and tangential relative displacements between the two particles. Note that the normal force  $N$  can be attractive or repulsive. The resisting moments  $M_N$  and  $M_T$  in the normal and tangential directions that oppose the accumulated relative rotations  $\theta_N$  and  $\theta_T$  are given by:

$$M_N = -8\sigma_T^* R^{*3} \theta_N \quad (4.8)$$

$$M_T = -4\sigma_N^* R^{*3} \theta_T \quad (4.9)$$

Forces and resisting moments for a couple of bonded discrete elements are illustrated in Fig. 4.6a. Kumar et al. [90] found that this microscopic beam model gives satisfactory results for the simulation of continuous materials and allows to obtain Poisson's ratio between -0.4 and 0.35 depending on the stiffness ratio  $\alpha = \frac{\sigma_T^*}{\sigma_N^*}$ . By calculating from simulations the Young's modulus and Poisson's ratio of bonded discrete element packing with different stiffness ratios and for different preparation routes, Kumar et al. provided valuable data allowing to calibrate effective normal and tangential stiffnesses  $\sigma_N^*$  and  $\sigma_T^*$ .

#### 4.2.2.2 Hertzian contacts

In the case of discrete elements in contact but not bonded, Hertzian contact is considered. This is typically the case for discrete elements not in contact in the first steps of the simulations or discrete elements not bonded initially in the DEM composites like contacts between fibers and other objects (see section 4.4.3). The normal force is given by the Hertzian law:

$$N^{Hertz} = \frac{4}{3} E^* R^{*1/2} \delta_N^{3/2} \quad (4.10)$$

where  $E^* = \left( \frac{1-\nu_1^2}{E_1} + \frac{1-\nu_2^2}{E_2} \right)^{-1}$ . In our case though, adhesion forces are included. The chosen adhesive model is the DMT model [104], and a tensile term is added to Eq. (4.10):

$$N^{DMT} = \frac{4}{3} E^* R^{*1/2} \delta_N^{3/2} + F_{DMT} \quad (4.11)$$

$$F_{DMT} = -2\pi w R^* \quad (4.12)$$



with  $w$  the work of adhesion and  $a$  the contact radius, which for Hertzian contact writes:

$$a = \sqrt{R^* \delta_N} \quad (4.13)$$

The tangential force model is of the Hertz-Mindlin type in the sticking mode while the norm of the tangential force is limited during sliding by Coulomb friction (friction coefficient  $\mu$ ):

$$\begin{aligned} T &= -8G^* a \delta_T & \text{if } 8G^* a \delta_T < \mu N^{\text{Hertz}}, \\ T &= -\frac{\delta_T}{|\delta_T|} \mu N^{\text{Hertz}} & \text{if } 8G^* a \delta_T \geq \mu N^{\text{Hertz}}, \end{aligned} \quad (4.14)$$

where  $G^* = \left( \frac{2(1+\nu_1)(2-\nu_1)}{E_1} + \frac{2(1+\nu_2)(2-\nu_2)}{E_2} \right)^{-1}$  is the effective shear modulus and  $\delta_t$  the accumulated tangential displacement. Forces for a couple of bonded discrete elements are illustrated in Fig 4.6b.

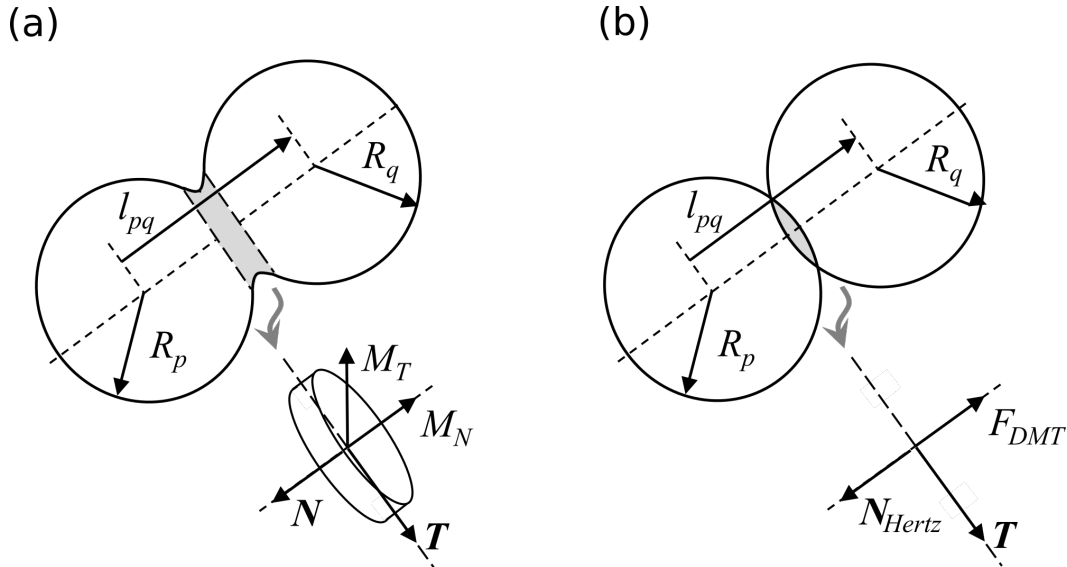


Figure 4.6: Sketch of the contacts between two spherical particles  $p$  and  $q$  transmitting normal and tangential forces and/or resisting moments in the case of (a) bonds, (b) hertzian contacts.

#### 4.2.2.3 Fracture criterion

One of the main objective of our DEM simulations is to simulate fracture and crack propagation so a fracture criterion must be considered in the model. A bond is broken and the contact law between the two discrete elements is modified if the chosen critical stress criterion is exceeded [105, 106].

The Rankine maximum principal stress criterion has been chosen for the simulations in this work. This criterion is particularly well adapted for brittle materials. Silica aerogels are nonetheless nano-porous ceramics displaying very unusual mechanical properties and other fracture criteria have been tested like the Mohr-Coulomb or Tresca criteria [86, 107]. However their use were either not adapted to our simulations



or too heavy to compute for simulations with large samples and / or high strain. The Rankine criterion states that failure occurs when the maximum principal stress reaches either the uniaxial tension strength, or the uniaxial compression strength. In our case, Rankine's equivalent stress  $\sigma_{b,R}$  writes:

$$\sigma_{b,R} = \frac{1}{2}(\sigma_{b,N} + \sqrt{\sigma_{b,N}^2 + 4\sigma_{b,T}^2}) \quad (4.15)$$

where  $\sigma_{b,N} = \frac{N}{4\pi R^{*2}}$  and  $\sigma_{b,T} = \frac{T}{4\pi R^{*2}}$  are the normal and tangential stresses at the bond scale. For a given bond, a critical stress  $\sigma_{Rc}$  is defined and the bond breaks if  $\sigma_{b,R}$  exceeds  $\sigma_{Rc}$ . Note that a bond may fracture even in compression with this model if the shear stress  $\sigma_{b,T}$  is sufficiently large.

The beam model still exists after bond failure but is modified in consequence. Tensile forces cannot be transmitted anymore but the broken bonds keep the same normal stiffness as an unbroken bond in compression. This may arise if a bond has broken in compression or if the contact is restored further in the simulation. Concerning tangential forces, the DMT model previously presented is applied. In consequence, a tangential resisting moment  $M_T$  still exists but the normal resisting  $M_N$  moment is no longer considered. Tangential forces for broken bonds are dictated by the Coulomb friction model.

#### 4.2.2.4 Contacts between particles and objects

For simulations with no periodic conditions, objects with infinite mass must be used to apply the proper strain rate on the samples. Such objects will only be needed in this work to simulate silica aerogel particles compression. The contacts between discrete elements and objects will be described, similarly to broken bonds, by equation 4.6 for compressive forces. Objects are, in our case, planes so the effective radius  $R^*$  is equal to the discrete element radius. No adhesive forces are introduced. Tangential forces are limited during sliding by Coulomb friction (equation 4.14).

### 4.2.3 Boundary conditions

Two solutions are available for boundary conditions in DEM simulations. The first one is to consider walls at the boundaries of the simulation box which are object with an infinite mass and a chosen stiffness. These conditions can be problematic for the extraction of macroscopic properties during the simulations because of the contact between planes and a limited number of spherical discrete elements. This is, however, the preferred solution when we simulate aggregates with a given shape like DEM silica aerogel particles for example.

The other solution is to create full-periodic conditions on the simulation box boundaries, meaning contacts exist between the discrete elements located on one side of the simulation box with the ones on the opposite side, as illustrated in Fig. 4.7. When distances are calculated between discrete elements, the following conditions are considered in the DEM algorithm (the origin of the coordinates is at the center of the

simulation box):

$$if(x_{pq} > 0.5L) \quad x_{pq} = x_{pq} - L \quad (4.16)$$

$$if(x_{pq} < -0.5L) \quad x_{pq} = x_{pq} + L \quad (4.17)$$

where  $x_{pq}$  is the distance along the x axis between discrete elements p and q and L is the simulation box length along the x axis. These full-periodic boundary conditions do not disturb the structure and the mechanical properties of the samples at the boundaries of the simulation box. These conditions are used in this work, particularly for DEM silica aerogel particulate composites.

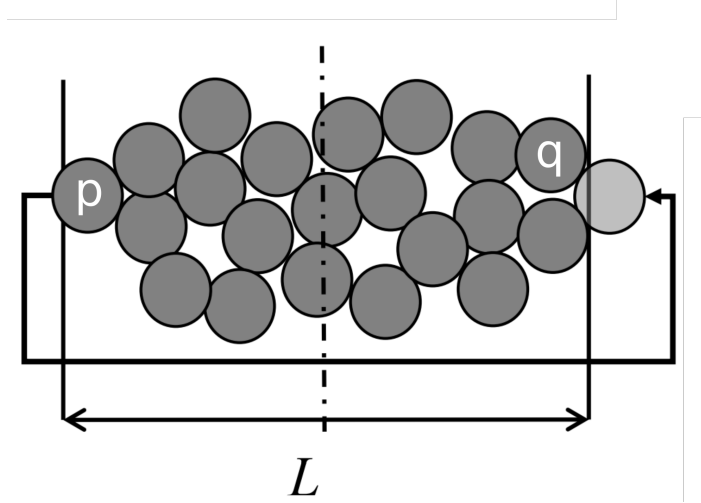


Figure 4.7: Sketch of the contact between two spherical particles  $p$  and  $q$  when full-periodic boundary conditions are applied.

## 4.2.4 Simulations stability

### 4.2.4.1 Numerical damping

In the dp3D code, as in any DEM code, the kinetic energy must be dissipated and oscillations are damped by introducing viscous forces and moments opposing the displacement or angular displacement of the discrete elements [90, 108]:

$$F_{d,N} = -4\beta\sqrt{2R^*m\sigma_N^*}\dot{\delta}_N, \quad F_{d,T} = -2\beta\sqrt{2R^*m\sigma_T^*}\dot{\delta}_T \quad (4.18)$$

$$M_d = 2\beta\sqrt{2R^*m\sigma_N^*}R^{*2}\dot{\theta}_{pq} \quad (4.19)$$

where  $\beta$  is an input parameter fixed at 0.05 to ensure underdamped oscillations. These viscous forces help in the stability of the simulations.

### 4.2.4.2 Kinetic energy management

The in-house DEM code (dp3D) use a quasi-static approach to compute the equilibrium positions of discrete elements at each time step. The quasi-static conditions are ensured by choosing strain rates low enough to ensure the equilibrium of the system. Ideally,

the strain-rates are chosen by considering the normalized kinetic energy per discrete element and by ensuring it stays below  $10^{-7}$  [109]:

$$\tilde{E}_{kin} = \frac{E_{kin}}{nmax(NR^*)} \quad (4.20)$$

where  $E_{kin}$  is the total kinetic energy of the system (accounting for rotation and translation terms) and  $n$  is the number of particles in the packing. An adaptation of the strain-rate can be used: increase of the strain-rate to save on CPU time if  $\tilde{E}_{kin} < 10^{-7}$  or decrease of the strain-rate if  $\tilde{E}_{kin} > 10^{-7}$ . Inertia effects (quasi-static conditions) can be considered negligible when  $\tilde{E}_{kin} < 10^{-7}$ .

### 4.2.5 Macroscopic stresses calculation

The macroscopic stress tensor resulting from an applied strain on a packing of bonded discrete elements is calculated using the Love's formulation [110]:

$$\Sigma_{ij} = \frac{1}{V} \sum_{\text{contacts}} F_i l_{pq,j}, \quad (4.21)$$

where the summation is made on all contacts and where  $V$  is the sample volume,  $F_i$  is the  $i^{th}$  component of the total contact force (with normal and tangential terms), and  $l_{pq,j}$  is the  $j^{th}$  component of the  $l_{pq}$  vector connecting the centers of two particles  $p$  and  $q$  (see Fig. 4.6).

## 4.3 Generation and testing of silica aerogel particles

Although silica aerogels are composed at the nanometer scale of discrete entities, their explicit representation within DEM would be computationally too demanding to model volumes as large as a few  $\mu\text{m}^3$  [91]. DEM can nonetheless be used to model efficiently damage and fracture of a continuum media. The objective here is to generate silica aerogel particles starting from discrete element packings and replicate their mechanical behaviour as observed during uniaxial compression tests.

### 4.3.1 Sample preparation

#### 4.3.1.1 Initial discrete element packing

Within this framework, the material is built as a random packing of spheres [87, 90]. Spheres do not represent real particles but are used to mesh a structure while providing a fully discontinuous framework handy for treating fracture phenomena.

The full preparation process of the random packing of spheres is described below and illustrated in Fig. 4.8:

- An initial gas of discrete elements is generated by locating the spheres randomly inside a periodic simulation box. No contacts are allowed between the spheres (coordination number  $Z = 0$ ) and a target relative density  $D$  is set to 0.3. The size dispersion of spheres is nearly monomodal with a 5% dispersion around the mean radius  $R$ .
- By applying a small control pressure  $P_c$  on the gas ( $P_c = 10^{-7}E$ , with  $E$  the Young's modulus of the particles) and by slowly moving the simulation box walls inwards, the gas is densified until the relative density reaches 0.5. The contacts that form during this stage between discrete elements are Hertzian (see section 4.2.2.2) with neither friction nor adhesive forces. This step is denominated as "jamming".
- The last densification step consists of imposing an affine displacement until the relative density reaches 0.65. This last step allows a high coordination number to be reached in the packing.

This generation process described by Kumar et al. [90] is called "weakly jammed preparation" as the jamming step is not carried out until the target relative density is reached ( $D = 0.65$ ). At this point the mean coordination number  $Z$  is around 5.39.

An additional step consists of bonding neighbouring discrete elements together according to the following criteria:

$$\kappa(R_p + R_q) > |\vec{l}_{pq}| \quad (4.22)$$

where  $\vec{l}_{pq}$  is the branch vector between the center of discrete elements  $p$  and  $q$  and  $\kappa$  is the interaction range. An interaction range of 1.075 has been chosen in our case and allows a bonded coordination number around 6.56 to be reached. Kumar et al. [90] showed that Poisson's ratio between 0 and 0.35 can be simulated with such a configuration in this situation which is compatible with silica aerogels ( $\nu \approx 0.2$ ).

#### 4.3.1.2 Shaping of aerogel particles

Aerogel particle imprints are extracted from X-ray tomography acquired just before compression as described in section 3.2.3. These imprints take the form of 3D binarized images which are then used to cut the correct aerogel particle shape from a random packing of spherical discrete elements generated as described in the preceding section. This last step consists of removing all the discrete elements external to the imprint.

Two different DEM packings were used with respectively 25  $\mu\text{m}$  and 15  $\mu\text{m}$  radius discrete elements. These two sizes allow the fracture behaviour of the particles to be observed with two discretization refinements (smaller elements lead to a more refined discrete representation of the particle). Five aerogel particles have been generated following this protocol as illustrated in Fig. 4.9. The process induced cracks observed inside the particles before compression can be introduced in the model by removing discrete elements located directly on the crack and by breaking the remaining bonds crossing the crack between the discrete elements which were not removed by the first

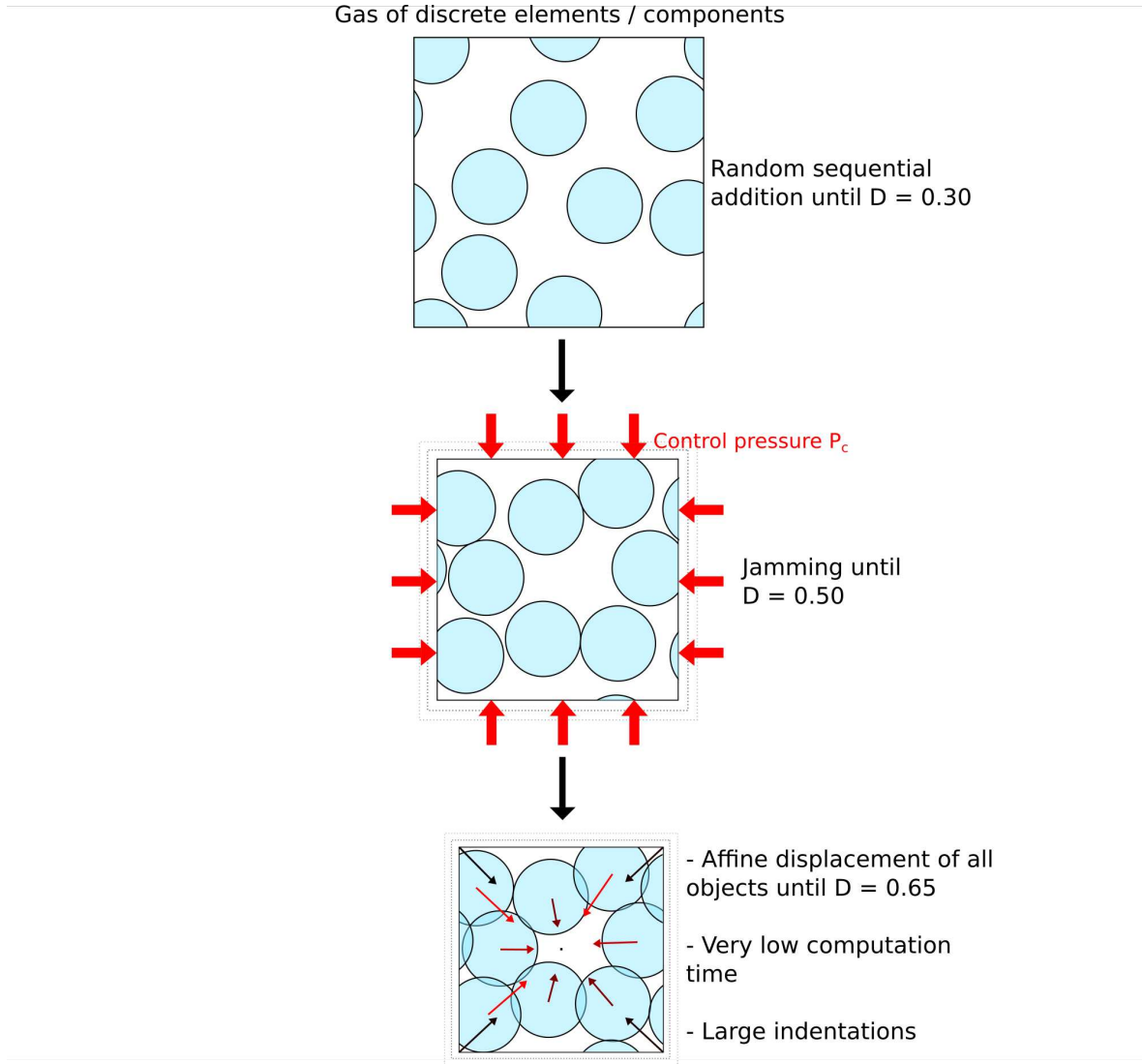


Figure 4.8: Packing processes of discrete elements and aggregates for the generation of DEM silica aerogel particles (SAP).

step (see Fig. 4.10). Two numerical versions of each aerogel particle are thus generated, one crack-free and one with the observed initial cracks. Finally, each silica aerogel particle exists in four DEM versions:

- 25  $\mu\text{m}$  discrete elements, no internal cracks
- 25  $\mu\text{m}$  discrete elements, with internal cracks
- 15  $\mu\text{m}$  discrete elements, no internal cracks
- 15  $\mu\text{m}$  discrete elements, with internal cracks

### 4.3.2 Uniaxial compression tests

The DEM simulated aerogel particles are compressed between two planes. Planes are considered as infinite radius particles and the discrete element-plane contact is a bond

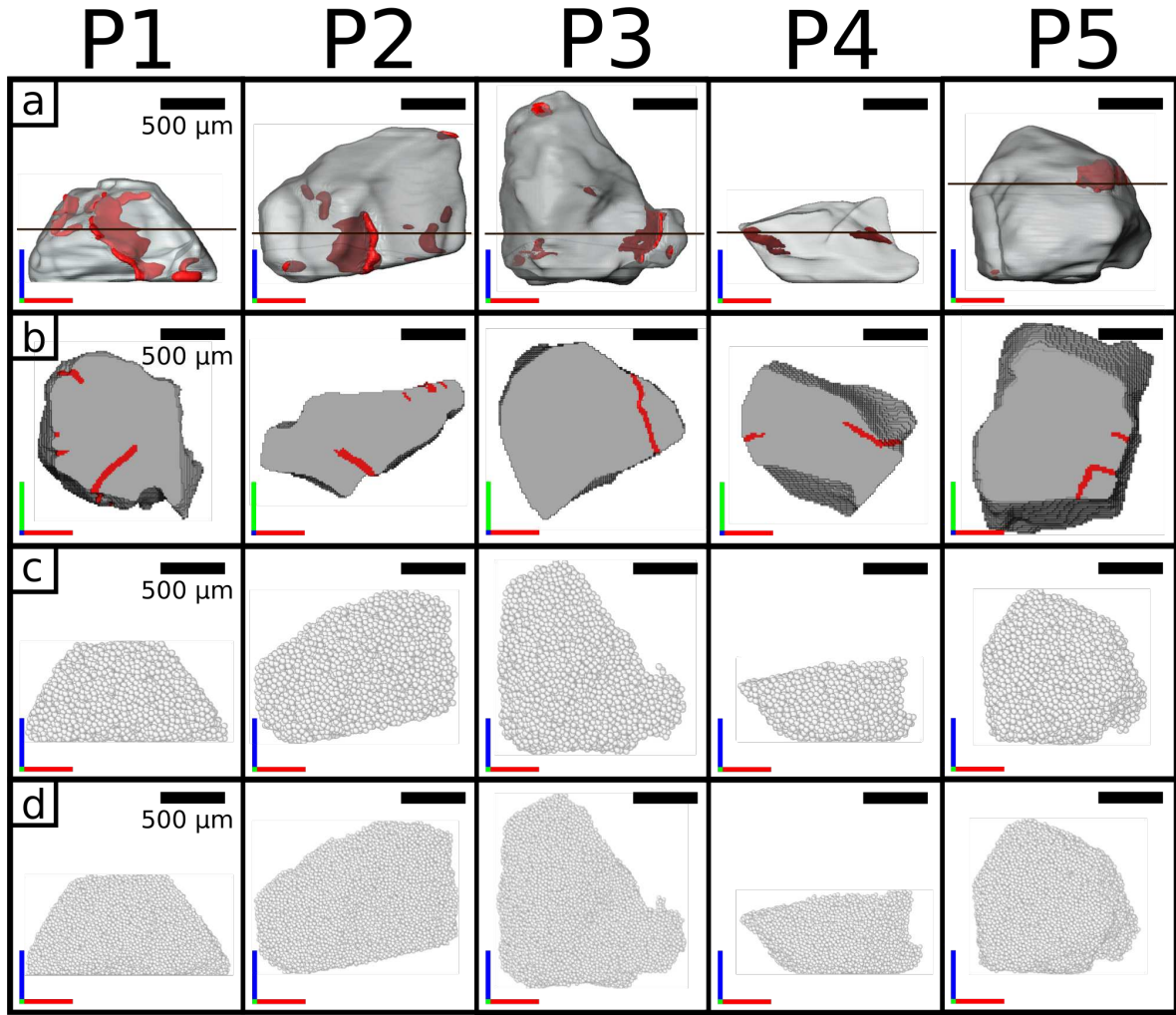


Figure 4.9: a) Aerogel particles with initial cracks reconstructed from X-ray tomography scans (in red). b) Cross section view within each particles at depth indicated on a). c) DEM aerogel particles prepared using  $25\ \mu\text{m}$  discrete elements. d) DEM aerogel particles prepared using  $15\ \mu\text{m}$  discrete elements. The numbering from P1 to P5 corresponds to a decreasing total crack length.

transmitting a purely normal force in compression (see section 4.2.2.4). The stiffness of the planes is chosen as identical to aerogel bond stiffness. The friction coefficient  $\mu$  is set to 0.5 for all contacts in the system and no adhesive forces are introduced ( $\mu$  has almost no influence on the behaviour of the DEM particles fracture). Figure 4.11 illustrates a typical compression of a simulated silica aerogel particle.

### 4.3.3 Model calibration

The DEM model parameters are calibrated to reproduce the observed mechanical behaviour of particles. In order to calibrate normal and tangential normalized stiffnesses of discrete elements,  $\sigma_N^*$  and  $\sigma_T^*$ , the experimental load and displacement during aerogel particle compression inside the X-ray tomograph are processed. For the same shape and the same orientation of the particles, the calibration is carried out individually for each aerogel particle by fitting the numerical load vs. displacement curves to the



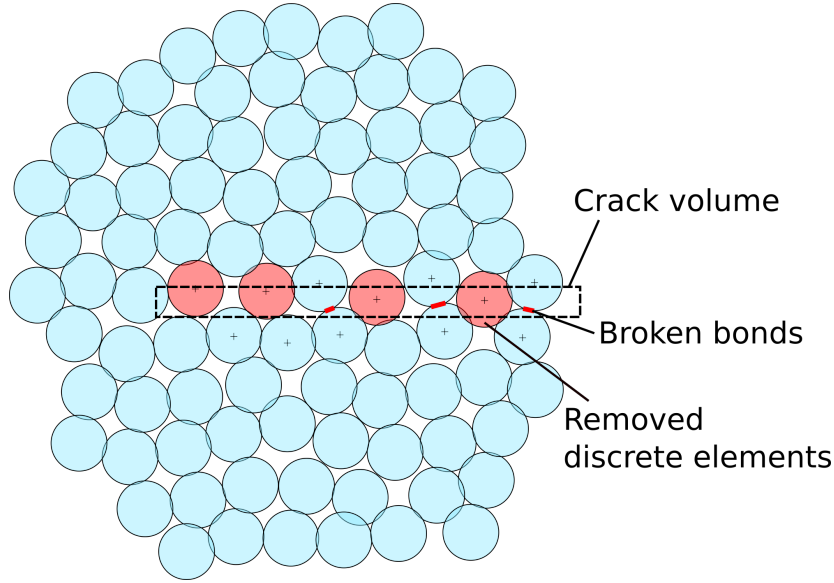


Figure 4.10: Crack preparation process. Discrete elements with their center contained in the crack volume are removed and the remaining bonds contained in the same volume are broken.

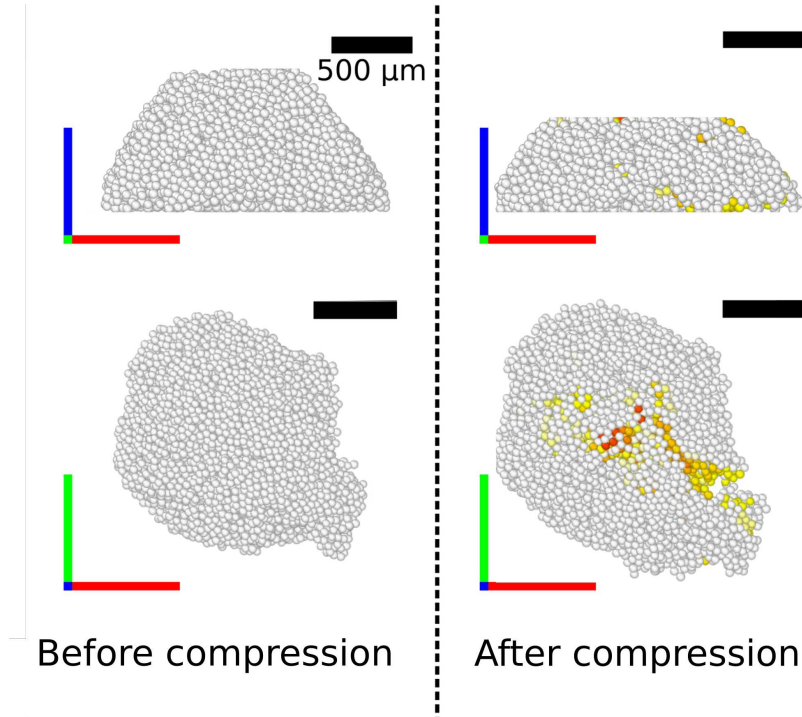


Figure 4.11: Large DEM silica aerogel particle compression. Bond fractures are illustrated chronologically from dark red (earliest broken bonds) to yellow (latest broken bonds) and white (intact bonds)

experimental fracture points  $(F_f, h_f)$  by tuning  $\sigma_N^*$ . Kumar et al. [90] have shown that the stiffness ratio  $\sigma_T^*/\sigma_N^*$  dictates the macroscopic Poisson's ratio. No practical solution has been found to measure the Poisson's ratio for the studied aerogels but literature suggests that silica aerogel Poisson's ratio exhibits no discernible variation with density or when using different synthesis processes as already noted on highly

porous ceramics [111]. We assume that our aerogel Poisson's ratio is 0.2 for all particles analyzed in this work [38, 112]. The resulting  $\sigma_T^*/\sigma_N^*$  is 0.233 [90]. The fracture of the particle is calibrated by tuning the critical stress  $\sigma_{Rc}$  as defined by the Rankine criterion (eq. (4.15)). The calibration process is based arbitrarily on the DEM aerogel particles without any initial cracks. The simulation results showed however that these cracks have a limited influence on the silica aerogel particles fracture behaviour (see chapter 5).

## 4.4 Generation and testing of silica aerogel particulate composites

DEM silica aerogel composites are complex heterogeneous (multi-components) and multi-scale samples. While only one material and one type of bond are simulated in the case of DEM silica aerogel particles, composites include different materials and contacts which must be defined and calibrated individually. Most of the composite samples generated in this work contain more than one million particles. Thus, computation times have been reduced artificially for DEM composites by artificially increasing the mass of discrete elements (simulation time step  $\Delta t \propto \sqrt{\frac{m}{k}}$ ). This point will be discussed in the next sections.

### 4.4.1 Sample preparation

Two main methods are available for the generation of realistic DEM composites. The first consists of using an imprint of real silica aerogel particulate composites produced by segmenting X-ray tomography images. This imprint is used as an overlay to assign the different materials of the composite in an already fully packed DEM packing. This method has the advantage to generate a structure identical to what has been observed using X-ray tomography. However, the creation of an imprint of the silica aerogel composite is especially difficult due to the necessity to scan a sufficiently large volume with a high resolution. Finally, the low X-ray absorption of silica aerogels made it impossible to properly segment X-ray tomography images (see chapter 3). Thus, the second method presented below was preferred.

The generation method chosen for this work consists of generating separately all the components of the composites and then incorporate them in a simulation box, forming a gas which can be compacted to the target relative density. This method necessitates realistic components to be generated to conform to the correct volume fractions. However, we cannot ensure that the final composite structure is as realistic as with the imprint method. Still, it provides also great advantages. Indeed, new possibilities are allowed by this method as the user can change at will the components shape, size, preferred orientation or volume fraction. In short, we are free to explore the influence of a larger set of parameters on the DEM samples mechanical behavior. For example, fibers may be introduced in the composite. The generation of the components and the compaction procedure are presented below.



#### 4.4.1.1 Components

The components generated before DEM composite compaction are divided in two populations:

- Discrete element agglomerates representing the macroscopic components of the silica aerogel particulate composites (large 10-12 aerogel particles and fibers).
- Individual discrete elements used as a filler between agglomerates (it represents the cement phase observed in real composites between large aerogel particles and formed by small inf100 aerogel particles bonded together by a latex).

Note that, for the "gas compaction" composite generation method to appropriately describe the structure of particulate composites, the macro-pores (larger than 50  $\mu\text{m}$  in diameter) must also be considered as objects until the DEM samples are fully compacted. The different components are presented below and in Fig. 4.12:

- **Silica aerogel large particles (SAP):** aggregates are generated following the procedure presented in section 4.3. Five different particle shapes have been generated to be incorporated in DEM composites. These aggregates contain between 4000 and 10000 discrete elements (radii equal to 25  $\mu\text{m}$ ).
- **Fibers:** made of 250 discrete elements aligned together, forming a linear pearl necklace. Discrete elements are bonded together using the microscopic beam model. These objects are embedded in the composite with an orientation condition and cannot form an angle with a chosen axis exceeding a critical angle (20 ° in this work). The structure of the composites containing fibers can thus be anisotropic to depict the anisotropy of experimental samples induced by the processing method (see section 3.3.2). The discrete elements forming these fibers are five times smaller than those in the silica aerogel aggregates.
- **Pores:** the size distribution of pores is bimodal in DEM composites (see Fig. 4.5). While three different aggregates containing approximately 10 discrete elements were generated to represent the larger pores observed using X-ray tomography, individual discrete elements are also incorporated to take into account a smaller population of pores observed in the real composites. The discrete element size is the same as in silica aerogel aggregates. Discrete elements associated with pores will be deleted once the DEM composite samples are fully densified.
- **Cement:** this phase is represented by individual discrete elements. The discrete element size is the same as in silica aerogel aggregates.

#### 4.4.1.2 Packing of composite samples

The objective is to compact the gas of components previously generated until a relative density of 0.65 is reached to provide a coordination number sufficiently large to simulate continuous materials using DEM [90]. A process similar to the compaction

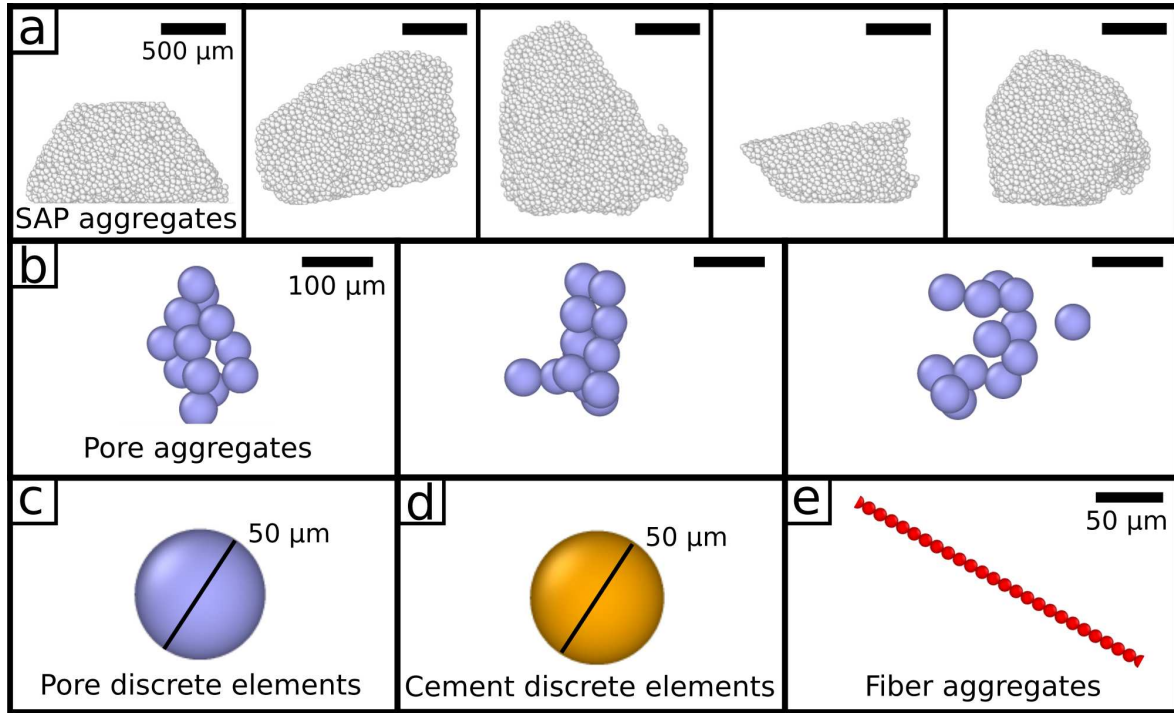


Figure 4.12: Components incorporated in DEM silica aerogel particulate composites.

used to generate DEM silica aerogel particles (see Fig. 4.8) is carried out with several differences. In the case of silica aerogel particles the generation and compaction process are:

- Jamming of the discrete element gas until  $D = 0.5$
- Affine displacement in the whole packing until  $D = 0.65$
- Shaping of the particle by using an X-ray tomography imprint

In the case of DEM composites, the silica aerogel aggregates introduced in the gas already have an internal relative density of 0.65 and the bonds have been calibrated to display the proper mechanical properties. Thus, we cannot allow the affine displacement step to change the structure of these objects. The compaction process (see Fig. 4.13) is:

- Jamming of the component gas until  $D = 0.6$
- Shrinkage of the periodic simulation box at a given strain rate
- Pre-processing of the composite packing (see section 4.4.1.3)

Although in both cases interaction laws do not differ (Hertzian contacts and bonds in the case of fibers), the second step is different from the jamming method used for silica aerogel particles. The jamming step consists of applying a macroscopic control pressure several orders smaller than the stiffness of the discrete elements to prevent too large indentation in the packing. The periodic boundaries of the simulation box are moved inwards during this process but the volume strain rate is reduced drastically

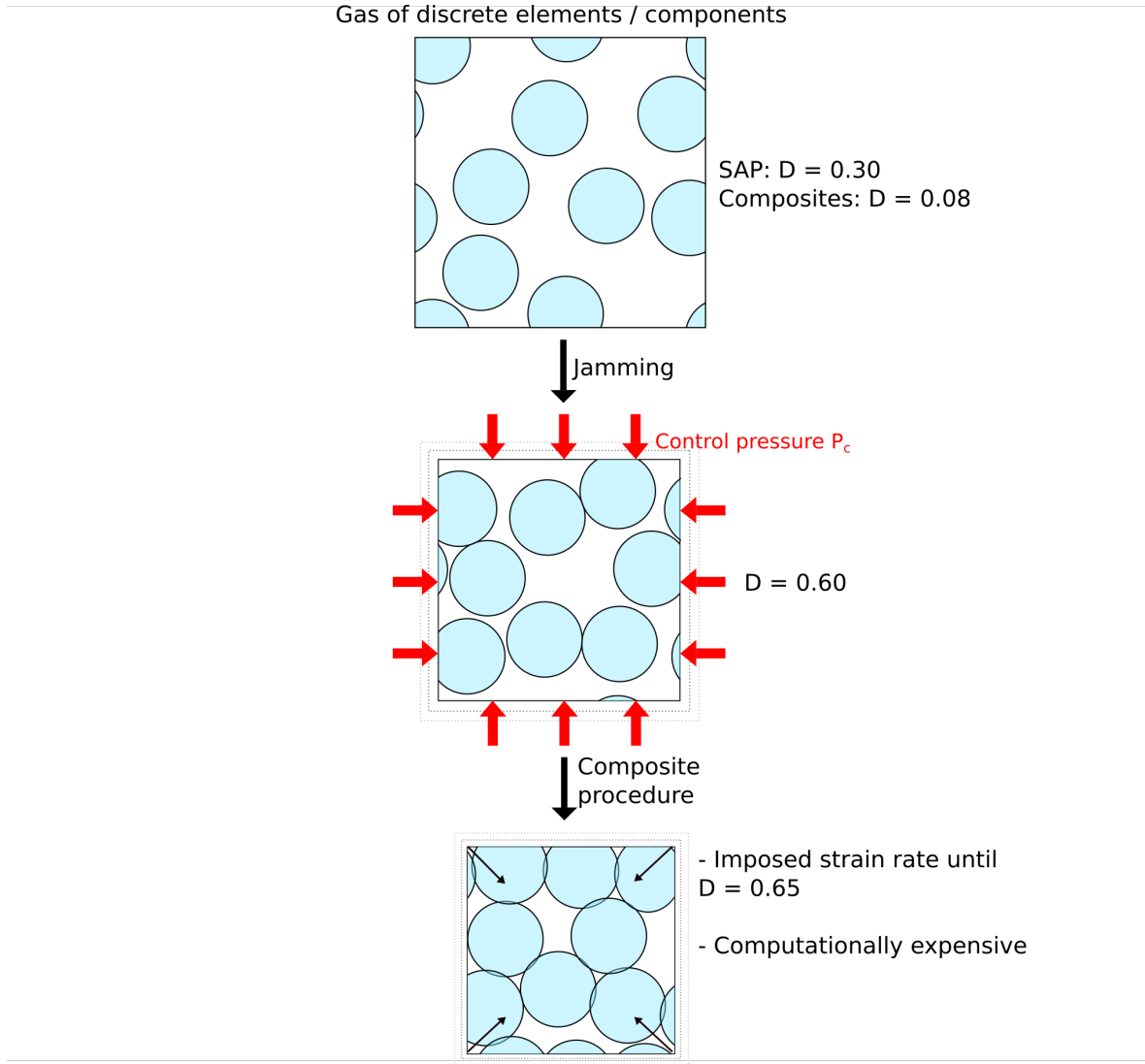


Figure 4.13: Packing processes of discrete elements and aggregates for the generation of DEM silica aerogel particulate composites.

as the rearrangement of the discrete elements and aggregates becomes more and more difficult. It is nearly impossible to reach relative densities larger than 0.63 using the jamming method and the computation time is far too long above 0.6. This is the reason why an affine displacement is carried out to densify the packing from 0.6 to 0.65 for silica aerogel particles. As this solution is not available for composite packings, it is replaced by an imposed volume strain rate of the packing. This method creates larger indentation between discrete elements than jamming but it has an admissible impact on the samples.

Discrete element agglomerates can be of two different nature: clumps and clusters. Clumped aggregates possess bonds as in all aggregates in our simulations but internal contacts in these aggregates are not computed during simulations. Thus, clumps are not able to deform, but can still be translated, rotated and transmit forces to the other external objects during simulations (including other clumps). In contrast, clusters are aggregates for which internal contacts are computed, and thus, can be deformed

during simulations. In the case of the DEM composites generated in this work, silica aerogel aggregates and pore aggregates are defined as clumps during sample generation because their final shape and properties have already been defined by referring to real silica aerogel particulate composites observed using X-ray tomography. Fiber aggregates are defined as clusters because their initial shape (straight line) differ from the shape observed in real composites (however, fibers were especially hard to see using X-ray tomography). Thus, fibers are allowed to deform during the compaction of the composites and their discrete element stiffness has been tuned in order to obtain final fibres with realistic curvatures (see section 4.4.3).

The presence of fibers in the composites necessitates supplementary precautions during compaction to obtain the proper curvature of these objects in the final DEM samples. Technical details on this point can be found in appendix A.

#### 4.4.1.3 Pre-processing of the packing

Once the DEM composites have been fully compacted until an effective density of 0.65 has been reached, several modifications of the packing must be carried out before testing and are illustrated on a typical DEM composite sample in Fig. 4.14:

- Pore aggregates and individual pore discrete elements are removed from the packing.
- The remaining clumps, silica aerogel aggregates, are redefined as clusters. Their deformation and fracture is allowed during composite fracture.
- Bonds between cement discrete elements and with silica aerogel aggregates discrete elements are created. Bonds inside aggregates are kept (both silica aerogel particles and fibers). No bonds are created between fiber discrete elements and the other entities. Contacts between fibers and silica aerogel particles will be defined as Hertzian contacts with adhesive and friction forces.
- A notch is cut inside the samples by removing all discrete elements and bonds included in a  $a \times nR \times t$  volume where  $a$  is the notch length,  $n$  is a parameter chosen by the user,  $R$  is the mean radius of discrete elements in the packing and  $t$  is the sample thickness. A typical notched DEM composite sample is showed in Fig. 4.14. Generally, we chose  $n = 4$ . Composite fracture simulation results show no significant variation below this value ( $n = 2$  or  $3$ ). The fiber network corresponding to this same sample is showed in Fig. 4.15 and illustrates how the fibers are oriented along the normal axis of the notch.

#### 4.4.2 Tensile tests and fracture toughness calculation

Notched DEM composite samples are tested by imposing a given strain rate in the direction normal to the notch plane. The objective is to calculate the fracture toughness  $K_{Ic}$ :

$$K_{Ic} = \sigma_f Y \sqrt{\pi a} \quad (4.23)$$



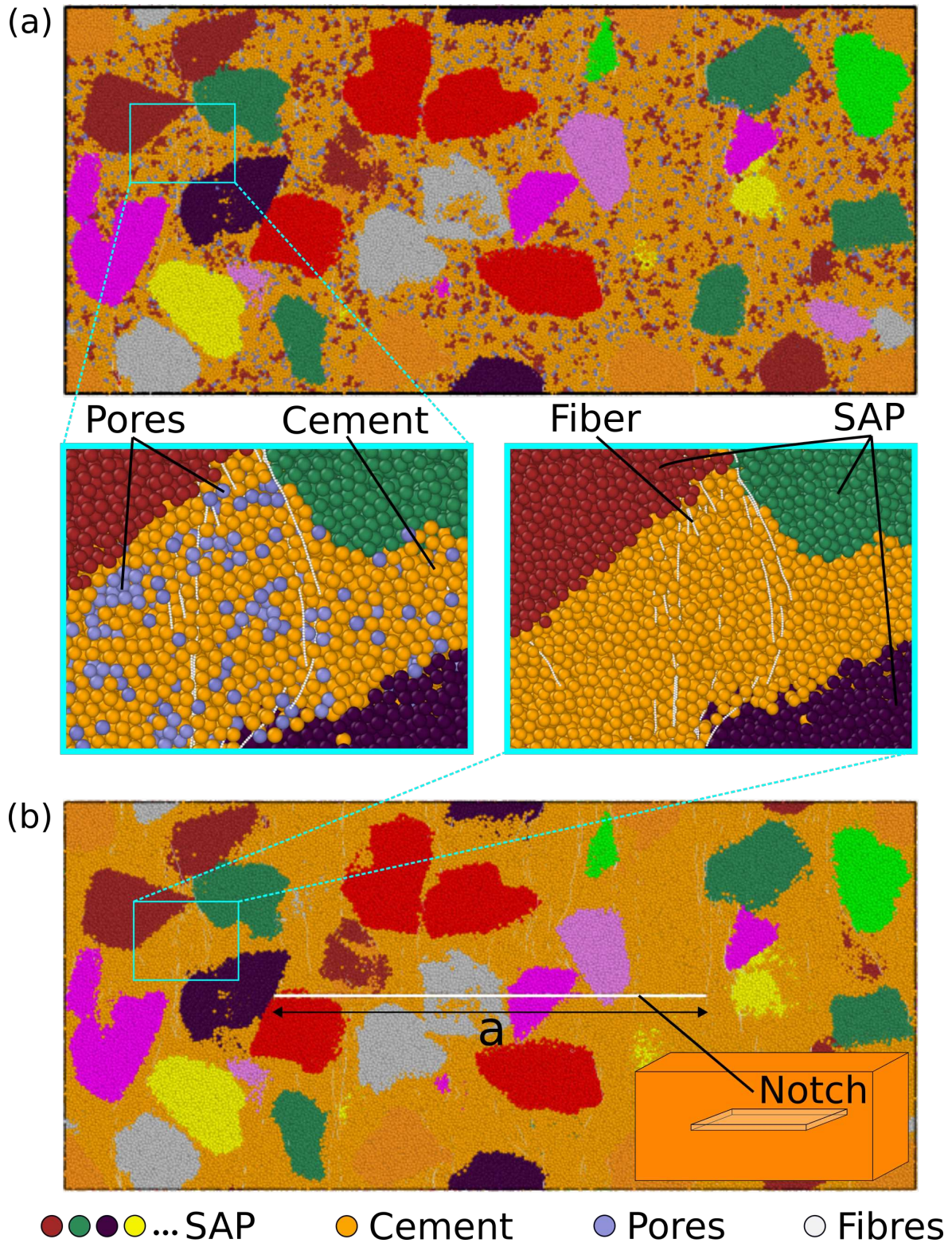


Figure 4.14: (a) DEM silica aerogel particulate composite sample after compaction. Note the presence of discrete elements for the pores. (b) DEM silica aerogel particulate composite sample after post-processing: pores have been removed, non-deformable clumped silica aerogel particles (SAP) changed into deformable clusters, generation of bonds, notch introduction.



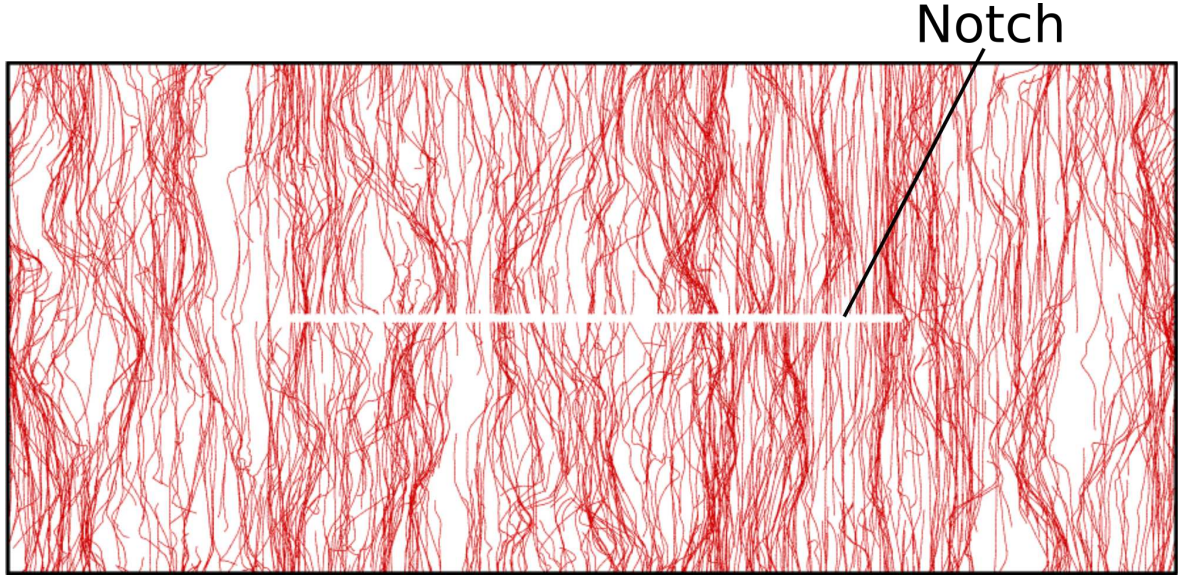


Figure 4.15: Final fiber network observed in a DEM composite notched sample. This is the same sample illustrated in Fig. 4.14 but other components than the fibers are here invisible for illustration purpose.

Where  $Y$  is a geometric factor and  $\sigma_f$  is the macroscopic tensile strength of the notched samples. The geometric factor  $Y$  depends on the configuration and takes into account the periodic conditions of the simulations. Indeed, because of periodic conditions we simulate an infinite array of notches and the resulting stress field is more complex than for a single notch. The correct value of  $Y$  for our sample geometry is taken from G.S. Wang [113] who calculated  $Y$  for a large panel of sample with doubly periodic cracks.

#### 4.4.3 Model calibration

While only two types of contacts were to be defined in DEM silica aerogel particles (bonds between discrete elements and contacts with plane objects, excluding the rare hertzian contacts), the situation is more complex in DEM composites. Five types of contacts must be calibrated.

##### Bonds inside silica aerogel clusters

These bonds have already been calibrated when isolated silica aerogel particles were tested. The same parameters are used in the input files for DEM composites (stiffnesses  $\sigma_N$ ,  $\sigma_T$  and Rankine critical stress  $\sigma_{Rc}$ ).

##### Bonds inside the cement

In order to assign realistic parameters to bonds between cement discrete elements, special samples, composed exclusively of the cement phase, were prepared and tested experimentally. These samples aimed to reproduce as closely as possible the cement formed by the agglomeration of smaller inf100 silica aerogel particles between the large 10-12 particles in standard particulate composites. Thus, large 10-12 particles were excluded from the preparation of these specific samples and the proportion of binder

had to be adapted (see section 3.3 for the detailed preparation process). A Young's modulus and a fracture toughness were calibrated for the cement phase using respectively compression on non-notched DEM cement samples and traction on notched DEM cement samples.

A DEM sample is prepared to represent as accurately as possible the cement structure obtained in full-sized DEM composite samples. It consists of a gas of discrete elements compacted in a full-periodic conditions simulation box to a relative density of 0.65 following the two steps applied to composite samples (jamming and shrinkage of the simulation box). Two types of individual discrete elements (same size) are generated:

- 90% of cement discrete elements
- 10% of pore discrete elements

While pore aggregates were also generated in standard DEM particulate composites (see Fig. 4.12), these large pores almost do not exist in cement experimental samples and are thus excluded from the DEM cement sample, keeping only the individual discrete element pores (50  $\mu\text{m}$  in diameter). Pore discrete elements are removed once the sample is fully compacted.

Once the DEM cement sample has been fully compacted, a notch is cut similarly to DEM particulate composites and uniaxial tension tests are carried out in order to tune the bond critical stress  $\sigma_{Rc}$ . The discrete element stiffnesses  $\sigma_N$  and  $\sigma_N$  are calibrated by compressing this same sample but without the notch. These parameters are calibrated so that the simulated Young's modulus and fracture toughness match the experimental ones.

#### **Bonds between the cement and silica aerogel clusters**

In real composites, large 10-12 particles and small inf100 particles are all bonded together with the same binder. Thus, we consider in DEM that bond stiffnesses and critical stress for contacts between cement discrete elements and silica aerogel clusters are the same as for contacts inside the cement.

#### **Bonds inside fiber clusters**

These bonds are calibrated by carrying out tensile tests on DEM fiber clusters. The normal stiffness of fiber discrete elements  $\sigma_N$  is tuned until the fiber aggregate presents the targeted Young's modulus (in our case, the Young's modulus of polypropylene).

#### **Contacts between fibers and other objects**

Contacts between fiber aggregates and other objects are the more complex to calibrate given the lack of experimental data providing precise quantitative information on these. Experimental SENB flexural tests are used to find the work of extraction of fibers from the composite matrix (see results in chapter 6). Based on what has been observed, we consider that fibers do not break during these tests. The work of

extraction of a single fiber  $W_{ext}$  is defined as [114, 115]:

$$W_{ext} = \int_0^{L_e} 2\pi r \tau x \, dx = \pi r \tau L_e^2 \quad (4.24)$$

where  $L_e$  is the length of the fiber embedded in the composite matrix,  $r$  is the fiber radius (we approximate the fiber section as a disk, which is not always the case experimentally) and  $\tau$  is the shear interfacial stress (see Fig. 4.16).

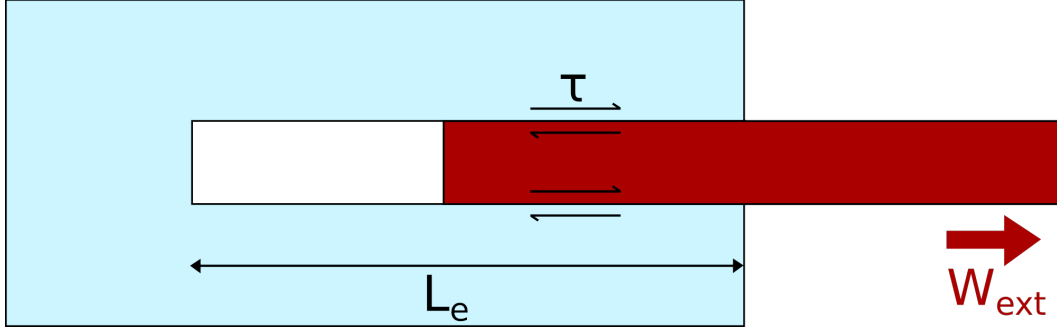


Figure 4.16: Sketch of the fiber extraction from a matrix.

The total work of extraction of all the fibers during flexural tests  $W_{ext/tot}$  is calculated from equation 4.24:

$$W_{ext/tot} = n_f \langle W_{ext} \rangle \quad (4.25)$$

$$\langle W_{ext} \rangle = \frac{1}{L_f/2} \int_0^{L_f/2} W_{ext}(L) \, dL = \frac{\pi r \tau L_f^2}{12} \quad (4.26)$$

$$n_f = f_v \frac{(H - a)b}{\pi r^2} \quad (4.27)$$

Where  $n_f$  is the number of fibers in the SENB sample fractured surface,  $\langle W_{ext} \rangle$  is the mean work of a single fiber extraction,  $L_f$  is the length of fibers incorporated in the composite,  $f_v$  is the volume fraction of fibers in the composite and  $H$ ,  $b$  and  $a$  are respectively the height, thickness and notch length of the SENB sample (see Fig. 4.17).

The total fracture work  $W_{SENB}$  during a flexural SENB test is:

$$W_{SENB} = W_s + W_{ext/tot} \quad (4.28)$$

Where  $W_s$  is the work necessary for the crack propagation in the silica aerogel composite matrix. In order to extract the experimental interfacial shear stress  $\tau$ ,  $W_{SENB}$  is calculated for all the SENB samples tested during the PhD work (with and without fibers).  $\tau$  is then calculated by combining equations (4.25) to (4.28):

$$\tau = \frac{12r \left( \langle W_{SENB/wf} \rangle - \langle W_{SENB/nf} \rangle \right)}{f_v (H - a) b L_f^2} \quad (4.29)$$

where  $\langle W_{SENB/wf} \rangle$  and  $\langle W_{SENB/nf} \rangle$  are the mean  $W_{SENB}$  values for the composite samples with fibers and without fibers, respectively.

Once the experimental value of  $\tau$  is evaluated, an adapted DEM simulation is



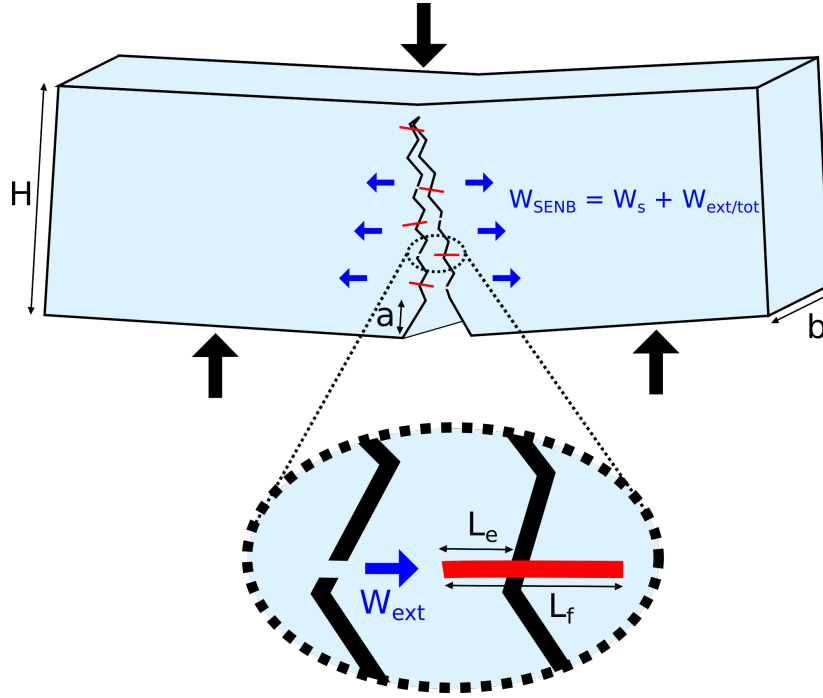


Figure 4.17: Sketch of the flexural tests on SENB samples. The total fracture work  $W_{SENB}$  is the sum of the fracture work in the silica aerogel matrix  $W_s$  and the total work of extraction of all the fibers  $W_{ext/tot}$ .

necessary to properly calibrate contacts between fibers aggregates and other discrete elements. A small composite sample, illustrated in Fig. 4.18a, containing only cement discrete elements and a single (straight) fiber aggregate is generated following the procedure discussed in sections 4.4.1.2. The numerical test consists of completely extracting the fiber aggregate by imposing a positive displacement rate at its free end and a null displacement rate at the other end of the sample (non-periodic conditions). The simulated interfacial shear stress is calculated using equation 4.24. As explained before, there are no bonds between fiber aggregates and other discrete elements in the DEM composites. The interfacial shear stress is calibrated using only adhesive and friction forces by tuning a work of adhesion  $w$  (see Eq. (4.11)) and a friction coefficient  $\mu$ . Fig. 4.18b shows a typical force-displacement curve during a single fiber extraction in DEM. The quasi-linear decrease of the applied load during fiber extraction is coherent with a constant interfacial shear stress.

## 4.5 Conclusion

In this chapter, the basic operation of the DEM model is presented, followed by the different contact laws specific to our simulations. We show that the silica aerogel particles and composites are meshed with spheres with no physical meaning which means a calibration is necessary for the microscopic properties of the discrete elements and the contact between them. This calibration leads to a realistic macroscopic behaviour of the silica aerogel particles and composites.

In order to keep manageable computation times, several choices have been made,

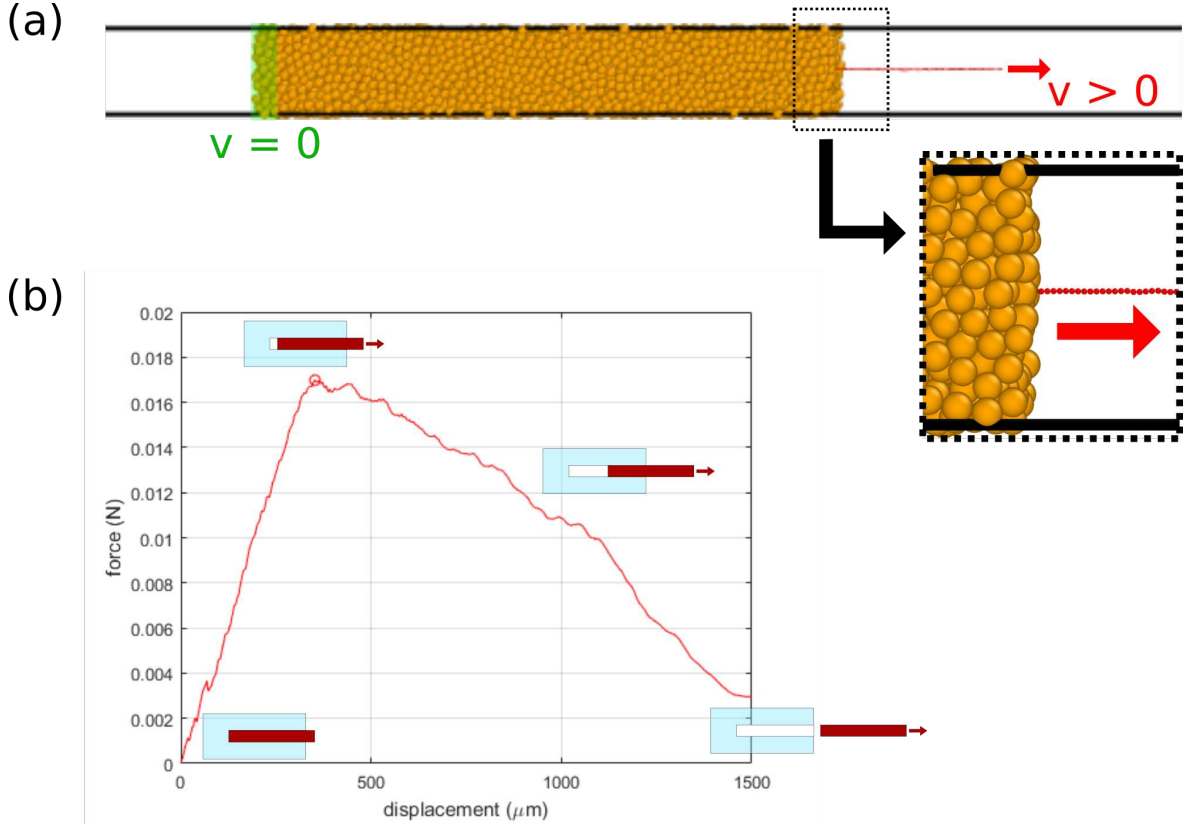


Figure 4.18: (a) DEM calibration sample: Single fiber pullout test. The fiber is the red necklace in the center of the sample. (b) Typical DEM single fiber extraction curve for given parameters  $\mu$  and  $w$ .

particularly for silica aerogel composite samples. First, while versions of silica aerogel particles exist meshed with 15  $\mu\text{m}$  diameter spheres (roughly 20000 spheres in a particle) and give better results than with 25  $\mu\text{m}$  diameter spheres (roughly 6000 spheres in a particle, see chapter 5), this last discrete element size has been chosen to keep a reasonable final number of discrete elements in the DEM composites. Similarly, the cement phase, which contains experimentally the small inf100 silica aerogel particles, is generated as a continuous phase in DEM with a given porosity. The simulation of the smaller silica aerogel particles would have required discrete element sizes much smaller than the 25  $\mu\text{m}$  diameter spheres currently used. Thanks to these restrictions on the discrete element size, our DEM model allows to simulate large composite samples ( $2.5 \times 2.5 \times \text{mm}^3$ ) generally not exceeding one million discrete elements. The computation time for the fracture of these composite samples can take up to two weeks.



## Chapter 5

# Mechanical properties of milimetric silica aerogel particles

### 5.1 Introduction

Silica aerogel particles are the main components of the particulate composite studied in this work. Their mechanical properties need thus to be studied in order to understand the mechanical behaviour of particulate composites and to successfully simulate composite samples using DEM. As described in chapter 3 (see section 3.3), two different particle size are incorporated in the composites: large 10-12 particles (1000-1250  $\mu\text{m}$ ) and small inf100 particles (below 100  $\mu\text{m}$ ). Due to the small size of inf100 particles, the majority of the results and analysis presented in this section concerns large 10-12 particles. The millimetric size and irregular geometry of these particles make it impossible to use conventional mechanical tests such as uniaxial compressions on cylindric samples, bending test on bars or brazilian tests. The main characterization procedure chosen for this work is uniaxial compression of the aerogel particles themselves. This test is well adapted to the aerogel particles size and shape. More than fifty aerogel particles were compressed in this work, providing enough data for statistical analysis of particles strength. The mechanical tests were paired with density measurements and X-ray tomography in order to link the measured properties to the possible density variation and the presence of process induced cracks. Here, DEM is used to simulate particle compression and contribute to the analysis of experimental results.

### 5.2 Morphology of large 10-12 silica aerogel particles

Large silica aerogel particles studied in this work and provided by Enersens company (Bourgoin-Jallieu) are faceted objects presenting irregular surfaces as illustrated by the SEM images in Fig. 5.1. The hypothesis is made that the irregularities (steps) observed on the facets of particles originates from the consecutive fractures of larger aerogel objects due to the high stresses during evaporative drying and to the sieving process of aerogel particles (see section 2.2.2.3). A network of process induced cracks in 10-12 aerogel particles is observed using X-ray tomography. These cracks are extremely difficult to precisely locate in cross-section images because of the scan resolution and the low absorption contrast between air and silica aerogel. Some of the largest process induced cracks could, however, be identified and are shown in Fig. 5.2a and 5.2b for the silica aerogel particles which were compressed inside the X-ray tomograph. Although the process induced crack network is certainly denser than what has been observed

experimentally, the identification of these large cracks is useful to study their influence through DEM simulations. The DEM particles shown in Fig. 5.2 are generated by using the X-ray tomography imprints of the particles compressed inside the X-ray tomograph. It can be chosen to incorporate or not the process induced cracks in these during the simulations.

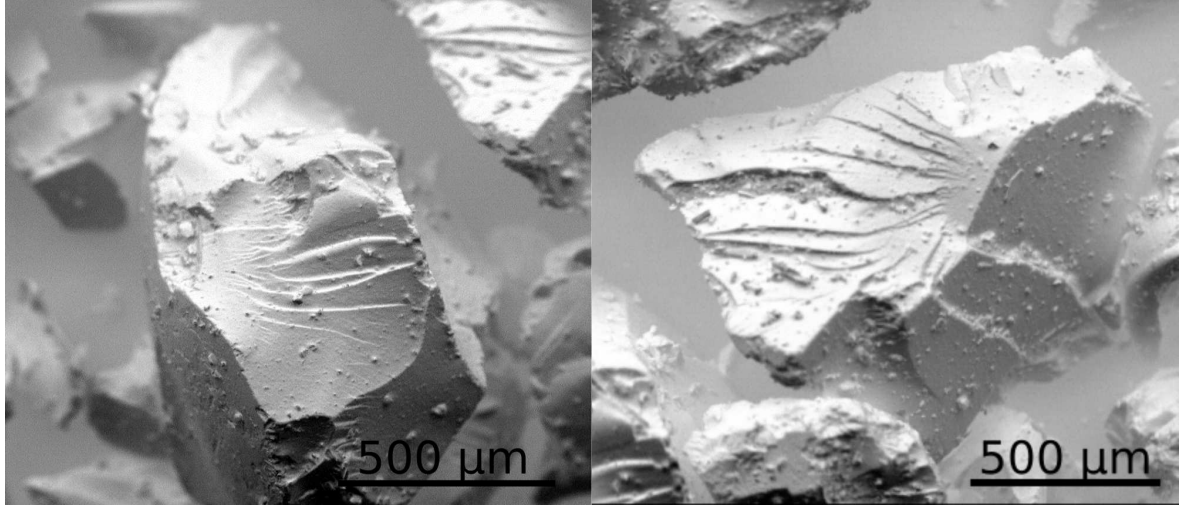


Figure 5.1: Large 10-12 particles visualized using SEM. Thin steps on particles facets correspond to crack deviation during fracture.

## 5.3 Experimental results

### 5.3.1 Particle compression: statistical procedure

In total, 60 aerogel particles have been deformed at constant speed to initiate crack aperture from a critical defect. Ten measurements have been dismissed: eight because the fracture could not be accurately observed during the compression and two because of a non-satisfactory behaviour (brittle failure from particle directly to dust). Fracture is defined from the detection of a fall or stabilization of the force in the force/displacement curve together with a visual detection of the fracture of the compressed particle. Particle fracture is noticed by a vertical crack (parallel to the loading direction). A representative example of a force/displacement curve is illustrated in Fig. 5.3. In most cases the force is still rising after fracture as the particle generally keeps its integrity, the different parts being held on by adhesive forces. Although somewhat arbitrary, this allows for a simple and consistent fracture criterion. The results obtained using this criterion are summarized in Fig. 5.4 (fracture force vs. normalized fracture height) for the two tested compression velocities. A large dispersion of the fracture force  $F_f$  and fracture height  $h_f$  is observed and no influence of compression velocity (in between 0.3 and 1.5 mm.mn<sup>-1</sup>) is discernible. Particles compressed following this procedure have error bars of  $\pm 0.01$  N for force and  $\pm 0.01$  for strain. In an attempt to decorrelate the fracture force from particle size, the normalized force  $F_f/h_0^2$  is calculated and plotted versus the initial height  $h_0$  of the particles in Fig. 5.5.

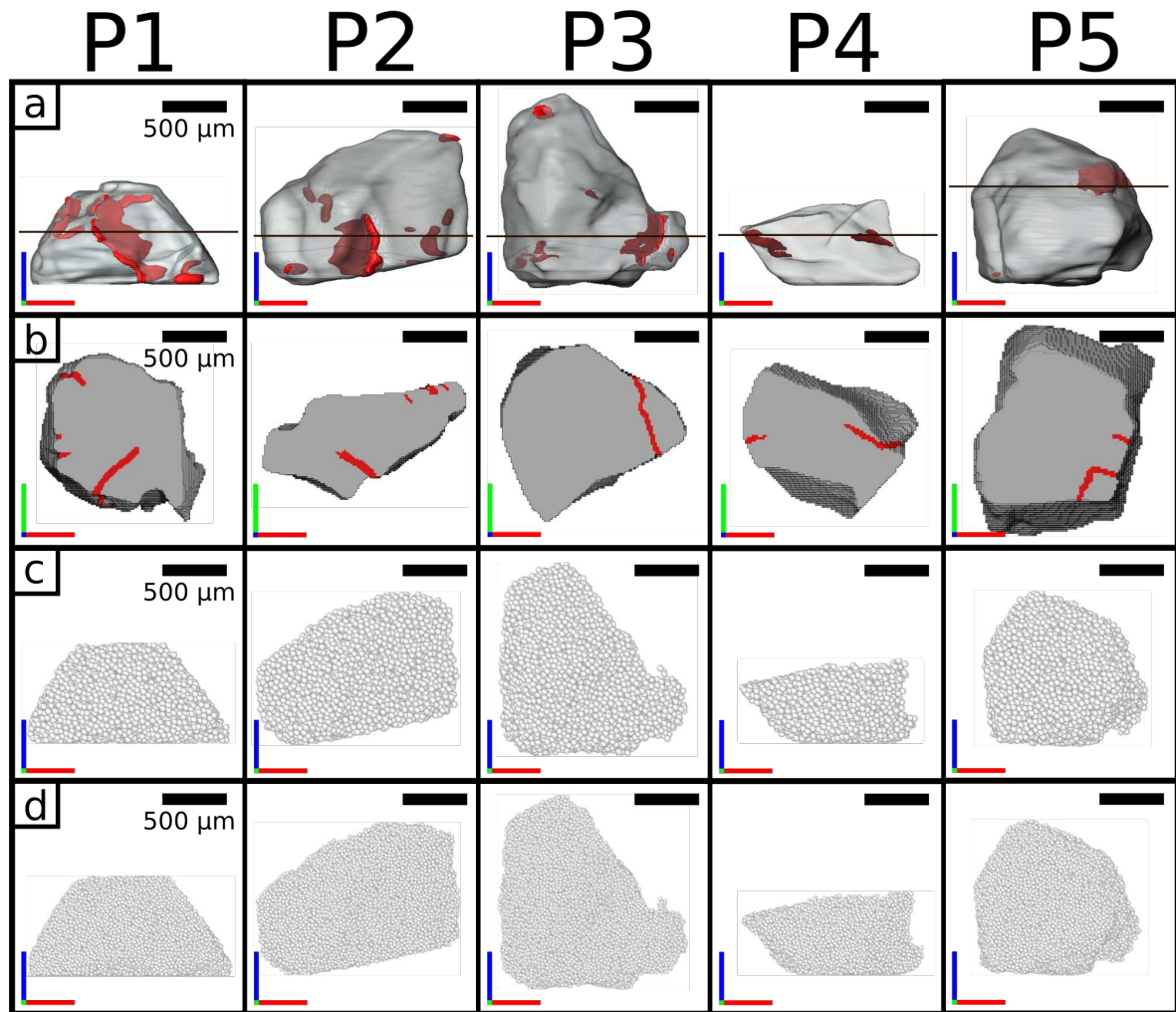


Figure 5.2: a) Aerogel particles with initial cracks reconstructed from X-ray tomography scans (in red). b) Cross section view within each particles at depth indicated on a). c) DEM aerogel particles prepared using 25  $\mu\text{m}$  discrete elements. d) DEM aerogel particles prepared using 15  $\mu\text{m}$  discrete elements. The numbering from P1 to P5 corresponds to a decreasing total crack length.

Initial height is an approximate indicator of the particles size as the height/width ratio is close to unity for our aerogel particles. Normalizing force by the initial particle height to the square is a basic simplification of aerogel particle geometry to propose some measure of strength. It can not describe fully the complex geometry of particles. A similar simplification has been proposed in soil mechanics for sand particles with similar shapes [116].

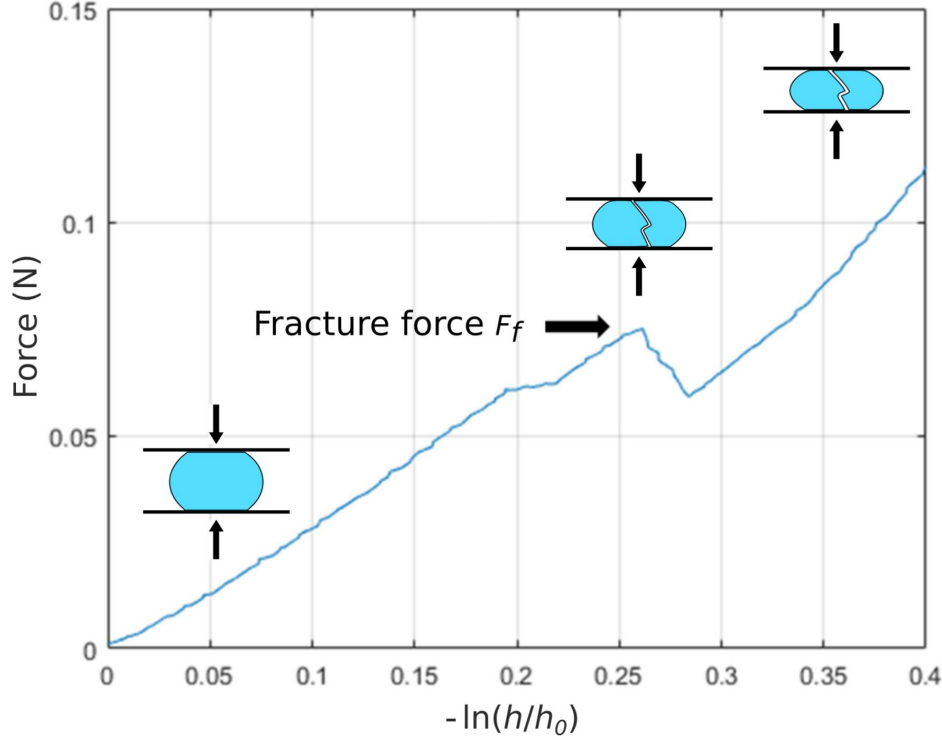


Figure 5.3: Experimental compression of an individual aerogel particle.  $h$  and  $h_0$  are the current and initial sample heights, respectively.

### 5.3.2 Particle compression with X-ray tomography observation

While a large number of silica aerogel particles have been tested following the statistical procedure, only a very limited number could be scanned using X-ray tomography during in-situ compression tests. In total, five aerogel particles have been compressed inside the X-ray tomograph, giving information on particles shape, density and defects. Particles density obtained from X-ray tomography volumes and individual weighing are presented in Table 5.1 as well as fracture force and normalized fracture height. Results from mercury porosimetry carried on large batches of aerogel particles are also included in this table (MP). It is worth noting that particle P4, which is significantly smaller than others, departs from other particles in terms of its density, which is significantly larger. At a first glance, density is not sufficient to warrant high fracture force, as P5 as a low density (0.10) and the highest load (0.16 N). The individually measured densities



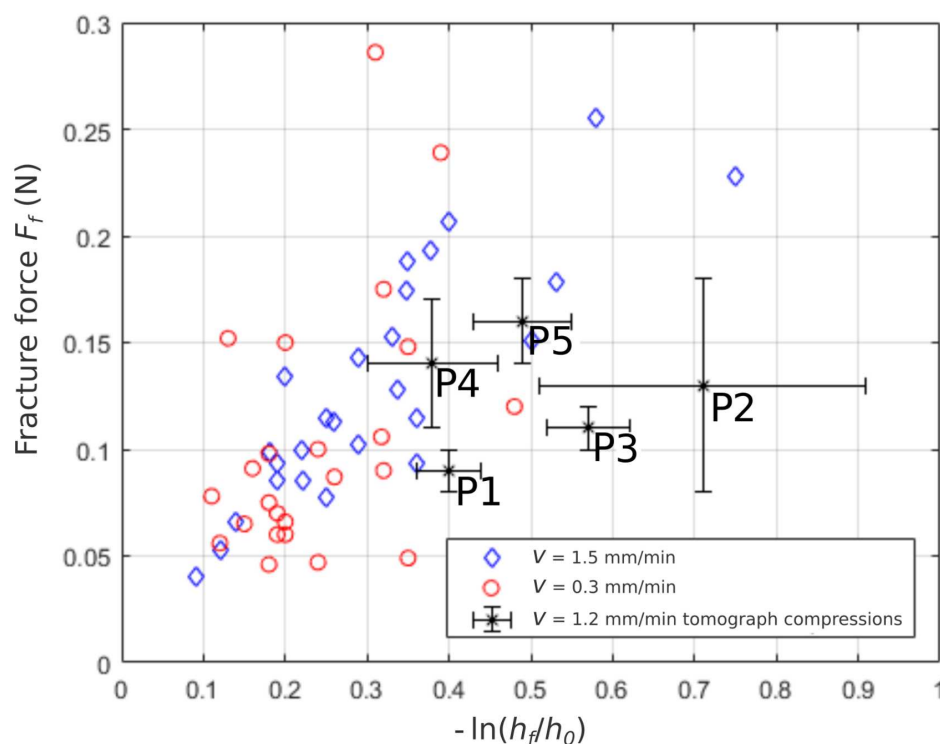


Figure 5.4: Fracture points  $(F_f, h_f)$  of aerogel particles following the two compression procedures : uniaxial particle compression carried out for two velocities. Samples P1 to P5 are those that have been scanned using X-ray tomography. Error bars of particles compressed following the statistical procedure are not shown for more clarity but are around 10% for fracture force and strain.



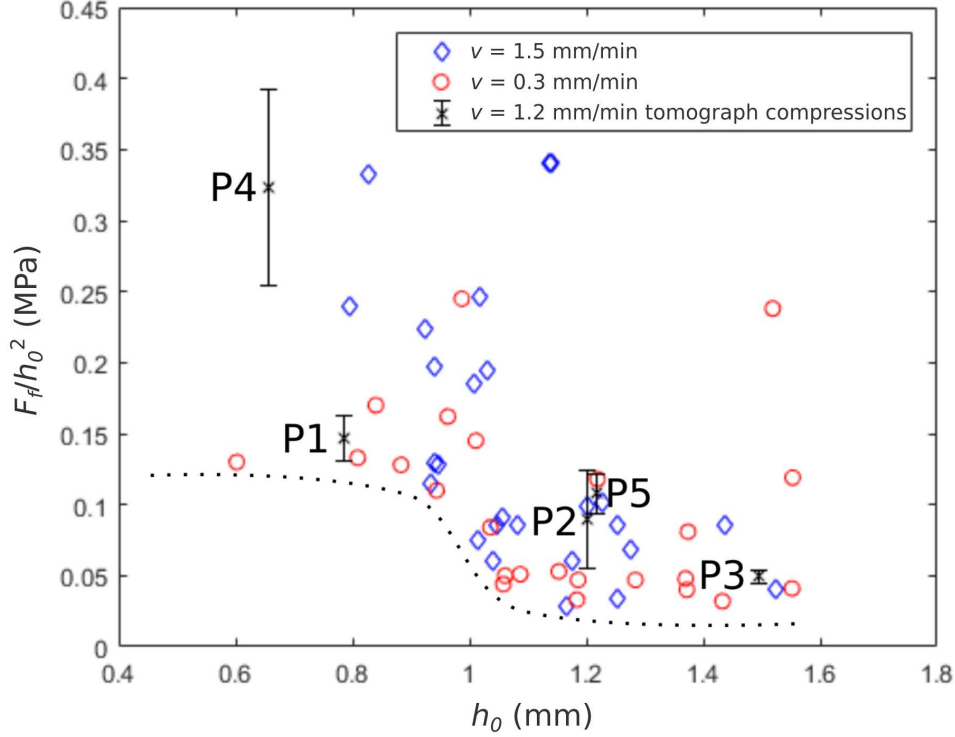


Figure 5.5: Normalized fracture force of compressed aerogel particles versus particle initial height  $h_0$ .

of P2, P3 and P5 are consistent with the mean density from mercury porosimetry.

Table 5.1: Experimental results from tomograph particle compression and mercury porosimetry (MP).  $h_f$  is particle height at fracture. Particle P1 was one of the first aerogel particles compressed inside the tomograph and density was not yet measured at this time.

	Number of SAP measured	Density g/cm <sup>3</sup>	Volume mm <sup>3</sup>	$-\ln(h_f/h_0)$	$F_f$ N
P1	1	n.a.	0.722	$0.40 \pm 0.04$	$0.09 \pm 0.01$
P2	1	$0.13 \pm 0.02$	0.684	$0.71 \pm 0.20$	$0.13 \pm 0.05$
P3	1	$0.10 \pm 0.02$	1.076	$0.57 \pm 0.05$	$0.11 \pm 0.01$
P4	1	$0.23 \pm 0.04$	0.300	$0.38 \pm 0.08$	$0.14 \pm 0.03$
P5	1	$0.11 \pm 0.02$	0.981	$0.49 \pm 0.06$	$0.16 \pm 0.02$
MP	$\sim 5000$	$0.10 \pm 0.01$			

In Fig. 5.4 the fracture forces of these five particles are illustrated together with the values from the statistical study and appear representative of the larger population tested outside the X-ray tomograph even if the values are slightly lower than the statistical study. This small difference might originate from the difference of friction with the compression tools between the two compression processes. Indeed, the graphite surface of the tools used during the statistical study induces less friction than the polycarbonate tools used for particles compressed inside the X-ray tomograph. Large error

bars are due to the difficulty to detect the fracture under the tomograph setup (see section 3.2.3).

## 5.4 DEM simulations results

### 5.4.1 Calibration of DEM particles

The five particles scanned using X-ray tomography are used to recreate numerically compression tests using the DEM model described in chapter 4. The DEM model is calibrated as described in section 4.3.3 without introducing the initial cracks observed in X-ray tomography. For each particle the calibrated normal stiffness ( $\sigma_N$ ) and Rankine critical stress of the bonds between discrete elements ( $\sigma_{Rc}$ ) are provided in Tables 5.2 and 5.3 for the two sizes of discrete elements used. These values are plotted in Fig. 5.6 as a function of particle density. The differences noted are relatively limited on the calibrated parameters between the two different discretizations. Both  $\sigma_N$  and  $\sigma_{Rc}$  increase with density, reflecting the stiffer and stronger mechanical response of denser particles.

Table 5.2: Calibration of bond normal stiffness  $\sigma_N$

	$\Sigma_N(R = 15 \text{ } \mu\text{m})$ MPa	$\Sigma_N(R = 25 \text{ } \mu\text{m})$ MPa	relative difference
P1	2.50	2.27	9.6%
P2	2.08	2.27	8.8%
P3	2.53	2.50	1.2%
P4	8.30	10.00	18.6%
P5	3.00	3.00	0%

Table 5.3: Calibration of critical bond strength  $\sigma_{Rc}$

	$\sigma_{Rc}(R = 15 \text{ } \mu\text{m})$ MPa	$\sigma_{Rc}(R = 25 \text{ } \mu\text{m})$ MPa	relative difference
P1	0.15	0.11	30.8%
P2	0.24	0.23	4.3%
P3	0.20	0.20	0%
P4	0.40	0.32	22.2%
P5	0.25	0.21	17.4%

### 5.4.2 Crack propagation in DEM and influence of initial cracks

In chapter 4 section 4.3.3 the five DEM aerogel particles (P1-P5) scanned by X-ray tomography have been calibrated and tested without introducing the initial observed cracks. By introducing these defects in the initial state of the particles before numerical compression, the fracture behaviour could be better described. Particle P1 has been chosen to illustrate the differences between DEM compression with and without initial

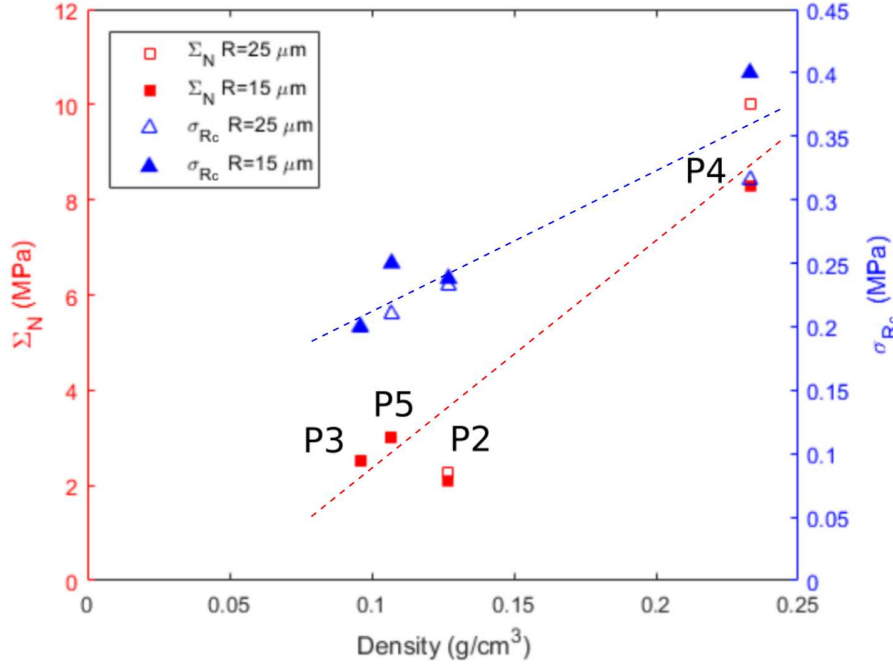


Figure 5.6: Calibrated DEM parameters  $\sigma_N$  and  $\sigma_{Rc}$  for the five simulated aerogel particles as a function of particle density. Straight lines are drawn to guide the eye.

cracks as illustrated in Fig. 5.7. The initial and final cracks obtained during experimental compression (X-ray tomography) are showed in red on the volume reconstruction of the particle (Fig. 5.7a) while broken bonds between discrete elements are showed on DEM particles (Fig. 5.7b). The color of discrete elements indicates the chronological order of the fractured bonds from dark red to yellow. The cracks paths obtained in DEM aerogel particles do not follow the path observed with X-ray tomography.

The force versus displacement curves for the DEM particle P1 are shown in Fig. 5.8. Fracture forces are measured on DEM curves by identifying the maximum on the force curve preceding the point corresponding to 0.1% broken bonds between discrete elements in the DEM particle. We can observe (Fig. 5.8) a clear drop of the fracture force of DEM aerogel particles with the addition of initial cracks in the model. For the sake of completeness the experimental and numerical fracture behavior of the other four aerogel particles is provided in the Appendix (see B). Fracture force values for the five DEM particles with and without initial cracks are summed up in Fig. 5.9. These fracture forces are mean values as each aerogel particle version (with or without initial cracks, using either 25  $\mu m$  or 15  $\mu m$  discrete elements) was simulated with different discretizations. These five discretizations were simply obtained by providing five different seeds for the random generation of the very initial packings of discrete elements. The objective of these different packings is to estimate the scattering of the simulation results due to the discretization of aerogel particles. The resulting uncertainty of DEM fracture force due to the discretization depends slightly on the considered aerogel particle but remains below 7%.

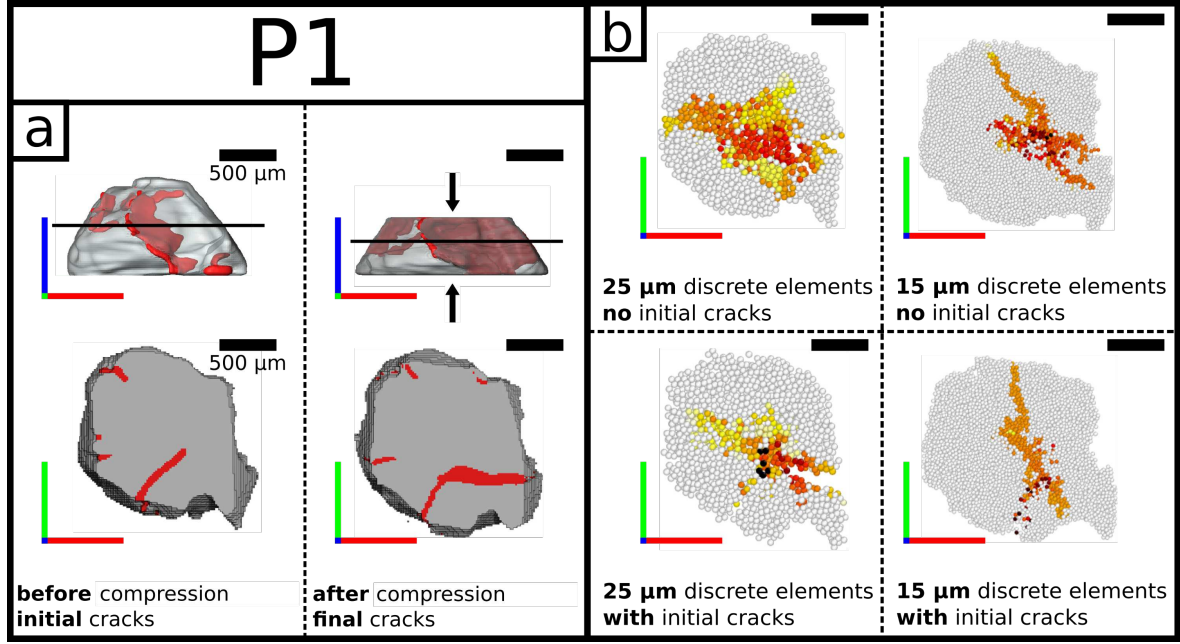


Figure 5.7: a) P1 particle volumes built from tomography compression test together with a cross section of interest. Top line: 3D representation, bottom line: cross section (location as indicated by a black line in top line) b) P1 particle cross sections at fracture load generated from coarse ( $25\ \mu\text{m}$ ) and fine ( $15\ \mu\text{m}$ ) discrete elements. Bond fractures are illustrated chronologically from dark red (earliest broken bonds) to yellow (latest broken bonds) and white (intact bonds).

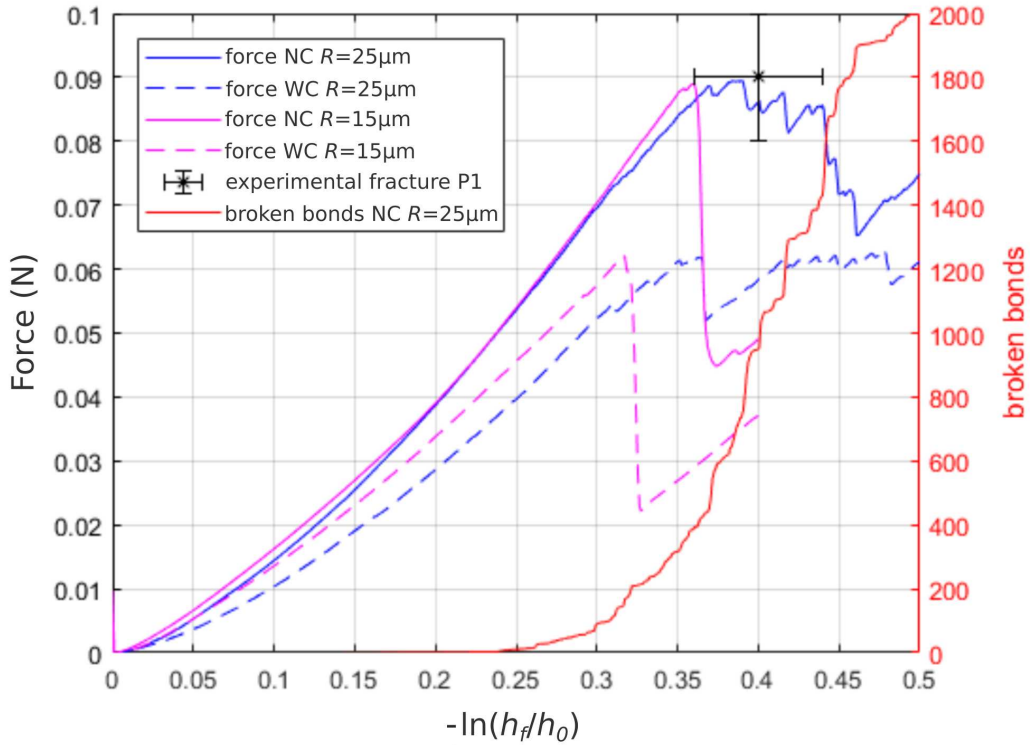


Figure 5.8: DEM compression of P1 with (WC) and without (NC) initial cracks generated from coarse ( $25\ \mu\text{m}$ ) and fine ( $15\ \mu\text{m}$ ) discrete elements. Experimental critical fracture of the particle is highlighted.

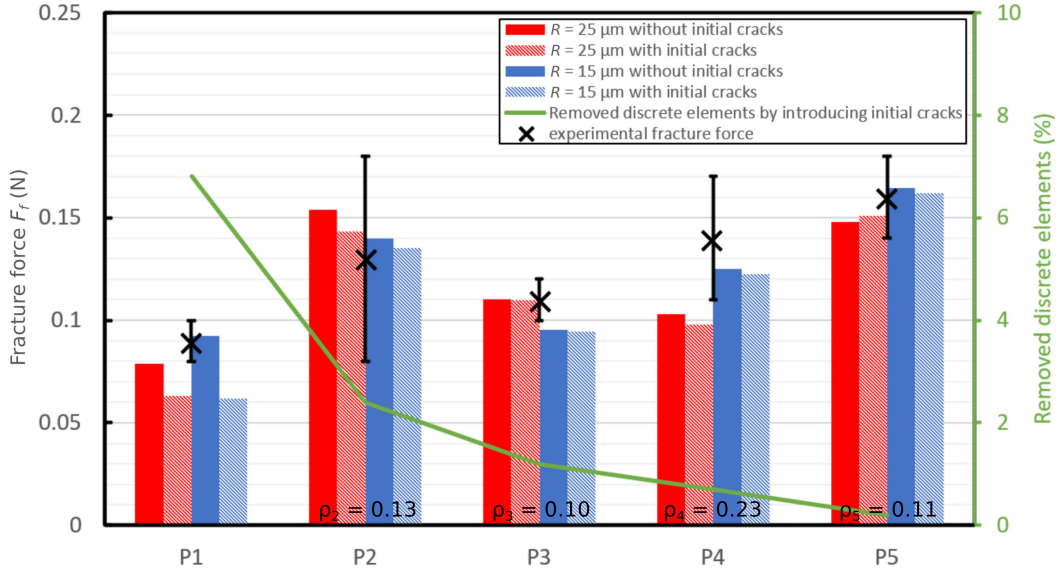


Figure 5.9: Fracture force for each simulated particle (P1-P5) with and without initial cracks introduced in the coarse ( $25 \mu\text{m}$ ) and fine ( $15 \mu\text{m}$ ) discrete elements mesh. The fraction of removed discrete element due to initial cracks introduction is plotted on the right hand side axis. The density  $\rho$  of the corresponding experimental SAP is indicated.

## 5.5 Discussion

### 5.5.1 Macroscopic behaviour of aerogel particles in compression

As shown in Fig. 5.4, fracture force values are quite scattered whatever the experimental procedure (outside or inside X-ray tomograph) as fracture depends on particle shape, size, orientation, density and initial defects. However, no clear difference was observed between the three tested velocities. Sensitivity to strain-rate for the tested aerogel particles can thus be considered negligible for compression rates between  $0.3$  and  $1.5 \text{ mm.mn}^{-1}$ . The five particles compressed inside the tomograph present fracture forces slightly lower than the results of the statistical study but still are coherent with the experimental dispersion. Error bars are large for some particles due to the difficulty to visually detect unambiguously the fracture while monitoring the X-ray projections of the particles during compression (see section 3.2.3). Particle P2 exhibits such a problem with thus large error bars.

The evolution of the normalized fracture force (units of a stress) with the initial height illustrated in Fig. 5.5 enables to determine if the scatter in particle strength is mainly due to their size or to intrinsic properties (density and defects/cracks) and shape. No clear tendency in the normalized fracture load is observed with the variation of the particle initial height  $h_0$ . The normalized fracture force is still very dispersed, which suggests density variation, initial defects and shape have also a great influence on aerogel particle strength. Interestingly, normalized fracture forces are not observed below  $0.1 \text{ MPa}$  for small initial particle height  $h_0$  (below  $1 \text{ mm}$ ). This could be explained by an increasing density and a lower probability to find critical initial

defects for small particle volumes. Density measurements carried out on large particle populations with mercury porosimetry and on individual particles for 4 out of 5 of the particles scanned with X-ray tomography tend to illustrate a possible link between size and density. Three particles scanned with X-ray tomography have a density close to the one measured over a large particle population with mercury porosimetry  $d_{MP} = 0.10 \pm 0.01 \text{ g.cm}^{-3}$  but the smallest particle studied (P4) is much denser ( $d_{P4} = 0.23 \pm 0.04 \text{ g.cm}^{-3}$ ). The three other particles having a density close to the mean density measured with mercury porosimetry suggests the total volume occupied by particles as dense as P4 is small enough to have no significant impact on the mean density of a large population of particles.

### 5.5.2 Weibull distribution

The statistical dispersion of fracture load in compression for the large population of individual aerogel particles (52 compressions) has been fitted with a Weibull distribution function. The probability of particle fracture is plotted as a function of the normalized force  $\sigma = \frac{F_f}{h_0^2}$  in Fig. 5.10

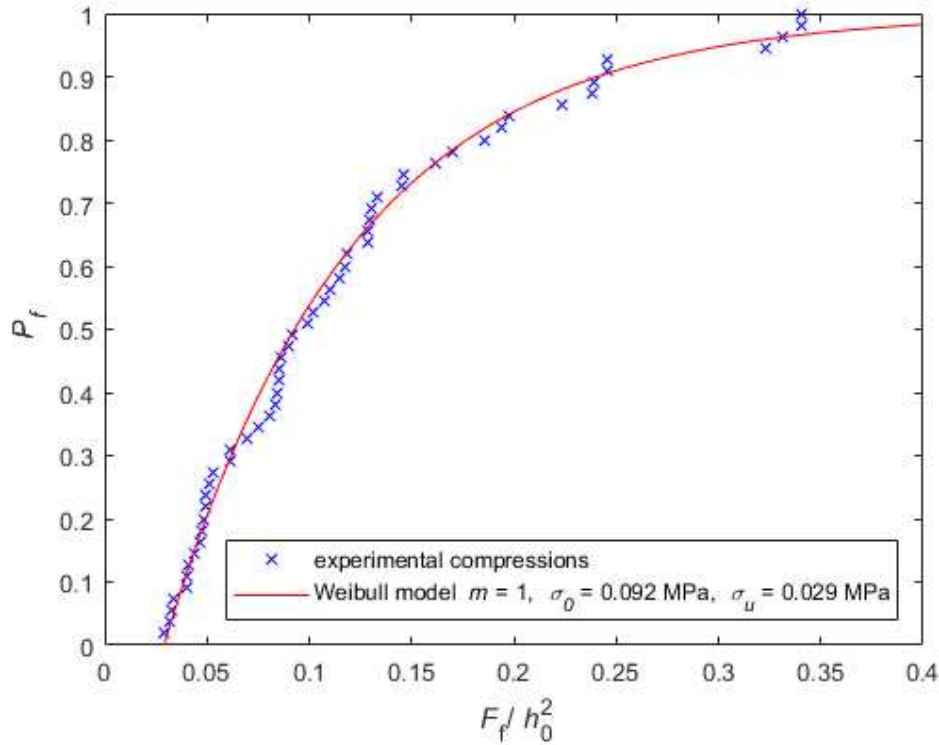


Figure 5.10: Weibull cumulative distribution fit carried out on the fracture by compression of aerogel particles. The fit leads to  $m \approx 1$  in Eq. (5.1).

The fracture probability  $P_f$  was fitted with the cumulative distribution function [117]:

$$P_f = 1 - \exp \left( - \left( \frac{\sigma - \sigma_u}{\sigma_0} \right)^m \right) \quad (5.1)$$

where  $\sigma_u$ ,  $\sigma_0$  and  $m$  are the translation, scale and shape fitted parameters, respectively.



The Weibull parameter  $m$  gives some information on the dispersion of the normalized fracture force.  $m$  is low for materials with a large strength dispersion and high for materials with low dispersion. The parameter  $m$  also called Weibull modulus does not describe in our case a volume effect linked to the probability of presence of a critical defect size in a given volume. Silica aerogels are porous materials with a very high density of defects and do not fulfill the assumptions of Weibull analysis [118, 119]. Weibull distribution law is in our case only used as a fit of the cumulative probability distribution of our statistical study. The fit from Eq. (5.1) leads to  $\sigma_u = 29$  kPa,  $\sigma_0 = 92$  kPa and  $m = 1$ . The latter value is extremely low. As a reminder, the Weibull modulus of most ceramics, which are already considered as brittle materials with some defects, is generally between 5 and 10. Huilca et al. did a Weibull analysis on individual rock aggregates [120]. The rock aggregates are larger than our aerogel particles (5 to 40 mm) but have similar irregular shapes. They found a  $m$  parameter between 1.56 and 3.05 meaning our aerogel particles have a fracture behaviour more scattered than for brittle rocks with similar aggregate shape. This might be explained by large variations in density, in particle shape and the possible presence of initial defects. Weibull fits were also realized by Woignier et al. [112] on silica aerogel monoliths synthesized using supercritical drying. The modulus  $m$  is found between 4 and 7. It is difficult to compare these values with our results as Woignier et al. were not as much dependent on aerogel objects shape as we are with the present aerogel particles. The fact our value for  $m$  is much lower is yet not surprising as supercritical drying introduces much less defects and density scattering in the synthesised aerogel objects than evaporative drying.

### 5.5.3 DEM determination of Young's modulus and tensile strength

As indicated in Tables 5.2 and 5.3, the relative difference of calibration parameters  $\sigma_N$  and  $\sigma_{Rc}$  between the two DEM discretization sizes is generally less than 20%. This low dependency to discretization means that the main factors influencing the calibration of the parameters  $\sigma_N$  and  $\sigma_{Rc}$  are linked to the nature of the material and not to the numerical effects of the model itself.  $\sigma_N$  and  $\sigma_{Rc}$  can thus be used with confidence to estimate the macroscopic Young's modulus and the fracture strength. The work of Kumar et al. [90] established relationships relating the discrete element bond stiffness to the macroscopic elastic behaviour of different packings obtained from various preparation routes including the one that was chosen in this work to model aerogel particles. These equations write:

$$E = Z_b D \sigma_N \frac{\kappa^n a_1 + a_2 \alpha}{2\pi 4 + a_3 \alpha} \quad (5.2)$$

$$\alpha = \frac{1 - b_2 \nu}{b_1 + b_3 \nu} \quad (5.3)$$

where  $E$ ,  $Z_b$ ,  $D$  and  $\kappa$  are the Young's modulus, the average coordination number, the packing density and the interaction range of the discrete element packing, respectively. The parameters  $n$ ,  $a_i$  and  $b_i$  are fitted ( $n = 2$ ,  $a_1 = 0.42$ ,  $a_2 = 7.45$ ,  $a_3 = 8.68$ ,  $b_1 = 0.55$ ,  $b_2 = 3.02$ ,  $b_3 = 5.75$ ) and originate from Kumar's work. The preparation route used

here is defined as "weakly jammed" and results in a packing density of  $D = 0.65$  and an average coordination number  $Z_b = 6.56$  with an interaction range  $\kappa = 1.075$ .

Similarly to the Kumar et al. study, Radi et al. [121] established a relationship between the macroscopic strength of a packing and the microscopic bond strength. Their equation writes:

$$\sigma_f = \sigma_{Rc}(c_1 Z_b D - c_2) \quad (5.4)$$

where  $\sigma_f$  is the macroscopic tensile strength,  $\sigma_{Rc}$  the Rankine critical stress of the bonds and  $c_i$  are fitted parameters ( $c_1 = 0.124$ ,  $c_2 = 0.067$ ).

These relations allow for the estimation of macroscopic properties from the calibrated microscopic parameters of the discrete element packing. For particles P2, P3 and P5 (of similar densities), the resulting estimations are  $E = 0.7 \pm 0.1$  MPa and  $\sigma_f = 100 \pm 10$  kPa. For particle P4  $E_{P4} = 2.6 \pm 0.3$  MPa and  $\sigma_{fP4} = 165 \pm 26$  kPa. It is encouraging that our model and calibration method lead to a Young's modulus close to 1 MPa as this value is consistent with various studies on the elastic response of silica aerogels as function of their density [27, 32]. As expected, the dense particle P4 has a much higher Young's modulus than other particles. Concerning the estimated fracture strength, the previously cited literature [27, 32] also measured tensile strength (three point bending tests, brazilian tests) for various silica aerogels with various densities. For densities around  $0.1 \text{ g.cm}^{-3}$  the tensile strength ranges between 10 and 100 kPa. This is consistent with our value of  $100 \pm 10$  kPa that is calculated from DEM simulations. According to Hiramatsu et al. [122], the fracture force normalized by the initial height to the square of the compressed particles is a correct estimation of the tensile strength. It is thus consistent to compare the fitted scale parameter  $\sigma_0$  obtained with the Weibull fit performed previously in section 5.5.2 with the tensile strength obtained with Eq. (5.4). The two estimations of the tensile strength based on experimentation ( $\sigma_0 = 92$  kPa) and simulation ( $\sigma_f = 100 \pm 10$  kPa) agree very well. The use of DEM calibrated micro-parameters has the advantage of removing aerogel particle shape and orientation from the possible source of strength scattering. When considering aerogel particles with similar densities, the strength displays a coefficient of variation of 10%. This remaining scattering should originate mainly from the presence of initial cracks.

#### 5.5.4 Influence of process induced cracks on the DEM mechanical behavior of aerogel particles

The introduction of cracks in DEM aerogel particles modifies their fracture behaviour. The objectives of the simulation are to quantify and to explain the influence of the initial cracks on particles behaviour, as well as to check if the numerical crack propagation matches what was observed in tomography.

A positive point for the DEM model is that the final cracks observed for the four configurations as illustrated for particle P1 in (Fig. 5.7) are located following a clearly identifiable path cutting the particles into two distinct main portions, especially for the thinly meshed particles ( $15 \mu\text{m}$  discrete elements) as the cracks are located in a much thinner zone compared to the  $25 \mu\text{m}$  meshed particle. Particles with and without initial



cracks do not fracture by following exactly the same path but the general behaviour is maintained. Still, the main cracks observed in DEM particles do not follow the fracture observed experimentally in tomography, except for the 25  $\mu\text{m}$  discretized particle for which some similarities can be found. The DEM model fails to reproduce the final crack pattern once the fracture is initiated as it seems to depend too much on the discretization of the model. Also, we believe that the boundary conditions of the experiment at the onset of crack growth (interaction between the platens and the particle) are difficult to reproduce exactly. The complex crack growth patterns after fracture depend too much on the full strain history to be reproduced accurately in DEM.

However the initiation of the cracks is mostly correct with initial broken bonds (shown in black or dark red in Fig. 5.7) localised around or at the extremity of the initial cracks. After its initiation, the crack follows a path imposed by the discrete element packing and so does not describe the real case. Thinly discretized particles (15  $\mu\text{m}$ ) are best suited for the acquisition of precise crack patterns but are four to five times more computationally expensive compared to the 25  $\mu\text{m}$  discretized particles.

Although the cracks morphological differences are minor for particle P1 with and without initial cracks, there is a quantitative difference between particles with and without initial cracks with a drop of the fracture force in compression of approximately 30% (Fig. 5.8). Fig. 5.9 indicates that particle P1 is the only simulated particle exhibiting a fracture force drop superior to 15% after initial cracks are introduced in the model. This is consistent with the fact that particle P1 is the particle with the largest relative number of discrete elements removed in the crack modelling process (7% versus 2.5% for P2, the second most impacted particle). Particles P2 to P5 exhibit much smaller variations of the fracture force when initial cracks are introduced. In general, a decrease of the fracture force is almost always observed when initial cracks are introduced but, apart from particle P1, it is low. It is thus safe to conclude that the initial cracks introduced in the DEM aerogel particles following our procedure have rarely a large influence both on the cracks morphology after crack initiation and on the fracture force values. It might be due to the orientation and localisation of the initial crack patterns which rarely weaken the aerogel particles in the uniaxial compression direction. The probability to find a well located and oriented crack increases with the amount of initial damage and only P1 presents a crack parallel to the loading conditions and located in a zone experiencing a high tensile stress (typically close to the center of the particle). It could also explain why tensile strengths lower than 0.1 MPa were not observed for small particles during experimental uniaxial compression (see Fig. 5.5) as the probability to find a well located and oriented defect might increase with particle volume.

## 5.6 Conclusions

Experimental compression tests and DEM simulations were carried out in order to investigate the mechanical behavior of millimetric silica aerogel particles produced by

evaporative drying.

A first experimental statistical study has shown that the values of fracture force are very much scattered, as quantified by Weibull statistics. This is due to the combination of the variability of the particles shape, orientation, density and the presence of initial defects. In order to decorrelate the influence of these parameters, an original methodology based on individual X-ray tomography images of particles coupled with DEM simulations is proposed. Individual density assessment of aerogel particles based on X-ray tomography volumes has shown significant density variation ( $0.1$  to  $0.23$  g/cm<sup>3</sup>) that explains an important part of the scattering. Particles with similar densities still exhibit important normalized fracture force variations that can be attributed to particles shape and orientation and to the potential presence of initial defects in the particles during compression test. The methodology consists of the numerical replication with DEM of a compression experiment, using the particle morphology and orientation from X-ray tomography images. The calibrated DEM parameters are used to assess the material Young's modulus and strength. This methodology gives encouraging results, with Young's modulus ( $0.7 \pm 0.1$  MPa ) and strength ( $100 \pm 10$  kPa) values for a density of around  $0.1$  g/cm<sup>3</sup> all consistent with literature data on supercritically dried monolithic aerogels. The remaining small scattering in strength ( coefficient of variation of 10%) is attributed to the methodology uncertainty itself and the inherent variability due to the presence of initial defects. The relatively modest influence of process induced defects is confirmed by DEM modeling that shows that for particle in compression, the initial cracks within the sample have rarely a highly detrimental effect on strength. It is consistent with the fact that the obtained value for strength is similar to reported values for monolithic aerogel of similar density. Still, one should keep in mind that for a purely homogeneous tensile loading (which might happen within a composite) the presence of initial cracks in the aerogel particle will probably be more critical.



## Chapter 6

# Properties of particulate silica aerogel composites

### 6.1 Introduction

The particulate composites studied in this work are mainly composed of the silica aerogel particles studied in chapter 5. The high volume fraction of these particles in the composites (around 90%) results in thermal conductivities almost as low as those of the silica aerogel particles themselves ( $\lambda_{particles} \approx 13 \text{mWm}^{-1}\text{K}^{-1}$ ). Still, thermal conductivity is degraded by inter-particle porosity, as the thermal conductivity of still air is approximately  $25 \text{mWm}^{-1}\text{K}^{-1}$ . It is also degraded by the presence of other essential components such as the polymer binder. The objective when fabricating silica aerogel particulate composites is to push the thermal performances to the extreme. Thus, efforts should focus on the minimization of inter-particle porosity and on the accompanying components of the silica aerogel. This approach may be compromised by the poor strength of these composites originating from the high porosity of silica aerogels. While their thermal performance can be improved by maximizing the volume fraction of silica aerogel, their mechanical strength benefits from a higher volume fraction of binder and the incorporation of reinforcing components like fibers. The work presented in this chapter aims at properly characterizing structural, thermal and mechanical properties of particulate composites in order to provide an acceptable compromise between thermal conductivity and mechanical strength (and fracture toughness). Experimental results are used to calibrate the DEM model, allowing the fracture of different model composite samples to be simulated. This numerical model is a valuable tool for studying the influence of various structural parameters on the composites Young's modulus, fracture strength and toughness.

### 6.2 Description of the studied composites

#### 6.2.1 Experimental composites

In this PhD, different types of silica aerogel particulate composites have been fabricated and studied by following the procedures described in chapter 3 (see section ... and section ...). These composites are listed in Table 6.1 with the corresponding nomenclature which will be used in the remaining of this chapter. The proportions of the different components are also illustrated in Fig. 6.1. These composites served different purposes described hereafter.

Composites samples STD-6 have been fabricated based on previous studies and empirical tests [29, 63]. They suggest the composition of this composite approaches

Table 6.1: Nomenclature and composition of experimental composites. 10-12 relates to large particles (1000-1250  $\mu\text{m}$ ) and inf100 to small particles ( $< 100\mu\text{m}$ ). All values are weight fractions.

Name	$w_{10-12}/w_{aerogel}$	$w_{10-12}$	$w_{inf100}$	$w_{SBA+XPCAS}$	Fibers	$w_{fibers}$
STD-6	0.6	0.51	0.35	0.14		
STD-7	0.7	0.58	0.28	0.14		
STD-0	0	0	0.73	0.27		
G-6	0.6	0.51	0.35	0.14	glass	0.01
PET-6	0.6	0.51	0.35	0.14	PET	0.01
PP10-6	0.6	0.51	0.35	0.14	PP	0.01

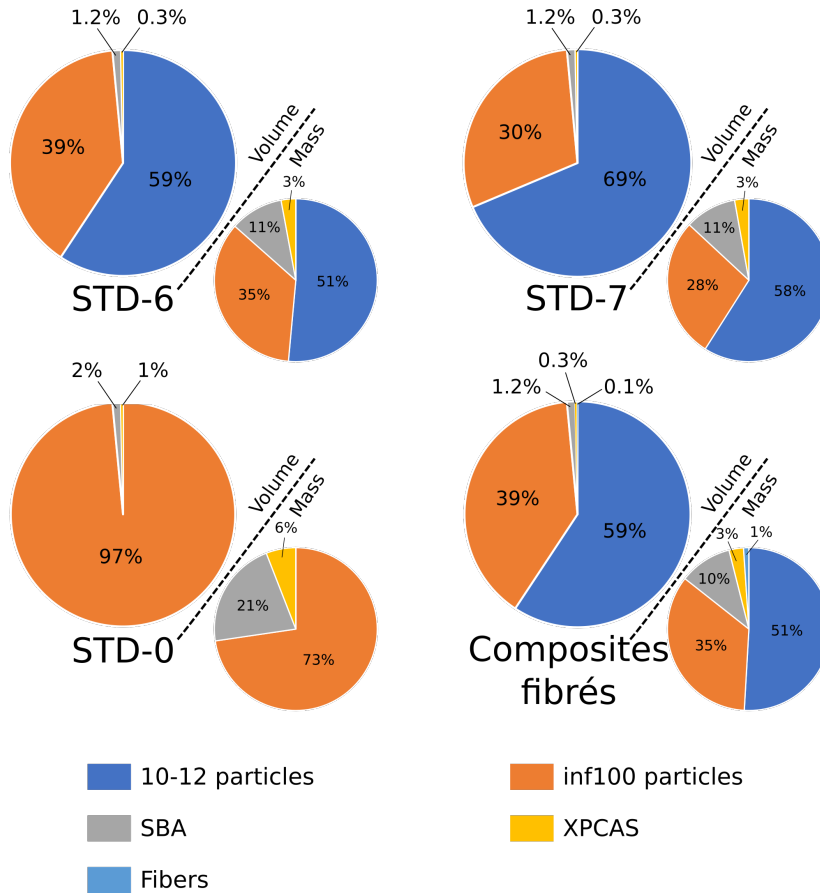


Figure 6.1: Composition of dry particulate composites fabricated in this work. Fractions are given in vol% in large histograms and in w% in small histograms. SBA + XPCAS form the binder (SBA is the latex and XPCAS is the surfactant).

an optimal silica aerogel particle size distribution, as well as a proportion of binder, providing reasonable mechanical strengths for the composite samples to be handled and a reference thermal conductivity ( $13\text{-}14 \text{ mWm}^{-1}\text{K}^{-1}$ , see chapter 2).

Composite samples STD-7 have a slightly different particle size distribution and were used to study its influence on the composite thermal and mechanical properties. Although the total silica aerogel particles surface that the binder needs to cover is different from the STD-6 composite, the proportion of binder incorporated during the fabrication process was not modified.

Composite samples STD-0 were fabricated in order to mimic as accurately as possible the cement phase alone that incorporates the small inf100 aerogel particles in STD-6 and STD-7 composites (see chapter 4, section 4.4.3). The proportion of polymer binder in these samples was adjusted so that its mass fraction is similar to that in the cement phase in samples STD-6. In standard composites STD-6, most of the binder is used to coat the inf100 aerogel particles as the total surface of the large 10-12 aerogel particles do not exceed 5% of the total free silica aerogel surface. Thus, the binder mass (latex + surfactant) is 2.5 times greater in STD-0 samples (with 100% inf100 particles) compared to STD-6 samples (with 40% inf100 particles). These samples provided essential data for the calibration of DEM simulations.

The composites containing fibers are labelled after the nature of the fiber incorporated in the material: glass fibers (G-6), polyethylene fibers (PET-6) and polypropylene fibers (PP10-6). The composition of these composites is almost identical to the STD-6 composite, the only difference being the small fraction of fibers in the materials incorporated following a slightly different fabrication protocol described in chapter 3, section 3.3. A fiber weight fraction of 1% amounts to approximately 0.1% volume fraction.

### 6.2.2 DEM composites

Following the preparation and calibration processes described in chapter 4, several DEM particulate composite samples have been generated. These DEM composites are listed in Table 6.2 and shown in Fig. 6.2.

Table 6.2: Nomenclature and composition of DEM composites.  $d_{aero}$  is the volume fraction of 10-12 particles  $f_{10-12}$  divided by the total volume fraction of silica aerogel particles  $f_{aerogel}$  ( $d_{aero} = \frac{f_{10-12}}{f_{aerogel}}$ ).  $N_{SAP}$  and  $N_{fibers}$  are the number of silica aerogel particles (SAP) and the number of fibers incorporated in the DEM composites. Porosity corresponds to the pores introduced in the discrete element packing (see Figs. 13 and 15 in chapter 4).

Name	$d_{aero}$	Porosity	$N_{SAP}$	$N_{Fibers}$	dimensions (mm <sup>3</sup> )
D-STD-5	0.5	0.1	60	0	2.5×2.5×15
D-STD-6	0.6	0.1	60	0	2.5×2.5×15
D-STD-7	0.7	0.1	60	0	2.5×2.5×15
D-LPo-6	0.6	0.05	60	0	2.5×2.5×15
D-HPo-6	0.6	0.15	60	0	2.5×2.5×15
D-PP5-6	0.6	0.1	60	369	2.5×2.5×15
D-PP10-6	0.6	0.1	60	738	2.5×2.5×15
D-PP15-6	0.6	0.1	60	1107	2.5×2.5×15
D-rSTD-6	0.6	0.1	10	0	2.5×2.5×2.5

As shown by Table 6.2, the influence of four different parameters has been studied in this work:

- Silica aerogel particles distribution with  $d_{aero}$  varying between 0.5 and 0.7 (DEM composites D-STD-5, D-STD-6 and D-STD-7), see Fig. 6.2a).
- Porosity varying between 0.05 and 0.15 (DEM composites D-LPo-6, D-STD-6 and D-HPo-6), see 6.2b).

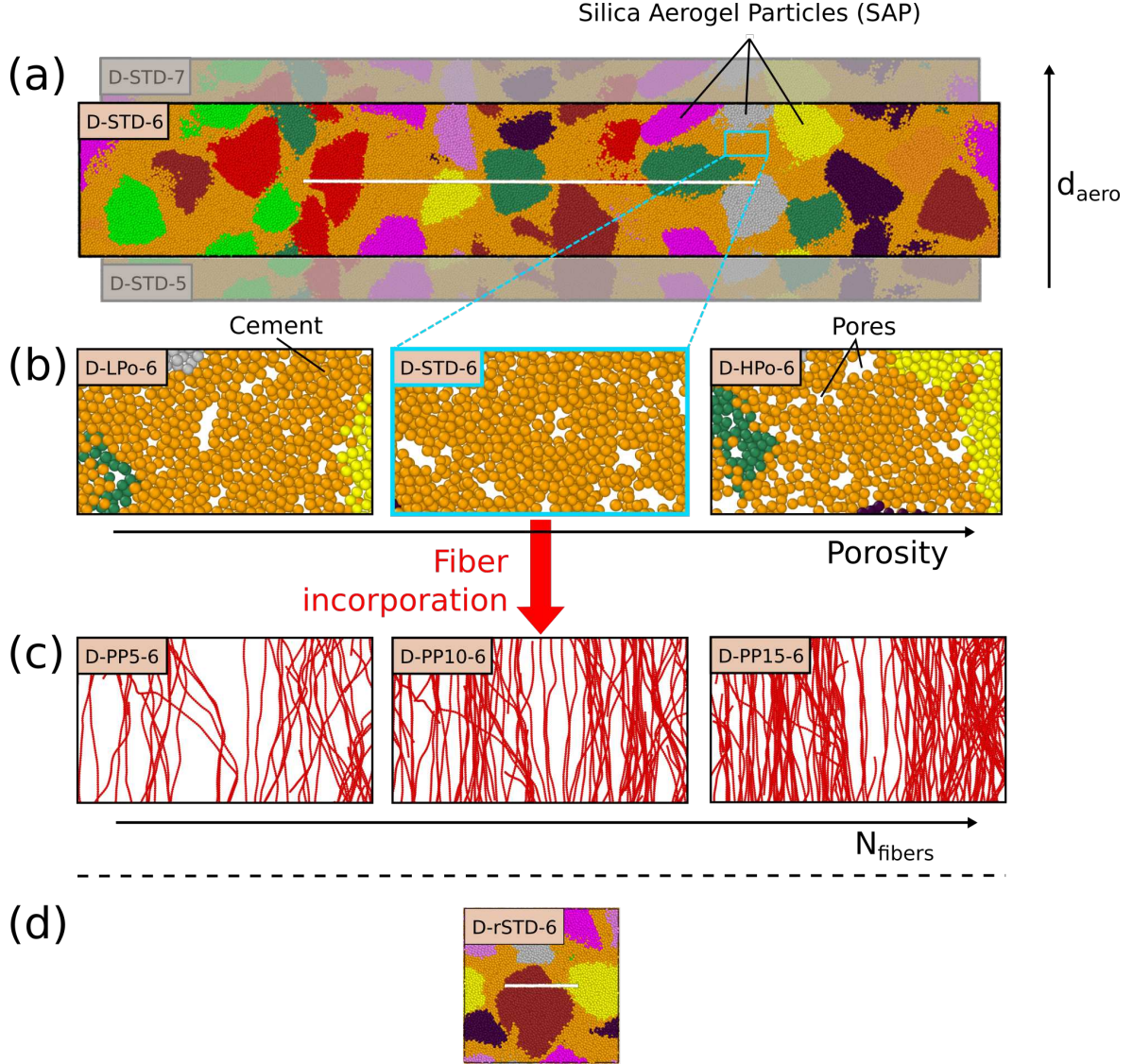


Figure 6.2: (a) Composites D-STD-5 to D-STD-7: increasing  $d_{aero} = \frac{f_{10-12}}{f_{aerogel}}$  ( $f_{10-12}$  and  $f_{aerogel}$  are volume fractions). The samples are notched in preparation for fracture toughness tests (see chapter 4, section 4.4.1.3). (b) Composites D-LPo-6 to D-HPo-6: increasing porosity. Thin slices of composite samples for visualisation purposes. (c) Composites D-PP5-6 to D-PP15-6: increasing fiber volume fraction. Components different from fibers are here invisible for visualisation purposes. (d) Reduced sample volume D-rSTD-6. Exact same composition than sample D-STD-6.

- Fibers volume fraction with a number of fiber aggregates varying between 369 and 1107, corresponding to a volume fraction varying between 0.05 % and 0.15 % (DEM composites D-PP5-6, D-PP10-6 and D-PP15-6), see 6.2c.
- DEM sample size with a volume six times smaller for composite D-rSTD-6 than for composite D-STD-6, see 6.2d.

Fig. 6.2a shows a typical sample D-STD-6 used for toughness tests. It is equipped with a notch as described in chapter 3 (see Fig. 15). Conditions are periodic in all three directions. As its name suggests, the DEM composite D-STD-6 has been generated to



model the experimental composite STD-6. While the composite D-PP10-6 attempts to simulate the experimental composite PP10-6, its structure differs from its experimental equivalent as the fibers has been perfectly dispersed and oriented with a maximum angle of  $20^\circ$  perpendicularly to the notch plan. In section 6.3.4 of this chapter we illustrate how this numerical structure is idealized compared to the state of the experimental PP10-6 composite samples. A sample D-rSTD-6 is generated and tested in order to check if the simulation results (elastic behaviour and fracture) converge once a certain sample volume is reached.

In chapter 4 we presented how the bonds between the discrete elements were calibrated. By defining these microscopic laws, the macroscopic behaviour and properties of the DEM composite samples can be retrieved as a result of the DEM model. The values of the calibrated microscopic properties are listed in Fig. 6.3.

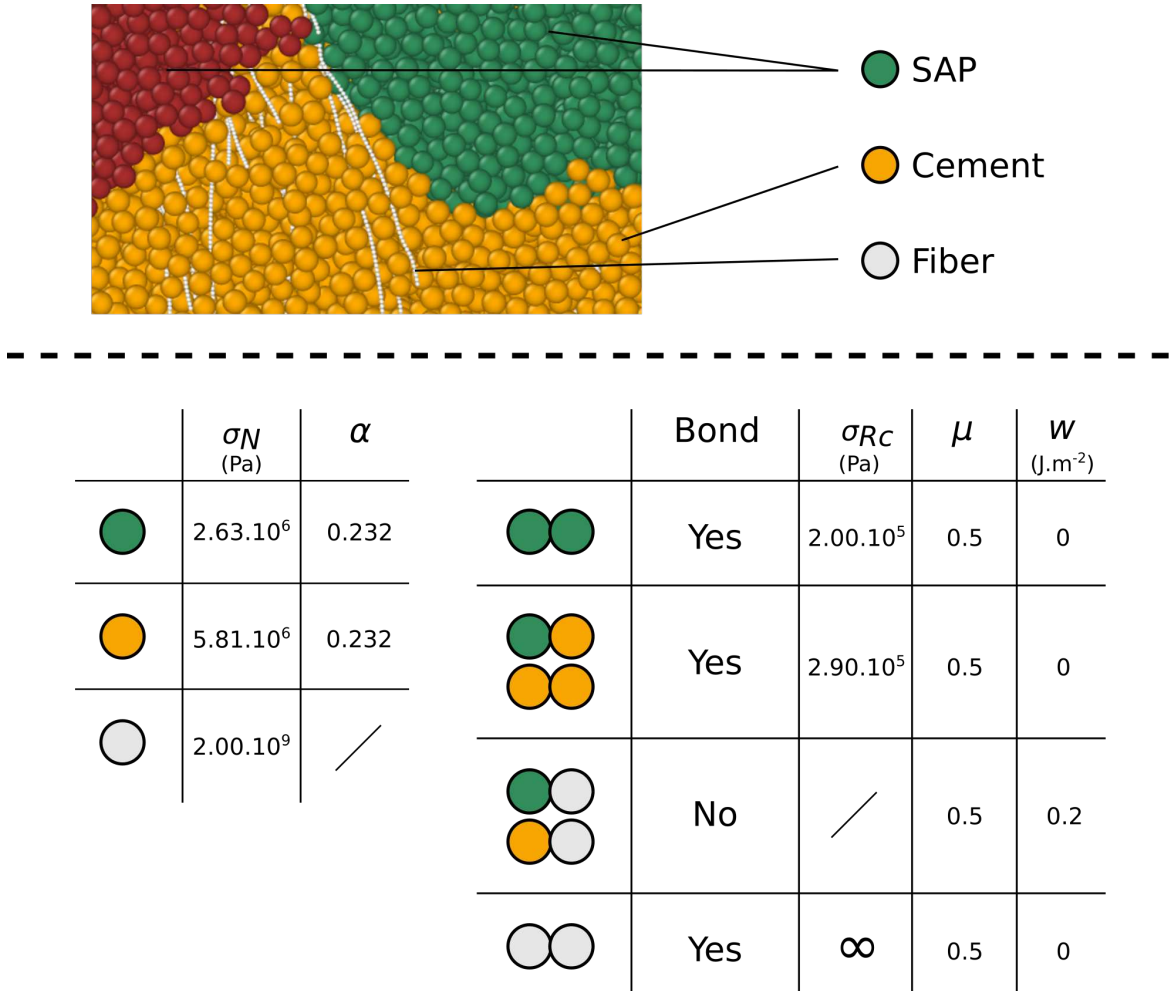


Figure 6.3: Calibration parameters of discrete elements properties: normal stiffness  $\sigma_N$  (Eq. 4.5) and stiffness ratio  $\alpha = \sigma_T/\sigma_N$ . Calibration parameters of the bonds between discrete elements: Critical Rankine strength  $\sigma_{Rc}$  (Eq. 4.15), friction coefficient  $\mu$  (Eq. 4.14), and work of adhesion  $w$  Eq. 4.11). Bond stiffnesses are calculated from particle stiffness by Eq. (5). These parameters are kept constant for all composites.

These values will be discussed later with the corresponding experimental results which allowed their calibrations. However, we can already point out that:



- The cement and the silica aerogel particles exhibit mechanical properties that are of the same magnitude. Still, the cement phase is clearly stiffer and somewhat stronger than the silica aerogel particles themselves. Fibers are several orders of magnitude stiffer than either the cement or the aerogel particles.
- Several simplifying assumptions have been made concerning the modelling of fibers in the DEM composites. Fibers are ideally dispersed while we have observed bundles of fibers experimentally (see Fig. 4.15, chapter 4). Fibers are quite well aligned in the simulation while it is not so clear from experimental observations. Fibers are not allowed to break.

## 6.3 Silica aerogel particulate composite structure

The composite cross-sections shown in this chapter were generated using a laboratory X-ray tomograph and the European Synchrotron Radiation Facility (ESRF). Refer to chapter 3 for the corresponding imaging and post-processing protocols (3.1.1.2).

The structure of the particulate silica aerogel composites STD-6, STD-7 and STD-0 can be divided into three different phases: silica aerogel particles, binder and pores. These different phases are illustrated in Figure 6.4 for a STD-6 sample.

### 6.3.1 Porosity

Pores between aerogel particles are inherent to the current fabrication process of the composites. Although some tests were carried out by EDF company, aiming to reduce the porosity by applying a pressure on wet samples during the drying step of the fabrication process, they did not prove sufficient to get rid of these macropores [63]. A. Perret et al. showed nonetheless that changing the surfactant molecule has a substantial influence on the pore size distribution [29].

Two pore sizes can be identified in Fig. 6.4a and 6.4b. The largest pores are forming between the large 10-12 silica aerogel particles and are generally larger than 50  $\mu\text{m}$ . Their presence seems to be associated to large silica aerogel particles as they are consistently in contact with at least one of these particles. It can be explained by the "wall effect", particularly well observed in concretes, and corresponding to a smaller compactness at the contact with the largest particles [123]. Moreover, no pore of such size has been observed fully immersed in the cement phase. We chose to consider the smallest pores, generally smaller than 50  $\mu\text{m}$ , as a component of the cement phase. Composite porosity have been estimated by processing X-ray tomography images, although the low contrast between silica aerogel particles and air only allowed a rough estimation of this quantity. The global macro-porosity (pores  $> 50 \mu\text{m}$ ) of the STD-6 composite samples has been measured at  $15 \pm 5\%$  using laboratory X-ray tomography images. This measure is consistent with the value of  $13 \pm 1\%$  measured by A. Perret et al. [29] on the same composites using the same method on X-ray tomography cross-sections with better image quality. The micro-porosity specifically contained in the cement phase (pores smaller than 50  $\mu\text{m}$  pointed in Fig. 6.4b) has been estimated

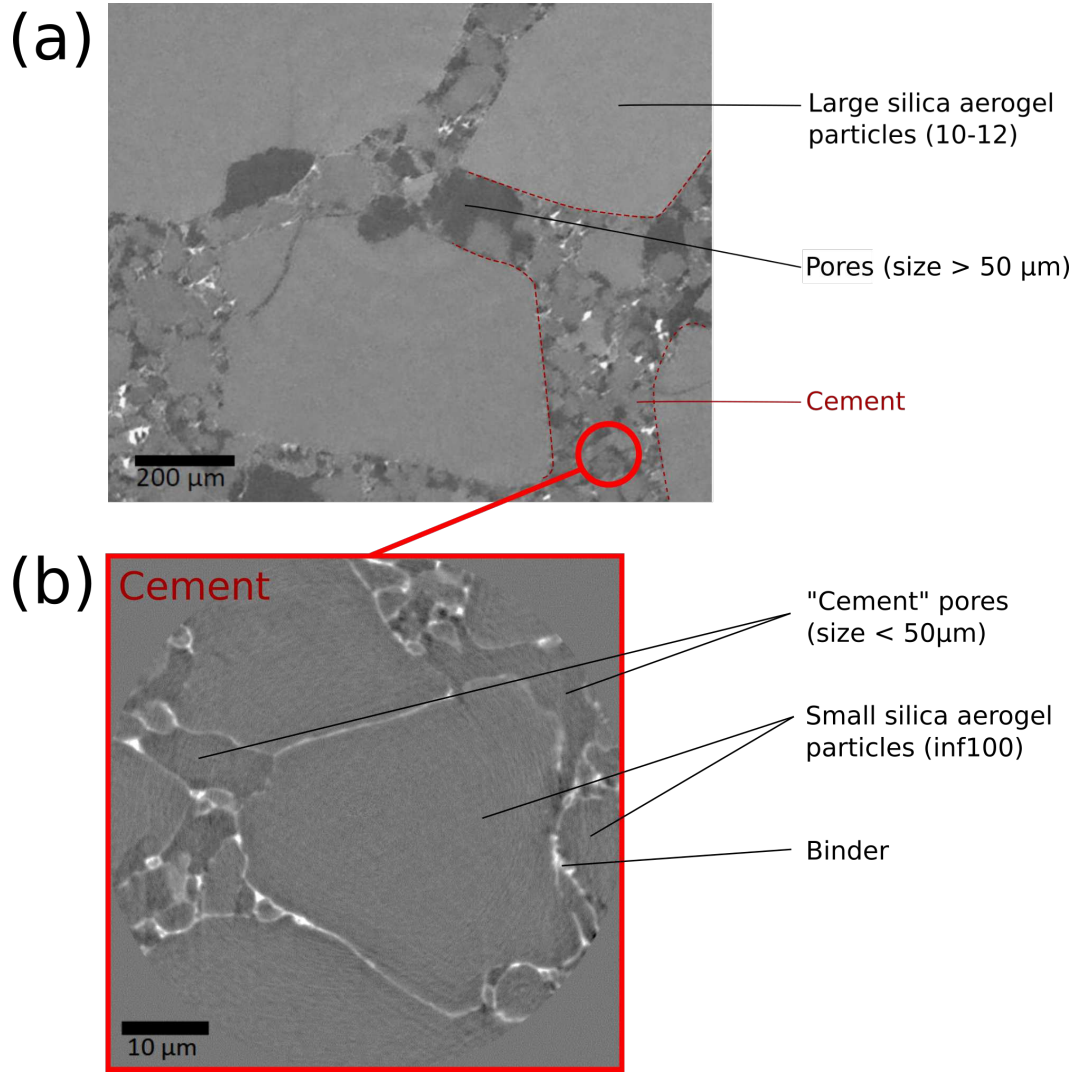


Figure 6.4: X-ray tomography cross-sections illustrating the core of a  $20 \times 20 \times 80 \text{ mm}^3$  STD-6 composite sample. From darkest to lightest gray levels: pores, silica aerogel particles and binder. (a) Laboratory X-ray tomography cross-section. (b) Synchrotron X-ray tomography cross-section.

at  $10 \pm 3\%$  using synchrotron X-ray tomography images (so there is 4% micro-porosity globally in the composite), indicating that macro-pores induced by the presence of large 10-12 silica aerogel particles (pointed in Fig. 6.4a) represent more than the half of the global porosity of the composite (see Table 6.3 for complete STD-6 composite composition).

As explained in chapter 4 (section 4.4.1.1) two pore sizes have been introduced in DEM particulate composites in order to reproduce the bimodal pore size distribution observed experimentally. While discrete element aggregates containing approximately 20 discrete elements have been generated to represent the pores larger than 100 μm, the smaller macro-pores are represented by individual discrete elements (diameter=50 μm) (see Fig. 6.5). These pore aggregates and discrete elements are removed from the DEM samples once the preparation stage is over (see chapter 4, section 4.4.1.3).

By introducing pores as material objects in the DEM composite packing, the total

Table 6.3: Composition of a STD-6 composite sample, taking into account the inter-particle porosity. Macro-pores are larger than 50  $\mu\text{m}$ .

Phase	vol%
Large 10-12 SAP	49%
Small inf100 SAP	34%
Binder	2%
Macro-pores	11%
Micro-pores	4%

Figure 6.5: Aggregates and individual discrete elements used during the preparation of DEM particulate composites. The presence of aggregates and individual spheres allows the introduction of a bimodal pore size in the DEM samples.

porosity and pore size distribution can be easily tuned by changing the volume fraction of these components. Thus, the influence of porosity on the macroscopic mechanical properties of the DEM composites can be easily studied.

### 6.3.2 Binder

A proper distribution of the polymer binder (latex SBA and surfactant XPCAS, see chapter 3 section 3.3) is an important parameter for the mechanical performances of silica aerogel particulate composites. Still, its volume fraction must remain as small as possible as the binder percolating network forms a thermal bridge from one face of the composite insulating panel to the other (see chapter 2, section 2.3.5.1).

The cross-section illustrated in Fig. 6.4b suggests that the binder is well distributed all over the aerogel particle surface in the core of a STD-6 composite sample. While the continuous distribution of the binder on the silica aerogel particles surface might be detrimental to the thermal performance of the particulate composites, it is a structural advantage for their mechanical performances. The continuous distribution of the binder has been confirmed using SEM images. These images have been obtained from the fracture surface of a STD-6 composite sample submitted to SENB flexural tests (see chapter 3 sections 3.4.3) and are showed in Fig. 6.6. In these images we can see a continuous layer of binder covering the silica aerogel particles, particularly in Fig.

**6.6b.** The thickness of the binder layers vary between 20 and 100 nm. Fig. **6.6c** illustrates a fractured silica aerogel particle with binder layers teared up during fracture. This suggests that the binder-particle interface is not a structural weakness in STD-6 composites. This point will be confirmed further in this chapter while analysing the results of DCDC tests (see section **6.5.1.1**).

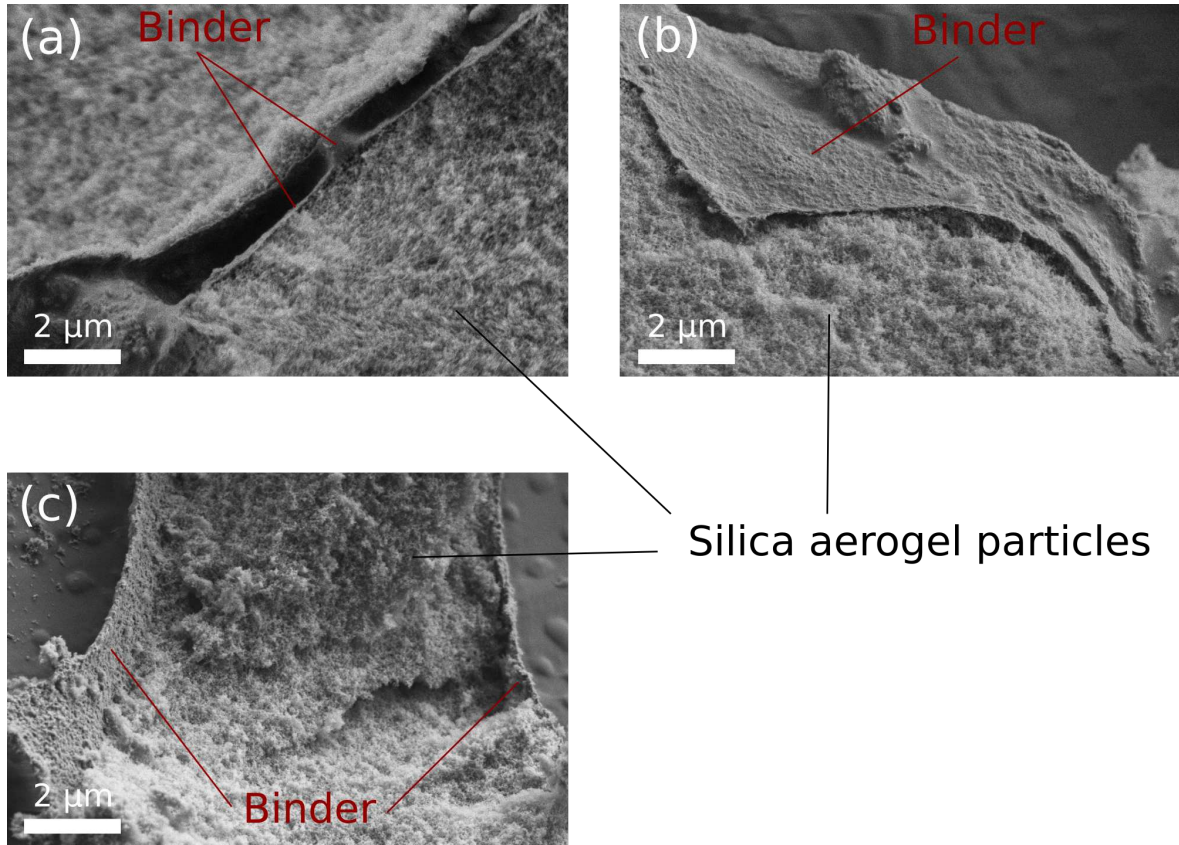


Figure 6.6: SEM images of a fractured surface from a STD-6 composite sample, EHT = 1 kV. (a) Interface between two silica aerogel particles bonded together. (b) Layer of binder on the surface of a silica aerogel particle. (c) Two layers of binder around the broken remains of a silica aerogel particle.

### 6.3.3 Fibers

The preparation process of the composites containing fibers necessitates both experimental and numerical adjustments as explained in chapters **3** and **4** (see **3.3.2** and **4.4.1.2**). Experimentally, the fibers are brought in contact with a fraction of the aqueous solution containing the binder to facilitate their incorporation into the composite and to facilitate bonding with silica aerogel particles. The targeted structure of the fiber-containing composites has well dispersed fibers, oriented perpendicular to the thickness of the composite panels in order to maximize the mechanical reinforcement while minimizing the presence of thermal bridges.

While the current preparation protocol is overall satisfactory, the final distribution of fibers in the microstructure varies with the nature of the fibers, as we will discuss now.



The main obstacle to the homogeneous distribution of fibers in the composites is their affinity to each other which can result in the formation of bundles even if the fibers are properly separated before their incorporation. A typical example of a poor fiber distribution is illustrated in Fig. 6.7a in the case of glass fibers (G-6 composites). In this example, we can see several thousands of fibers bundled together. On the contrary, PP10-6 composite samples present satisfactory fiber distribution as shown in Fig. 6.7b. However, the resolution of these X-ray CT scans is too low to analyse fiber orientation.

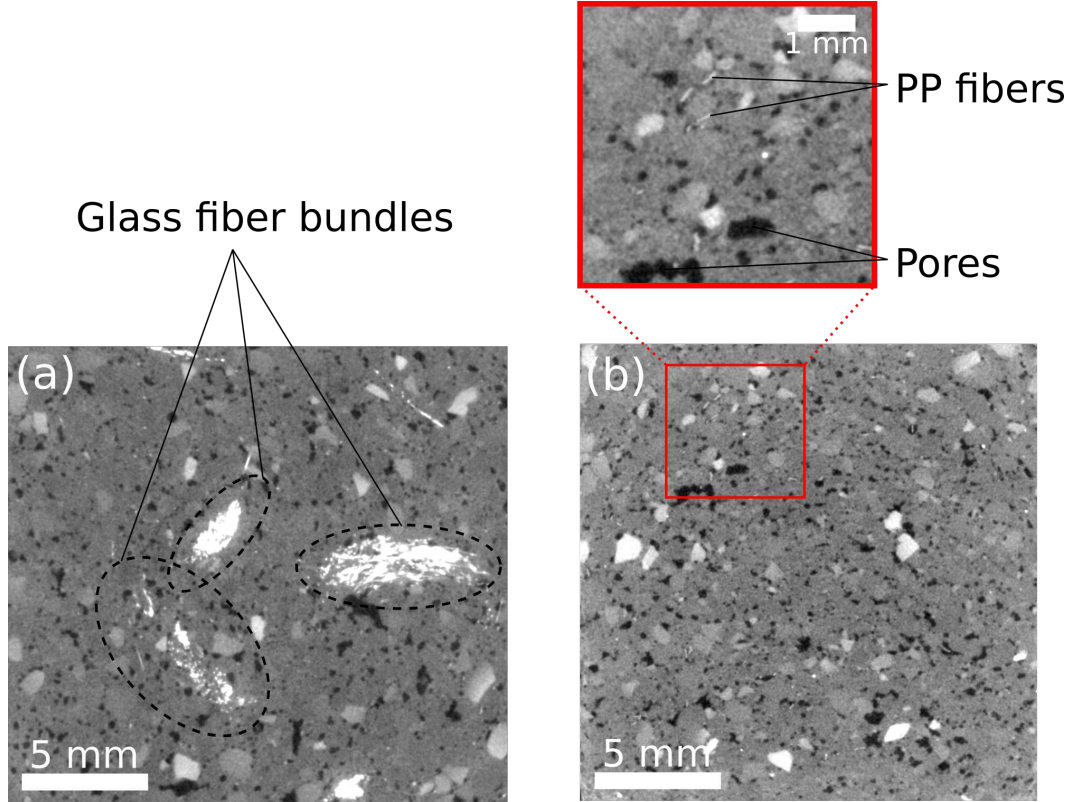


Figure 6.7: X-ray tomography cross-sections of silica aerogel particulate composites. (a) Glass fiber composite (G-6). (b) Polypropylene fiber composite (PP10-6).

Another difficulty noted while incorporating fibers in composites is the appearance of drying-induced cracks in the samples. Such cracks are not acceptable both for mechanical and thermal performances of the material. During drying of the wet composites, water evaporation induces a shrinkage gradient in the composite samples. Some of the fibers tested in this work seem to hinder partially this phenomenon, which results in the appearance of cracks of different dimensions depending on the nature of the fibers. Such cracks were found in PET fiber composites (PET-6) and in some of the glass fiber composites (G-6) and are illustrated in Fig. 6.8b. While similar cracks may be observed in composites STD-6 and PP10-6 (respectively shown in Fig. 6.8a and 6.8c), the phenomenon is much less severe.

In the context of this thesis, it was chosen not to further investigate the origins of drying-induced cracks or the reason why some fibers cluster in bundles and not others. Indeed, this would lead to a complete study of the surface chemistry of the fibers and their affinity with silica aerogels and binders, which are not the topics to be developed

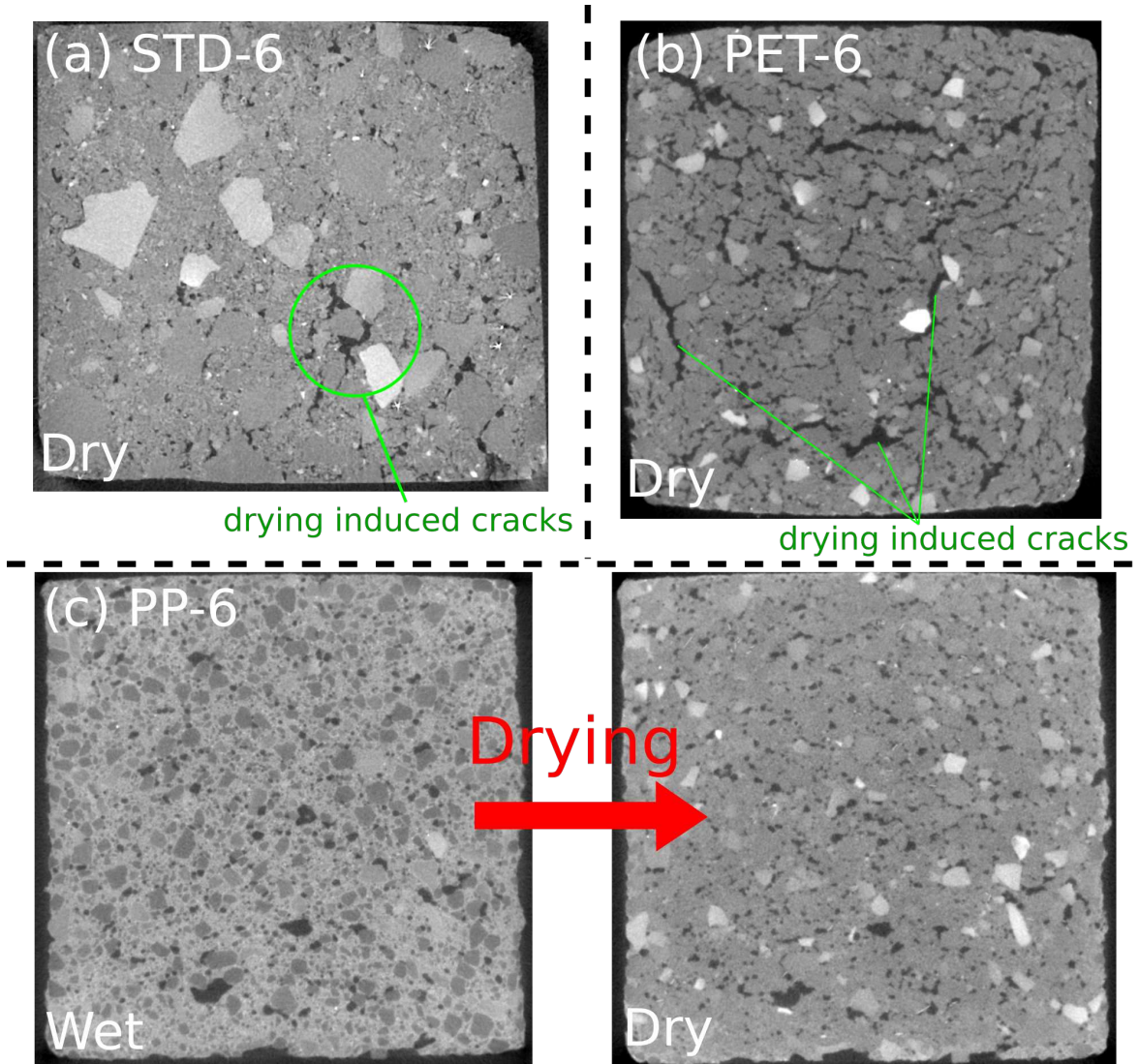


Figure 6.8: X-ray tomography cross-sections of silica aerogel particulate composites, 25  $\mu\text{m}$  resolution. (a) STD-6 sample dried at 40  $^{\circ}\text{C}$  40% relative humidity during 24 hours. (b) PET-6 sample dried at 40  $^{\circ}\text{C}$  40% relative humidity during 24 hours. (c) PP10-6 sample dried at 40  $^{\circ}\text{C}$  40% relative humidity during 10 minutes and 24 hours. The large 10-12 silica aerogel particles are darker than the cement while the samples are wet because all the water is located in the cement and, thus, rise its X-ray absorption.

here. For this reason, once it has been identified that PP fibers are well distributed in the particulate composites and do not induce the appearance of cracks during the drying of the samples, it has been decided to carry out most of the experimental tests and further analysis for the STD and PP10-6 composites.

### 6.3.4 Polypropylene fibers

The polypropylene fibers used for the preparation of PP10-6 composite samples originate from a batch initially intended to be incorporated in concretes in order to improve their fire resistance. Their shape and dimensions are variable and very different from simple cylindrical objects. SEM imaging has been carried out on PP fibers, for some

of them already incorporated inside the composite matrix. The corresponding SEM images are shown in Fig. 6.9. While some fibers have a circular section like the ones illustrated in Fig. 6.9a and 6.9c, the majority of the fiber volume incorporated in the composites exhibits more irregular shapes like the fiber in Fig. 6.9b. These fibers can also take the form of larger objects like the one showed in Fig. 6.9d. In this last case, these large PP blocks do not originate from the regrouping of smaller fibers in the form of bundles like what has been observed for glass fibers. X-ray tomography scans using a synchrotron source (ESRF, Grenoble, France) showed that these objects have an homogeneous composition and their shape originate directly from their manufacturing process. For example, a block illustrated using holotomography (synchrotron source) is showed in Fig. 6.10a and displays a rectangular section of  $50 \times 400 \mu\text{m}^2$ .

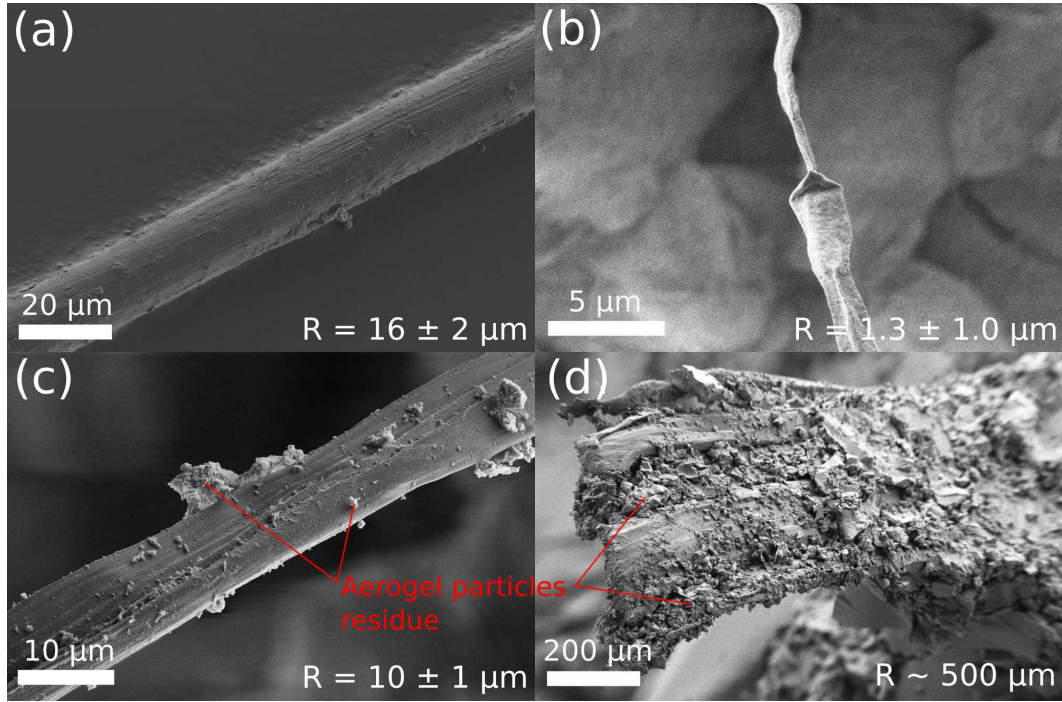


Figure 6.9: Different PP fibers observed using SEM. (a) One of the scarce PP fibers with a circular section present in the batch. (b) Single 1  $\mu\text{m}$  PP fiber with an irregular shape. (c) Single PP fiber pulled out from the composite matrix. (d) Large block of PP pulled out from the composite matrix.

We discussed in section 6.3.2 the effectiveness of the binder covering the silica aerogel particles, but the question is raised whether the same binder is also capable of binding the PP fibers and the silica aerogel particles together. Fig. 6.10b gives some hints in this regard as thin binder layers (in white in the figure) are present at the interfaces between silica aerogel particles and PP fibers. The surfaces of the PP fiber were observed using SEM in order to further examine the affinity of the binder with the fibers. The fiber surfaces observed result either of pulled out fibers from a composite matrix or fibers impregnated with a solution containing the binder. The corresponding SEM images are shown in Fig. 6.11. Before any binder is put in contact with the PP fibers, their surface aspect is rough with linear trenches all oriented along their length as illustrated in Fig. 6.11a. These trenches completely disappear for the fibers



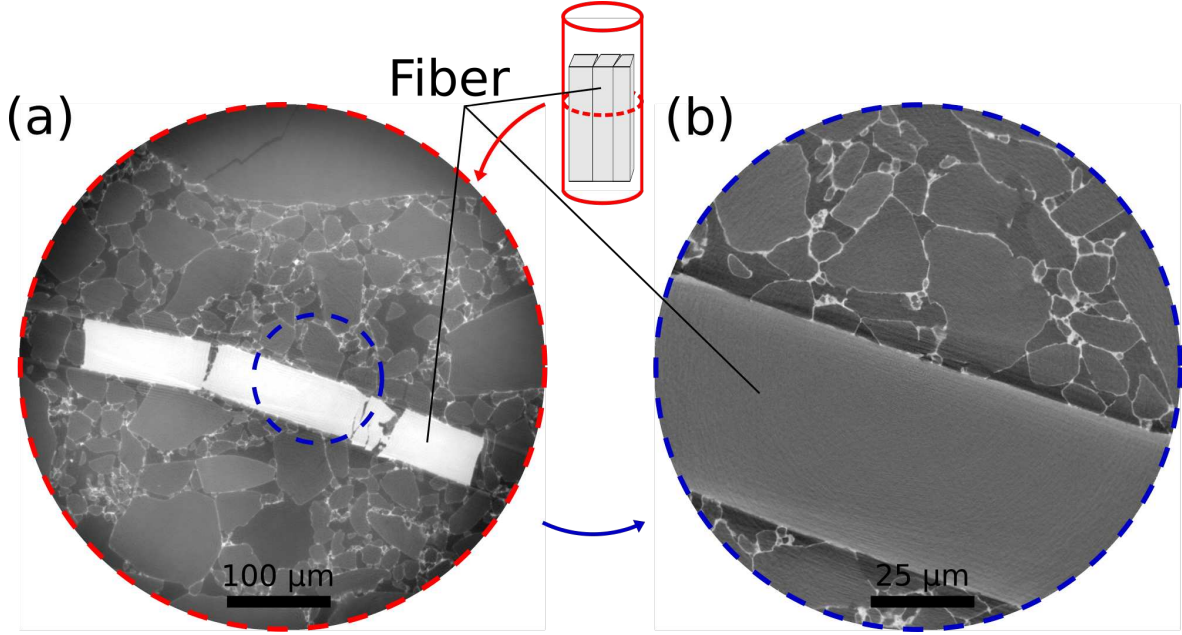


Figure 6.10: X-ray tomography cross-sections of a PP block embedded in the composite matrix of a PP10-6 composite sample. (a) 200 nm resolution. (b) 50 nm resolution.

impregnated with a binder solution. Fig. 6.11b shows that these fibers are continuously covered by a binder layer and, in some areas, pockets of binder in excess are formed. The presence of these pockets suggests that too much binder has been brought into contact with the fibers and that excess binder forms pockets before the solution is fully dry. These pockets are also observed on fibers pulled out from a PP10-6 composite matrix as showed in Fig. 6.11c. We can thus safely conclude that the binder, initially chosen to bind together silica aerogel particles, is compatible and efficient with the PP fibers used in this work. Moreover, the binder pockets on the surface indicate that enough binder is introduced during the silica aerogel particulate composite preparation.

## 6.4 Composites elastic behaviour

### 6.4.1 Experimental results

#### 6.4.1.1 Indentation

Particulate composites have been indented using spherical tips by following two different procedures described in chapter 3, section 3.4.1. These tests allowed the Young's modulus  $E$  to be measured as summarized in Table 6.4. Using a micro-indenter (measures with a contact radius larger than a millimeter), while the Young's modulus values are similar for composites STD-6, STD-7 and PP10-6, composite STD-0 exhibits a higher value. This highlights the influence of the binder on the elastic behaviour of the composites as there is 2.5 times more binder in STD-0 composites compared to the others. With nano-indentation tests, we can also note that the Young's modulus of the 10-12 particles is lower than the one of STD-6 and STD-7 composites, while the Young's modulus of the cement is larger than the one of STD-6 and STD-7 composites.

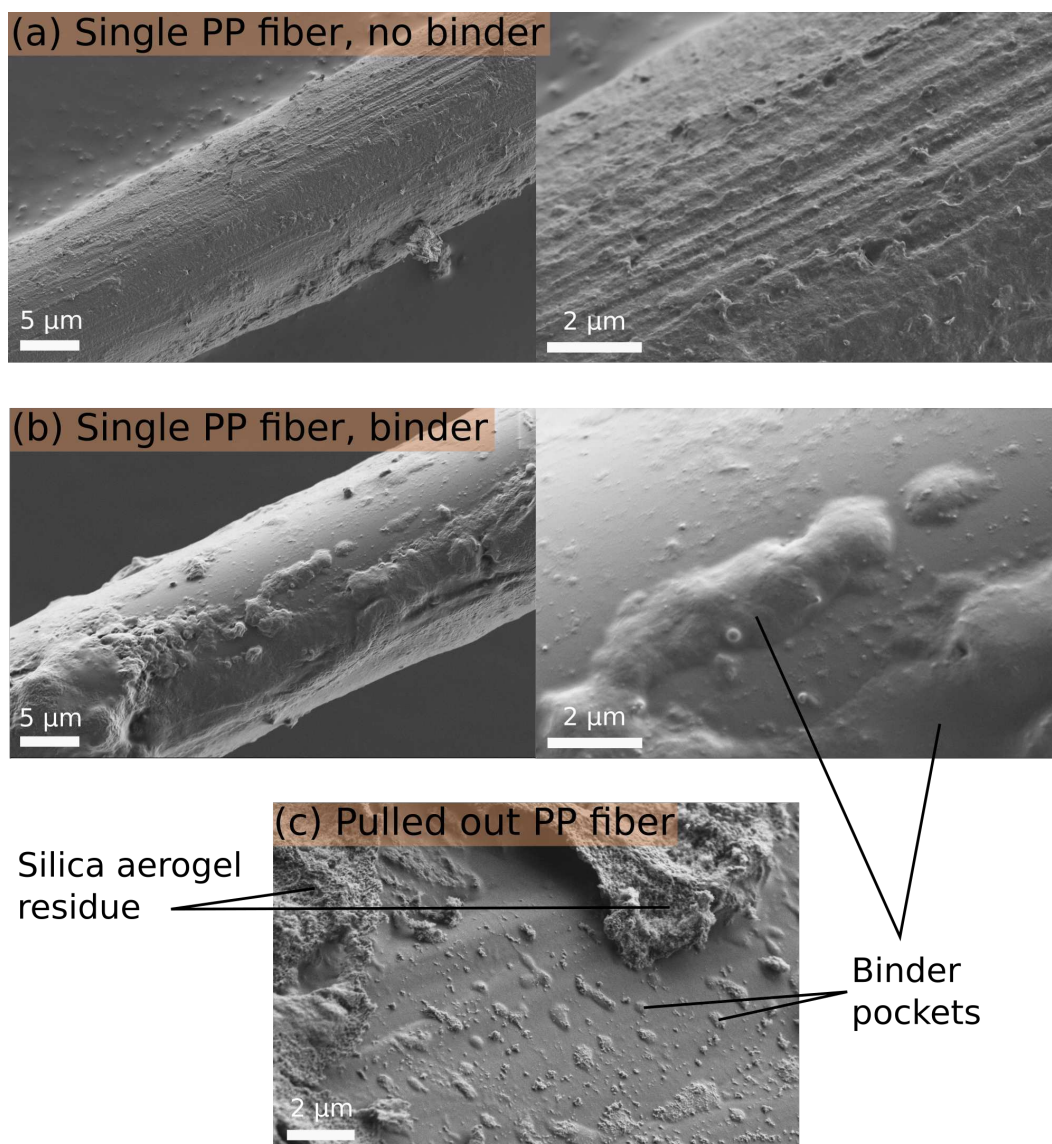


Figure 6.11: (a) Single cylindrical PP fiber without any binder. The trenches observed on the surface are typical for the PP fibers studied in this work. (b) Single cylindrical PP fiber, first impregnated with a solution containing the binder and then dried at ambient pressure and temperature. (c) PP fiber surface pulled out from the composite matrix of a PP10-6 composite sample.

A typical indentation curve is shown in Fig. 6.12a and illustrates how most of the deformation induced during the loading of the tip is reversible during unloading. We can note the presence of relaxation during the dwell between the loading and the unloading phase. Still, the loading and unloading curves do not overlap (hysteresis), indicating that some energy is dissipated during the test. This behaviour is very similar to that observed in the case of silica aerogel monoliths. Fig. 6.12b originates from a Kucheyev et al. study concerning spherical tip indentation on silica aerogel monoliths [124]. Kucheyev suggests that this phenomenon could be related to the formation of cracks that close upon complete unloading, Van der Waals interaction between nanoligaments, dissipative motion of the air filling the nanopores, or a combination of the three.

Some STD-6 samples have been tested for different indenter velocities. The corre-

Table 6.4: Young's modulus  $E$  measured through indentation tests. Two different methods are used (indenter and nano-indenter, see chapter 3 section 3.4.1), leading to different contact surfaces  $A$  with a contact radius  $R_c$ .

Name	Method	$R_c$ (mm)	Number of tests	$E$ (MPa)
STD-6	indenter	1.4	20	$1.9 \pm 0.1$
STD-7	indenter	1.4	10	$1.9 \pm 0.1$
STD-0	indenter	1.4	10	$2.3 \pm 0.2$
PP10-6	indenter	1.4	10	$2.0 \pm 0.2$
10-12 particles	nano-indenter	0.12	3	$1.6 \pm 0.6$
Cement	nano-indenter	0.12	3	$2.5 \pm 0.3$

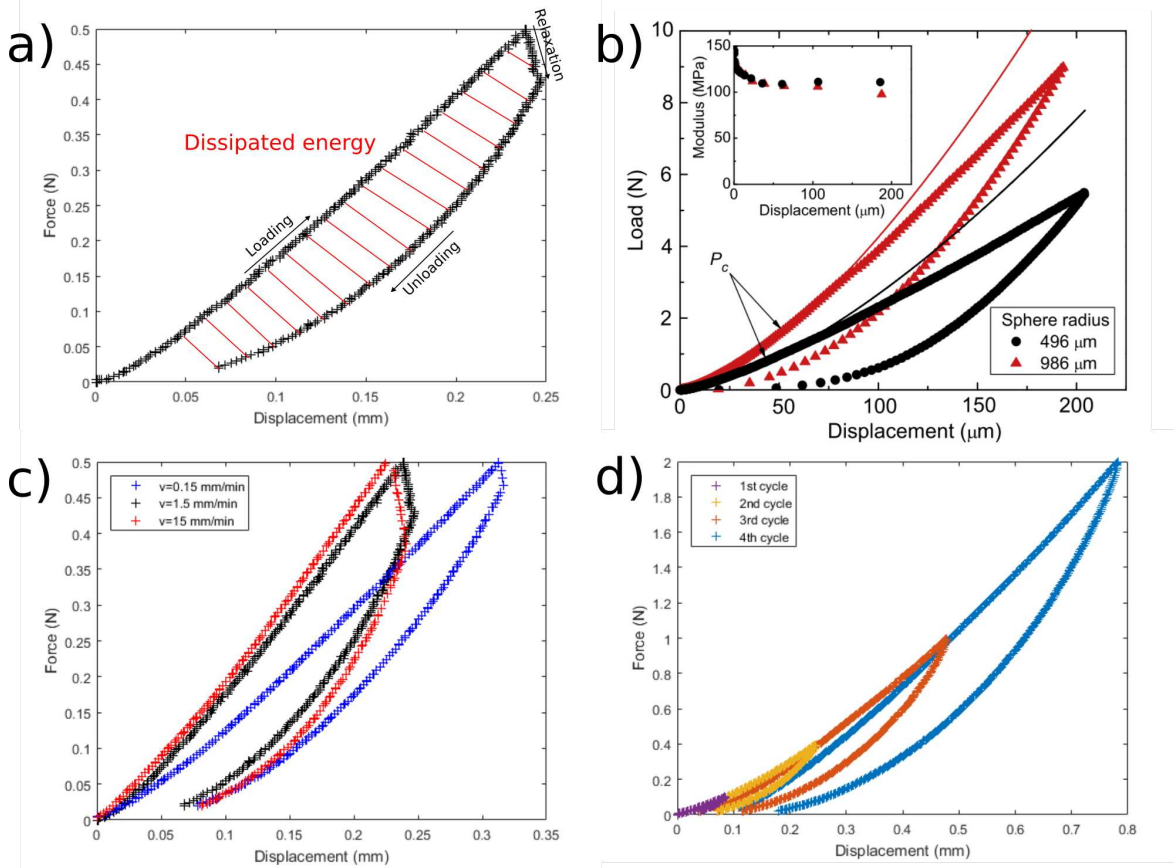


Figure 6.12: Instrumented indentation, spherical tip. (a) Single cycle on STD-6 composite sample. (b) Indentation curves from Kucheyev et al. [40]. These silica aerogels are denser than the one used in this work ( $\rho = 340 \text{ kgm}^{-3} > 100 \text{ kgm}^{-3}$ ). (c) Different crosshead velocities for a same STD-6 composite sample. (d) Multiple loading cycles on a STD-6 composite sample.

sponding curves are shown in Fig 6.12c. Although no differences have been detected for the Young's modulus (measured at the start of the unloading stage) and the hardness for these velocities, it can be observed that the shape of the curves is modified as higher displacements of the indenter are reached for low velocities. The energy dissipated in the process also decreases slightly.

In an attempt to understand if samples are damaged during indentation tests, some cyclic loadings and unloadings were carried out on a STD-6 sample (with no dwell between the loading and unloading phases). The corresponding curves are shown in

Fig. 6.12d. The loading section of the different cycles perfectly for the two first cycles. Further cycles lead to some irreversible plastic deformation. After four cycles with increasing maximum load (max load of the last cycle is 2 N), an imprint 200  $\mu\text{m}$  deep remains while it is only 70  $\mu\text{m}$  deep for standard indentation tests (max load 0.5 N, see Fig. 6.12a).

The characterization of STD-0 composite samples allowed the calibration of the elastic behaviour of the cement phase in DEM composite simulations following the procedure described in chapter 4, section 4.4.3. The similar Young's modulus values measured at two different scales for composite STD-0 and the cement phase confirms that the structure and porosity of STD-0 composite samples is similar to the cement phase contained in STD-6 and STD-7 composites, as intended during their preparation.

#### 6.4.1.2 Uniaxial compression

The Young's modulus has also been calculated from uniaxial compression tests on cylindrical particulate composite samples. These samples were prepared and tested following the procedures described in chapter 3, section 3.4.2. The results are summarized in Table 6.5. Similarly to the values measured during indentation tests, no differences are measured between the Young's modulus of composites STD-6, STD-7 and PP10-6. The values measured during uniaxial compression are lower than those measured with instrumented indentation (approximately 40% lower than during indentation tests) but the order of magnitude of the Young's modulus stays around 1-2 MPa.

Table 6.5: Young's modulus measured through experimental uniaxial compression tests.

Name	Number of tests	$E$ (MPa)
STD-6	6	$1.2 \pm 0.1$
STD-7	6	$1.0 \pm 0.1$
PP10-6	6	$1.1 \pm 0.1$

#### 6.4.2 DEM results

The Young's modulus of DEM composites have been measured numerically by uniaxial compression on samples without any notch. The stiffness  $C = \frac{2F_f}{\epsilon_f S} \times \frac{L}{a}$  of DEM notched composite samples have also been measured during the same tensile tests used for the measurement of the fracture toughness ( $F_f$  is the fracture force,  $\epsilon_f$  is the fracture strain,  $S$  is the section area of the samples in notch plan,  $L$  is the length of the notched samples and  $a$  is the length of the notch). The corresponding results are listed in Table 6.6 and summarised in Fig. 6.13.

The Young's modulus and normalized force of all samples exhibit similar values. This is because the introduction of a notch does not modify drastically the microstructure in the elastic region. In any case, Table 6.6 indicates that  $C$  is consistently smaller or equal than  $E$ , as it should.



Table 6.6: Young's modulus  $E$  of DEM composites tested by uniaxial compression and stiffness  $C$  of DEM notched composite samples tested in tension.  $C$  is obtained from large strains in tension (roughly 0.06) while  $E$  is obtained at 0.001 strain in compression. Standard deviations are computed from the number of samples ( $E$ ) or from the total number of different locations of notches for all samples ( $C$ ).

Name	Number of samples	$E$ (MPa)	Number of notches	$C$ (MPa)
D-STD-5	2	$1.25 \pm 0.03$	3+3	$1.2 \pm 0.1$
D-STD-6	5	$1.15 \pm 0.02$	3+3+2+2+2	$1.1 \pm 0.1$
D-STD-7	2	$1.03 \pm 0.03$	3+3	$1.0 \pm 0.1$
D-LPo-6	1	1.34	3	$1.3 \pm 0.1$
D-HPo-6	1	1.00	3	$1.0 \pm 0.1$
D-PP5-6	1	1.50	3	$1.5 \pm 0.1$
D-PP10-6	1	1.85	3	$2.0 \pm 0.1$
D-PP15-6	1	2.35	3	$2.5 \pm 0.1$
D-rSTD-6	1	1.47	3	$1.3 \pm 0.2$

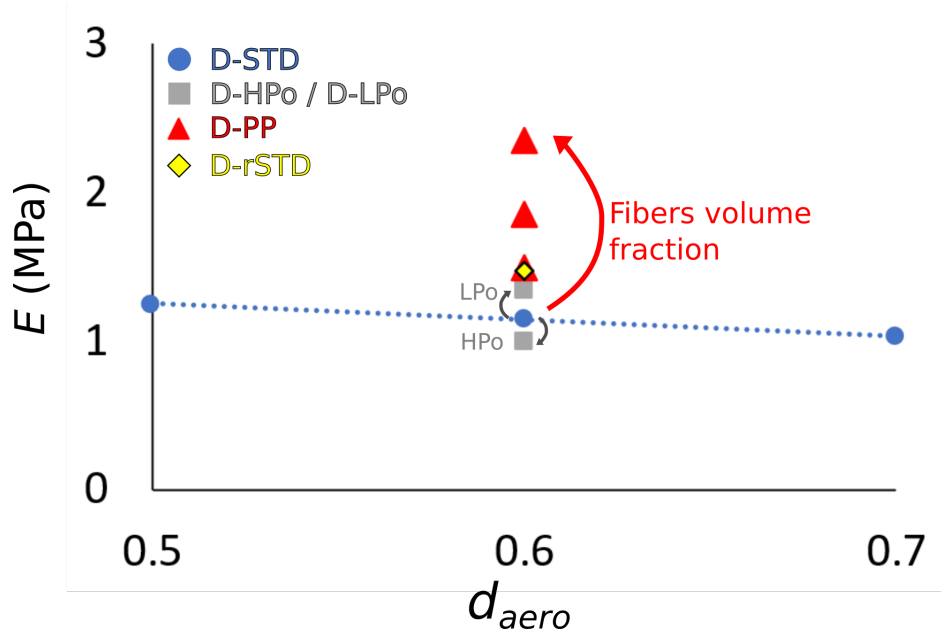


Figure 6.13: Young's modulus  $E$  evolution with the variation of the different parameters tested in the DEM model: cement volume fraction (D-STD), porosity (D-HPo / D-LPo), fiber volume fraction (D-PP, 0.05, 0.1 and 0.15%) and sample volume reduction (D-rSTD).  $d_{aero} = \frac{f_{10-12}}{f_{aerogel}}$  ( $f_{10-12}$  and  $f_{aerogel}$  are volume fractions).

We can see that increasing the porosity (D-LPo-6 to D-HPo-6) or decreasing the cement volume fraction (D-STD-5 to D-STD-7) reduces the stiffness of the composites. This last evolution was predictable given that the stiffness of the cement has been calibrated to a higher value than the one of silica aerogel particles. The embedding of fibers has a greater impact on the Young's modulus compared to all other parameters studied in the DEM model as it almost double  $E$  when the fiber volume fraction is tripled (D-PP5-6 to D-PP15-6, see Fig. 6.13). We note that the reduced sample (D-rSTD-6) exhibits both higher stiffness and Young's modulus than its larger counterpart (D-STD-6). This indicates that caution needs to be taken to have a sufficiently large

numerical sample to have a representative volume element. Since all other samples (not reduced) have the same volume they can be compared with each other.

### 6.4.3 Discussion

While the Young's modulus values obtained experimentally through uniaxial compression are close to the ones obtained using DEM, at least for non-fibrous composites, the results obtained through indentation are almost twice as high as shown in Fig. 6.14. The two experimental methods have their strong and weak points:

- While the uniaxial compression method allows to analyze the full volume of a cylinder containing hundreds of large 10-12 silica aerogel particles, the indentation method analyzes a limited volume containing around 10 large particles.
- Much more measurements have been done with the indentation method which provides more reliable statistics compared to uniaxial compression.

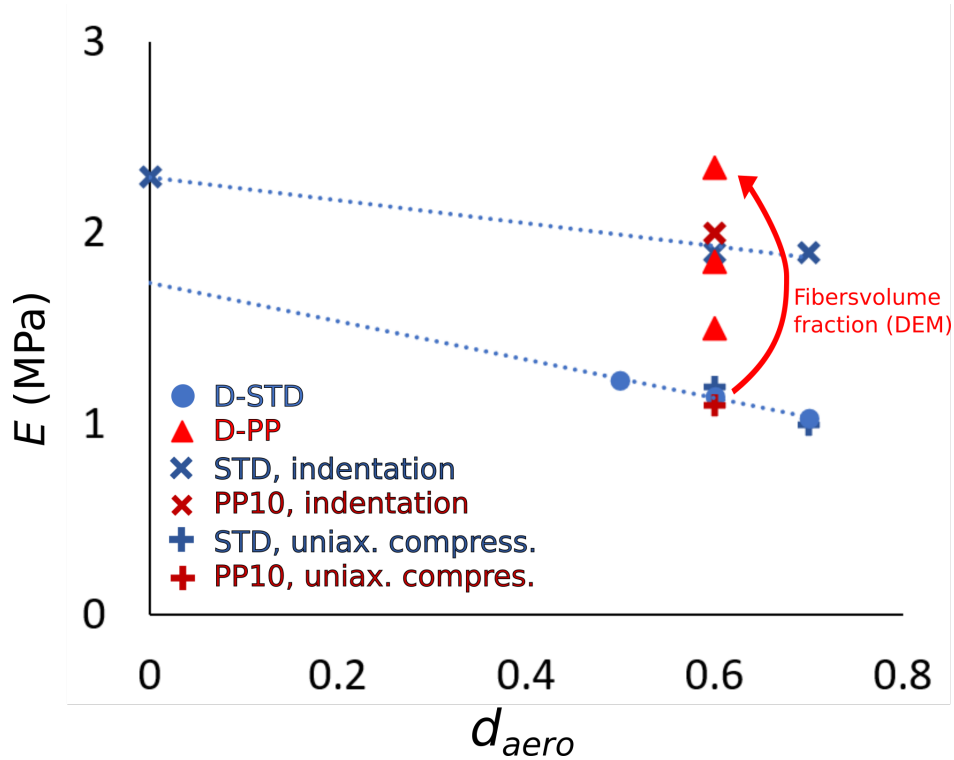


Figure 6.14: Young's modulus  $E$  evolution with the variation of the different parameters tested experimentally and in the DEM model: cement volume fraction (D-STD) and fiber volume fraction (D-PP).  $d_{aero} = \frac{f_{10-12}}{f_{aerogel}}$  ( $f_{10-12}$  and  $f_{aerogel}$  are volume fractions)

The elastic behaviour of the cement phase in DEM simulations has been calibrated based on the Young's modulus measurements of samples STD-0 using the indentation method. This choice has been dictated for practical reasons. The full DEM composite elastic behaviour is in better agreement with the compression tests than with the indentation tests. The reason for this result is not clear at this point.

When comparing the Young's modulus obtained through experimental uniaxial compression and through DEM simulations, we can conclude that the values match for non-fibrous composites (D-)STD-6 and (D-)STD-7. The slight decrease in the values when the cement volume fraction decreases from samples (D-)STD-6 to (D-)STD-7 is even observed in both cases (20% experimentally and 12 % in simulations, see Fig. 6.14). It is different, though, for the PP10-6 composite (corresponding to the D-PP10-6 DEM composite), with a Young's modulus much higher in simulations than experimentally. This can be explained by the fact that the Young's modulus is measured numerically by compressing samples along the preferential orientation axis of the fibers while this orientation is difficult to control experimentally. X-ray tomography scans carried out in this work did not allow to provide quantitative or even reliable qualitative information on the fibers orientation in experimental composites but we can safely assume that the orientation dispersion is higher experimentally than the 20° maximum disorientation angle imposed for DEM composites D-PP.

## 6.5 Composite fracture behaviour

### 6.5.1 Experimental results

#### 6.5.1.1 DCDC tests

Double Cleavage Drilled Compression (DCDC) tests carried out in this work are particularly complex to analyze quantitatively because of the limits in sample dimensions imposed by the X-ray tomograph set-up used for these tests (see chapter 3, section 3.4.4 for full sample preparation and testing protocols). The tests carried out inside the X-ray tomograph aimed to provide information on the propagation path of cracks in STD-6 composites. One of the main interests of DCDC tests is the stable propagation of two cracks along the compression axis, meaning several tomography scans can be carried out while the cracks propagation is paused by stopping momentarily the compression. X-ray tomography cross-sections provide valuable information on the crack evolution in composites by inspection of the fracture history of a DCDC sample during loading.

Fig. 6.15a illustrates the crack propagation history. It indicates the important role of macro-pores on the crack path. Pores clearly deviate the two cracks which started to propagate approximately vertically from the central hole. The two macro-pores in close vicinity to the central hole attract the crack. This phenomenon is well-documented in the literature on porous brittle materials to which our material pertain [125, 126]. Fig. 6.15b also demonstrates that the crack takes full advantage of the composite structure of the material to propagate. The crack may be deviated by a large aerogel particle and propagate around it through the interface with the cement (as demonstrated by the presence of a large number of unbroken particles in close vicinity to the crack). The crack can also propagate within large particles as evidenced by the presence of broken particles along the path.

Similar DCDC samples have been compressed outside the X-ray tomograph using



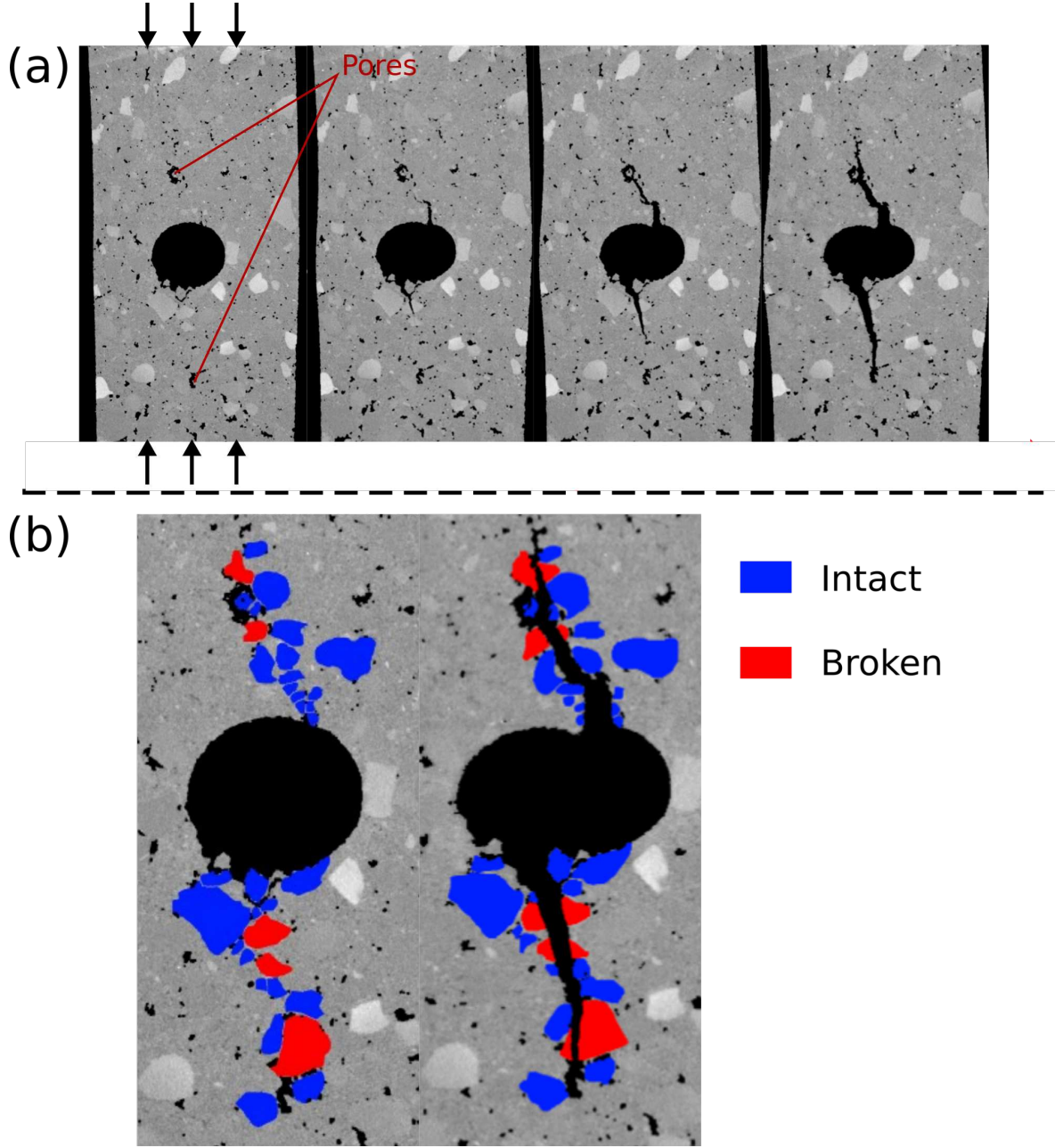


Figure 6.15: (a) Tomography cross-sections of a DCDC silica aerogel composite sample compressed along its vertical axis. (b) Segmented large 10-12 silica aerogel particles located on the path taken by the two vertical cracks. Blue particles were not damaged during fracture while red particles were broken.

a conventional compression machine. A model proposed by Nielsen et al. [79] and described in chapter 3, section 3.4.4 allows the fracture toughness to be estimated from the axial stress and from the crack length curve. The corresponding curves are illustrated in Fig. 6.16 and the results are summarized in Table 6.7. Due to the difficulties in the preparation of these samples, very few have been successfully tested. The preferred procedure for the determination of fracture toughness is the flexural tests on SENB samples.

The curves showed in Fig. 6.16 illustrate how the crack propagation varies strongly

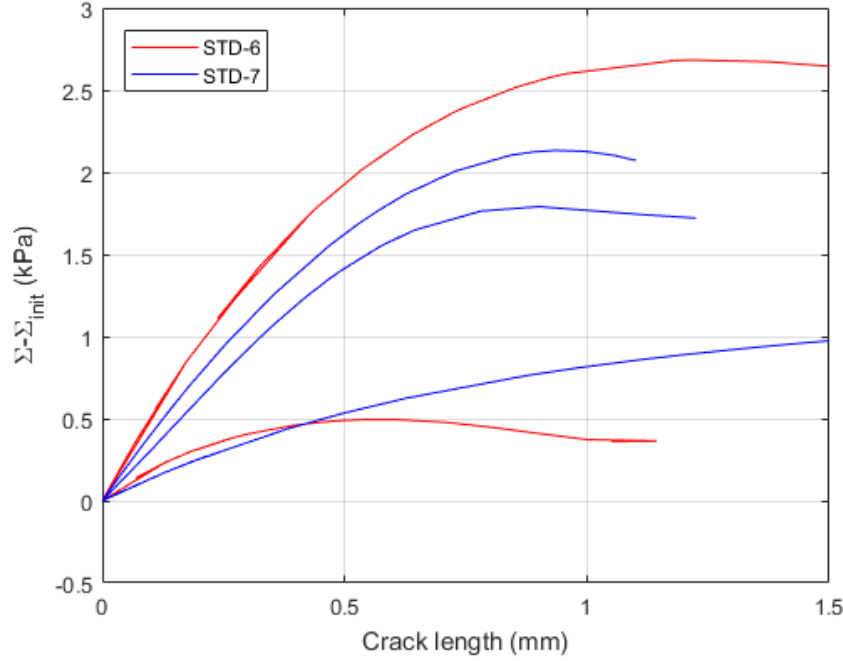


Figure 6.16: Differential axial stress  $\Sigma - \Sigma_{init}$  versus crack length during DCDC tests for five different particulate composite samples (see chapter 3, section 3.4.4 for curve analysis procedures).  $\Sigma_{init}$  is the stress for which cracks are initiating in the DCDC samples. It is different for each sample.

Table 6.7: Fracture toughness  $K_{1c}$  measured experimentally through DCDC tests.

Name	Number of samples tested	$K_{1c}$ (kPam <sup>1/2</sup> )
STD-6	2	0.96±0.18
STD-7	3	1.03±0.14

from one sample to another. This can be explained by the small sample dimensions leading to a limited number of 10-12 silica aerogel particles, the largest components of the particulate composites (up to 2 mm in diameter). The DCDC tests are thus extremely dependent on the heterogeneity of the samples. The stress for which the cracks initiate is also variable for the different samples. For the five samples tested in this work, this initial stress  $\sigma_0$  vary between 30 and 50 kPa while the differential axial stress ( $\sigma - \sigma_0$ ) when the cracks propagate does not exceed 3 kPa as shown in Fig. 6.16. Finally, the calculated fracture toughness of a sample depends more on the stress at which cracks initiates than on the subsequent development of the curves 6.16 (see chapter 3, section 3.4.4 for the full fracture toughness calculation procedure).

DCDC tests lead to  $K_{1c}$  values that are of the order of 1 kPam<sup>1/2</sup>. This is coherent with the literature on silica areogel [127]. However, these tests, as discussed above, are too sensitive to many experimental factors and too largely scattered to be fully trusted for  $K_{1c}$  values. We rely instead on SENB flexural tests.

### 6.5.1.2 SENB flexural testing

Flexural testing on Single Edge Notched Beams (SENB) is a reliable method for the measurement of the fracture toughness of brittle materials. The corresponding protocol is described in chapter 3, section 3.4.3 along with the sample preparation procedure. The results are summarized in Table 6.8. Two examples of load curves are illustrated in Fig. 6.17, highlighting the differences between STD-6 and PP10-6 samples. While the cracks propagate very easily in STD composite samples once sample failure has begun, crack propagation in PP10-6 composites is hindered by fiber bridging. An additional work is needed for the crack to propagate as demonstrated by the larger area under the load-displacement curve. The mean maximum force is also higher for PP10-6 samples than for STD-6 samples which leads to a larger fracture toughness for the PP10-6 composite. The effect of fiber bridging can also be observed during the experimental procedure as the fibers moving out of the composite matrix make a distinctive noise. Fig. 6.17 also shows that the initial part of the curve before any sign of damage is nearly the same for the sample with or without fiber. This is in qualitative agreement with our finding that the Young's modulus (or the stiffness, depending on the measurement method) does not change with the introduction of 1wt.% fiber (Tables 6.4 and 6.5).

Table 6.8: Fracture toughness  $K_{1c}$  measured experimentally through flexural tests on SENB samples.

Name	Number of samples tested	$K_{1c}$ (kPam <sup>1/2</sup> )
STD-6	10	2.6±0.3
STD-7	10	2.5±0.1
STD-0	10	3.7±0.8
PP10-6	6	4.3±0.2

Similarly to indentation tests, the crosshead speed has been modified in order to detect a potential rate-dependence of silica aerogel particulate composites. No differences have been observed in the maximum load for crosshead velocities between 0.15 and 15 mm min<sup>-1</sup>.

### 6.5.1.3 Uniaxial compression

Compressive strengths have been calculated from uniaxial compression tests on cylindrical particulate composite samples. These samples were prepared and tested following the procedures described in chapter 3, section 3.4.2. The results are summarized in Table 6.9. A similar compressive strength  $\Sigma_f$  has been computed between the three composites tested with this method (STD-6, STD-7 and PP10-6).

The compressive strength is challenging to measure because of the gradual deterioration of samples during compression. Small chunks of the cylinders are detaching from the lateral surface, decreasing constantly the section of the samples. While the lateral surface of the cylinders breaks, the core of the samples stays intact much longer during testing, often resulting in samples still intact along their vertical axis when the test is stopped due to the critical reduction of the cylinders section. Two examples

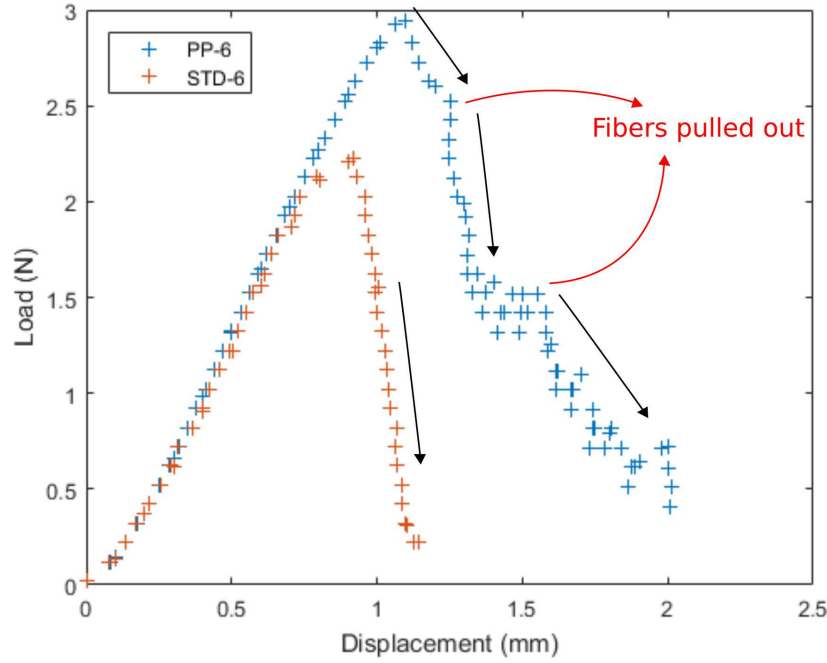


Figure 6.17: Typical load-displacement curves for flexural tests on SENB composite samples STD-6 and PP-10-6. During the failure of PP10-6 samples, the fibers are occasionally pulled out of the composite matrix, creating the steps observed on the corresponding curve.

Table 6.9: Compressive strength  $\Sigma_f$  measured experimentally through uniaxial compression tests.

Name	Number of samples tested	$\Sigma_f$ (kPa)
STD-6	12	$113 \pm 12$
STD-7	12	$109 \pm 18$
PP10-6	9	$117 \pm 10$

of compression samples are shown in Fig. 6.18. The stress-strain curves are similar for the different composites with occasional matter loss during the whole compression process (see Fig. 6.18c). We observed that the PP10-6 composite sample was losing less material during the compression than the STD-6 sample due to the fibers holding the broken parts together.

### 6.5.2 DEM results

The fracture toughness values simulated during tensile tests on notched DEM composite samples are summarized in Table 6.10 and in Fig. 6.19. Two examples of crack propagation are illustrated in Fig. 6.20a and 6.20b respectively for a D-STD-6 and a D-PP10-6. The preparation procedure of samples without any fiber (a simple removal of the fibers in PP samples) ensures that the initial structure of samples with and without fibers is strictly comparable.

Figs. 6.19 and 6.20a-b show that a very small amount of fiber (0.1% in vol.) plays

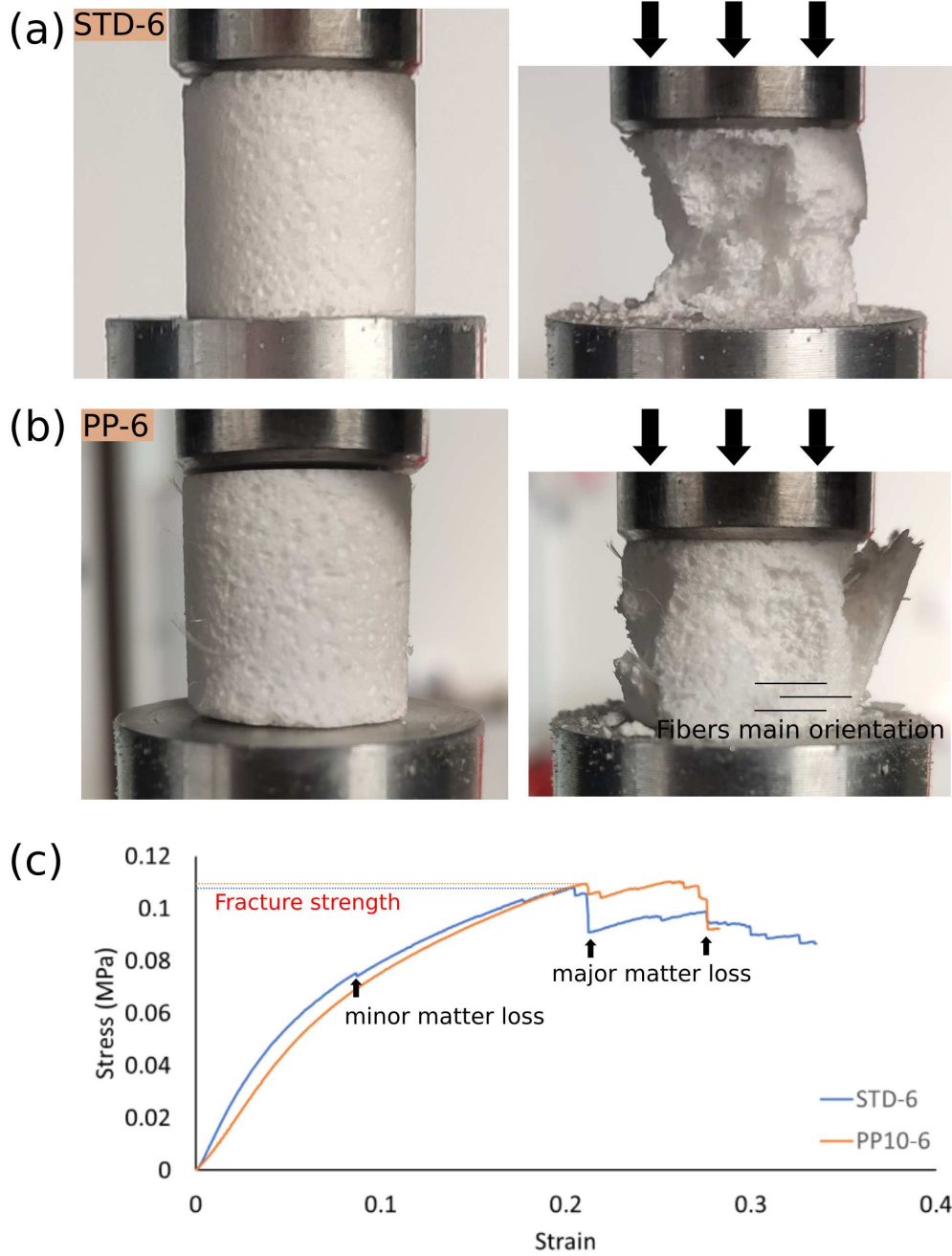


Figure 6.18: a) Uniaxial compression of a STD-6 composite sample. b) Uniaxial compression of a PP10-6 sample. The fibers main orientation is indicated but all the fibers are not ideally oriented in this direction. c) Stress-strain curves corresponding to samples (a) and (b).

an important role in the fracture behavior of DEM silica aerogel composites. The crack initiates, as it should, from the tips of the notch. While in the example shown in Fig. 6.20, it starts from a silica large particle on both extremities, remember these samples are in 3D and measure 2.5 mm in the  $y$  direction. Once the crack has initiated, we note that in both samples, it propagates through particles as we observed in X-ray tomography (Fig. 6.15). However, it propagates without branching nor much deviation in the sample without fiber. For the fiber composite, we observe that the crack exhibits

Table 6.10: Fracture toughness  $K_{Ic}$  measured for simulated DEM composites.

Name	Number of tests	$K_{Ic}$ (kPam <sup>1/2</sup> )
D-STD-5	6	3.04±0.04
D-STD-6	10	2.80±0.10
D-STD-7	6	2.62±0.09
D-rSTD-6	3	2.80±0.50
D-LPo-6	3	3.20±0.07
D-HPo-6	3	2.53±0.06
D-PP5-6	3	4.9±0.2
D-PP10-6	3	6.9±0.3
D-PP15-6	3	9.0±0.3

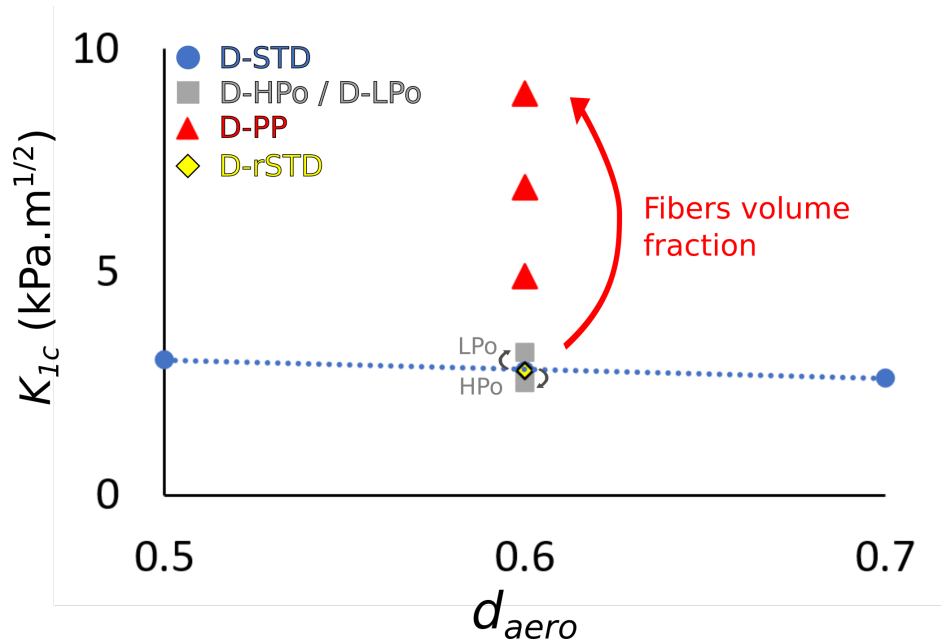


Figure 6.19: Fracture toughness  $K_{Ic}$  evolution with the variation of the different parameters tested in the DEM model: cement volume fraction (D-STD), porosity (D-Hpo / D-LPo), fiber volume fraction (D-PP, 0.05, 0.1 and 0.15%) and sample volume reduction (D-rSTD).  $d_{aero} = \frac{f_{10-12}}{f_{aerogel}}$  ( $f_{10-12}$  and  $f_{aerogel}$  are volume fractions)

a much more tortuous path (recall that these are 3D simulations). In particular, the crack does not fully percolate from the notch tip to the periodic extremities on the  $x$  axis as shown in Fig. 6.21, which shows only the crack.

Concerning the quantitative macroscopic parameters that can be extracted from these simulations, we can first note that similarly to the Young's modulus simulated on DEM composites, the porosity and the volume fraction of the cement phase have an impact on fracture toughness. Second, the presence of fibers nearly triples the fracture toughness and keeps the samples in a single piece while the cracks propagate along the entire length of the samples. The curves shown in Fig. 6.22a and 6.22c illustrate this phenomenon. In the case of the D-STD-6 sample, the composite simply breaks in two parts leading to a zero normalized force once the cracks has propagated along the whole sample length. In the case of the D-PP10-6 sample, the normalized force



stays flat after a maximum is reached, corresponding to the unbreakable fibers being pulled out while the crack segments illustrated in Fig. 6.20 continue to develop. Fig. 6.22b shows the macroscopic stress contribution of the different components of a D-PP10 composite sample. These contributions are calculated from an equation similar to the Love's formulation (see chapter 4, equation 4.21). For each material  $\text{mat}_m$  (SAP, cement or fibers):

$$\Sigma_{ij,\text{mat}_m} = \frac{1}{V} \sum_{\text{contacts mat}_m} F_i \left( R_p - \frac{1}{2} \delta_n \right) n_j, \quad (6.1)$$

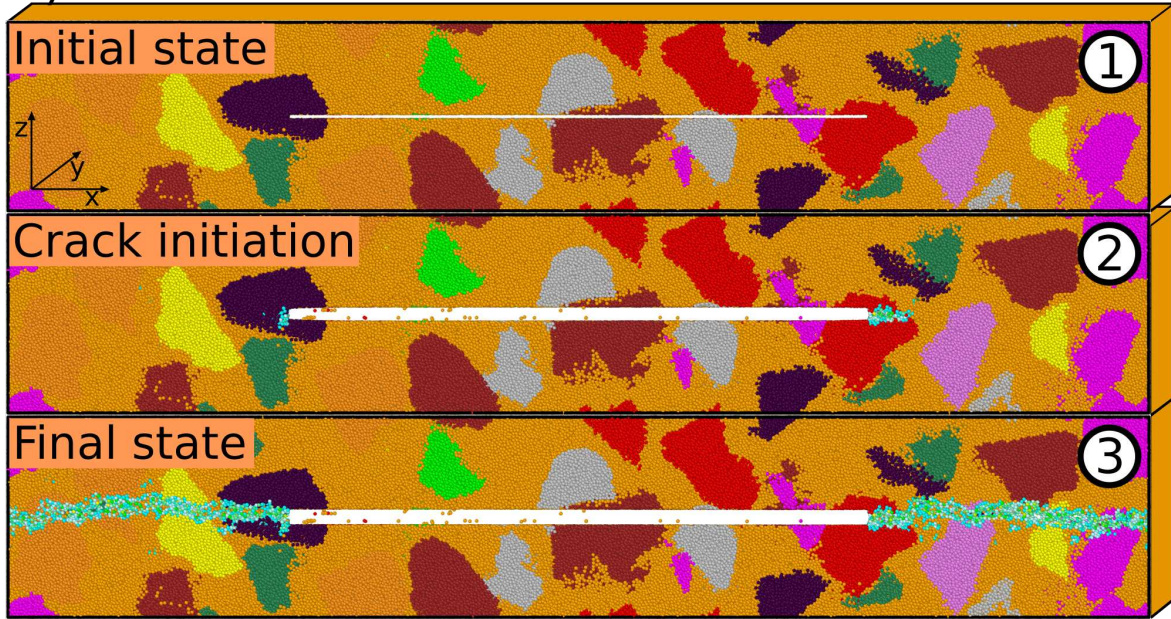
where the summation is made here on all contacts that involve a particle of material  $\text{mat}_m$ .  $\delta_n$  is the geometrical indentation between the two particles at the contact,  $R_p$  is the radius of the discrete element  $p$  and  $n_j$  is the  $j^{\text{th}}$  component of the normal vector  $\mathbf{n}$ . By using the stress contribution of the fibers when cracks starts to propagate (approximately 25 kPa), we can estimate that the mean stress applied on a single fiber during our simulations is around 20 MPa. Although this stress is certainly larger close to the notch tips, it is still much lower than the PP fibers tensile strength (600 MPa). This gives some weight to our hypothesis that fibers are unbreakable in the DEM simulations.

### 6.5.3 Discussion

The fracture toughness values found experimentally using the flexural tests method match very well with the DEM values for samples (D-)STD-6 and (D-)STD-7 as shown in Fig. 6.23. This is an encouraging achievement for the DEM model built in this work since the macroscopic fracture property of the particulate composites has been retrieved simply from the separate calibration of the different components of the composite (cement, large silica particles). This indicates, that we can be reasonably confident in the predictive capability of our DEM simulations, despite the inevitable simplifications that come with a model. In particular, we made several simplifying assumptions concerning the stiffness and the strength of the bonds that connect the large particles to the cement. The stiffness is directly computed from the individual stiffnesses as for two elastic springs in series (Eq. 4.5 in chapter 4). The strength of the bonds has been given the same value as the strength of the bonds inside the cement (45 % higher than the strength of the bonds inside the large particles).

The volume fraction of the cement phase has a small but discernible impact on the fracture toughness in simulations. The decreasing fracture toughness with decreasing cement volume fraction can be understood in DEM by considering the fraction of cement in contact with the notch tips in the two sample. Indeed, as the two tips of the notches are in contact with the full depth of the DEM samples (approximately 2.6 cm), this means that a decrease of the volume fraction of the cement decreases proportionally the linear fraction of the cement in contact with the notch tips. This, in turn decreases the fracture strength. The same analysis can be applied when porosity is modified. A higher porosity increases the probability that a pore is in contact with the notch tips, thus decreasing the fracture toughness of the sample.

a) D-STD-6



b) D-PP-6

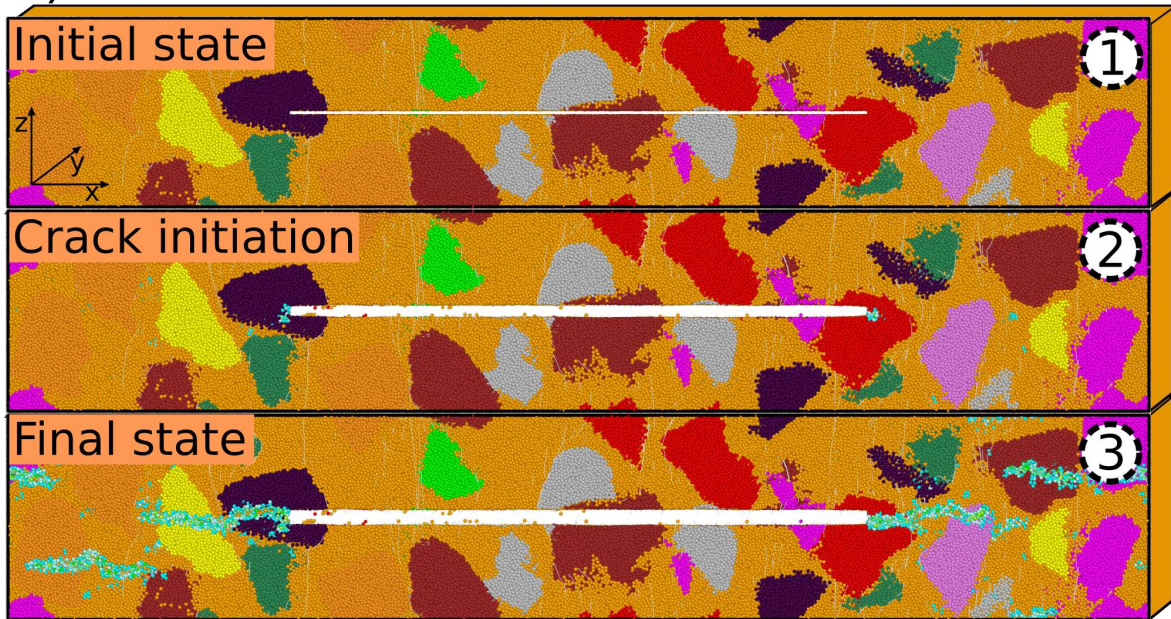


Figure 6.20: Crack propagation history for two DEM composite samples. Particles in cyan color are particles which have lost at least one bond. a) D-STD-6 sample b) D-PP10-6 sample. The fibers are oriented perpendicularly to the notch plan. The number 1, 2 and 3 relate to particular strains as indicated in Fig. 6.22a. Particles inside the notch are particles that were detached (isolated) by the notch removal. They do not affect the overall behaviour. Periodic conditions are imposed on all three axis as evidenced for the  $z$  axis by connecting images 1, 2 and 3.

A substantial increase in fracture toughness has been measured experimentally with fibers addition (approximately 65 % increase from composites STD-6 to PP10-6, see Fig. 6.23). This is a positive outcome regarding the mechanical improvement of silica



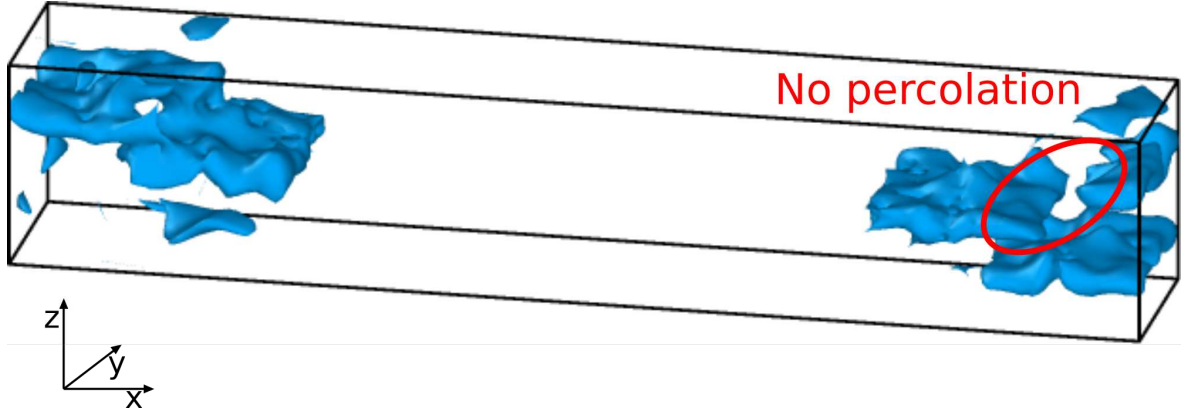


Figure 6.21: Final state of the D-PP10-6 sample illustrated in Fig. 6.20. For illustration purpose, all components different from the cracks are invisible and a surface mesh is constructed from Ovito [128]. The different crack portions observed in Fig. 6.20 do not percolate from the notch tips to the periodic extremities on the  $x$  axis.

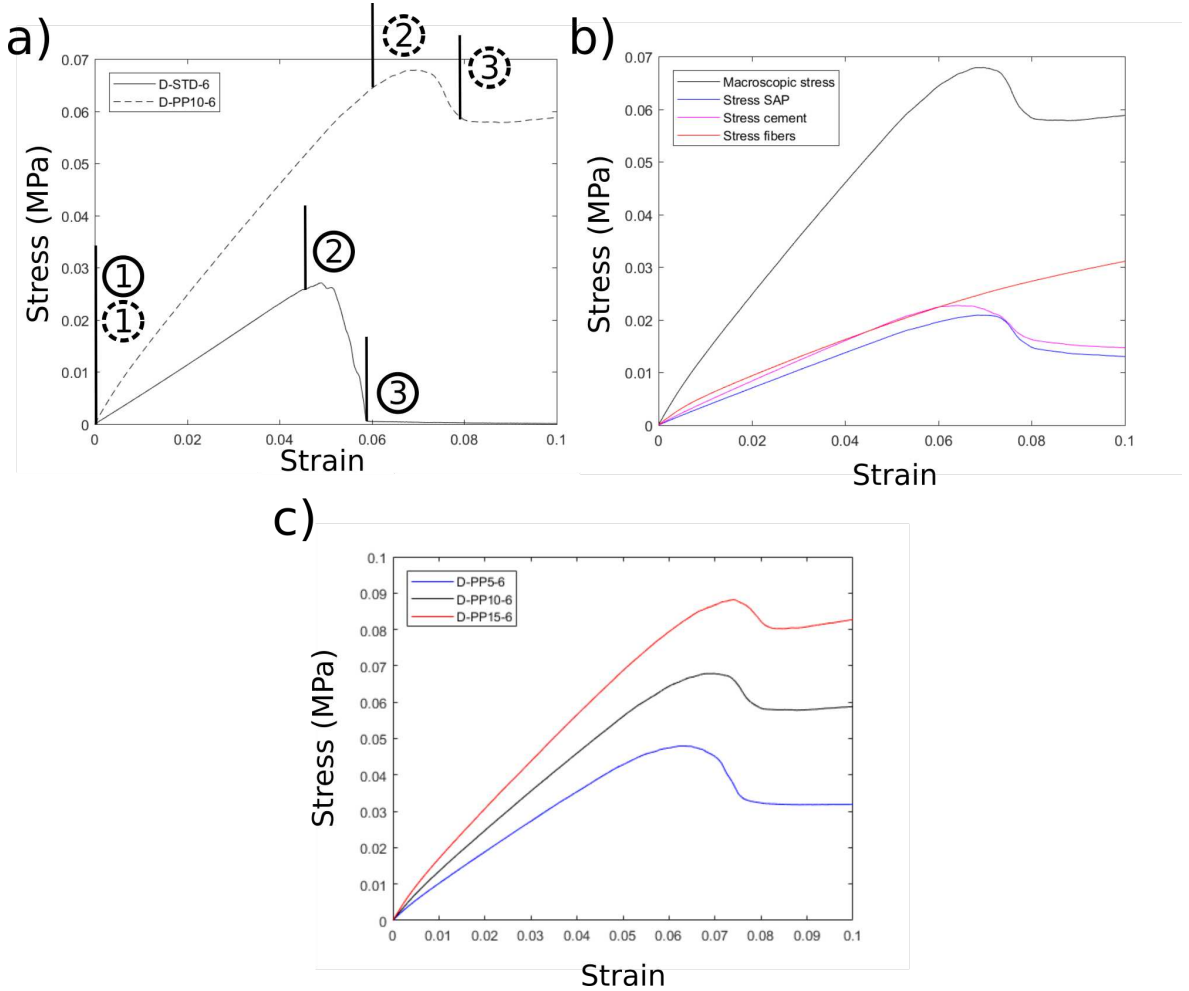


Figure 6.22: Normalized force vs. strain curves for: a) tensile test of D-STD-6 and D-PP10-6 notched samples, b) tensile test of a D-PP10 notched sample with the contribution of the three different components (SAP, cement and fibers) calculated using Eq. 6.1, c) tensile test of a D-PP05, a D-PP10 and a D-PP15 notched samples.

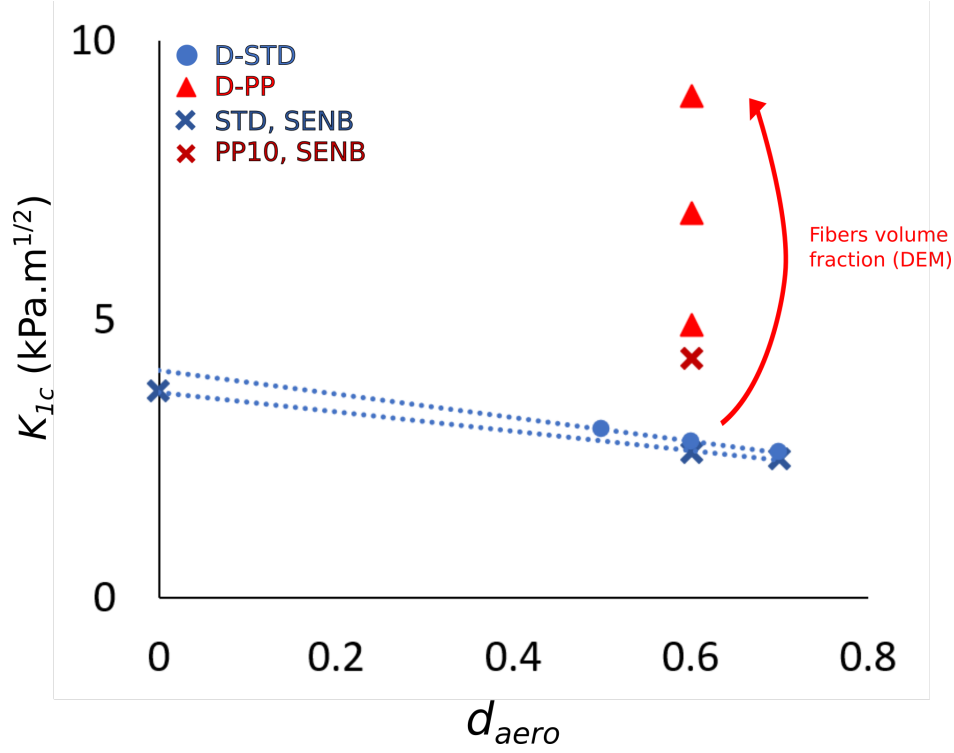


Figure 6.23: Fracture toughness  $K_{1c}$  evolution with the variation of the different parameters tested experimentally and in the DEM model: cement volume fraction (D-STD) and fiber volume fraction (D-PP).  $d_{aero} = \frac{f_{10-12}}{f_{aerogel}}$  ( $f_{10-12}$  and  $f_{aerogel}$  are volume fractions).

aerogel particulate composites. An increase in fracture toughness is also obtained numerically. It is much larger than the experimental one (approximately 260 % increase). This difference may be related to the ideal distribution of the fibers and their equally ideal orientation (perpendicular to the cracks propagation plan). This is hardly the case experimentally (see section 6.3.4). Moreover the fibers were not allowed to break during the simulations. It has been observed on SEM images that the large bundles of fibers do not break while they are pulled out during the flexural tests on SENB samples and no individual fiber failure (fibers around 10  $\mu$ m in diameter) was observed even if this cannot be considered as a general truth. Yet, even if the high improvement in fracture toughness with the addition of fibers in simulations can be tempered by the absence of fiber failure, the fracture toughness value obtained for the DEM composite D-PP10-6 can be considered as the maximum fracture toughness which can be potentially obtained experimentally if the fibers are perfectly dispersed and oriented in one direction. Thus, the values obtained by DEM should be seen as an upper bond to be reached if processing conditions improve towards ideal conditions.

## 6.6 Composite thermal properties

### 6.6.1 Flux-meter testing

The flux-meter equipment used in this PhD work has already been used on silica aerogel particulate composites by A. Perret [29], providing a valuable reference for the calibration of the equipment and the validation of measures. The measurement procedure of the thermal conductivity is described in chapter 3, section 3.5.1. The experimental results are summarized in Table 6.11. The thermal conductivity value of  $13.4 \text{ mWm}^{-1}\text{K}^{-1}$  for the composite STD-6 matches the previous results of A. Perret although slightly lower than what was expected on this same composite (around  $15 \text{ mWm}^{-1}\text{K}^{-1}$ , see [29]) and is consistent with the thermal conductivity of the silica aerogel particles provided by Enersens company ( $12\text{-}13 \text{ mWm}^{-1}\text{K}^{-1}$ ). The fact that the thermal conductivity of silica aerogel particles is virtually undegraded by the addition of a polymer binder is a positive for the project. However, the addition of fibers (0.1% volume fraction) has a clear negative impact on thermal conductivity as it increases by  $1.4 \text{ mWm}^{-1}\text{K}^{-1}$  the thermal conductivity. Although, this inconvenience could be partially negated if the fibers were to be perfectly oriented perpendicularly to the insulating panels thickness. Such a feat is currently impossible given the current composite preparation procedure.

Table 6.11: Thermal conductivities measured on composite samples using a flux-meter.

Name	Number of measurements	$\lambda \text{ (mWm}^{-1}\text{K}^{-1}\text{)}$
STD-6	2	$13.4 \pm 0.1$
PP10-6	3	$14.8 \pm 0.6$

### 6.6.2 Current Transformer (CT)-meter testing

CT-meter measurements allowed the gaseous component of the thermal conductivity of particulate composites to be separated from the radiative and solid components. This is achieved by measuring the temperature response of composite samples to a heat pulsation in a vacuum chamber. The full protocol and sample preparation procedure is described in chapter 3, section 3.5.2. It is possible to use a simple model to fit the experimental curves and calculate pore sizes in the composites [129]. In our case we chose a model describing a bimodal pore size distribution:

$$\lambda = \lambda_s + \lambda_r + \lambda_g \quad (6.2)$$

$$\lambda_g = \lambda_{g0} \left( \frac{\Phi_1}{1 + 2\beta \frac{l_a}{\delta_1} \frac{P_0}{P}} + \frac{\Phi_2}{1 + 2\beta \frac{l_a}{\delta_2 P} \frac{P_0}{P}} \right) \quad (6.3)$$

where  $\lambda_s$ ,  $\lambda_r$  and  $\lambda_g$  are respectively the solid conduction, radiative and gaseous conduction components of the thermal conductivity.  $\lambda_{g0}$  is the free air conduction (here  $\lambda_{g0} = 26.2 \text{ mWm}^{-1}\text{K}^{-1}$ ),  $P_0$  is the lowest pressure for which a thermal conductivity has been measured,  $P$  the pressure,  $\beta$  is a constant specific to the gas (here for air,

$\beta = 1.5$ ),  $l_a$  is the mean free path of air molecules (here,  $l_a = 67$  nm),  $\delta_1$  and  $\delta_2$  are the pore sizes and  $\Phi_1$  and  $\Phi_2$  are the volume fractions of pores.

We know that the intrinsic nano-porosity of our silica aerogel particles is around 95 % with a mean pore size of  $7 \pm 1$  nm thanks to the PhD work of A. Perret [29]. Moreover the inter-particles macro-porosity of our particulate composites is around 15 % (see section 6.3.1). Thus we can set:

- Macro-pores:  $\Phi_1 = 0.15$
- Nano-pores:  $\Phi_2 = 0.95 \times \Phi_1 = 0.8075$  and  $\delta_2 = 7$  nm.

We can then use the model described by equations (6.2) and (6.3) to extract an estimation of the pore size  $\delta_1$  in composites STD-6 and PP10-6 tested using the CT-meter measurement procedure. The resulting pore sizes are  $\delta_1(STD - 6) = 7 \pm 3$   $\mu\text{m}$  and  $\delta_1(PP10 - 6) = 0.5 \pm 0.2$   $\mu\text{m}$ . The corresponding fitted curves are shown in Fig. 6.24 and the fitted values for  $\delta_1(STD - 6)$  and  $\delta_1(PP10 - 6)$  are shown in Table 6.12.

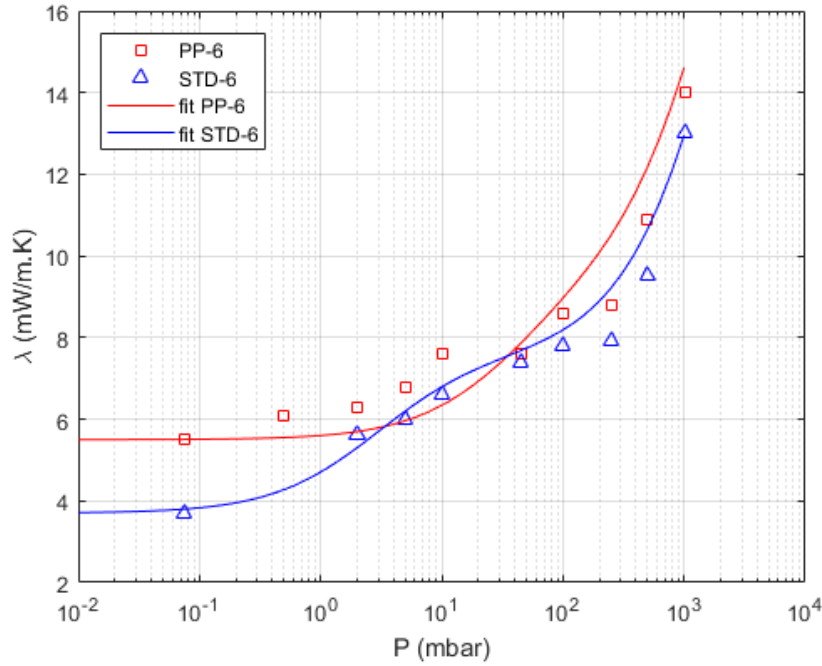


Figure 6.24: Evolution of the thermal conductivity with pressure measured with a CT-meter. The fitted curves originate from the model described by equation 6.3.

Table 6.12: Parameters used to fit the porosity model defined by equation 6.3 to the CT-meter measurements shown in Fig. 6.24.

Name	$\Phi_1$	$\Phi_2$	$\delta_1$ ( $\mu\text{m}$ )	$\delta_2$ ( $\mu\text{m}$ )
STD-6	0.15	0.8075	7	0.007
PP10-6	0.15	0.8075	0.2	0.007

First, we note that the PP10-6 composite exhibits a higher thermal conductivity than the STD-6 composite at low pressure ( $1.8 \text{ mWm}^{-1}\text{K}^{-1}$  difference), meaning that



the component  $\lambda_s + \lambda_r$  is larger when fibers are incorporated in the silica aerogel particulate composites. This difference is close to the one obtained using the fluxmeter measurement procedure ( $1.4 \text{ mWm}^{-1}\text{K}^{-1}$ ) and thus highlights the influence of fibers on the solid component (and to a lesser extent on the radiative component) of the thermal conductivity of our composites. However, it seems this difference is smaller when  $P$  is higher than 1 mbar for still unknown reasons.

Second, the macro-porosity  $\delta_1$  found is 30 times smaller for the PP10-6 composite than for the STD-6 composite. This result is questionable as such a large difference in the pore size distribution was not observed when comparing qualitatively X-ray tomography images. Yet, only a proper quantitative study of the porosity in our composites using adapted pycnometry characterization methods would allow to challenge this result.

## 6.7 Conclusion

Different silica aerogel particulate composites have been prepared and experimentally tested in this chapter. A wide range of visualization and characterization methods have been implemented to measure structural, mechanical and thermal properties. This allowed to study how these composites are influenced by the different components contained in the samples while feeding the discrete element model with data essential for the calibration of the DEM simulations. Similarly, different DEM composites have been generated and tested. Some of these numerical composites are the direct equivalent of composites prepared experimentally, like the reference composite D-STD-6 which has been generated to be the numerical counterpart of the experimental composite STD-6. Other numerical composites were generated in order to study the influence on the macroscopic mechanical behaviour of the composites of parameters that were not, or could not be studied experimentally. In general, the coupling between experimental and numerical studies led to a better understanding of the silica aerogel particulate composites mechanical behaviour and helped to the identification of leads for their mechanical reinforcement while conserving a low thermal conductivity.

The main points highlighted in this chapter are the following:

- X-ray tomography observations showed how the mechanical and thermal performances of the composites can be tempered by the excessive presence of macro-pores in the composites. This was confirmed numerically with the observation of the decrease of fracture strength with the increase of macro-porosity in DEM composite samples.
- SEM and X-ray tomography observations showed the satisfactory coating of the silica aerogel particles by the polymer binder. It also appears that this same binder is compatible with the polypropylene fibers introduced in the composites for their mechanical improvement. Moreover, the polypropylene fibers were the only one leading to a satisfactory composite structure as the glass fibers and PET fibers also tested during the PhD lead to the formation of prohibitive cracks during the drying step.

- Polypropylene fibers embedded in the experimental composites cannot, for most of them, be considered as cylindrical fibers as several blocks of various shapes and dimensions have been observed in SEM images. However, it has been chosen to simulate fibers in DEM as if they were all slender cylinders with a 10  $\mu\text{m}$  in diameter. While an increase in the fracture toughness has been observed both experimentally and numerically when fibers are embedded in the composites, the gain is much more important for the simulated composites. As the DEM composites idealize the shape, distribution and orientation of fibers, they give us insight into the potential mechanical improvement that experimental composites could benefit from.
- An increase of the thermal conductivity of the composites have been measured experimentally ( $+1.4 \text{ mWm}^{-1}\text{K}^{-1}$ ) between standard composite samples STD-6 and fiber reinforced composite samples PP10-6 (fibers volume fraction: 0.1%). Complementary thermal analysis (CT-meter) revealed that the addition of fibers is indeed responsible for this increase. This confirms that a compromise must be found between mechanical and thermal performances when embedding fibers in our particulate composites.

The discrete element model created and calibrated during the PhD proved to be successfully predicting the Young's modulus and fracture toughness evolution when structural parameters are modified (cement volume fraction, inter-particle macro-porosity, fibers volume fraction, ...). It also provides numerical results close to the experimental measurements. For the time being, the dp3D code only provides a post-processing tool to compute thermal conductivity from the conductivity of each component. For aerogel materials, this is clearly not sufficient as the Knudsen effect needs for example to be taken into account. Thus, it is not yet able to find a compromise between fracture toughness improvement and thermal conductivity conservation. The addition of a post-processing tool to compute properly thermal conductivities from numerical microstructures would allow to explore and optimize the composites numerically before attempting to replicate them experimentally. Not only the fiber size, shape and quantity could be optimized but also other parameters like silica aerogel particles size distribution, binder efficiency, macro-porosity, etc...



## Chapter 7

# General conclusion and prospects

### 7.1 Conclusion

This PhD work was motivated by the understanding of the mechanics of Silica Aerogel Particles (SAP) and of particulate composites in order to improve the strength and the fracture toughness of super-insulating panels designed for the thermal insulation of buildings. For this purpose, experimental characterizations of structural, mechanical and thermal properties of SAP and particulate composites were carried out. A DEM model was developed and calibrated using experimental results as input. This dialogue between experimentation and simulation allows the mechanics of SAP and of particulate composites to be explored in detail. Moreover, it offers degrees of freedom in the investigation that would be unattainable by confining ourselves to the experimental or numerical aspect of this study.

The literature review presented in chapter 2 provided an insight into the current understanding of the properties of silica aerogels used in particulate form in this work. Their nano-structure and extremely high porosity is at the origin of their low thermal conductivity but also their low mechanical strength and fracture toughness. This explains why products designed for thermal insulation of buildings are almost always composite materials. The silica aerogel particulate composite studied in this work is based on previous works [29, 63, 69] which showed that an additional mechanical reinforcement with binder and fibres is necessary for the material to resist transportation and handling.

The structural, mechanical and thermal characterization of SAP and particulate composites required the use of specific methods adapted to soft and brittle materials (presented in chapter 3). Silica aerogels are electrical insulators and have a low X-ray absorption due to their high porosity. Thus, SEM and X-ray tomography visualization methods had to be adapted in order to provide 2D and 3D images of our materials. Still, one of the major experimental challenges of this work was the mechanical characterization of millimetric SAP. The size and shape of these objects required the use of non-standard characterization methods such as in-situ uniaxial compression on individual particles in a X-ray tomograph. Silica aerogel particulate composites were easier to characterize as samples produced were bigger with more standard shapes as the material can be moulded.

The DEM model developed in this work is particularly well adapted to simulate the fracture of brittle materials like SAP and of our particulate composites. This is due to the discontinuous nature of the mesh that simply defines local fracture by the breaking of elastic bonds between spherical discrete elements. The discrete elements considered in this work have no physical counterpart in the real material. This is why their microscopic mechanical properties as well as those of the bonds need to be calibrated

using experimental results. These calibration methods are presented in chapter 4, in addition to the hypothesis of the DEM model, the generation of numerical SAP and composites, and the numerical testing methods used to obtain macroscopic mechanical properties such as the Young's modulus or the strength of SAP.

The mechanical and structural characterization results of SAP were extremely dispersed. Density measurements showed that while the majority of the SAP displays a density close to  $0.10 \text{ gcm}^{-3}$ , some of them are denser by a factor two (maximum measured at  $0.23 \text{ gcm}^{-3}$ ). This density variation plays a significant role, along with shape and size variations of particles, during uniaxial compression tests. The DEM model helped to quantify the influence of these parameters apart from the influence of intrinsic defects and cracks initially present before experimental testing. Different DEM SAP, generated and calibrated using X-ray tomography in-situ compression tests, have been tested. The global crack pattern differs between DEM particles and real particles. However, the DEM model gives more realistic results when the discrete element size is reduced and when initial cracks, observed experimentally, are introduced in the DEM SAP. The influence of these initial cracks is certainly underestimated in simulations as these are based on cracks detected by X-ray tomography whose resolution does not allow all defects to be identified. The calibration of the DEM SAP using experimental in-situ compression tests allowed to extract the silica aerogel Young's modulus which is consistent with indentation measurements, and its strength, consistent with the one estimated experimentally by Weibull statistics.

The last part of this PhD also combines experimental characterizations and DEM simulations in order to generate and calibrate large DEM composite samples for the simulation of fracture and crack propagation. The original generation procedure of the DEM composites allows to control freely the volume fraction, size, orientation, stiffness or strength of the different components and thus to study their influence on the mechanical behaviour. The embedding of fibers in the composites, experimentally challenging, is of course easier numerically. We took advantage of this possibility to generate some idealized structures that provide insight into the potential mechanical improvement of experimental composites. In general, experimental mechanical characterization results are consistent with DEM simulation results. This allows to explore the evolution of the Young's modulus and fracture toughness when structural parameters are modified.

## 7.2 Prospects

We believe that the work performed during this PhD has significantly improved our understanding of the mechanical behavior of SAP and particulate composites. In particular, the role of fibers has been investigated. However, numerous areas remain to be explored both experimentally and numerically. Some guidance is proposed in this section.

### 7.2.1 Composite preparation process

We saw in chapter 6 (see section 6.3.4) that the embedding of fibers in experimental composites is challenging due to the difficult dispersion of fibers in the composite matrix and to the potential crack propagation during the drying step. The most appropriate fibers used in this work regarding these two difficulties are polypropylene (PP) fibers which reinforce our experimental composites by improving the fracture toughness by approximately 50 % for a volume fraction of 0.1 %. However, the shape and size of these fibers are problematic as the major part of the fiber volume takes the form of large polymer blocks, not as effective as a strictly monomodal size distribution of thin cylindrical fibers like the ones simulated in DEM composites. Thus, DEM simulations predict a fracture toughness at least double that of fiberless composites. These fibers are ideally dispersed, are oriented perpendicularly to the crack propagation plan and have all the same dimensions (10  $\mu\text{m}$  in diameter). A promising prospect would be to investigate new types of fibers and preparation methods allowing the production of composite samples with a fiber distribution closer to what has been simulated in this work. Such an optimization would require selecting a proper fiber surface chemistry, compatible with the binder and allowing a good dispersion in the composite matrix.

The processing of particulate composites could also be improved by designing appropriate tools for the mixing step. Currently, this step is performed manually as no standard automated tools are adapted for mixing volatile and brittle SAPs (see chapter 3, section 3.3.2). This creates reproducibility problems because the SAP can be more or less damaged during the process depending on the force applied by the operator. Moreover, manual mixing is adapted to the preparation of small composite quantities. A continuation of the project will thus require preparing and studying large composite panels instead of the small sample beams prepared during this PhD work. Manual work will then no longer be suitable because of the large quantity of SAP requiring hours to mix efficiently.

### 7.2.2 Complementary characterization of SAP

In chapter 5, we showed that while the majority of SAP have a density close to 0.1  $\text{gcm}^{-3}$ , some individual SAP have much larger densities (one was measured with a density of 0.23  $\text{gcm}^{-3}$ ). An experimental procedure is already available for the measurement of the density by weighing individually the SAP and then scanning them using X-ray tomography (see 3.2.3). Still, it is difficult to study a large batch of SAP using this procedure, which is time consuming. It would be useful for the refinement of the DEM model to carry out a statistical study by using X-ray tomography to quantify the density of individual SAP. This, however, cannot be performed using an X-ray laboratory source as the non-monochromatic beam creates a complex dependency of the grey-scale in X-ray tomography volume with SAP density. A solution would be to use a synchrotron source, which provides a linear dependency between gray-scale and density.



### 7.2.3 Precise measurement of fiber shear interfacial stress

In DEM composites, the calibration of the contact law between fibers and other components is based on the experimental measurement of a shear interfacial stress  $\tau$  corresponding to the stress observed at the composite matrix / fiber interface while a fiber is pulled out (see Fig. 4.16). In this work, this stress is estimated based on the model described in section 4.4.3 using the data collected during experimental flexural SENB tests (see Equation 4.29). The estimation of  $\tau$  is based on several assumptions and is particularly dependent of the fiber radius  $r$  chosen in Equation 4.29. We saw in chapter 6, section 6.3.4 that the PP fibers embedded in experimental composites have various shapes and sizes, which makes it difficult to choose a radius  $r$  in our model and estimate the interfacial shear stress  $\tau$ . A solution for estimating  $\tau$  much more precisely would be to measure the force/displacement curve while a single PP fiber with known dimensions is pulled out from the composite matrix (in opposition to SENB tests where hundreds of fibers are pulled out at the same time). However, this method would require an experimental equipment able to precisely measure and apply forces inferior to 50 mN.

### 7.2.4 Extended thermal characterization and simulation

The thermal study of our particulate composites was limited to the experimental characterization of a limited number of composite samples (STD-6, PP-6). These measurements enabled to characterize the negative impact of an increase in fibers fraction on the thermal conductivity of our composites. While the DEM model is providing consistent fracture toughness evolution when embedding fibers compared to experimental composites, it is not able to simulate heat transfers. The discrete element code used in this work has a functionality allowing to simulate heat transfers in static samples (no deformation) but it would need to be adapted to our composite samples and a new calibration process will be required in order to obtain realistic thermal conductivity values. Such a tool used in parallel with mechanical simulations would allow a trade-off to be reached between the mechanical and thermal performances of our composites by optimizing structural parameters (porosity, cement volume fraction, fibers, ...).

### 7.2.5 DEM model structural parameters exploration

The generation of the DEM composite samples allows to study the influence of a vast panel of structural parameters. Ironically, these composites were generated by densifying the different components together (SAP, cement, pores, fibers). Indeed the X-ray tomography volumes were too difficult to segment and the volumes scanned too small to generate large composite samples using directly these 3D images as imprints to allocate the different phases in a discrete element packing. If this imprint method had been successful, generated DEM composite samples would have been much more difficult to modify. Our current generation method gives a total control on the components packed in the composites and on the contact laws between them. Parameters whose influence is tedious to be studied experimentally can be modified quite easily

to explore some avenues. For example, DEM simulations clearly confirmed that the fibers have a beneficial influence on the fracture toughness of composite samples but little work has been done on the influence of their shape and size. Moreover, while it is highly suspected that the fibers do not break during experimental and DEM samples fracture (see section [6.5.2](#)), the calibration of the DEM fibers tensile strength would allow to verify this assumption.

Using the DEM tool proposed in this work, an ideal workflow would consist of exploring potential avenues for mechanical improvements while ensuring that thermal properties are not overly degraded. The avenues explored must be compatible with the actual process capabilities. Furthermore, as illustrated by the fiber introduction, we must remember that DEM simulations are based on a model, whose assumptions tend to greatly simplify and idealize the experimental conditions.



## Appendix A

# DEM composite sample compaction with fibers: additional data

### Composites without fibers

When no fibers are incorporated in the gas, strain rates are the same in all directions as the composite exhibits an isotropic structure. In this situation the initial and final size ratios of the simulation box are identical in all 3 directions.

### Composites with fibers

The composites containing fibers require a slightly different preparation route. As explained before, fibers are all aligned along the same axis with a given angular dispersion when incorporated in the components gas. Thus, no strain should be applied in this direction as fibres would present unwanted multiple curvatures as illustrated in Fig [A.1](#). For example, as a sample without fibers would be compacted with equal strain rates in all three main directions, a sample with fibers oriented along the  $Z$  axis will be compacted along the  $X$  at  $Y$  axis but not along the  $Z$  axis. Moreover, strain rates along the two other directions are multiplied by 1.5 in order to keep the same volume strain rate between samples with and without fibres. We must take into account that an anisotropic strain will change the sample final dimensions. It can be problematic if one of the simulation box dimensions is too thin and a silica aerogel aggregate (as they are the larger objects in the simulation box) is allowed to contact itself due to periodic conditions. The initial dimensions are thus modified adequately for the the final dimensions to be the same as composite samples without fibres.

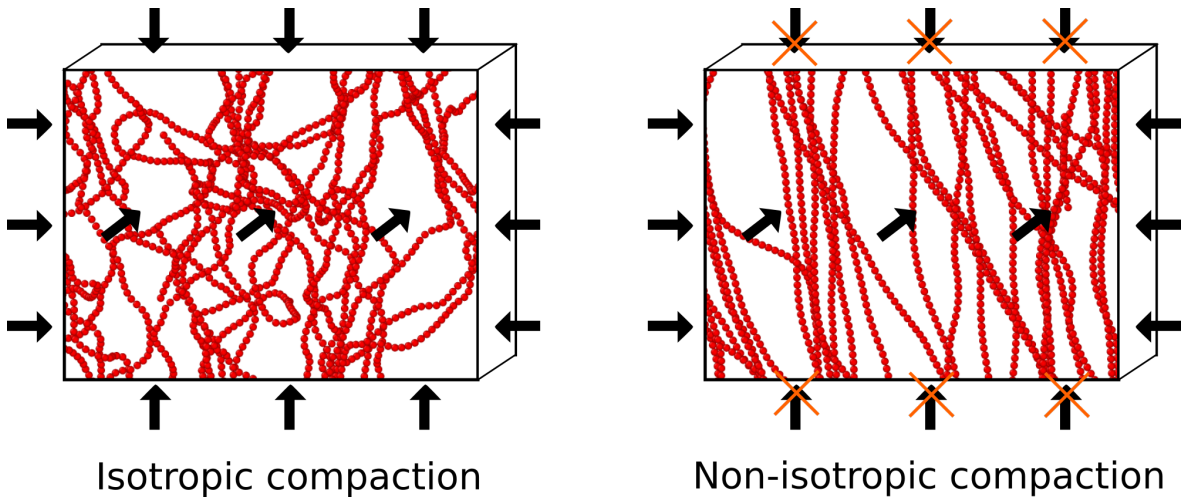


Figure A.1: Fibers morphology inside DEM composites after compaction. Other components are here invisible for illustration purpose.



## Appendix B

# Fracture of DEM aerogel particles P2 to P5

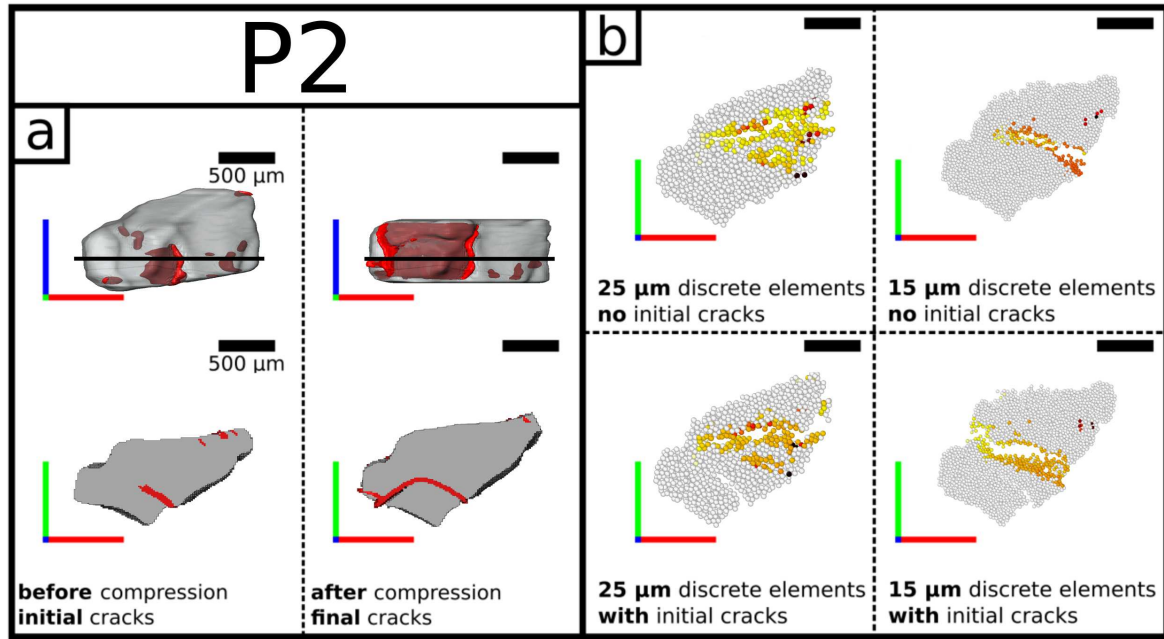


Figure B.1: a) P2 particle volumes built from tomography compression test. b) P2 particle volumes built using 2 types of discrete elements with DEM. The bond fractures are illustrated chronologically from hot to cold colors.



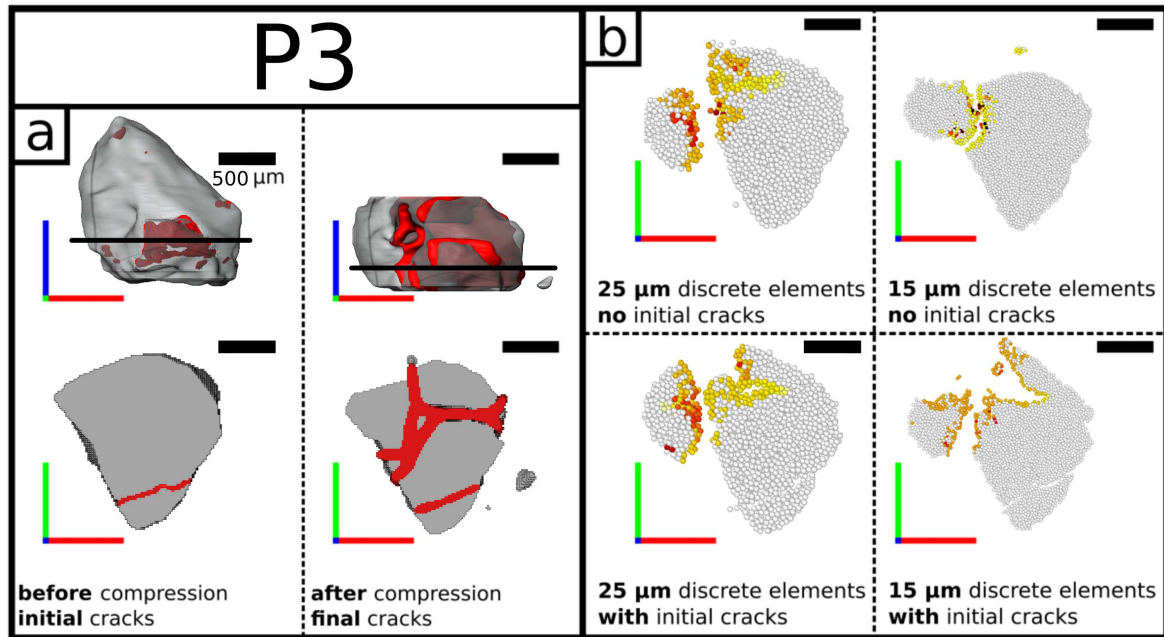


Figure B.2: a) P3 particle volumes built from tomography compression test. b) P3 particle volumes built using 2 types of discrete elements with DEM. The bond fractures are illustrated chronologically from hot to cold colors.

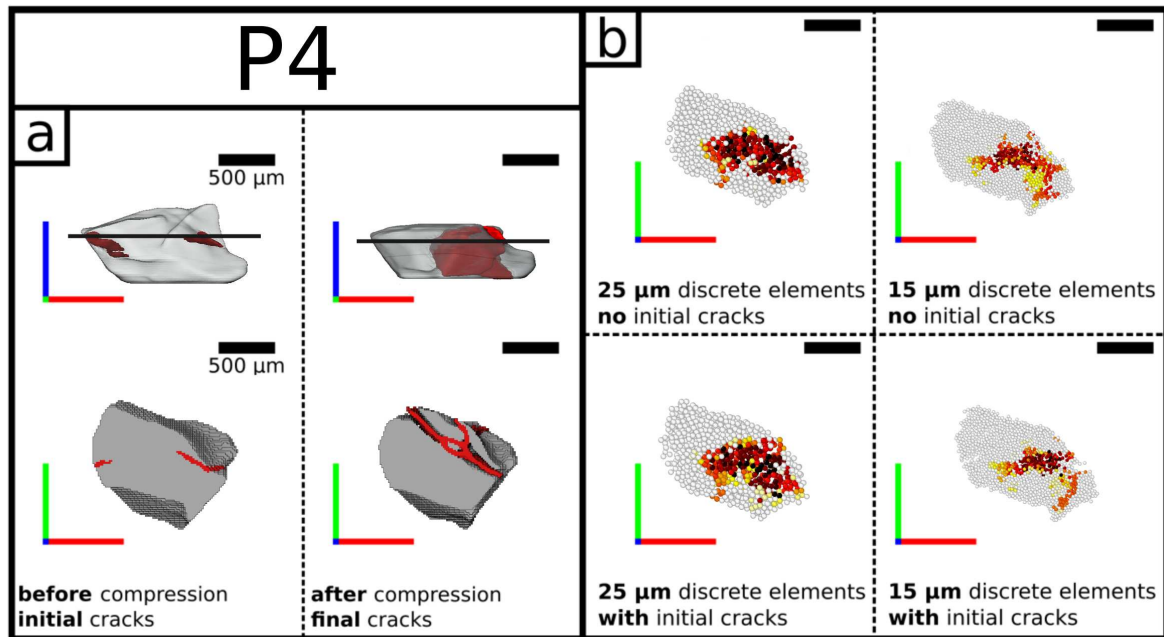


Figure B.3: a) P4 particle volumes built from tomography compression test. b) P4 particle volumes built using 2 types of discrete elements with DEM. The bond fractures are illustrated chronologically from hot to cold colors.

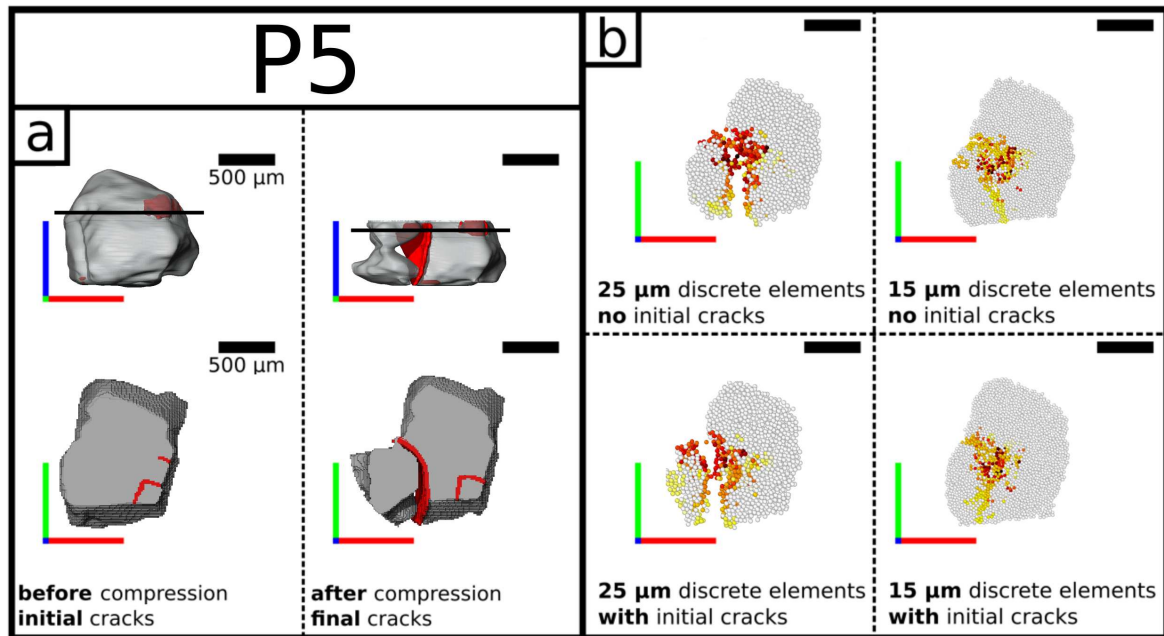


Figure B.4: a) P5 particle volumes built from tomography compression test. b) P5 particle volumes built using 2 types of discrete elements with DEM. The bond fractures are illustrated chronologically from hot to cold colors.



## References

1. Ritchie, H. & Roser, M. *CO and Greenhouse Gas Emissions* 2020. <https://ourworldindata.org/co2-and-other-greenhouse-gas-emissions>.
2. Iea. *Electricity - Fuels Technologies* <https://www.iea.org/fuels-and-technologies/electricity>.
3. Etienne, G., Martin, C., Gael, C., Bonnefoy, O., Perez, M., Evelyne, K. & Genevieve, F. *Modelisation du comportement mecanique et thermique des silices nano-architecturées* PhD thesis (2019).
4. Diascorn, N. *Elaboration et caractérisation d'aérogels superisolants thermiques hybrides à base de silice et de polyuréthane* PhD thesis (École nationale supérieure des mines de Paris, 2015).
5. Thapliyal, P. C. & Singh, K. Aerogels as Promising Thermal Insulating Materials: An Overview. *Journal of Materials* **2014**, 1–10. ISSN: 2314-4866 (2014).
6. Rigacci, A., Einarsrud, M. A., Nilsen, E., Pirard, R., Ehrburger-Dolle, F. & Chevalier, B. Improvement of the silica aerogel strengthening process for scaling-up monolithic tile production. *Journal of Non-Crystalline Solids* **350**, 196–201. ISSN: 00223093 (2004).
7. Maleki, H., Durães, L. & Portugal, A. An overview on silica aerogels synthesis and different mechanical reinforcing strategies. *Journal of Non-Crystalline Solids* **385**, 55–74. ISSN: 00223093 (2014).
8. Tamon, H., Sone, T. & Okazaki, M. Control of mesoporous structure of silica aerogel prepared from TMOS. *Journal of Colloid and Interface Science* **188**, 162–167. ISSN: 00219797 (1997).
9. Li, M., Jiang, H., Xu, D., Hai, O. & Zheng, W. Low density and hydrophobic silica aerogels dried under ambient pressure using a new co-precursor method. *Journal of Non-Crystalline Solids* **452**, 187–193. ISSN: 00223093 (2016).
10. Lee, O. J., Lee, K. H., Jin Yim, T., Young Kim, S. & Yoo, K. P. Determination of mesopore size of aerogels from thermal conductivity measurements. *Journal of Non-Crystalline Solids* **298**, 287–292. ISSN: 00223093 (2002).
11. Roiban, L., Foray, G., Rong, Q., Perret, A., Ihiawakrim, D., Masenelli-Varlot, K., Maire, E. & Yrieix, B. Advanced three dimensional characterization of silica-based ultraporous materials. *RSC Advances* **6**, 10625–10632. ISSN: 20462069 (2016).
12. Kistler, S. Coherent expanded aerogels. *The journal of physical chemistry* (1932).
13. Lamy-Mendes, A., Pontinha, A. D. R., Alves, P., Santos, P. & Durães, L. Progress in silica aerogel-containing materials for buildings' thermal insulation. *Construction and Building Materials* **286**, 122815. ISSN: 09500618 (2021).
14. Shea, K. J. & Loy, D. A. Bridged Polysilsesquioxanes . Molecular-Engineered Hybrid Organic - Inorganic Materials, 3306–3319 (2001).

15. Lamy-Mendes, A., Silva, R. F. & Durães, L. Advances in carbon nanostructure-silica aerogel composites: A review. *Journal of Materials Chemistry A* **6**, 1340–1369. ISSN: 20507496 (2018).
16. Strøm, R. A., Masmoudi, Y., Rigacci, A., Petermann, G., Gullberg, L., Chevalier, B. & Einarsrud, M. A. Strengthening and aging of wet silica gels for up-scaling of aerogel preparation. *Journal of Sol-Gel Science and Technology* **41**, 291–298. ISSN: 09280707 (2007).
17. Vareda, J. P., Lamy-Mendes, A. & Durães, L. A reconsideration on the definition of the term aerogel based on current drying trends. *Microporous and Mesoporous Materials* **258**, 211–216. ISSN: 13871811 (2018).
18. Kim, C. Y., Lee, J. K. & Kim, B. I. Synthesis and pore analysis of aerogel-glass fiber composites by ambient drying method. *Colloids and Surfaces A: Physico-chemical and Engineering Aspects* **313–314**, 179–182. ISSN: 09277757 (2008).
19. Baetens, R., Jelle, B. P. & Gustavsen, A. Aerogel insulation for building applications: A state-of-the-art review. *Energy and Buildings* **43**, 761–769. ISSN: 03787788 (2011).
20. Xia, T., Yang, H., Li, J., Sun, C., Lei, C., Hu, Z. & Zhang, Y. Tailoring structure and properties of silica aerogels by varying the content of the Tetramethoxysilane added in batches. *Microporous and Mesoporous Materials* **280**, 20–25. ISSN: 13871811 (2019).
21. Egeberg, E. & Engell, J. Freeze Drying of Silica Gels Prepared From Siliciumethoxid. *Le Journal de Physique Colloques* **24**, C4–23–C4–28. ISSN: 0449-1947 (1989).
22. Ordóñez-Miranda, J., Ezzahri, Y. & Joulain, K. Size effects on the thermal conductivity of nano aerogels. *Therminic 2017 - 23rd International Workshop on Thermal Investigations of ICs and Systems* **2017-January**, 1–5 (2017).
23. Erbert, H. in *Aerogels handbook: Advances in Sol-Gel Derived Materials and Technologies* (eds Aegerter, M., Leventis, N. & Koebel, M.) 537–563 (Springer, 2011).
24. Kaganer, M. G. Thermal Insulation in Cryogenic Engineering. *IPST Press: Jerusalem, Israel* (1969).
25. Zhao, J. J., Duan, Y. Y., Wang, X. D. & Wang, B. X. An analytical model for combined radiative and conductive heat transfer in fiber-loaded silica aerogels. *Journal of Non-Crystalline Solids* **358**, 1303–1312. ISSN: 00223093 (2012).
26. Wei, G., Liu, Y., Zhang, X., Yu, F. & Du, X. Thermal conductivities study on silica aerogel and its composite insulation materials. *International Journal of Heat and Mass Transfer* **54**, 2355–2366. ISSN: 00179310 (2011).
27. Wong, J. C., Kaymak, H., Brunner, S. & Koebel, M. M. Mechanical properties of monolithic silica aerogels made from polyethoxydisiloxanes. *Microporous and Mesoporous Materials* **183**, 23–29. ISSN: 13871811 (2014).

28. Kocon, L & Phalippou, J. Aérogels . Aspect matériau. *Techniques de l'ingénieur* (2005).
29. Anouk, P. *Méthodologie de caractérisation microstructurale 3D de matériaux poreux structurés pour la thermiques* PhD thesis (2016).
30. Hrubesh, L. W. & Pekala, R. W. Thermal properties of organic and inorganic aerogels. *Journal of Materials Research* **9**, 731–738 (1994).
31. Neugebauer, A., Chen, K., Tang, A., Allgeier, A., Glicksman, L. R. & Gibson, L. J. Thermal conductivity and characterization of compacted, granular silica aerogel. *Energy and Buildings* **79**, 47–57. ISSN: 03787788 (2014).
32. Woignier, T., Primera, J., Alaoui, A., Etienne, P., Despestis, F. & Calas-Etienne, S. Mechanical Properties and Brittle Behavior of Silica Aerogels. *Gels* **1**, 256–275. ISSN: 2310-2861 (2 Dec. 2015).
33. Pekala, R. W., Hrubesh, L. W., Alviso, C. T. & Lemay, D. A comparison of mechanical properties and scaling law relationships for silica aerogels and their organic counterparts (1990).
34. Arvidson, J. M. & Scull, L. L. Compressive Properties of Silica Aerogel at 295, 76, and 20 K. *Advances in Cryogenic Engineering Materials*, 243–250 (1986).
35. Faivre, A., Duffours, L., Colombel, P. & Despestis, F. Mechanical behaviour of aerogels and composite aerogels submitted to specific penetration tests. *Journal of Sol-Gel Science and Technology* **90**, 67–75 (2018).
36. Gronauer, M., Kadur, A. & Fricke, J. Mechanical and Acoustic Properties of Silica Aerogel. *Springer Proceedings in Physics Aerogels*, 167–173 (1986).
37. Gonçalves, W., Morthomas, J., Chantrenne, P., Perez, M., Foray, G., Martin, C. L. & Foray, G. Elasticity and strength of silica aerogels: A molecular dynamics study on large volumes. *Acta Materialia* **145**, 165–174. ISSN: 13596454 (2018).
38. Haranath, D., Wagh, P. B., Pajonk, G. M. & Rao, A. V. Influence of sol-gel processing parameters on the ultrasonic sound velocities in silica aerogels. *Materials Research Bulletin* **32**, 1079–1089. ISSN: 00255408 (8 1997).
39. Phalippou, J, Woignier, T, Rogier, R, Phalippou, J, Woignier, T & Rogier, R. Fracture toughness of silica aerogels. **50** (1989).
40. Kucheyev, S. O., Hamza, A. V., Satcher, J. H. & Worsley, M. A. Depth-sensing indentation of low-density brittle nanoporous solids. *Acta Materialia* **57**, 3472–3480. ISSN: 13596454 (12 2009).
41. Marshall, D. B., Cook, R. F., Padture, N. P., Oyen, M. L., Pajares, A., Bradby, J. E., Reimanis, I. E., Tandon, R., Page, T. F., Pharr, G. M. & Lawn, B. R. The Compelling Case for Indentation as a Functional Exploratory and Characterization Tool. *Journal of the American Ceramic Society* **98**, 2671–2680 (2015).
42. Rao, A. V., Bhagat, S. D., Hirashima, H. & Pajonk, G. M. Synthesis of flexible silica aerogels using methyltrimethoxysilane (MTMS) precursor. *Journal of Colloid and Interface Science* **300**, 279–285. ISSN: 00219797 (1 Aug. 2006).



43. Kassou (Benane), B. *Mécanique des lits de silices granulaires pour l'optimisation des cœurs de panneaux isolants sous vide (PIV)* PhD thesis (2018).
44. Rouanet, S., Floess, J. & Eberhardt, H. Aerogels for optimized performance in vacuum insulation panels. *International SAMPE Symposium and Exhibition (Proceedings)* **46**, 1263–1270 (Jan. 2001).
45. Liang, Y., Wu, H., Huang, G., Yang, J. & Wang, H. Thermal performance and service life of vacuum insulation panels with aerogel composite cores. *Energy and Buildings* **154**, 606–617. ISSN: 03787788 (Nov. 2017).
46. Zimmerman, M. Vacuum insulation - Challenges and opportunities for becoming a standard insulation technology. *8th international vacuum insulation symposium* (2007).
47. Gonçalves, M., Simões, N., Serra, C. & Flores-Colen, I. A review of the challenges posed by the use of vacuum panels in external insulation finishing systems. *Applied Energy* **257**, 114028 (2020).
48. Isaia, F., Fantucci, S., Capozzoli, A. & Perino, M. Vacuum Insulation Panels: Thermal Bridging Effects and Energy Performance in Real Building Applications. *Energy Procedia* **83**, 269–278 (2015).
49. Morel, B. *Vieillissement thermohydrrique de silices nanométriques* PhD thesis (Université François-Rabelais, 2008).
50. *What is a Vacuum Insulation Panel?* <https://www.kingspan.com/meati/en-in/product-groups/insulation/knowledge-base/articles/general/what-is-a-vacuum-insulation-panel>.
51. Buratti, C., Merli, F. & Moretti, E. Aerogel-based materials for building applications: Influence of granule size on thermal and acoustic performance. *Energy and Buildings* **152**, 472–482 (2017).
52. Gao, T., Jelle, B. P., Ihara, T. & Gustavsen, A. Insulating glazing units with silica aerogel granules: The impact of particle size. *Applied Energy* **128**, 27–34 (2014).
53. Nosrati, R. H. & Berardi, U. Hygrothermal characteristics of aerogel-enhanced insulating materials under different humidity and temperature conditions. *Energy and Buildings* **158**, 698–711 (2018).
54. Berardi, U. Aerogel-enhanced systems for building energy retrofits: Insights from a case study. *Energy and Buildings* **159**, 370–381 (2018).
55. Cuce, E., Cuce, P. M., Wood, C. J. & Riffat, S. B. Toward aerogel based thermal superinsulation in buildings: A comprehensive review. *Renewable and Sustainable Energy Reviews* **34**, 273–299 (2014).
56. *Spaceloft Insulation for Building and Construction* <https://www.aerogel.com/markets/building-and-construction/>.

57. Hanif, A., Diao, S., Lu, Z., Fan, T. & Li, Z. Green lightweight cementitious composite incorporating aerogels and fly ash cenospheres – Mechanical and thermal insulating properties. *Construction and Building Materials* **116**, 422–430 (2016).
58. Zeng, Q., Mao, T., Li, H. & Peng, Y. Thermally insulating lightweight cement-based composites incorporating glass beads and nano-silica aerogels for sustainably energy-saving buildings. *Energy and Buildings* **174**, 97–110 (2018).
59. Lu, J., Jiang, J., Lu, Z., Li, J., Niu, Y. & Yang, Y. Pore structure and hardened properties of aerogel/cement composites based on nanosilica and surface modification. *Construction and Building Materials* **245**, 118434 (2020).
60. Ng, S., Jelle, B. P., Zhen, Y. & Wallevik, H. Effect of storage and curing conditions at elevated temperatures on aerogel-incorporated mortar samples based on UHPC recipe. *Construction and Building Materials* **106**, 640–649 (2016).
61. Ng, S., Jelle, B. P. & Stæhli, T. Calcined clays as binder for thermal insulating and structural aerogel incorporated mortar. *Cement and Concrete Composites* **72**, 213–221 (2016).
62. *Sto-Aeverso Innendämmplatte* [https://www.stoag.ch/fr/produits/guide-produits/produktdetail\\_321011799.html](https://www.stoag.ch/fr/produits/guide-produits/produktdetail_321011799.html).
63. Yrieix, B., Morel, B., Foray, G. & Bogner, A. *Aerogel based material that is superinsulating at atmospheric pressure* Patent WO/2012/168617. 2012.
64. *Kwark® silica aerogel granules or powder* 2021. <https://enersens.eu/kwark/>.
65. Withers, P. J., Bouman, C., Carmignato, S., Cnudde, V., Grimaldi, D., Hagen, C. K., Maire, E., Manley, M., Plessis, A. D. & Stock, S. R. X-ray computed tomography. *Nature Reviews Methods Primers* **1**, 18. ISSN: 2662-8449 (1 Dec. 2021).
66. Villanova, J., Cloetens, P., Suhonen, H., Laurencin, J., Usseglio-Viretta, F., Lay, E., Delette, G., Bleuet, P., Jauffrès, D., Roussel, D., Lichtner, A. Z. & Martin, C. L. Multi-scale 3D imaging of absorbing porous materials for solid oxide fuel cells. *Journal of Materials Science* **49**, 5626–5634. ISSN: 15734803 (2014).
67. Zhao, B., Wang, J., Coop, M. R., Viggiani, G. & Jiang, M. An investigation of single sand particle fracture using X-ray micro-tomography. *Géotechnique* **65**, 625–641 (2015).
68. Wang, W. & Coop, M. R. Breakage behaviour of sand particles in point-load compression. *Géotechnique Letters* **8**, 61–65 (2018).
69. Foray, G., Chal, B., Perret, A., Roiban, L., Masenelli-Varlot, K. & Maire, E. in *Translucent silica aerogel: properties, preparation and applications* (ed Buratti, C.) 306 (Nova Science publishers., 2019). ISBN: 978-1-53615-329-3.
70. *Fiji - ImageJ* <https://imagej.net/Fiji>. Accessed: 2020-15-12.
71. Oliver, W. C. & Pharr, G. M. *An improved technique for determining hardness and elastic modulus using load and displacement sensing indentation experiments* (1992), 1564–1583.

72. Fischer-Cripps, A. C. *Nanoindentation* (Springer, 2002).
73. Philippe, C. *Détermination des propriétés mécaniques de céramiques poreuses par essais de microindentation instrumentée sphérique* PhD thesis (2013).
74. Li, X. & Bhushan, B. A review of nanoindentation continuous stiffness measurement technique and its applications. *Materials Characterization* **48**, 11–36 (2002).
75. *ASTM D5045 - 14* <https://www.astm.org/Standards/D5045.htm>.
76. Nielsen, C., Amirkhizi, A. V. & Nemat-Nasser, S. The effect of geometry on fracture strength measurement using DCDC samples. *Engineering Fracture Mechanics* **91**, 1–13. ISSN: 00137944 (2012).
77. He, M. Y., Turner, M. R. & Evans, A. G. Analysis of the double cleavage drilled compression specimen for interface fracture energy measurements over a range of mode mixities. *Acta Metallurgica Et Materialia* **43**, 3453–3458. ISSN: 09567151 (1995).
78. Idonije, K., Motuku, M., Shehata, I. & Aglan, H. Evaluation of the stress intensity factor of brittle polymers based on the crack arrest concept. *Journal of Reinforced Plastics and Composites* **12**, 778–786. ISSN: 07316844 (1993).
79. Nielsen, C., Amirkhizi, A. V. & Nemat-Nasser, S. An empirical model for estimating fracture toughness using the DCDC geometry. *International Journal of Fracture* **188**, 113–118. ISSN: 15732673 (2014).
80. Collet, F. & Pretot, S. Thermal conductivity of hemp concretes : variation With formulation, density and water content. *Construction and Building Materials* **64**, 612–619 (2014).
81. Batty, W., Probert, S., Ball, M. & O’Callaghan, P. Use of the thermal-probe technique for the measurement of the apparent thermal conductivities of moist materials. *Applied Energy* **18**, 301–317. ISSN: 0306-2619 (1984).
82. Healy, J. J., de Groot, J. J. & Kestin, J. The theory of the transient hot-wire method for measuring thermal conductivity. *Physica B+C* **82**, 392–408. ISSN: 03784363 (1976).
83. Radjai, F. & Richefeu, V. Contact dynamics as a nonsmooth discrete element method. *Mechanics of Materials* **41**. Advances in the Dynamics of Granular Materials, 715–728. ISSN: 0167-6636 (2009).
84. Cundall, P. A. & Strack, O. D. L. A discrete numerical model for granular assemblies. *Géotechnique* **29**, 47–65 (1979).
85. Radi, K. Bioinspired materials : Optimization of the mechanical behavior using Discrete Element Method (2020).
86. André, D., Jebahi, M., Iordanoff, I., luc Charles, J. & Néauport, J. Ô. Using the discrete element method to simulate brittle fracture in the indentation of a silica glass with a blunt indenter. *Computer Methods in Applied Mechanics and Engineering* **265**, 136–147. ISSN: 00457825 (2013).

87. André, D., Girardot, J. & Hubert, C. A novel DEM approach for modeling brittle elastic media based on distinct lattice spring model. *Computer Methods in Applied Mechanics and Engineering* **350**, 100–122. ISSN: 00457825 (2019).
88. Le, B. D., Dau, F., Charles, J. L. & Iordanoff, I. Modeling damages and cracks growth in composite with a 3D discrete element method. *Composites Part B: Engineering* **91**, 615–630. ISSN: 13598368 (2016).
89. Leclerc, W., Haddad, H. & Guessasma, M. On the suitability of a Discrete Element Method to simulate cracks initiation and propagation in heterogeneous media. *International Journal of Solids and Structures* **108**, 98–114. ISSN: 00207683 (2017).
90. Kumar, R., Rommel, S., Jauffrès, D., Lhuissier, P. & Martin, C. L. Effect of packing characteristics on the discrete element simulation of elasticity and buckling. *International Journal of Mechanical Sciences* **110**, 14–21. ISSN: 00207403 (2016).
91. Liu, Q., Lu, Z., Zhu, M., Yuan, Z., Yang, Z., Hu, Z. & Li, J. Simulation of the tensile properties of silica aerogels: The effects of cluster structure and primary particle size. *Soft Matter* **10**, 6266–6277. ISSN: 17446848 (2014).
92. Guesnet, E., Bénane, B., Jauffrès, D., Martin, C. L., Baeza, G. P., Foray, G., Meille, S., Olagnon, C. & Yrieix, B. Why fumed and precipitated silica have different mechanical behavior: Contribution of discrete element simulations. *Journal of Non-Crystalline Solids* **524**, 119646. ISSN: 00223093 (2019).
93. Tatone, B. S. A. & Grasselli, G. International Journal of Rock Mechanics & Mining Sciences A calibration procedure for two-dimensional laboratory-scale hybrid finite – discrete element simulations. *International Journal of Rock Mechanics and Mining Sciences* **75**, 56–72. ISSN: 1365-1609 (2015).
94. Hazay, M. Introduction to the Combined Finite- Discrete Element Method, 30–32 (2004).
95. Yan, C., Zheng, Y., Huang, D. & Wang, G. A coupled contact heat transfer and thermal cracking model for discontinuous and granular media. *Computer Methods in Applied Mechanics and Engineering* **375**, 113587. ISSN: 00457825 (2021).
96. Plimpton, S. Fast parallel algorithms for short-range molecular dynamics. *Journal of computational physics* **117.1**, 1–19 (1995).
97. Verlet, L. Computer experiments on classical fluids. I. Thermodynamical properties of Lennard-Jones molecules. *Physical review* **159.1**, 98 (1995).
98. Ogarko, V. & Luding, S. A fast multilevel algorithm for contact detection of arbitrarily polydisperse objects. *Computer Physics Communications* **183**, 931–936. ISSN: 00104655 (2012).
99. Burns, S. J., Piiroinen, P. T. & Hanley, K. J. Critical time step for DEM simulations of dynamic systems using a Hertzian contact model. *International Journal for Numerical Methods in Engineering* **119**, 432–451 (2019).

100. Martin C. L., B. D. & Shima, S. Study of particle rearrangement during powder compaction by the Discrete Element Method. *Journal of the Mechanics and Physics of Solids* **51**, 667–693 (2003).
101. C. L., M. Elasticity, fracture and yielding of cold compacted metal powders. *J. Mech. Phys. Solids* **52**, 1691–1717 (2004).
102. Martin C. L., B. D. & Delette, G. Discrete element simulations of the compaction of aggregated ceramic powders. *Journal of the American Ceramic Society* **89(11)**, 3379–3387 (2006).
103. Martin, C. L. & Bordia, R. K. Influence of adhesion and friction on the geometry of packings of spherical particles. *Phys. Rev. E* **77**, 31307 (2008).
104. Derjaguin, B., Muller, V. & Toporov, Y. Effect of contact deformations on the adhesion of particles. *Journal of Colloid and Interface Science* **53**, 314–326. ISSN: 0021-9797 (1975).
105. Potyondy, D. O. & Cundall, P. A. A bonded-particle model for rock. *International Journal of Rock Mechanics Mining Sciences* **41**, 1329–1364 (2004).
106. Carmona H. A., W. F. K. K. F. & Herrmann, H. J. Fragmentation processes in impact of spheres. *Physical Review E - Statistical, Nonlinear, and Soft Matter Physics* **77(5)**, 1–10 (2008).
107. Gladky, A. & Kuna, M. DEM simulation of polyhedral particle cracking using a combined Mohr–Coulomb–Weibull failure criterion. *Granular Matter* **19**, 41 (2017).
108. Guesnet, E. Modélisation du comportement mécanique et thermique des silices nano-architecturées (2018).
109. Agnolin, I & Roux, J.-N. Internal states of model isotropic granular packings. I. Assembling process, geometry, and contact networks. *Phys. Rev. E* **76**, 61302 (2007).
110. Christoffersen J., M. M. M. & Nemat-Nasser, S. A Micromechanical Description of Granular Material Behavior. *Journal of Applied Mechanics* **48(2)**, 339 (1981).
111. Meille, S & Garboczi, E. J. Linear elastic properties of 2D and 3D models of porous materials made from elongated objects. *Modelling and Simulation in Materials Science and Engineering* **9**, 371–390 (2001).
112. Woignier, T., Primera, J., Alaoui, A., Despetis, F., Calas-Etienne, S., Faivre, A., Duffours, L., Levelut, C. & Etienne, P. *Techniques for characterizing the mechanical properties of aerogels* **1**, 6–27. ISBN: 1097101905173 (2020).
113. Wang, G. S. The interaction of doubly periodic cracks. **42**, 249–294 (2004).
114. Kim, J.-K. & Mai, Y.-W. *Engineered interfaces in fiber reinforced composites* (Elsevier, 1998).
115. Chou, T.-W. *Microstructural Design of Fiber Composites* (Cambridge University Press, 1992).

116. McDowell, G. R. & Bolton, M. D. On the micromechanics of crushable aggregates. *Geotechnique* **48**, 667–679. ISSN: 00168505 (1998).
117. Weibull, W. A statistical theory of the strength of materials. *Generalstabens Litografiska Anstalts Förlag* (1939).
118. Lu, C., Danzer, R. & Fischer, F. D. Scaling of fracture strength in ZnO: Effects of pore/grain-size interaction and porosity. *Journal of the European Ceramic Society* **24**, 3643–3651. ISSN: 09552219 (2004).
119. Zok, F. W. On weakest link theory and Weibull statistics. *Journal of the American Ceramic Society* **100**, 1265–1268. ISSN: 15512916 (2017).
120. Huillca, Y., Silva, M., Ovalle, C., Quezada, J. C., Carrasco, S. & Villavicencio, G. E. Modelling size effect on rock aggregates strength using a DEM bonded-cell model. *Acta Geotechnica* **0123456789**. ISSN: 18611133 (2020).
121. Radi, K., Jauffrès, D., Deville, S. & Martin, C. L. Elasticity and fracture of brick and mortar materials using discrete element simulations. *Journal of the Mechanics and Physics of Solids* **126**, 101–116. ISSN: 00225096 (2019).
122. Hiramatsu, Y. & Oka, Y. Determination of the tensile strength of rock by a compression test of an irregular test piece. *International Journal of Rock Mechanics and Mining Sciences* **3**, 89–90. ISSN: 01489062 (1966).
123. De Larrard, F. Concrete optimisation with regard to packing density and rheology (Aug. 2009).
124. Kucheyev, S. O., Stadermann, M., Shin, S. J., Satcher, J. H., Gammon, S. A., Letts, S. A., Van Buuren, T. & Hamza, A. V. Super-compressibility of ultralow-density nanoporous silica. *Advanced Materials* **24**, 776–780. ISSN: 09359648 (2012).
125. Hedjazi, L., Martin, C., Guessasma, S., Della Valle, G. & Dendievel, R. Application of the Discrete Element Method to crack propagation and crack branching in a vitreous dense biopolymer material. *International Journal of Solids and Structures* **49**, 1893–1899. ISSN: 0020-7683 (2012).
126. Carlsson, J. & Isaksson, P. Crack dynamics and crack tip shielding in a material containing pores analysed by a phase field method. *Engineering Fracture Mechanics* **206**, 526–540. ISSN: 00137944 (2019).
127. Woignier, T., Despetis, F., Alaoui, A., Etienne, P. & Phalippou, J. Mechanical Properties of Gel-Derived Materials. *J. Sol-Gel Sci. Technol.* **19**, 163–169 (2000).
128. Stukowski, A. Visualization and analysis of atomistic simulation data with OVITO - the Open Visualization Tool. *Modelling and Simulation in Materials Science and Engineering* **18**, 015012. ISSN: 0965-0393 (2010).
129. Quenard, D. in *2nd International Symposium on nanotechnology in construction Bilbao* (2005).







